The Effects of Capillary Hysteresis on the Measurement of Matric Suction Using Thermal Conductivity Sensors

A Thesis

Submitted to the College of Graduate Studies and Research

in Partial Fulfillment of the Requirements

for the Degree of

Master of Science

in the

Department of Civil Engineering

University of Saskatchewan

Saskatoon, Canada

by

Man Feng

Spring 1999

Copyright

Acknowledgements

The author would like to take this opportunity to express his thanks to his supervisor, Professor D. G. Fredlund for his guidance and support.

The author would also like to thank many people in the geotechnical group at the University of Saskatchewan for their assistance and information provided during the course of this study. Thanks are extended to Dr. Fangshen Shui and Mr. Y. Jamshid who provided much of the valuable assistance in the laboratory work. The author is particularly grateful to Mr. Dale Pavier who made the first editing of the manuscripts of this thesis and provided other valuable assistance.

The author would also like to express special thanks to his friends, colleagues, family, and especially his wife, who provided support and encouragement throughout the course of this project.

Abstract

Matric suction has proven to be a key parameter in the study and application of soil mechanics for unsaturated soils. Field measurements of suction are necessary in many engineering analyses, such as the prediction of total heave, the analysis of the slope stability due to changes in soil suction, and the monitoring of moisture flux through a soil cover or barrier structure used to impede contaminant transport. There are a number of methods to measure soil suction in the field. The thermal conductivity sensor proves to be one of the most promising means of *in situ* suction measurement.

The thermal conductivity sensor measures matric suction by measuring the rate of dissipation of thermal energy in the ceramic sensor tip. The thermal diffusivity of the ceramic is dependent upon the water content of the ceramic. The water content is a function of the matric suction in the surrounding soils. This function is referred to as capillary function or soil-water characteristic curve and exhibits hysteresis. In other words, the same value of matric suction may correspond to different ceramic water contents, thus different sensor outputs, depending upon the drying and wetting history. The objective of this study is to investigate the properties of capillary hysteresis of the sensor ceramic and its effects on the measurement of matric suction.

Two groups of laboratory tests involving drying and wetting processes were carried out; one group measured the relationship between water content and matric suction of the sensor ceramics, the other group measured the relationship between sensor output and matric suction for a newly developed sensor. The result shows that, although the hysteresis loop is relatively narrow compared with those of coarse-grained materials found in the literature, the effects of capillary hysteresis on suction measurement using the thermal conductivity sensor are not negligible. If the capillary hysteresis is not taken into account, the maximum possible relative error of suction measurement caused by the capillary hysteresis is from 24% to 50% for the sensors used in the tests. The problems associated with the conventional method of calibration are also discussed in the thesis.

To make the suction measurement more accurate, the sensor output versus suction relationship of each of the possible wetting and drying processes should be measured in calibrating the sensor. However this calibration is impractical. Therefore, it is desirable to predict the hysteresis curves from limited measured data using a mathematical procedure.

There are a number of models found in the literature to simulate the capillary hysteresis of a porous material. Some of these models were examined using the experimental data of the sensor ceramic. It was found that the models in the literature either require a large amount of measured data to make the prediction, or fail to reproduce the measured curves of hysteresis. Therefore, an analytical approximation was developed which used a curve fitting method to fit the measured main drying curve and to predict the main wetting curve and the primary scanning curves.

Based on the above experimental and modeling studies, suggestions were made on the calibration of the sensor.

Table of Contents

List of Figures

List of Tables

CHAPTER 1

Introduction

1.1 BACKGROUND

The study of soil mechanics has largely concentrated on the properties of saturated soils as a result of Terzaghi's convincing evidence in support of the principle of effective stress in the mid of 1930's. However, the climatic conditions that give rise to the development of unsaturated soils can be found on every continent. Engineers are aware that many of the problems encountered in practice involve unsaturated soils. The construction of earth filled dams, highways and airport runways all make use of compacted unsaturated soils. The main property that makes an unsaturated soil distinct from, and more complex than, a saturated soil, is that the pore-water pressure in an unsaturated soil is negative.

A single stress state variable, the effective stress, $(\sigma - u_w)$, can be used to satisfactorily describe the stress state and predict the behavior of a saturated soil. Since the early 1950's, attempts have been made to extend the concept of effective stress to unsaturated soils. However, all these efforts encountered difficulties in describing the behavior of unsaturated soils. Fredlund and Morgenstern (1977) suggested the use of any two combination of the three stress state variables, $(\sigma - u_w)$, $(\sigma - u_a)$ and $(u_a - u_w)$, to describe the stress state of an unsaturated soil. The net normal stress, $(\sigma - u_a)$, and matric suction, $(u_a - u_w)$, are chosen for their clarity in physical meaning and convenience in practical applications.

The net normal stress, $(\sigma - u_a)$, is usually easier to determine since the pore-air pressure, (u_a), can be considered to be zero when the soils is exposed to atmospheric

air pressure. Thus the determination of matric suction, $(u_a - u_w)$, becomes a key factor in applying the theory of unsaturated soil mechanics in solving the engineering problems associated with unsaturated soils.

Field measurements of soil suction are necessary in many cases, such as the prediction of total heave, the analysis of the stability of a slope due to suction change, the monitoring of moisture flux through a soil cover or liner structure used to impede contaminant transportation, and automatic irrigation systems in agriculture. In all of these cases, the soil suction and suction change need to be monitored for a fairly long period. An accurate and reliable *in situ* suction measurement device for long term monitoring should be able to meet the following requirements:

(1) provides accurate and reliable suction readings,
(2) can accommodate a wide range of suction with an acceptable accuracy,
(3) sensitive to suction changes in the surrounding soils,
(4) insensitive to the dissolved salts in the pore-water and to the changes of ambient temperature,
(5) can be connected to an automatic data acquisition and controlling system, and
(6) have sufficient durability in the field soil environment.

Commonly used devices for measuring soil suction in the field include tensiometers, psychrometers, filter papers, and thermal conductivity sensors (Fredlund and Rahardjo, 1993).

The main disadvantage of the tensiometer is its low measuring range which is limited to less than 100kPa of suction. Suction measurements using psychrometers are highly susceptible to the ambient temperature. A controlled temperature environment of ± 0.001°C is required in order to measure total suction to an accuracy of ± 10 kPa (Krahn and Fredlund, 1972). Even though psychrometers are useful for measuring high suction in soil, *in situ* measurements of total suction using psychrometers are generally not recommended because significant temperature fluctuations occur in the field (Fredlund and Rahardjo, 1993).

The filter paper method appears to have a wide range of suction measuring capability. However, the measurement must be performed with great care (Fredlund and Rahardjo, 1993). Engineers are also concerned with the accuracy of suction measurement using filter paper (Al-Khafafa and Hanks, 1974; Greacen et al., 1987). Only the "non-contact" filter paper procedure can be assured of measuring total suction. The "contact" procedure could measure the matric suction or total suction depending on the contacts between the filter paper and the soil (van der Raadt et al., 1987). Furthermore, the filter paper is difficult to connect to an automatic monitoring system. The data have to be collected manually.

Thermal conductivity sensor proves to be one of the most promising means of *in situ* measurement of soil suction (Lee and Fredlund, 1984; Rahardjo et al., 1989; Sattler and Fredlund, 1989; Wang et al., 1989; Fredlund, 1992; Fredlund and Wong, 1993). The sensor is insensitive to ambient temperature and salinity changes, and can make relatively accurate matric suction measurement from a few kilopascals up to several hundreds kilopascals. Research done on the thermal conductivity sensor showed that the thermal conductivity sensor is sensitive to changes in suction in surrounding soils, and, if properly designed, can monitor suction in field soils over long periods of time (Loi et al., 1989). The sensor can also be connected to an automatic data acquisition and controlling system. All these properties of the thermal conductivity sensor make it suitable for *in situ* monitoring of soil suction. The next chapter provides a detailed description of the theory of operation of the thermal conductivity sensor.

There have been several types of thermal conductivity sensors commercially available. In the mid-1970's, Moisture Control System Inc. of Findlay, OH, manufactured MCS6000 thermal conductivity sensor. The sensor appeared to be quite suitable for field usage. Relatively accurate measurements of matric suction were obtained in the range of 0 to 300 kPa (Lee and Fredlund, 1984). Field monitoring study showed that the MCS6000 sensor was quite responsive. However, Moisture Control System Inc. discontinued production in early 1980, and the MCS6000 sensor is no longer commercially available.

In the early 1980's, Agwatronics Inc. in Merced, CA commenced production of the AGWA thermal conductivity sensor, which was replaced by a new design, the AGWA-II sensor in 1984. However, there have been difficulties and shortcomings experienced with the use of the AGWA-II sensors (Fredlund et al., 1992). These include the deterioration of the electronics with time, low strength and durability of the ceramic tips. Significant failure rate of the AGWA-II sensors was reported during long term monitoring (Wong et al., 1989). AGWA-II sensors are not commercially available.

To meet the need for a new thermal conductivity sensor of low cost and good performance, a research group was set up in the Department of Civil Engineering, University of Saskatchewan, in September 1996. The research program is sponsored by NSERC (National Science and Engineering Research of Canada) and a number of industrial organizations. The program includes the development of strong and durable ceramic tips that have a relatively wide range of pore size distribution to accommodate a wider range of suction measurements, the design of the electronics that provide accurate and sensitive measurement, and the development of a proper procedure for data interpretation in order to improve the accuracy of the measurement.

1.2 OBJECTIVES

Ambient temperature, salinity of pore-water in surrounding soils and wetting and drying hysteresis have been the main concerns in the measurement of matric suction using thermal conductivity sensors. Research done on MCS6000 and AGWA-II sensors showed that the thermal conductivity sensors are insensitive to environmental temperature and salinity changes and responsive to suction changes (Lee and Fredlund, 1984; van der Raadt et al., 1987; Sattler and Fredlund, 1989; Rahardjo et al., 1989). Although the phenomenon of wetting and drying hysteresis in using thermal conductivity sensor have been noticed for many years (Lee and Fredlund, 1984; Wong et al., 1989; Fredlund, 1992), little research has been done on the influence of dying and wetting hysteresis on the measurement of matric suction using thermal conductivity sensors.

Matric suction is measured by an indirect method with the thermal conductivity sensors. There are three relationships that indirectly relate the output of the sensor to the matric suction:

(1) the output of the thermal conductivity sensor is a voltage, which is inversely related to the thermal conductivity of the ceramic block,

(2) the thermal conductivity of the ceramic block is dependent upon the water content of the ceramic block, and

(3) the water content of the ceramic block is a function of the matric suction applied on the ceramic block by the surrounding soil.

The first two relationships are reversible, whereas, the third, the relationship between water content of the porous block and the matric suction in soil may be hysteretic. In other words, the water content of the porous block may be different for drying and wetting processes even the same matric suction is applied. The hysteresis of the relationship between the water content of a porous material and applied matric suction on the material is usually referred to as capillary hysteresis.

A part of the research program leading towards the development of a new thermal conductivity sensor is to develop a proper procedure of data interpretation that takes into account the hysteresis effects. The objective of this study is to investigate the effects of wetting and drying hysteresis on the suction measurement using the thermal conductivity sensor and includes,

(1) an investigation of the capillary hysteresis of the ceramic block of the new sensor developed by the research program,

(2) an evaluation of the effect of capillary hysteresis on the measurement of matric suction, and

(3) the development of a proper procedure for data interpretation that takes into consideration the effects of capillary hysteresis.

1.3 SCOPE OF THE THESIS

Almost all the studies done in the past decades on the capillary hysteresis of porous material are within two fields, fields of soil sciences and petroleum recovery research. Chapter 2 presents a literature review on research done on the properties of capillary

hysteresis, with an emphasis on water movement in porous material. Chapter 2 also includes a brief review of the theory of operation and the historical development of the thermal conductivity sensor.

There is an increasing awareness on the key role of the soil-water characteristic curve (SWCC) in solving problems in the area of unsaturated soil mechanics. A literature review on capillary hysteresis also provides information for research in other areas of unsaturated soil mechanics.

A preliminary design of a new sensor, sensor Beta-97, has been finished in the Department of Civil Engineering at the University of Saskatchewan, Canada. A small number of Beta-97 sensors have been produced for laboratory tests and field monitoring. Laboratory tests were carried out on the hysteresis of the water retention characteristics of the sensor ceramic and the output of the Beta-97 sensor. The test results are presented in Chapter 3.

Chapter 4 presents a discussion of the testing results, including the properties of the capillary hysteresis of the sensor ceramic, the influence of the capillary hysteresis on the matric suction measurement, and comments on the calibration procedure.

Attempts are made in Chapter 5 to find a proper hypothetical model or analytical approximation that is able to predict the hysteresis curves from a limited amount of calibrated data. Some of the available hypothetical models of capillary hysteresis are tested using the measured hysteresis data of the sensor ceramic and the hysteresis data of the sensor output.

Chapter 6 summarizes the research and makes recommendations for future studies.

CHAPTER 2

Theory and Literature Review

Extensive research has been done to study the use of porous material for measuring soil suction using the theory of heat conduction. This chapter summarizes some significant conclusions regarding the development, the application and the evaluation of the thermal conductivity sensor.

The capillary hysteresis properties of some porous materials have received profound study in the areas of soil sciences and petroleum disciplines. This chapter also reviews the experimental studies of the properties of water capillary hysteresis of porous materials and the development of the hypothetical models of capillary hysteresis.

2.1 THE THERMAL CONDUCTIVITY SENSOR

This section describes the thermal conductivity sensor, including the theory of operation, details of the structure, calibration and measurement procedures, and the development.

2.1.1 Theory of Operation

When a part of a solid body is heated, the heat will dissipate to the other area of the material. The rate of heat dissipation, or thermal diffusivity, within the solid body is a function of the specific heat, thermal conductivity and density of the material. The thermal diffusivity of a homogeneous, isotropic body is defined as

$$k = \frac{K}{\rho c} \tag{2.1}$$

where

k = thermal diffusivity of the material

K = thermal conductivity of the material

C = specific heat of the material

ρ = density of the material.

A thermal conductivity sensor consists of a cylindrical porous block containing a temperature sensing element and a miniature heater (Fig. 2.1).

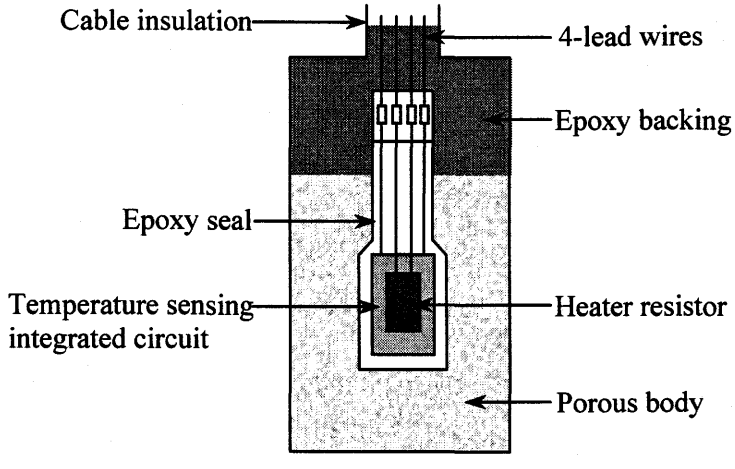

Figure 2.1 A cross-sectional diagram of the thermal conductivity sensor (from Phene et al., 1971a)

A thermal conductivity measurement is performed by measuring the rate of heat dissipation within the porous ceramic block. The heater at the center of the block converts a controlled amount electrical energy to thermal energy. A portion of the thermal energy will be dissipated throughout the porous block. Since air has a lower thermal conductivity, a lower specific heat and a lower density than water, the rate of thermal energy dissipation within the porous block will change with the water content of the porous block. When the porous block, the pore-water and the pore-air are taken as a whole unit, the thermal diffusivity of the block generally increase as a result of the

combination effects of the increases of thermal conductivity, specific heat and density of the block with the water content. More thermal energy will be dissipated as the water content in the block increase, and vice versa.

The undissipated energy will result in a temperature rise at the center of the porous block. The temperature rise is measured by the sensing element after a specific time interval, and its magnitude is inversely proportional to the water content of the porous block. The temperature rise is expressed in a voltage output.

The thermal diffusivity of the porous block varies in accordance with the water content of the block. The water content of the block is dependent upon the matric suction applied to the porous block by the surrounding soil. Therefore, the thermal diffusivity of the porous block can be calibrated with respect to an applied matric suction, as shown in Fig. 2.2.

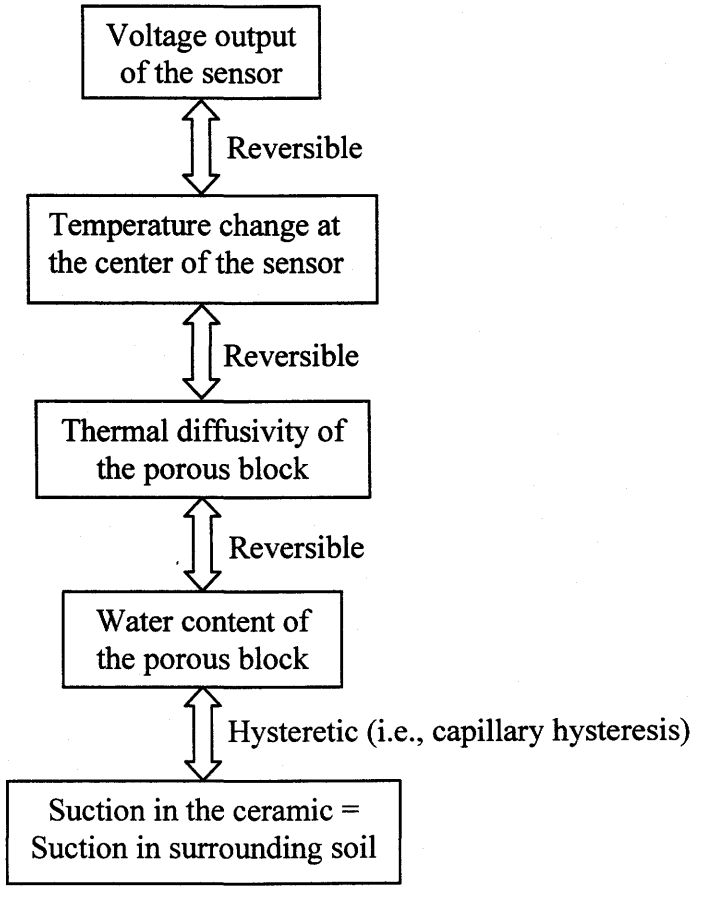

Figure 2.2 Indirect measurement of matric suction using thermal conductivity sensor

2.1.2 Historical Development and Evaluations

Shaw and Baver (1939), in their investigation of the thermal conductivity of soil, proposed an electrical device to determine the water content of the soil. The electrical circuit mainly consists of a Wheatstone Bridge, with one of the four resistors to be placed in soil. The resistance of the resistor increases with temperature. If a large electrical current is allowed to flow through the resistor, the temperature of the resistor continues to rise until it reaches a point where the heat dissipates into the surrounding soil as fast as it is generated by this resistor. The temperature rise at equilibrium is dependent upon the thermal diffusivity of the surrounding soil. The temperature rise of this resistor can be determined by its resistance change, which is in turn indicated by the current flowing through the micrometer of the Wheastone Bridge. It was found that the changes in salt concentration of pore-water did not significantly affect the thermal diffusivity of the soil (Shaw and Baver, 1939). However, as indicated by Cummings and Chandler (1940), since different soils have different relationships between thermal diffusivity and water content, each type of soil requires separate calibration in order to relate the thermal diffusivity measurements to the water content of the soil.

Johnston (1942) suggested that the thermal conductivity sensor be enclosed in a porous medium that had a calibration curve. The porous cover could then be brought into equilibrium with the soil under consideration. Johnson (1942) used plaster of paris to encase the heating and sensing elements.

Bloodworth and Page (1957) used a thermistor both as heating elements and as temperature indicator, and concluded that thermistor, when cast in porous material, served as an accurate moisture-indicating device. However, since the thermistor has a nonlinear resistance characteristic and will be affected by soil temperature, either a separated calibration or a correction is required for its use at a different temperature. Three materials were studied for use as a porous medium to enclose the electronics. These included plaster of paris, fired clay or ceramic, and dental stone powder–castone. The castone was found to be the best material for the porous medium (Bloodworth and Page, 1957).

Phene et al. (1971a and 1971b) presented a theoretical analysis and the construction details for a thermal conductivity sensor to eliminate several problems encountered in the past studies. A sensor was developed that used a P-N diode as the temperature sensor. The P-N diode was wrapped with 40-gauge Teflon-coated copper wire that served as the heating coil. The sensing and heating unit was embedded in a porous block. Gypsum, ceramic, and mixture of ceramic and castone were examined as potential porous block materials. It was found that the ceramic provides a solid stable matrix and a linear relationship of sensor output with matric suction between 0 and 600 kPa.

The matric suction of a porous body is dependent upon temperature. This dependence is also a function of the texture of material (Richardo and Weaver 1944). Phene et al. (1971b) calibrated their sensors under three different temperatures. It was found that matric suction was not temperature dependent at matric suctions lower than 1000 kPa for their sensors. For a castone porous body, the temperature dependence was significant in the higher suction range because of the decrease in sensitivity of the sensor.

It is desirable to keep the porous block as small as possible to shorten the time required for suction equilibrium between the porous block and the surrounding soils. However, the porous block must be large enough to contain the heat pulse within the block to eliminate the influence of the surrounding soil. Phene at al. (1971b) also presented a theoretical analysis of determining the dimensions of the porous block.

Based on the studies conducted by past researchers, Moisture Control System Inc. of Finlay, OH, USA, commercially developed the MCS6000 thermal conductivity sensor in the mid-1970s. The sensor consisted of two temperature sensing diodes, a miniature heater and electronic circuits. The temperature-sensing element and the heater were embedded in a cylindrical porous ceramic block that was contained in a Polyvinyl Chloride (PVC) module.

Based on the results of laboratory suction measurement using MCS6000 sensors, Lee and Fredlund (1984) concluded that the MCS6000 sensor was relatively sensitive and accurate in measuring soil suction up to 100 kPa. The sensor commences losing its sensitivity at higher suction value. At values of suction between 100 to 200

kPa, the sensor possesses an accuracy of approximately ±10% in terms of suction. For suction higher than 200 kPa the results are considered questionable. Temperature was also found to affect the results of MCS6000 sensor. As the ambient temperature increased the measured matric suction decreased (Lee and Fredlund, 1984).

The measured suction by sensors installed dry was higher than that measured by sensors installed saturated. Lee (1983) believed that was caused by the hysteresis of the relationship between matric suction and water content.

Moisture Control System Inc. ceased production of the MCS6000 in early 1980s, and the MCS6000 is no longer commercially available.

In 1981, Agwatronics Inc. in Merced, CA, USA, began production of the AGWA sensor based on the research by Phene et al. (1971a and 1971b). Because there were several difficulties associated with this sensor, the AGWA sensor was replaced by the AGWA-II sensor in 1984. The AGWA-II sensors consisted of a 1000 ohm heater and a thermistor embedded in a cylindrical ceramic block.

When evaluating the AGWA-II sensors, Wong et al. (1989) found that the AGWA-II sensor was relatively sensitive and accurate in measuring suction in the range of 175 kPa or lower. For higher suction, the sensitivity and accuracy was reduced because of the non-linear response of the sensor. The results also indicated that the sensor output was relatively stable with time. However, there were also some uncertainties and limitations associated with the sensor (Wong et al., 1989; Rahardjo et al., 1989; Fredlund, 1992). These included the sensor failure when submerged in water for a prolonged period and the low strength of the porous block. The AGWA-II sensors are no longer commercially available.

Fredlund et al. (1994) presented a detailed description on the design consideration of a thermal conductivity sensor, based on the research works conducted at the University of Saskatchewan. The design aspects that should be given consideration include the pore size distribution of ceramic block, the strength and durability of the ceramic block, the temperature sensor, the heating source, the sealant of electronics, and data acquisition systems. A research program on the development of a new thermal conductivity sensor is currently in progress in the Department of Civil Engineering, University of Saskatchewan.

2.1.3 Calibration and Measurement

Calibration is recognized as a first and fundamental step towards the use of the thermal conductivity sensor. The accuracy of measurement is dependent upon the calibration of the sensor. Fredlund and Wong (1989) and Fredlund (1992) presented a detailed calibration procedure for the thermal conductivity sensor using a modified pressure cell.

The sensor ceramic tip is saturated by submergence in water for a few days (Fredlund and Wong, 1989). The saturated sensor is then embedded in a soil slurry that is placed on the high air entry ceramic disk of the pressure cell. Matric suction is applied in increments by increasing the air pressure within the pressure cell, while maintaining the water pressure below the high air entry disk at atmospheric conditions. Each increment of suction is maintained constant for a sufficient time to allow the water flow to reach equilibrium. A calibration curve is obtained by plotting the applied suction versus the voltage output of the sensor at equilibrium under each suction increment.

A difficulty was experienced in using soil slurry as water flow media. If the soil contains a high percentage of clay, shrinkage of the soil generally occurs and the soil will lose full contact with the embedded sensors or with the high air entry disk, resulting in inaccurate measurement. If course-grained soil is used, the low water permeability of the coarse-grained soil at high suction generally makes the time for equilibrium too long and makes the calibration time consuming. A fine silty soil is recommended as this interface soil (Fredlund et al., 1992).

The method of using interface soil to embed sensors to provide water flow continuity has gradually been replaced by the method of using only a thin layer of kaolinite paste between the sensor and the high air entry disk. Because the kaolinite layer is thin, good contact can be assured at any suction value, meanwhile, the hydraulic conductivity of kaolinite at high suction (i.e., a few hundred kilopascals) is still relatively high.

A typical calibration curve for an AGWA-II sensor is shown in Fig. 2.3. The non-linear behavior of the AGWA-II sensors may be approximated by a bilinear curve as illustrated in Fig. 2.3 (Fredlund and Sattler, 1992).

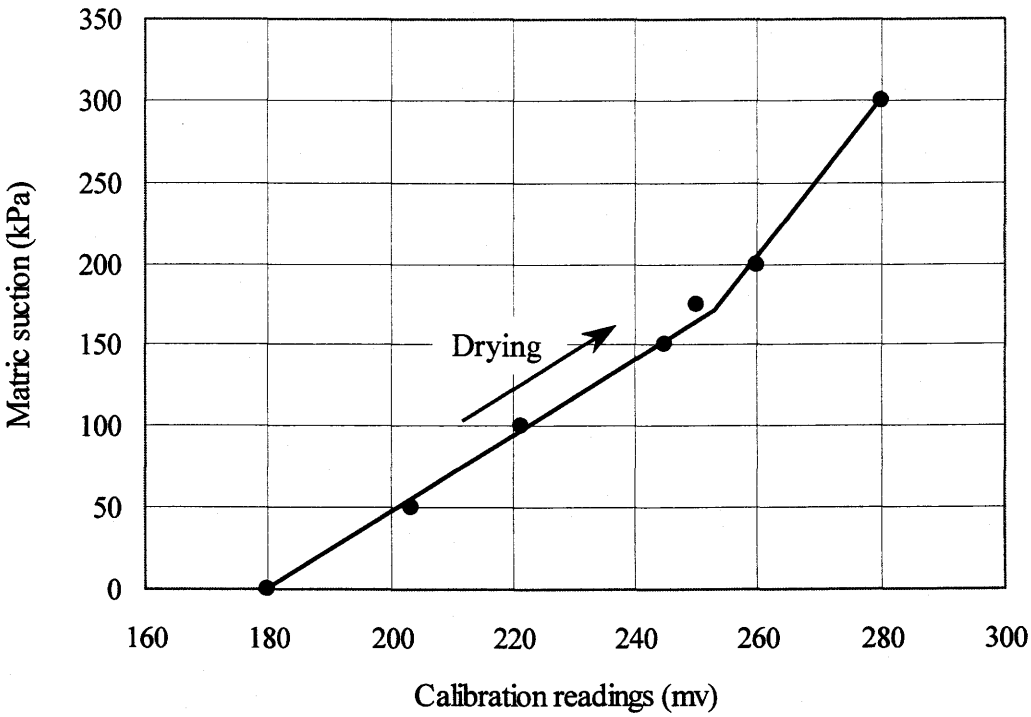

Figure 2.3 The calibration curve for an AGWA-II sensor (From Fredlund and Sattler, 1992)

The AGWA-II sensors have been used for laboratory and field measurements of matric suction on various soils (Fredlund et al., 1992; Loi et al., 1989; Sattler and Fredlund, 1989; Wong et al., 1989). Figure 2.4 shows the laboratory testing result on a highly plastic clay from Saskatchewan, Canada. The measurements were performed using two sensors. One sensor was initially saturated while the other sensor was initially dry. The response of both sensors were monitored immediately and at various elapsed times after their installation.

It was generally found that the two response curves did not yield the same value of suction at equilibrium. The suction measured by the initially dry sensor was usually slightly higher than that measured by the initially saturated sensor. This was believed

to be caused by hysteresis (Fredlund et. al., 1994). Little research has been done to-date on the hysteresis associated with the suction measurement using thermal conductivity sensors. It was also found the time required for the initially dry sensor to come to equilibrium with the soil specimen is less than the time required for the initially saturated sensor to come to equilibrium (Fredlund, 1992).

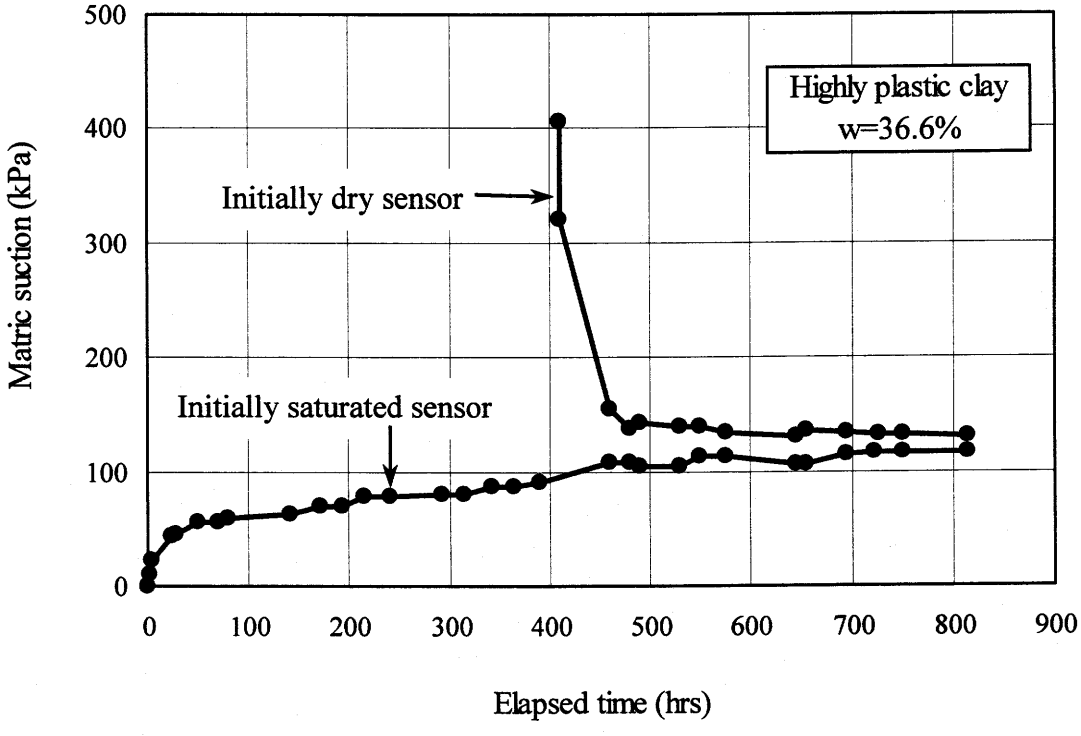

Figure 2.4 A result of the laboratory matric suction measurement using two AGWA-II sensors (From Fredlund and Rahardjo, 1988)

2.2 DEFINITIONS RELATED TO CAPILLARY HYSTERESIS

Terms associated with capillary hysteresis are defined in the following paragraphs, including surface tension, contact angle, capillary pressure, hysteresis, and soil-water characteristic curve.

2.2.1 Surface Tension

The air-water interface (i.e., contractile skin) is in a state of tension, which is called surface tension. The surface is said to be in a state of uniform tension if, (a) at each point, surface tension is perpendicular to a line dividing the surface to two parts and has the same value whatever the direction of this line, and (b) surface tension has the same value at all points in the surface (Dullien, 1979).

For mechanical equilibrium of the surface, the surface tension is balanced by the normal pressure exerted on both sides of the surface. The force equilibrium can be expressed by Laplace's equation,

$$P_1 - P_2 = 2\sigma \frac{1}{r_m} \tag{2.2}$$

Where

P_1 and P_2 = the normal pressure on both side of the surface

σ = the surface tension

r_m = the mean radius of curvature of the surface.

If the fluids are water and air, P_1 is the air pressure u_a, and P_2 is the water pressure u_w, then, Eq. (2.2) becomes,

$$u_a - u_w = 2\sigma \frac{1}{r_m} \tag{2.3}$$

Where

(u_a - u_w) = the difference between pore-air and pore-water pressures acting on the contractile skin, or the matric suction.

2.2.2 Contact Angle

Figure 2.5 shows a drop of liquid placed on a smooth plain solid surface. Liquid may remain a drop displaying a finite angle of contact between the two boundaries: liquid/gas and solid/liquid. In Fig. 2.5, σ_{lg} is the surface tension of the liquid-gas interface. σ_{sg} and σ_{sl} are forces of the same nature as the surface tensions that act on the line of contact and are associated with the solid-gas and solid-liquid interfaces, respectively. The contact angle is the angle defined by the tangent to the liquid/gas boundary constructed at a point on the three phase line of contact and the tangent to solid/liquid boundary constructed at the same point, as the angle θ shown in Fig. 2.5.

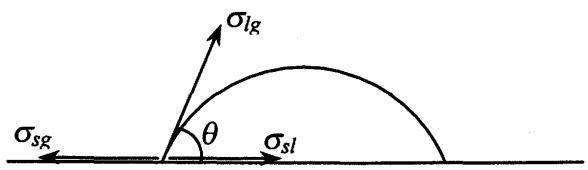

Figure 2.5 Schematic illustration of contact angle (from Dullien, 1979)

2.2.3 Capillary Pressure

Figure 2.6 shows a single circular capillary (pore) with variations in its cross sections. Suppose that the capillary is filled with a wetting liquid (e.g. water) and subsequently a non-wetting liquid (e.g. air) penetrates and displaces the wetting liquid until force equilibrium is achieved, as defined by the following equation (from Dullien, 1979),

$$P_1 - P_2 = \frac{2\sigma}{R}\left|\cos(\theta + \phi)\right| \qquad (2.4)$$

Where

P_1 and P_2 = the normal pressure on both side of the surface

R = the radius of the capillary

r = the radius of curvature of the surface.

The value of $(P_1 - P_2)$ is the pressure difference between the concave and convex side of the meniscus, and is defined as capillary pressure. If the wetting liquid is water and non-wetting liquid is air, the capillary pressure is equivalent to the matric suction $(u_a - u_w)$.

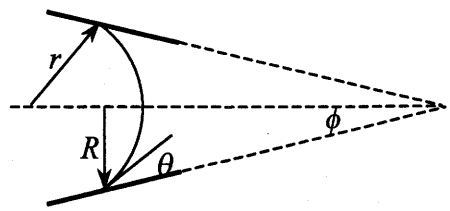

Figure 2.6 Menisci in a conical capillary (from Dullien, 1979)

2.2.4 Hysteresis

Hysteresis is a phenomenon in many processes, such as the magnetization of ferromagnetics, solid transitions in crystals and alloys, liquid movement in porous materials etc. (Everett and Whitton, 1952). Figure 2.7 shows a system defined by the independent and dependent variables.

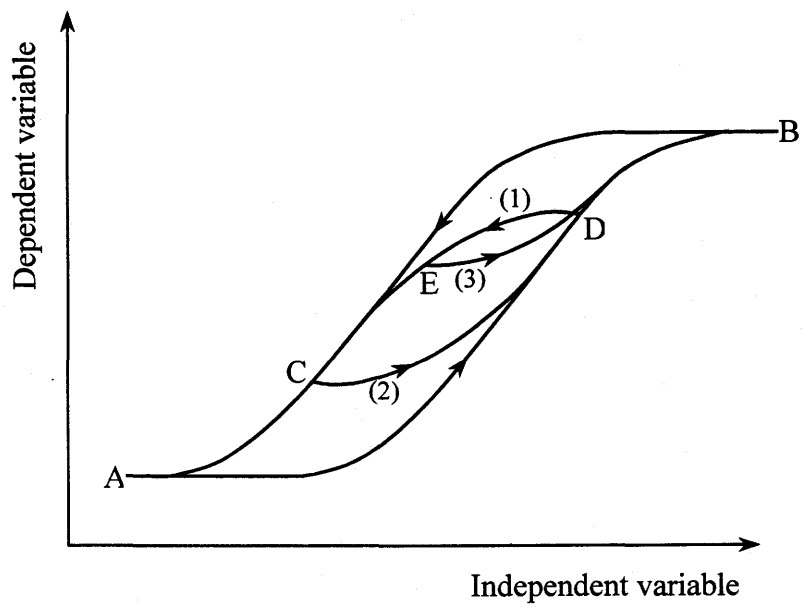

Figure 2.7 A hysterical process and the scanning curves

If the system is taken from state A to a state B along a given path the dependent variable will pass through a certain set of values, (i.e., ADB in Fig. 2.7). If now the independent variable is returned along the same path from B to A, the path taken by the dependent variable during the change from B to A is BCA. Even though the changes are carried out extremely slowly, the path of B to A, (i.e., BCA), is different from the path during the change from A to B (i.e., ADB). The term "hysteresis" is used to describe all phenomena of this type. Loop ADBCA is usually called the main hysteresis loop. The main hysteresis loop is reproducible.

If the direction of change of independent variable is reversed at a intermediate point between A and B, curves within the main hysteresis loop are obtained, such as curves 1, 2 and 3 in Fig. 2.7. These curves are called scanning curves. The scanning curves that have their starting points (i.e., the points of reversal) on either of the two branches of the main loop are referred to as primary scanning curves (curve 1 and 2 in Fig. 2.7). The scanning curves that have their starting points on the primary scanning curves or on other scanning curves are referred to as secondary scanning curves (curve-3 in Fig. 2.7).

When immiscible fluids flow into or out of a porous medium driven by capillary pressure, the flow may also exhibit hysteresis depending upon the direction of flow. The hysteresis of immiscible flow driven by the capillary pressure is referred to as the capillary hysteresis.

2.2.5 Capillary Pressure Function of a Porous Medium

The capillary pressure function of a porous medium is defined as the relationship between the content of the wetting fluid and the capillary pressure in the porous medium. In soil science and geotechnical engineering, this curve is also referred to as the soil-water characteristic curve. Figure 2.8 shows a typical plot of a soil-water characteristic curve, along with some of its key characteristics.

The initial drying curve in Fig. 2.8 is obtained by draining of an initially saturated sample to the point of residual saturation. The main wetting curve is obtained by rewetting the porous body from the point of residual saturation to zero

matric suction. Consequently draining of the porous body from zero suction to the point of residual saturation gives the main drying curve. Because air is entrapped in the pores when the porous body is rewetted, the initial drying curve is always located above the main hysteresis loop.

The air entry value is the suction at which air starts to enter into the pores of the porous body. The residual saturation is the degree of saturation where a large suction change is required to remove additional water from the porous body.

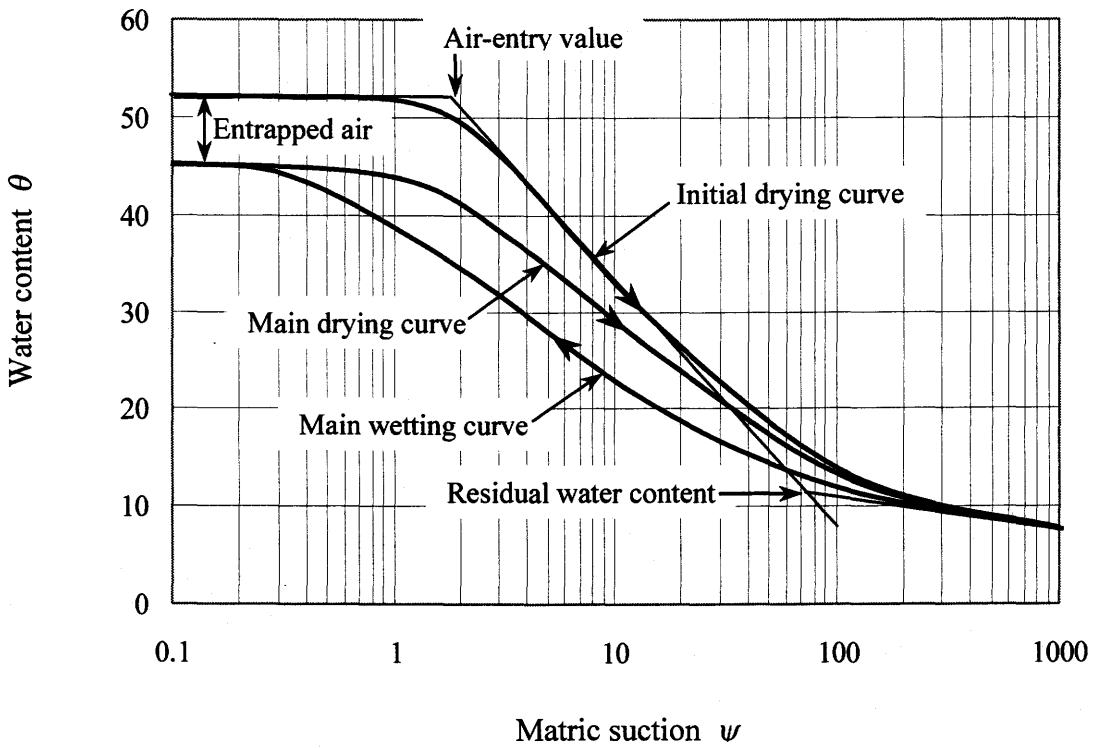

Figure 2.8 Schematic plot of a soil-water characteristic curve

2.3 CAUSES OF CAPILLARY HYSTERESIS

The flow of the mixture of air and water in a porous material is a complex phenomenon. Capillary hysteresis is related to a number of factors. The molecular interaction between the solid and fluid makes the capillary hysteresis more complicated. The following paragraphs describe some of the commonly recognized causes of capillary hysteresis, including the inkbottle effect, the contact angle hysteresis and the adsorption hysteresis.

2.3.1 Ink-bottle Effect (Haines jump)

A porous material is composed of solid matrix and randomly distributed pores of various sizes. Figure 2.9(a) shows two identical capillary tubes with irregular cross sections at right angle to a free water surface. The tube on the left is initially filled and then allowed to drain into the water reservoir (drying process), and the tube on the right is initially empty and then allowed imbibing water from the reservoir (wetting process).

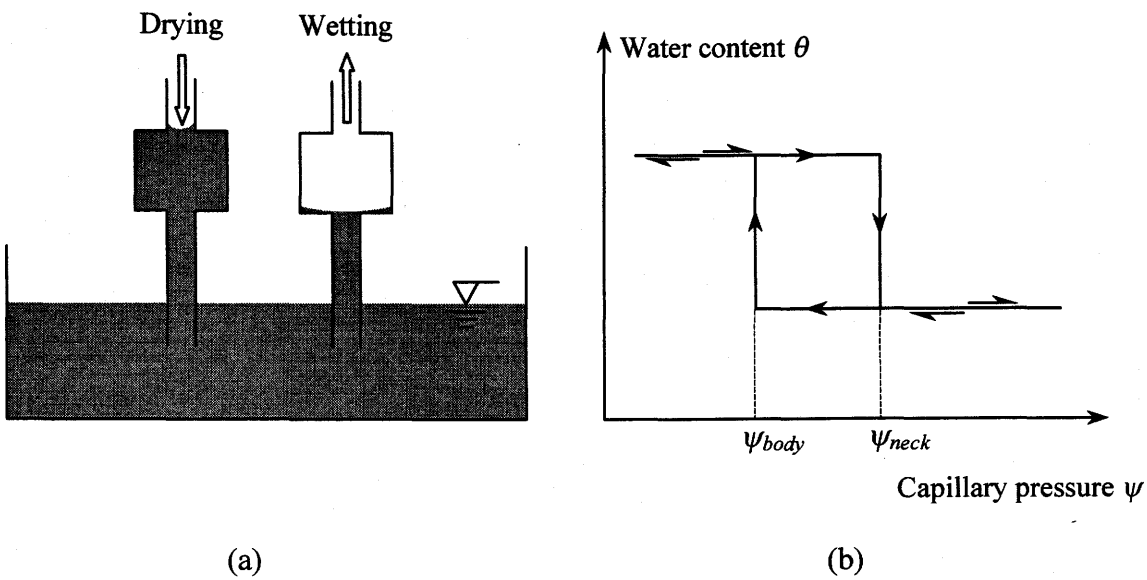

Figure 2.9 The ink-bottle effect on the capillary hysteresis

The emptying and filling of the pores are not reversible due to the difference in the size of the pore neck and the size of the pore body. When the pore is drying (i.e., suction increases), the factor limiting the water movement is the size of the pore neck, as illustrated in Fig. 2.9 (a). The suction must overcome the capillary pressure created by the air water interface within the pore neck, ψ_{neck}, before the pore itself can drain. Once this capillary pressure is overcome, the pore is drained spontaneously, or in a "jump action". When the pore is filling, the factor limiting the movement of water into the pore space is the size of the pore body. Water fills the pore neck but cannot enter the pore body until soil suction is sufficiently reduced to be below the capillary pressure corresponding to the radius of the pore body, ψ_{body} . The filling of the pore is also a spontaneous process. Figure 2.9 (b) is the capillary pressure function of this idealized pore.

The situation of an ordinary porous medium is, of course, much more complex than indicated by the simplified pore model, but it is supposed that an analogous mechanism exists in a porous medium. A porous medium can be assumed to be composed of a large amount of simplified pores with different body and neck size. The combination effect of the jump capillary hysteresis of all the pores makes a porous medium have smooth drying and wetting curves, and always contain more water on a drying process than on a wetting process.

The jump change hypothesis is usually called the ink-bottle effect, and also called "Haines jump", since Haines (1930) first described this phenomenon in trying to explain the capillary hysteresis of water flow in soils.

2.3.2 Contact Angle Hysteresis

The contact angle between an air-water interface and a solid surface exhibits hysteresis (Johnson and Dettre, 1964; Dettre and Johnson, 1964). The advancing angle (i.e., the contact angle measured when water moves towards a surface) is often found to be larger than the receding one (i.e., the contact angle measured when water recedes) (Morrow, 1974). According to Dullien (1979), there appear to be three types

of causes of contact angle hysteresis. The first is the contamination of either the liquid or the solid surface. Secondly, surface roughness causes contact angle hysteresis. The third cause appears to be the surface immobility on a macromolecular scale.

Morrow and co-workers (1965, 1967, and 1971) have performed a systematic study of the dependence of the capillary pressure function upon the contact angle. It was found that the advancing and receding contact angles measured at internally roughened tubes of PTFE (polytetra-fluoroethylene) differed substantially from the intrinsic contact angle measured at a smooth surface. The test results showed that there could be a significant contact angle hysteresis with a rough surface.

2.3.3 Adsorption Hysteresis

Adsorption hysteresis can be interpreted using Fig. 2.10 (Iwata et al., 1988). In Fig. 2.10(a) water exists between two flat surfaces that are parallel to each other. The distance between the surfaces is $2h_1$, and the thickness of adsorbed water is h_2. Water in state A is adsorbed by Van der Waals forces and the water in state B is retained by surface tension effects. Generally, h_1 is larger than h_2 when water under the two states is in equilibrium with the same water vapor pressure. The chemical potential of water in state A equals to that in state B. State A corresponds to a wetting process, and state B corresponds to a drying process.

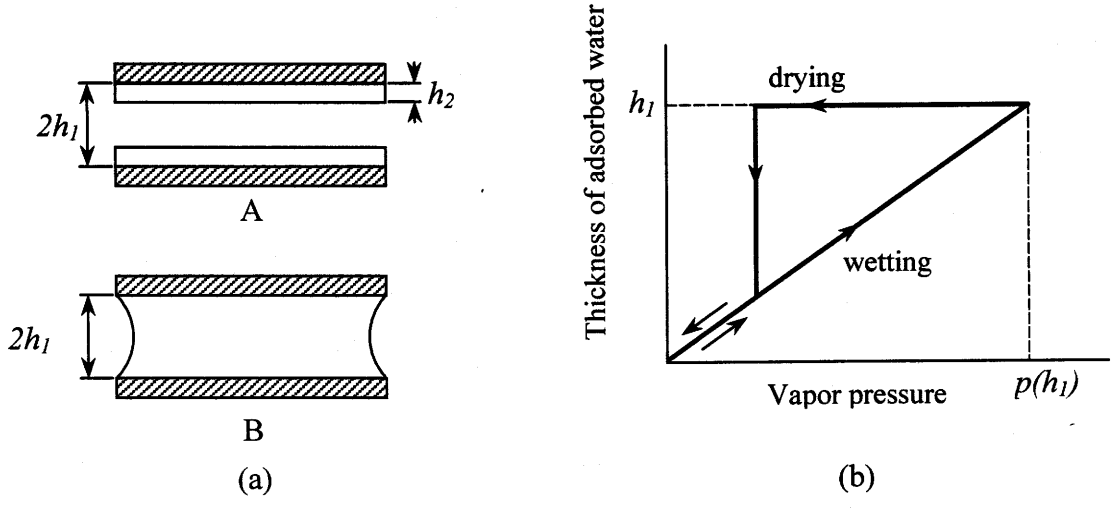

Figure 2.10 Schematic representation to explain hysteresis due to the capillary condensation (From Iwata et al., 1988)

The vapor pressure $p(h)$ is assumed to be in equilibrium with water of thickness h adsorbed by a flat clay surface. If vapor pressure is increased sufficiently slowly from zero to $p(h_1)$, the thickness of the adsorbed water increases to h_1 and the adsorbed water of the two surfaces is connected. The adsorbed water exists between the two surfaces in the state of B as shown in Fig. 2.10(a). If the vapor pressure is then decreased to zero again, the thickness of the adsorbed water will not change until the vapor pressure is lowered to a certain value. When this value of vapor pressure is reached, the adsorbed water will drain spontaneously. The relationship between water vapor pressure $p(h)$ and thickness of the adsorbed water h is given by the curves shown in Fig. 2.4(b). Evidently, the h - p relationship exhibits hysteresis. The mechanism described above may be regarded as capillary condensation that explains adsorption hysteresis. Other capillary condensation theories are described in detail by Everett (1967).

2.4 LABORATORY TESTS DONE ON CAPILLARY HYSTERESIS OF WATER FLOW IN POROUS MEDIA

Experiments dealing with the hysteresis in the soil-water characteristic curves of various types of soils have been conducted in laboratory and in the field. The main purpose of the tests was twofold, (1) to determine whether the hysteresis effects are significant or not, with respect to practical circumstances, and (2) to characterize properly the water capillary hysteresis in porous media. This section presents a brief review of the test procedures and some of the typical results.

2.4.1 Test Methods

Five methods of determining water content and suction relationship are known, but there are innumerable variations of each. The methods are,

Long column method - A long column of a porous medium is allowed to reach equilibrium in the earth's gravitational field with a source of water at its base and an infiltration at a certain rate at its top. The suction and the water content at different heights are controlled by changing the rate of infiltration at the top of the column.

When the rate of infiltration is increased or decreased, the soil experiences a wetting process or a drying process, correspondingly. Water content is measured by gamma ray attenuation. The suction is monitored at different heights in the column using tensiometers. This method is useful for determining water content versus suction and permeability versus suction relationships at relatively low values of suction only (Collins, 1961; Poulovassilis, 1970; Topp, 1971).

Centrifuge – A short column of initially saturated porous material is placed in a centrifuge. The centrifuge is run at a fixed angular velocity until the water contained in the sample has reached equilibrium with the centrifugal force imposed by the rotation. The water content is measured and the suction is calculated. The centrifuge method has been used mostly for obtaining the water content versus suction relationship on a drying cycle (Russell and Richards, 1938).

Vapor pressure – A sample of a porous material with known water content is placed in a closed container and the evaporative flux is allowed to equalize inside the container. The suction in the sample is correlated with the vapor pressure of water at equilibrium. This method is used mostly for the measurement of high suctions. The time required for equilibrium is usually long (Wilson, 1990).

Pressure cell – The pressure cell test is also called the pressure plate test (ASTM D2325). A sample of porous medium is placed in contact with another fully saturated porous medium (usually a pressure plate) having an air entry value such that it will not desaturated at any suction imposed during the experiment. The water is connected to the other side (usually underneath the pressure plate). Suction is imposed on the sample by regulating the air pressure above the pressure plate or the water pressure underneath the plate. The water content of the sample is determined by weighing the sample or by measuring the amount of water that was drained or imbibed (Richards and Fireman, 1943). This method was used in the experimental program of this thesis.

Brooks method – A method has been devised by R. H. Brooks (1980) which has great utility in respect to obtaining water content versus suction relationships on an imbibition cycle. With the Brooks system, a carefully metered quantity of water is added to a porous sample. After the water pressure in the porous sample reaches

equilibrium, the suction is measured using a pressure cell. The water content is determined from the known quantity of water added.

Method 1, the long column method, has been extensively used by most of the researchers dealing with the hysteresis of water flow in soil. The relationships between two of the three parameters, water content, suction and coefficient of permeability, can be measured simultaneously. In this thesis, only the work done on the relationship between water content and suction is discussed.

2.4.2 Materials and Typical Test Results

Typical laboratory and field tests on the hysteresis of water content versus suction relationships are shown in Table 2.1 chronologically. Most of the tests were carried out in the 1960s and 1970s. The materials used as porous media were mostly of coarse-grained materials, including glass beads, sands and loam.

Table 2.1 A summary of the experiments found in the literature on the water capillary hysteresis of porous media

	Author(s)	Sample	Method	Material(s)	Max. suction (kPa)
1962	Poulovassilis	Remolded	Tension plate	Glass beads	2.6
1966	Topp & Miller	Remolded	Long column (unsteady)	Glass beads	8.0
1967	Cary	Remolded	Pressure cell	Sand	33.3
1969	Topp	Remolded	Long column (unsteady)	Sandy loam	28.0
1970	Poulovassilis	Remolded	Long column (steady)	Glass beads	2.8
1970	Poulovassilis	Remolded	Long column (steady)	Sand	3.8

Table 2.1 A summary of the experiments found in the literature on the water capillary hysteresis of porous media (continued)

	Author(s)	Sample	Method	Material(s)	Max. suction (kPa)
1970	Tzimas	Remolded		Sand	9.0
1970	Poulovassilis	Remolded	Long column (steady)	Sand	5.2
1971	Topp	Remolded	Long column (unsteady)	Silty loam, Clay loam	40.0
1971	Vachaud & Thony	Remolded	Long column	Sand	10.0
1975	Royer & Vachaud	Field		Sand & Chalky clay	40.0
1975	Waston, Reginato & Jackson	Field		Clay loam	60.0
1975	Poulovassilis	Remolded	Long column	Sand	5.2
1979	Tzimas	Undisturbed	Long column	Sand	7.5

In the early period of the research, glass beads were tested (Poulovassilis, 1962; Topp and Miller, 1966; Poulovassilis, 1970). The glass beads of various grades were mixed and sintered or compacted together to form a porous medium. The time required for equilibrium for a suction increment is fairly short for such materials. Poulovassilis (1962) reported that the equilibrium time varied from 3 to 24 hours for a sintered glass beads body of various grades, depending upon the prevailing suction. The suction required to drain the glass beads materials to the residual saturation was low. Topp and Miller (1966) reported that the suction at the residual saturation was only 8 kPa for the glass beads material used in their tests (Table 2.1).

Sands, silty loam, sandy loam and clay loam were also tested. All of these materials were either coarse-grained or loosely compacted, with big pore size and high

saturation permeability. The suction at residual saturation (or maximum suction) was generally smaller than 40 kPa. Even for a clay loam, with a dry density of 1280 Mg/m^3 and a porosity of 0.525, the suction at residual saturation is only 42.5 kPa (Topp, 1971).

Laboratory tests carried out by most of the researchers show a significant hysteresis in relationships of water content versus suction for coarse-grained materials. Figure 2.11(a) and (b) show the hysteresis loop and primary scanning curves of the Rubicon sandy loam (Topp, 1969).

Field measurements on the hysteresis in the relationships between water content and suction were also carried out (Royer and Vachaud, 1975; Waston, 1975). Figure 2.12 shows the field monitoring results on Bouron fine sand (Royer and Vachaud, 1975). The measurement was made for eight months, with three raining periods, May 10 to 19 (45mm of rain), August 10 to 15 (74mm of rain) and November 14 to December 10 (a fairly wet period), and three continuous or discontinuous drainage periods. This field monitoring result clearly shows that the capillary hysteresis in field condition is as significant as the laboratory results and gives almost the same shape and hysteresis loop and scanning curves.

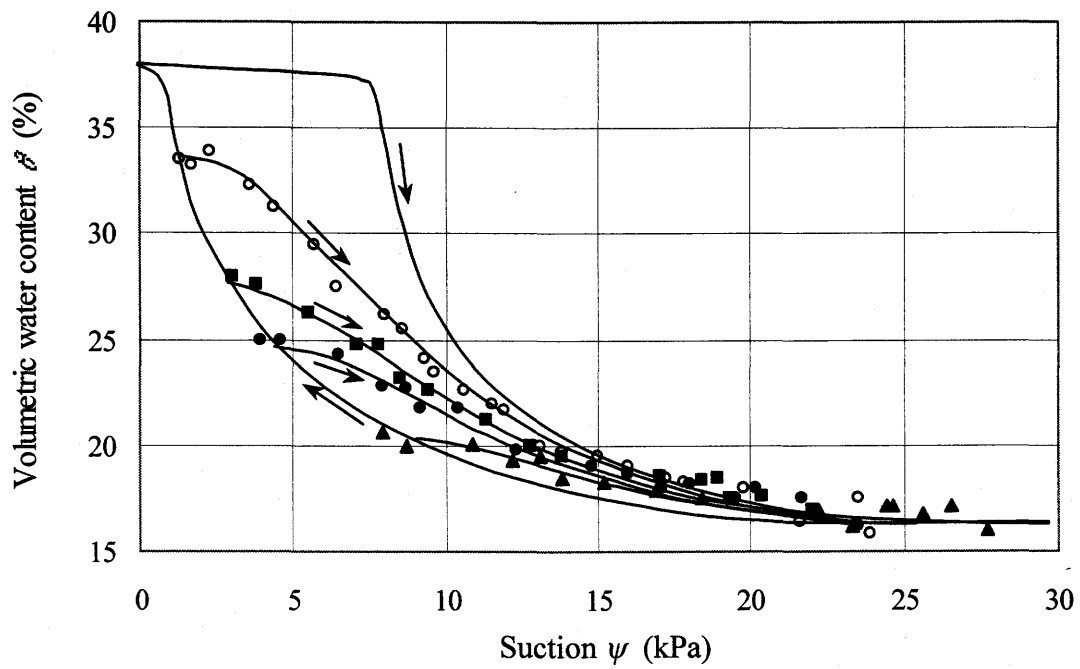

Figure 2.11(a) Main hysteresis loop and primary drying scanning curves of the Rubicon sandy loam (From Topp, 1969)

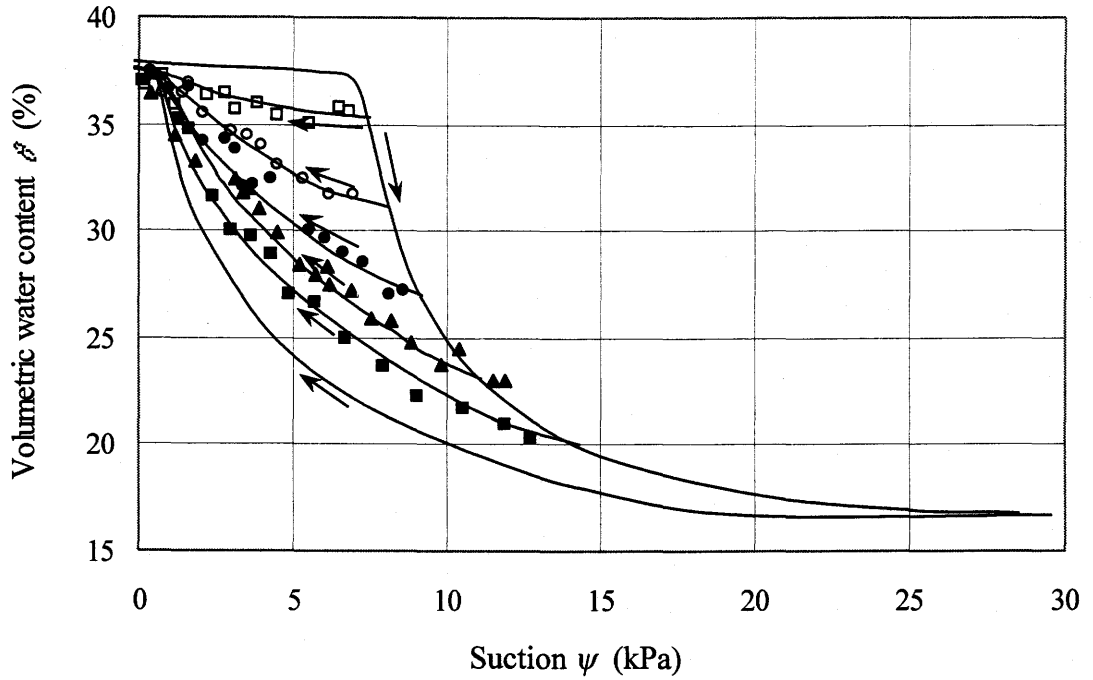

Figure 2.11(b) Main hysteresis loop and primary wetting scanning curves of the Rubicon sandy loam (From Topp, 1969)

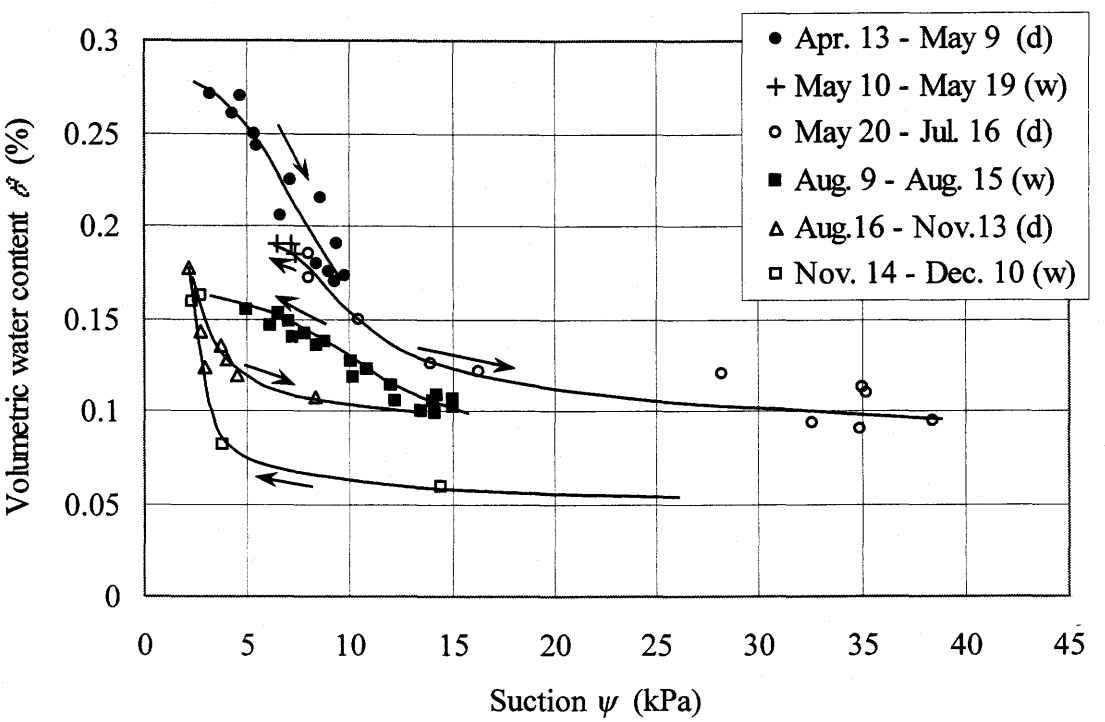

Figure 2.12 Field monitoring results on Bouron fine sand (Royer and Vachaud, 1975)

2.5 MODELING OF CAPILLARY HYSTERESIS

Where both drying and wetting occur during an unsaturated flow process, the analysis of soil water characteristic curves has to take into account the effects of capillary hysteresis. Solving problems in which two or more cycles of wetting and drying take place requires such large quantities of data that the amount of the experimental work needed is prohibitive. Therefore, hypothetical models or analytical approximations to describe the hysteresis properties of porous media are generally used in computation.

Domain models of hysteresis have been the most widely used models in analyzing the hysteresis in water characteristics of porous media. Néel (1942, 1943) developed the first of these models. Everett and Whicton (1952), Everett and Smith (1954), and Everett (1954, 1955) extended and generalized this type of model. The adoption of the domain model for soil water involves a substitution of pores for magnetic domains. Poulovassilis (1962) was among the first to apply this model to the capillary hysteresis of porous media. The following sections briefly describe the domain theory for capillary hysteresis and the development of the domain models and other models of capillary hysteresis.

2.5.1 Domain Theory for Capillary Hysteresis

Haines (1930) was among the first to clarify the hysteresis phenomenon when studying the water flow through soils. Haines (1930) attributed the capillary hysteresis to the pore construction of the porous media. The fact that pore construction causes capillary hysteresis is usually called "ink-bottle" effects. The water in the pores is drained or filled through a jump type of action. When the suction is increased to a certain value, ψ_d, the pore is drained spontaneously, and when the suction is lowered to a certain value, ψ_w, the pore is filled spontaneously. Therefore, the suctions, ψ_d and ψ_w, can specify the water characteristics of a pore.

A porous body may be regarded as a system made up of domains. A domain is composed of a group of pores having only two states, either empty or full of water. Each of the domains retains its identity and is completely specified by a pair of small

suction ranges, ψ_w to $\psi_w + d\psi_w$ and ψ_d to $\psi_d + d\psi_d$. The range, ψ_w to $\psi_w + d\psi_w$, represents the suction range over which the pores in this domain are refilled with water, and the other range, ψ_d to $\psi_d + d\psi_d$, represents the suction range over which the pores in this domain are dried. This behavior of the pore is independent of all the other pores surrounding it. In other words, the pores in a domain are filled or drained at the specifying suction ranges of the domain, no matter whether the surrounding pores are empty or filled. The blockage of the surrounding pores to the access of water or air to the pore under consideration is not considered in the independent domain theory.

Since the suction ranges for each domain are specified, all the domains can be indicated according to their specifying ranges in the ψ_d, ψ_w plane of the rectangular coordinate system of Fig. 2.13. All domains are in the area of triangle of OAB, since for no domain does ψ_w exceed ψ_d (Fig. 2.13).

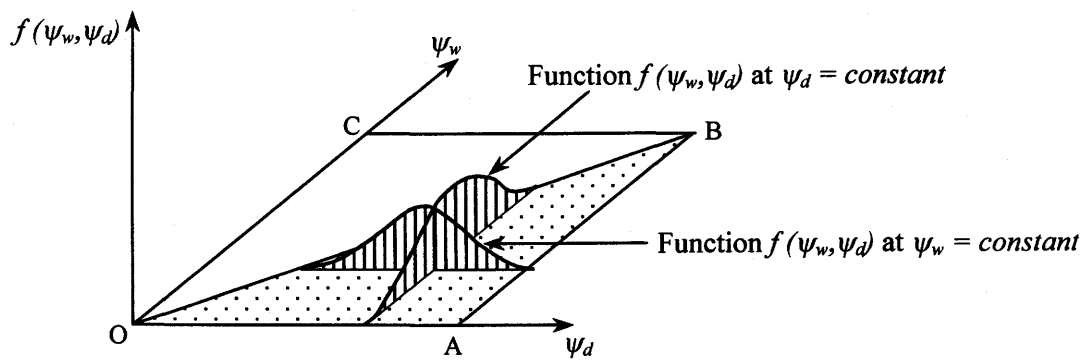

Figure 2.13 Perspective view of the distribution function, $f(\psi_w, \psi_d)$, plotted above the ψ_d, ψ_w plane

A distribution function $f(\psi_w, \psi_d)$ is defined such that $f(\psi_d, \psi_w)d\psi_d\, d\psi_w$ describes the relative volume of pore space that is filled for a change from ψ_w to $\psi_w + d\psi_w$ and drained for a change from ψ_d to $\psi_d + d\psi_d$. Distribution function $f(\psi_w, \psi_d)$ has a positive value varying from point to point within the triangle OAB while it is zero outside the triangle (Fig. 2.13). After a sequence of processes of drying and wetting, the water content is obtained by

$$\theta(\psi) = \iint f(\psi_w, \psi_d) d\psi_w d\psi_d \tag{2.5}$$

or

$$f(\psi_w, \psi_d) = \frac{\partial^2 \theta}{\partial \psi_w \partial \psi_d} \tag{2.6}$$

Figure 2.14 shows schematically the main drying and wetting processes and the diagram of filled pores for each process. The triangular diagram illustrating the filled pores is usually called Néel's diagram. The drying process is characterized by movement of a plane vertical to the ψ_d, ψ_w plane and parallel to the ψ_w axis from left to right, and the wetting process is characterized by the movement of a plane vertical to the ψ_d, ψ_w plane and parallel to the ψ_d axis from top to bottom, as shown in Fig.2.14.

If θ_r (Fig.2.14) represents the residual water content, the effective water content can be defined as follows (Mualem, 1973),

$$\theta_e(\psi) = \theta(\psi) - \theta_r \tag{2.7}$$

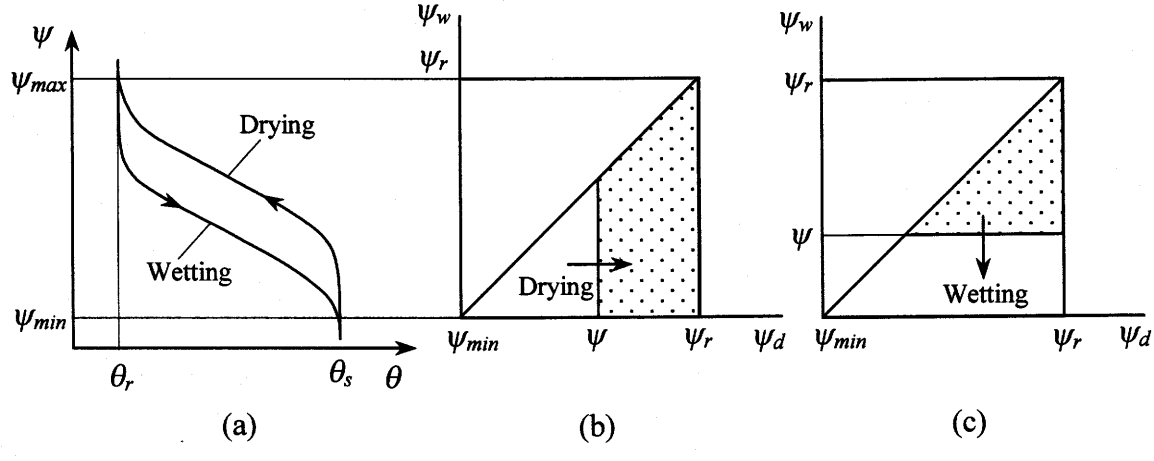

Figure 2.14 Néel's diagram for the main drying and wetting curves

(a) Schematic illustration of capillary hysteresis.

(b) Filled pore diagram (dotted area) for the main drying process.

(c) Filled pore diagram for the main wetting process (from Mualem, 1973)

The main drying and wetting boundaries can be obtained by integrating the dotted areas in Figs. 2.14(b) and 2.14(c), respectively.

$$\theta_d(\psi) = \int_{\psi}^{\psi_r} \int_{\psi_{\min}}^{\psi_d} f(\psi_w, \psi_d) d\psi_w d\psi_d + \theta_r \tag{2.8a}$$

$$\theta_w(\psi) = \int_{\psi}^{\psi_r} \int_{\psi_w}^{\psi_r} f(\psi_w, \psi_d) d\psi_d d\psi_w + \theta_r \tag{2.8b}$$

By differentiating Eqs. 2.8a and 2.8b, the slopes of the drying and wetting boundary curve at a point corresponding to a specific value of suction, ψ, are obtained as follows.

$$\frac{\partial \theta_d}{\partial \psi} = -\int_{\psi_{\min}}^{\psi} f(\psi_w, \psi) d\psi_w \tag{2.9a}$$

$$\frac{\partial \theta_w}{\partial \psi} = -\int_{\psi}^{\psi_r} f(\psi, \psi_d) d\psi_d \tag{2.9b}$$

The primary drying scanning curve, the primary wetting scanning curve and the corresponding diagrams of the filled pores are shown in Fig. 2.15.

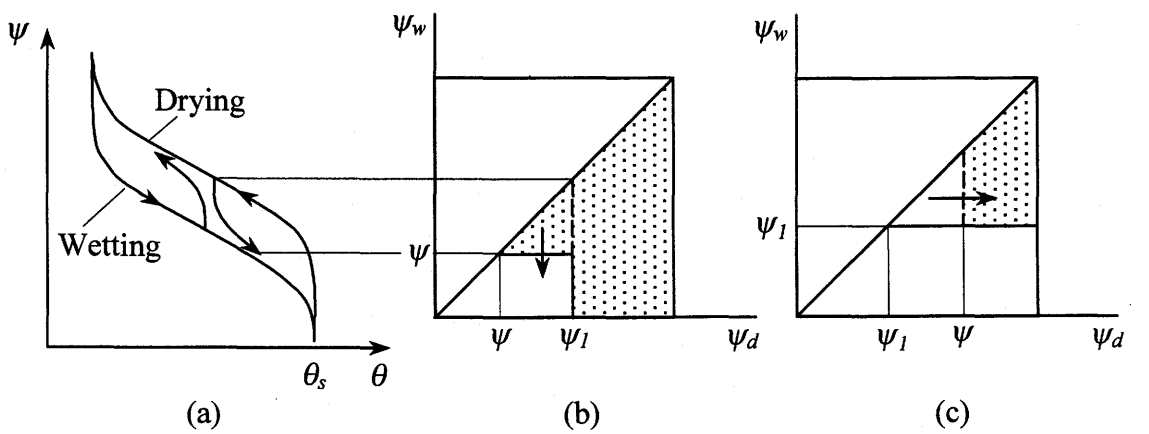

Figure 2.15 Néel's diagram for the primary scanning curves

(a) Primary scanning curves

(b) Filled pore diagram (dotted region) for primary wetting scanning curve.

(c) Filled pore diagram for the primary drying scanning curve (from Mualem, 1973)

Figure 2.15(b) is the Néel's diagram of the primary wetting curve. The reversal from main drying to primary wetting occurs at a suction of ψ_1 on the drying boundary curve, wetting to suction ψ. Figure 2.15(c) is the Néel's diagram of the primary drying curve. The reversal from main wetting to primary drying occurs at suction of ψ_1 on the wetting boundary curve, drying to suction ψ.

The primary drying scanning curve and the primary wetting scanning curve are obtained by integrating the shaded area in Figs. 2.15(b) and 2.15(c), respectively.

$$\theta_w(\psi,\psi_1) = \theta_d(\psi_1) + \int_{\psi}^{\psi_1}\int_{\psi_w}^{\psi_1} f(\psi_w,\psi_d)d\psi_d d\psi_w \qquad (2.10a)$$

$$\theta_d(\psi,\psi_1) = \theta_w(\psi_1) - \int_{\psi_1}^{\psi}\int_{\psi_1}^{\psi_d} f(\psi_w,\psi_d)d\psi_w d\psi_d \qquad (2.10b)$$

where

$\theta_d(\psi,\psi_1)$ = the primary drying scanning curve starts at suction ψ_1 on the main wetting boundary

$\theta_w(\psi,\psi_1)$ = the primary wetting scanning curve starts at suction ψ_1 on the main drying boundary.

This generalized domain model is referred to as the Néel-Everett independent domain model. All other domain models were developed based on the basic theory of the Néel-Everett independent domain model. The distribution function $f(\psi_w, \psi_d)$ is computed using the Néel's diagram. The details of the procedure for computing the distribution function $f(\psi_w, \psi_d)$ are presented in Chapter 5.

2.5.2 Development of the Domain Theory for Capillary Hysteresis

A few hypothetical models including the Néel-Everett independent domain model have been developed to simulate the capillary hysteresis of a porous medium. The models are mostly domain models, as listed in Table 2.2.

Table 2.2 A chronological list of the hysteresis models found in the literature

Researcher	Year	Properties of the model	Required measured data
Néel-Everett	1942–1955	Independent domain model	
Enderby	1955, 1956	Extension of Néel-Everett's independent domain model to a dependent model	
Poulovassilis	1962	Application of Néel-Everett's independent domain model in water capillary hysteresis of soils	Main hysteresis loop and one family of primary scanning curves
Philip	1964	Simplified Néel-Everett's independent domain model based on a similarity hypothesis	Main hysteresis loop
Everett	1967	Extension of Néel-Everett's independent domain model to a dependent model	
Topp	1971	Extension of Néel-Everett's independent domain model to a dependent model	Main hysteresis loop, one family of primary scanning curves and one scanning curve of the other family
Mualem (model-I)	1973	Further simplification to Philip's similarity hypothesis	Main hysteresis loop
Mualem (model-II)	1974	Further simplification to model-I	Main hysteresis loop

Table 2.2 A chronological list of the hysteresis models (continued)

Mualem & Dagan (model-III)	1975	Extension of model-II to a dependent domain model	Main hysteresis loop and one primary scanning curve
Parlange	1976	Further simplification of Mualem's similarity hypothesis	One branch of the main hysteresis loop
Mualem (model II-1)	1977, 1984	Further simplification of model-II	One branch of the main hysteresis loop
Mualem & miller (model-III_{expl})	1979	Improvement of model-III	Main hysteresis loop and one primary scanning curve
Nimmo	1992	A semi-empirical model	Main drying curve and two points on the main wetting curve

Good agreement between predicted and measured data was found for a glass beads medium (Poulovassilis, 1962) and for sand samples (Talsma, 1970; Poulovassilis, 1970) using the Néel-Everett independent domain model. In contrast, disagreement between theory and experiments was reported for glass beads material (Topp and Miller, 1966; Morrow and Hurris, 1965), for sand (Vachaud and Thony, 1971), for sandy loam (Topp, 1969) and for silty loam and clay loam (Topp, 1971). Topp (1971) suggested that the independent domain theory apply only to data obtained from static equilibrium or steady state flow condition but that it fails to depict hysteresis properly in case of unsteady flow.

Further generalization of independent domain theory was presented by Enderby (1955 and 1956) in order to take into account the reversible change of the process and the dependence of the two bistable states of a pore on the capillary head over the range of bistability. The potential advantages of the model are, however, offset by its complexity and difficulty in application.

Everett (1967) himself has suggested an extension of the independent domain model, and the parallel development was presented by Topp (1971) to include interaction between pores. Poulovassilis and Childs (1971), and Poulovassilis and El-Ghamry (1978) by considering the dependence of domains, have moved in a similar direction. All these efforts resulted in the development of the dependent domain models. The dependent domain models need more measured data than the independent domain model, and this fact, as well as their complexity, makes them of little practical use.

In order to make the domain model a practical tool, further simplification was made by Philip (1964) by incorporating the following similarity hypothesis into the domain model.

$$f(\alpha,\beta) = -g(\beta)\cdot h(\frac{\alpha}{\beta})\cdot\frac{1}{\beta} \qquad (2.11)$$

where

α: the (arithmetically) smallest value of ψ, at which, under equilibrium conditions, an infinitesimal volume element of pore space may be occupied by air

β: the (arithmetically) largest value of ψ, at which, under equilibrium conditions, the element may by occupied by water.

With this similarity hypothesis, the primary and secondary scanning curves may be predicted from only the drying and wetting boundary curves. By adopting an arbitrary, but plausible, form of h function, the whole hysteresis character of the medium could be estimated from a single boundary curve. Unfortunately, the mathematical operations resulting from the definition of the model, in which one inverse and two direct numerical Laplace transforms are involved, have apparently prevented its application (Mualem, 1973).

Mualem (1973) made a further simplification to Philip's formulation, using the similarity principle proposed by Philip (1964), by assuming the pore water distribution

function $f(\psi_w, \psi_d)$ to be represented as a product of two independent distribution functions $h(\psi_d)$ and $l(\psi_w)$ as the following equation.

$$f(\psi_w, \psi_d) = h(\psi_d) \cdot l(\psi_w) \tag{2.12}$$

This simplification led to a quite simple model of predicting the scanning curves using only the main hysteresis loop, and is referred to as the Mualem model-I,.

Mualem (1974) made a further simplification to the model-I by using the normalized variables $\bar{r}$ and $\bar{\rho}$:

$$f(\bar{r}, \bar{\rho}) = h(\bar{r}) \cdot l(\bar{\rho}) \tag{2.13}$$

where,

$$\bar{r} = \frac{r - R_{min}}{R_{max} - R_{min}} \text{ and } \bar{\rho} = \frac{\rho - R_{min}}{R_{max} - R_{min}}$$

r = the radii of the openings of the pores in a group (domain)

ρ = the radii of the pores within the group (domain)

R_{max} and R_{min} = maximum and minimum values of r or ρ, corresponding to ψ_{min} and ψ_{max} in model-I.

This hypothesis led to a practical model and is referred to as model-II. Model-II has successfully reproduced scanning curves for a variety of coarse-grained materials whose experimental data were available (Mualem, 1974). The development of the corresponding dependent domain model (Mualem and Dagan, 1975) provided a means of allowing for pore "blocking" - the prevention of sudden change in a pore's water content by elimination of water or air pathways to the pore. The pore "blocking" may have a significant role in the capillary properties of some porous media.

Parlange (1976) made a further simplification of the similarity hypothesis by assuming that the distribution, $f(\psi_w, \psi_d)$, is independent of ψ_w, i.e.,

$$f(\psi_w, \psi_d) = h(\psi_d) \tag{2.14}$$

This assumption made it possible to predict the whole hysteresis relationships by only the wetting boundary or by the drying boundary plus one point on the wetting

boundary. The required measured data are greatly reduced by this simplification. However, when making a detailed examination on Parlange's model, Mualem and Morel-Seytoux (1978) concluded that the hypothesis on which Parlange's model is based failed to exhibit some basic observed properties of soil water hysteresis. This model is unsatisfactory to use either of the two main branches to predict the other branch and scanning curves (Mualem and Morel-Seytoux, 1978).

Mualem (1977) also made a further simplification to the previous similarity models. The pore water distribution function is assumed to be,

$$f(\psi_w, \psi_d) = h(\psi_d) \cdot h(\psi_w) \text{ or } f(\bar{r}, \bar{\rho}) = h(\bar{r}) \cdot h(\bar{\rho}) \qquad (2.15)$$

This hypothesis yielded two different models to predict the hysteresis relationship from only one branch of the main hysteresis loop.

Nimmo (1992) stated that the above simple models developed by Parlange (1976) and Mualem (1977) were not able to properly simulate the capillary hysteresis for most situations. Nimmo (1992) also pointed out that, "on a fundamental level, there is no significant evidence that the phenomena that cause hysteresis are manifested in a main drying curve." Nimmo (1992) proposed a semi-empirical model that has been designed to provide a good representation of the main wetting curve and the scanning curves, given the main drying curve and two measured points on the main wetting curve. Two hypotheses are involved in this model. The first is that the fraction of pore space that is non-hysteretic, in any pore size range, is independent of pore size. The second hypothesis specifies that the pore body-size distribution function for each pore neck size is the same and is closely related to the pore neck-size distribution function. However, the measured data on the main drying curve have to be fitted using a certain equation, and the formulation of the model involves integration of the equation. It not easy to find such an equation that can fit the measured data on the main drying curve and meanwhile make the formulations of the model solvable.

Attempts are made in Chapter 5 to apply the above models on the experimental data of the water capillary hysteresis of the ceramic of the new thermal conductivity sensor. The models that are tested using the experimental data of the sensor ceramic will be described in detail in Chapter 5.

CHAPTER 3

Laboratory Testing Program and Presentation of Data

The laboratory test program was set up to study the capillary hysteresis behavior of the ceramic tip of the new sensor, and the effects of the hysteresis on suction measurements when using the new sensor. The first section of this chapter describes the test method and the properties of the sensor ceramic. The other sections deal with the test results that are presented under the following categories:

(1) initial drying curve and main hysteresis loop,
(2) primary scanning curves,
(3) boundary wetting curve,
(4) wetting and drying outside the main hysteresis loop, and
(5) the increase of water content of an initially dry sensor ceramic submerged in water.

3.1 MATERIALS AND TEST METHOD

This section is presented in two portions, one on the properties of the new sensor and sensor ceramic which were used in the laboratory tests, the other on the apparatus and test procedures.

3.1.1 The Beta-97 Thermal Conductivity Sensor

A research group was set up in 1996 to develop a new thermal conductivity sensor that would be able to meet the requirements of field monitoring of matric suction. Based

on the research done on the electronics and the tip ceramics, a preliminary design of a new thermal conductivity sensor, sensor Beta-97, was finished and the sensor was produced in a small number for laboratory and field testing. The sensor Beta-97 has a diameter of 28.5mm and a height of 38.5 mm. It consists of an IC temperature sensor and a heating resistor embedded in a ceramic tip (Fig. 3.1).

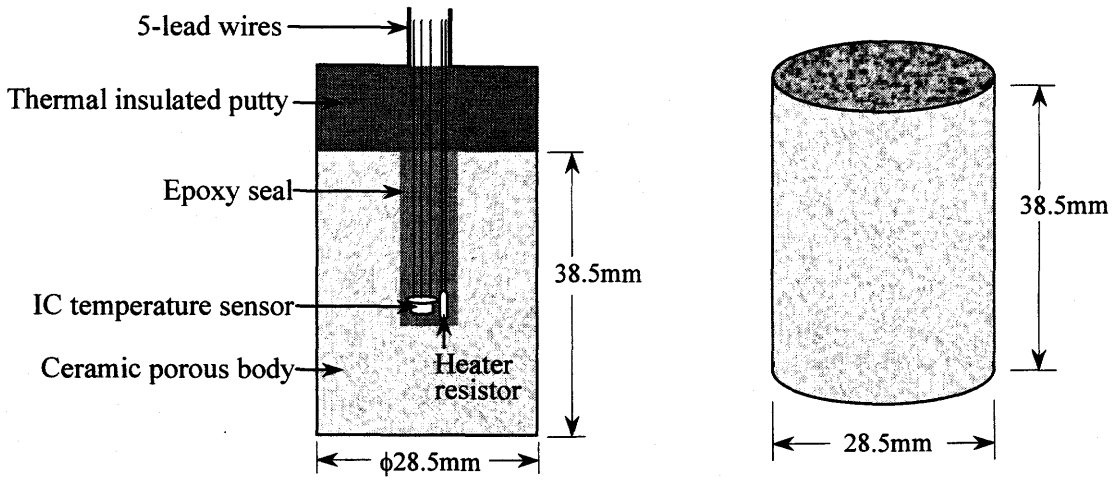

(a) The structure of the sensor (b) The ceramic tip

Figure 3.1 Cross-section of the sensor Beta-97 and the dimensions of the ceramic tip

A thermally conductive but electrically insulated epoxy was used to embed the resistor and IC sensor. The lead wires from the resistor and temperature sensor are held in place by a ceramic repair putty cap on the top of the ceramic tip. This cap also serves as a thermal insulator to stop the heat from flowing out through the thermally conductive epoxy embedding the electronics.

Two groups of tests were carried out. One group measured the water retention characteristics of three ceramic specimens (the "freshly baked" cylindrical ceramic block with no hole or electronics, as shown in Fig. 3.1(b)), denoted as Ceramic-1, 2 and 3. The other group measured the relationship between the sensor output and matric suction of six sensors, i.e., Sensors 1 to 6. The word "sensor" here and in the

following sections represents the whole thermal conductivity sensor with a ceramic tip and the electronics. The sensor output is a voltage.

The three ceramic specimens were from three different batches of production based on the same recipe and manufacturing procedure. The ceramic tips of the six sensors were produced in another two batches using the same procedure. The ceramic tips of Sensor-1, 2 and 3 were from one batch and those of Sensor-4, 5 and 6 were from another batch. The ceramic tips had a compressive strength of approximately 1600 kPa and a saturated coefficient of permeability of 2.0×10^{-6} m/s. The ceramic was covered with a protective coating to improve the hardness of the ceramic surface. The physical properties of the three ceramic specimens are summarized in Table 3.1.

Table 3.1 The physical properties of the three ceramics

Ceramic No.	Dry density γ_d (g/cm^3)	Void Ratio e	Porosity n (%)	Diameter (mm)	Height (mm)
1	0.814	1.56	60.9	28.5	38.4
2	0.836	1.52	60.3	28.4	38.3
3	0.824	1.53	60.5	28.4	38.5

3.1.2 Apparatus

The pressure cells designed at the University of Saskatchewan were used in the laboratory tests. The setup of the apparatus is illustrated in Fig. 3.2 and Fig. 3.3.

The pressure cell utilizes an axis-translation technique that produces a pressure difference or matric suction across the high air entry disk. The matric suction is controlled by changing the air pressure in the pressure cell while keeping the water pressure underneath the high air entry disk constant. A burette is used to monitor the amount of water flow as the water content of the ceramic tip changes to reach equilibrium with the applied matric suction. A thin layer of kaolinite paste is placed between the ceramic tip and the high air entry disk to ensure good contact and continuity of water flow between the ceramic block and the disk. The kaolinite layer also helps to hold the ceramic tip in place.

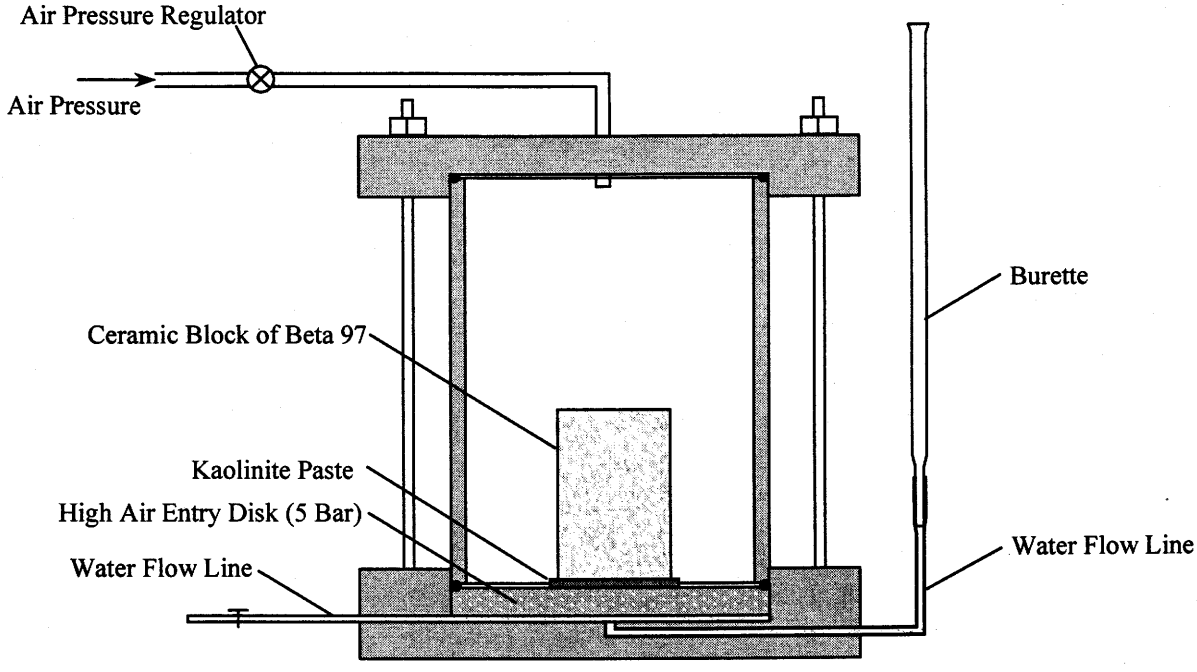

Figure 3.2 Apparatus for measuring the water retention characteristics of the ceramics

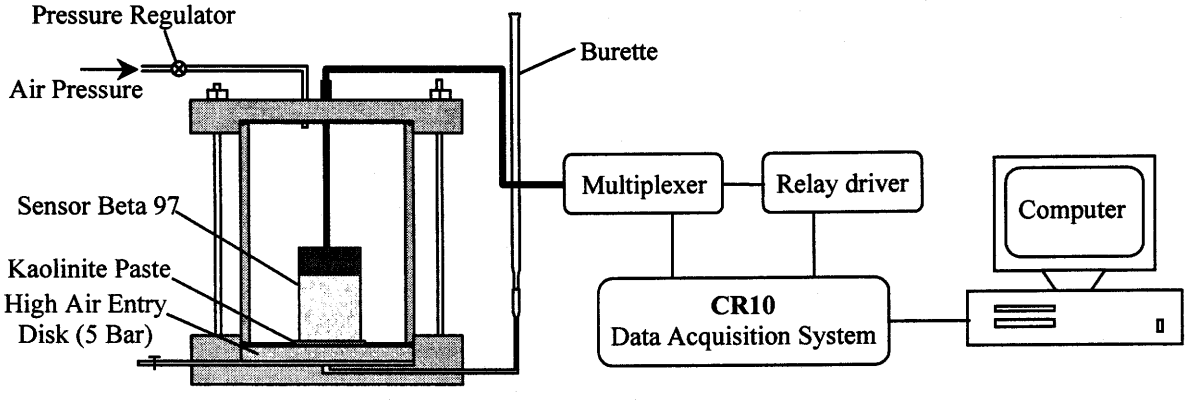

Figure 3.3 Apparatus for measuring the sensor output versus suction relationships of the sensors

The ceramic disk has an air entry value of 5 bar. It was saturated using the vacuum method, (which will be described in detail in the following section), before

being installed in the pressure cell. The water pressure underneath the ceramic disk was maintained at pressures in the range of 7 to 10 kPa by keeping the water level in the burette at a higher elevation.

3.1.3 Experimental Program

This section gives a brief description of the tests carried out in the experimental program, including the purpose and testing procedure of each test.

Method for saturating the sensor ceramic tips and the ceramic disks

The sensor ceramics and high air entry disks were saturated using the vacuum method. The apparatus consists mainly of a vacuum chamber, a vacuum pump and a water tank. The setup of the apparatus is shown in Fig. 3.4.

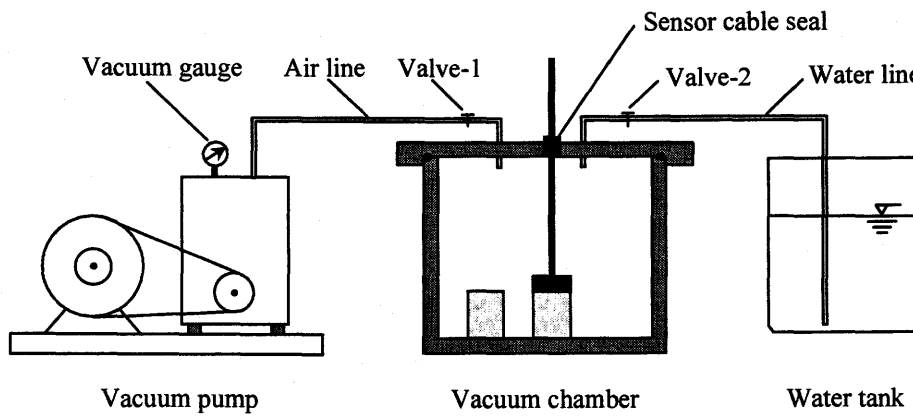

Figure 3.4 Apparatus for saturating the sensor ceramic tips

The ceramic tips or the high air entry disks were placed in the vacuum chamber, with Valve-1 (to pump) open and Valve-2 (to water tank) closed. The vacuum pump was started to evacuate air out of the chamber until a vacuum of about one atmosphere was reached. This vacuum was maintain for approximately one half hour, then Valve-2 (to water tank) was opened slightly to allow water to flow into the chamber at such a rate as to maintain the vacuum in the chamber during the inflow of water. When the

ceramic tips were submerged in water, Valve-2 was closed. The vacuum pump was kept running for another half-hour. Valve-1 was closed and the vacuum pump was stopped. The water line was removed from the water tank and Valve-2 was opened to release the vacuum in the chamber. The ceramic tips were left in the water for a certain period of time and were saturated under the atmospheric pressure. It was found from the tests that usually a few hours was enough to saturate the ceramic tips of sensor Beta-97.

Test procedures of initial drying curve and main hysteresis loop

The saturated ceramic or the sensor with a saturated ceramic tip was installed in the pressure cell. The pressure cell was closed and air pressure was applied. The water within the ceramic tip was allowed to drain through the saturated high air entry disk in response to the applied suction. As the water flow reached equilibrium with the applied matric suction, the change in water content of the ceramic specimen was measured by taking the readings of the burette, and the response of the sensor was monitored using the CR-10 data acquisition system. At equilibrium, the ceramics (without electronics) were taken out and weighed on a balance. The water below the high air entry disk was flushed regularly in order to remove any diffused air.

The initial drying curve was obtained by increasing the matric suction of the initially saturated ceramic tip or sensor from zero to a maximum value of 400 kPa in the order of 7, 15, 30, 60, 100, 200 and 400 kPa, with each increment being maintained constant until equilibrium was reached. The maximum matric suction of 400 kPa was chosen not to exceed the air entry value of the ceramic disk, which was 5 bar.

At the end of the initial drying process, the matric suction was decreased in increments in the reverse order of the drying process until zero matric suction was reached. The main wetting curve was plotted using the ceramic water content or sensor output as vertical axis and the applied matric suction as horizontal axis.

When the matric suction was reduced to zero in the main wetting process and equilibrium was reached, the matric suction was increased again from zero to 400 kPa to obtain the main drying curve. The suction was increased using a similar incremental

order as in the initial drying process with each increment maintained until equilibrium was reached.

Test procedure of primary scanning curves

By decreasing the matric suction from the 400 kPa by one step to a certain intermediate value between 0 to 400 kPa and then increasing it in increments to 400 kPa, a drying scanning curve was obtained. Similarly, a wetting scanning curve was obtained by increasing the matric suction from zero directly to a certain intermediate value between 0 to 400 kPa and then decreasing it again in increments to zero.

Test procedure of boundary wetting curve

To obtain the boundary wetting curve, a ceramic specimen or the ceramic tip of a sensor was first air-dried. The air-dried ceramic specimen or the tip of the sensor was installed in the pressure cell. A matric suction of 400 kPa was then applied. Since the initial suction in the air-dried ceramic was higher than 400 kPa, the ceramic imbibed water from underneath the high air entry disk. When the water content increase of the ceramic reached equilibrium with the applied suction of 400 kPa, the matric suction was further decreased in increments to zero, with each increment being maintained constant until equilibrium was reached. The ceramic specimen was weighed, and the sensor output recorded, at equilibrium for each increment.

Test procedure of wetting and drying outside the main hysteresis loop

When a fully saturated ceramic specimen is desaturated, the relationship between water content and matric suction follows the initial drying curve. Saturation is never reached when rewetting the ceramic due to air being entrapped during the process of water flowing into the ceramic. The initial drying curve is always higher than the main drying curve. There is a gap between the initial drying curve and the main hysteresis loop. Tests were carried out on ceramics undergoing wetting and drying processes in this gap, as shown in Fig 3.5 schematically.

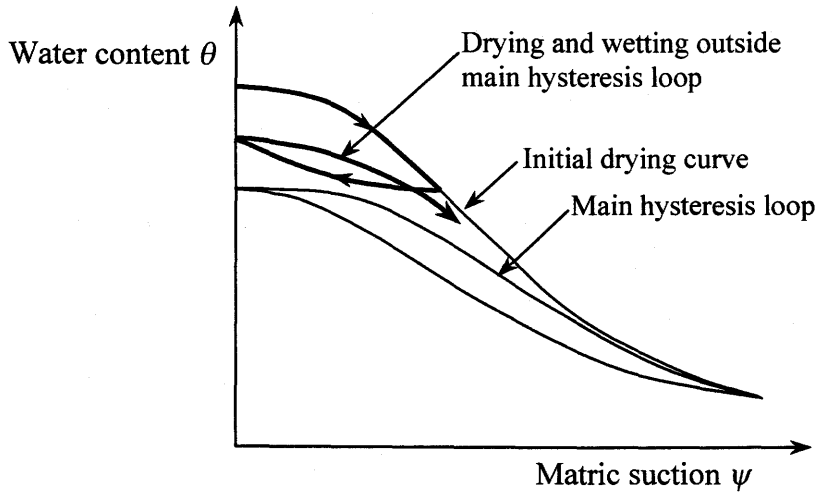

Figure 3.5 Schematic illustration of drying and wetting outside the main hysteresis loop

A fully saturated ceramic was desaturated following the initial drying curve to an intermediate value between 0 to 400 kPa in increments, and then rewetted by decreasing the matric suction to zero in the reverse order. A scanning curve was obtained that might not be within the main hysteresis loop, especially when the suction at the point of reversal was relatively low. When the suction reached zero, the degree of saturation might be higher than that on the main wetting curve but lower than 100%. Then the suction was increased again, and a drying curve that was totally or partly outside the main hysteresis loop was obtained, as schematically illustrated in Fig. 3.5.

3.2 THE EQUALIZATION TIME FOR EACH SUCTION INCREMENT

Each suction increment was maintained until equilibrium was reached. The change in water volume flow into or out of the ceramic with time was recorded using the burette for the ceramic specimens, and the output of each sensor was monitored at a time interval of one hour. The change in water volume, $\Delta\theta$, or the output of the sensor, V, was plotted versus the log scale of elapsed time, as shown in Fig. 3.6. Equilibrium was assumed to have been reached when a turning point on $\Delta\theta$ or V versus $log\ t$ curves was exceeded.

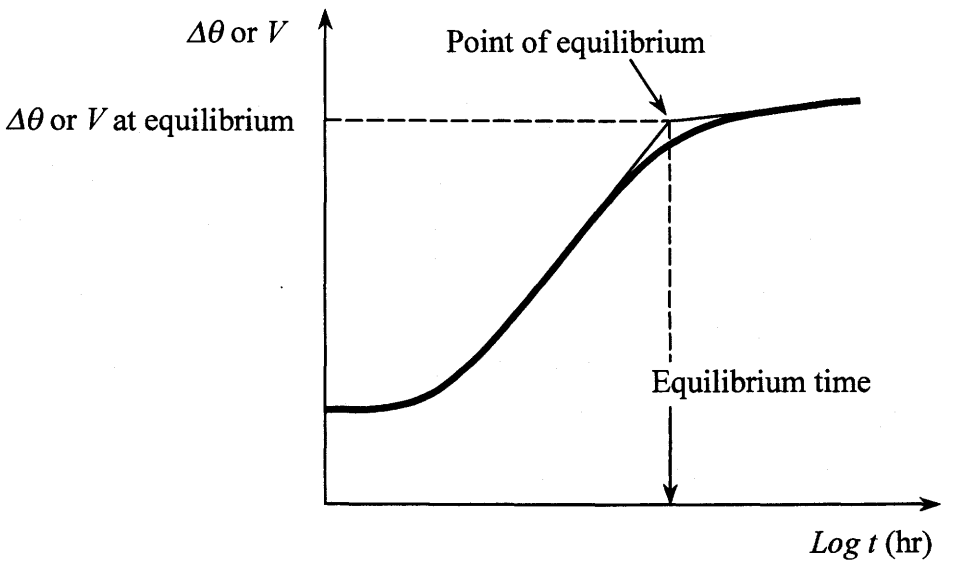

Figure 3.6 Schematic illustration for the determination of the point of equilibrium under each suction increment

Wetting and drying processes were involved in the whole testing program. Each wetting or drying process consisted of several suction increments. The matric suction was maintained constant under each suction change until equilibrium was reached and then another suction increment was applied.

When a suction increment is applied, water startes to flow into or out of the ceramic tip under a one-dimentional unsteady-state condition through the ceramic disk. There are several factors affecting the equalization time. These include the matric suction gradient along the height of the sensor ceramic tip and the degree of saturation at a certain time at a point in the ceramic tip. The coefficient of permeability

of the high air entry disk also affects the equalization since the coefficient of permeability of the 5 bar ceramic disk is only 1.21×10^{-9} m/s (Fredlund, 1993). This value is smaller than the saturated permeability of sensor ceramic tip, which is 2×10^{-6} m/s.

Figures 3.7 to 3.9 show the relationships between water content and elapsed time of one of the three ceramic specimens, Ceramic-2. Both the drying and the wetting processes of three suction increments, 0 to 7 kPa, 55-100 kPa and 206-410 kPa, are shown in Figs. 3.7 to 3.9, respectively.

A phenomenon common to all the sensors and ceramic specimens in the tests is that the equalization time for the suction increments in the low suction range and those in the high suction range are longer than those in the intermediate suction range. For Ceramic-2 shown in Fig. 3.7 to 3.9, the equalization times of 0-7 kPa, 55-103 kPa and 206-410 kPa are 70, 20 and 100 hours respectively for the drying processes, and 30, 100, 200 hours respectively for the wetting processes. Generally, the equalization times of suction increments of 0-7 kPa, 7-15 kPa and 200-400 kPa are longer than the equalization time of suction increments of 15-30 kPa, 30-60 kPa, 60-100 kPa and 100-200 kPa.

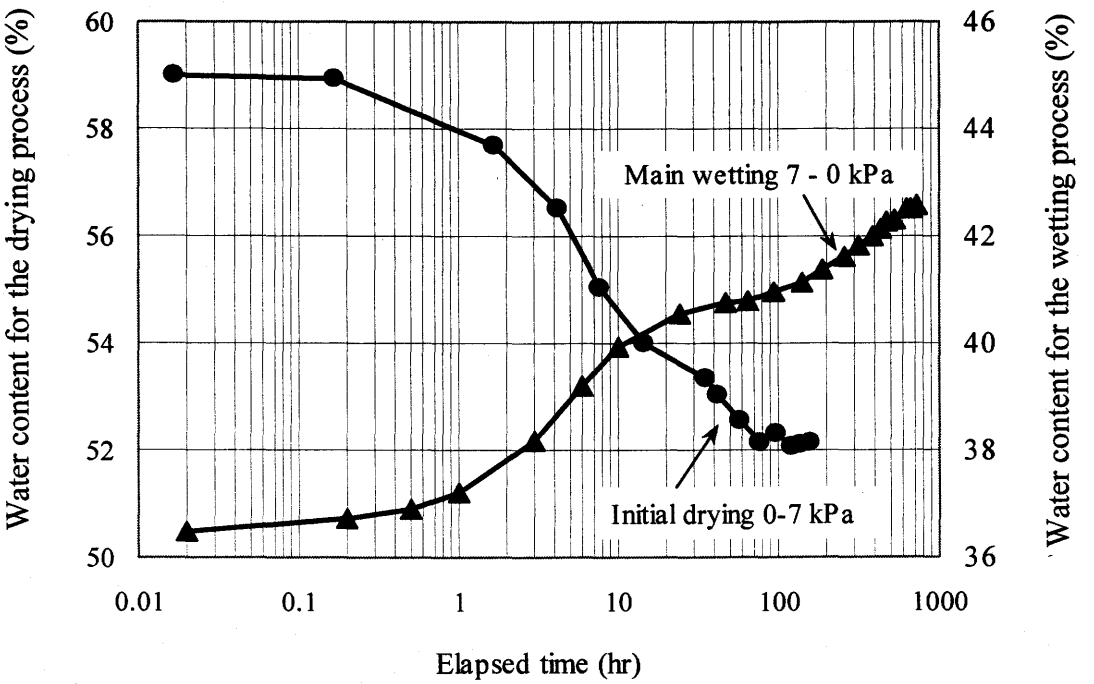

Figure 3.7 Drying and wetting processes for suction increment of 0-7 kPa of Ceramic-2

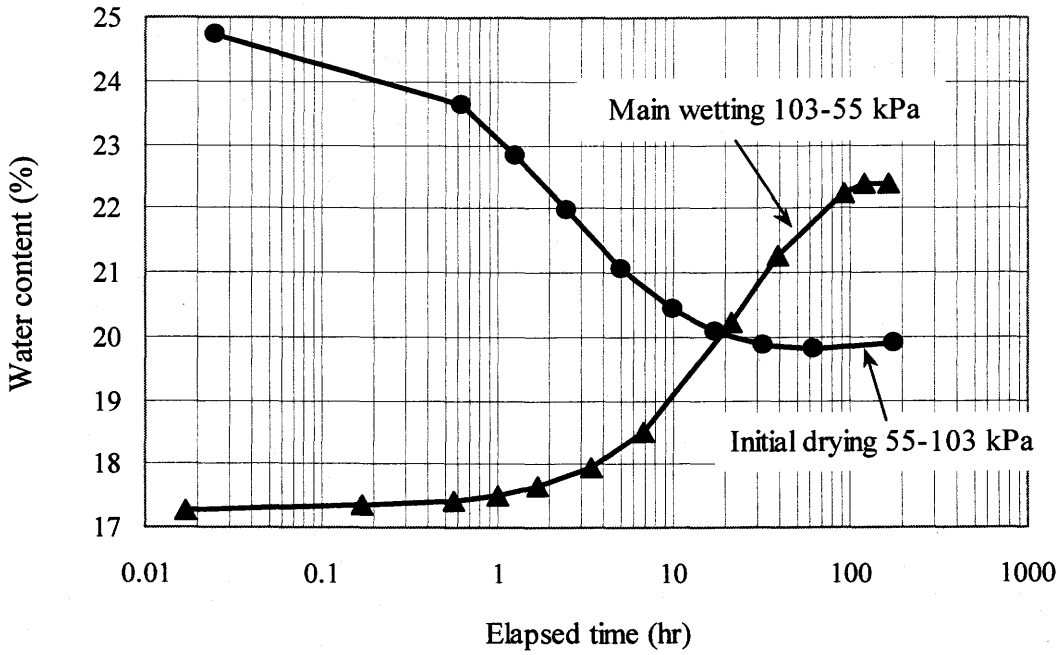

Figure 3.8 Drying and wetting processes for suction increment of 55-103 kPa of Ceramic-2

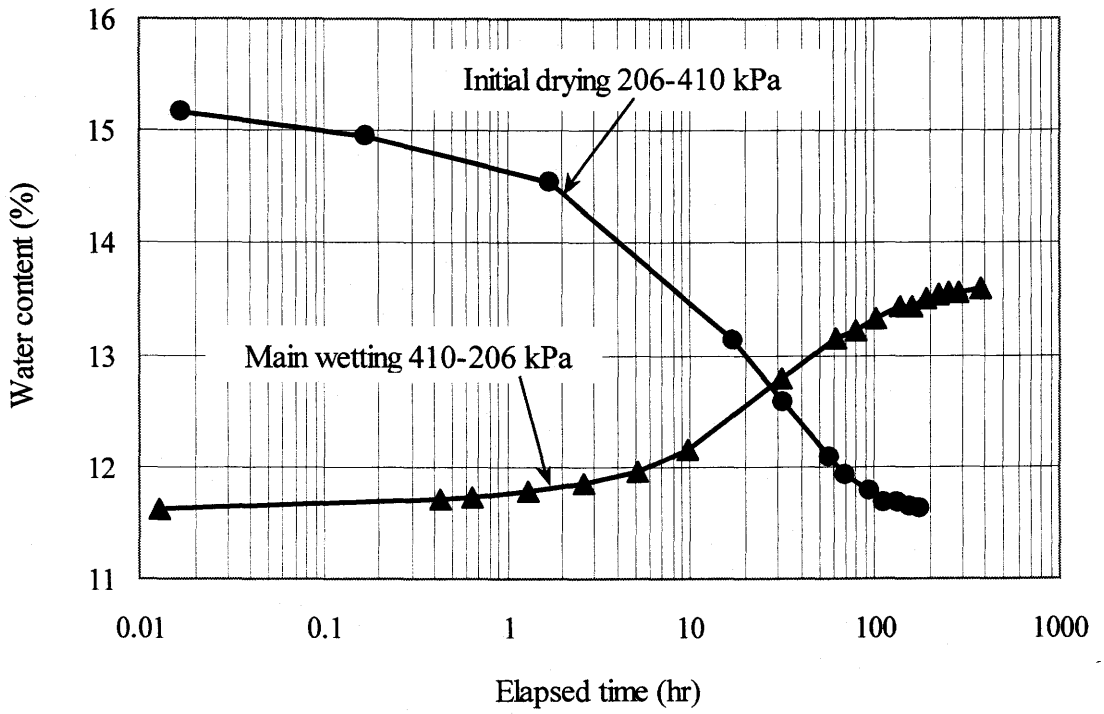

Figure 3.9 Drying and wetting processes for suction increment of 206-410 kPa of Ceramic-2

The reasons for the longer equalization time for the suction increments of 0-7 kPa and 7-15 kPa are (1), the suction gradient along the height of the ceramic is low and, (2) a relatively large amount of water flows into or out of the ceramic during these suction increments. The reason for the longer equalization time in the high suction range (i.e., suction increment of 200-400 kPa) is the low coefficient of permeability of the ceramic at high suction.

The wetting process of 7-0 kPa does not show an "S" shape. A "quasi-equilibrium" state was reached at elapsed time of around 30 hours. However, the water content continued to increase after this "quasi-equilibrium". This is similar to the behavior of a ceramic submerged in water as described in the following sections. The reason is believed to be the escape of the entrapped air from the pores of the ceramic.

3.3 TEST RESULTS OF INITIAL DRYING CURVE AND MAIN HYSTERESIS LOOP

The wetting and drying processes are expressed as a function of $\theta(\psi)$ for the ceramics and $V(\psi)$ for the sensors, where θ represents the water content of the ceramic, V represents the voltage output of the sensor, and ψ represents matric suction.

Figures 3.10 to 3.12 show the initial drying curves and the main hysteresis loops of θ versus ψ relationships for the three ceramics. Figures 3.13 to 3.18 show the initial drying curves and the main hysteresis loops of the V versus ψ relationships for the six sensors.

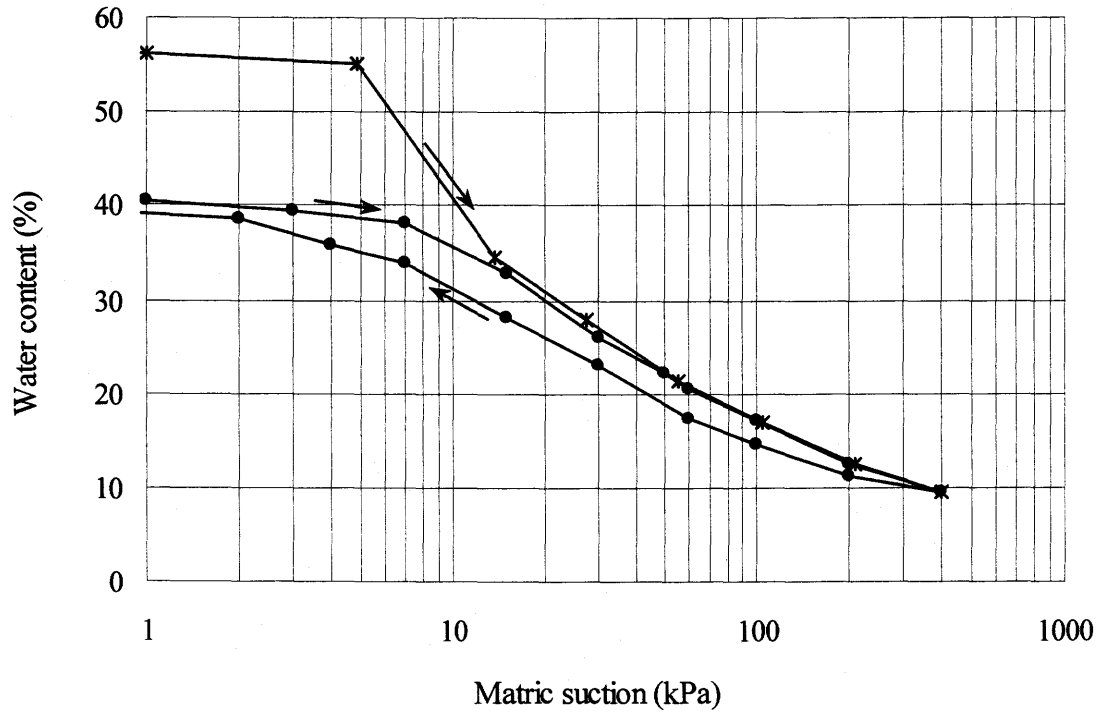

Figure 3.10 Measured initial drying curve and main hystersis loop of Ceramic-1

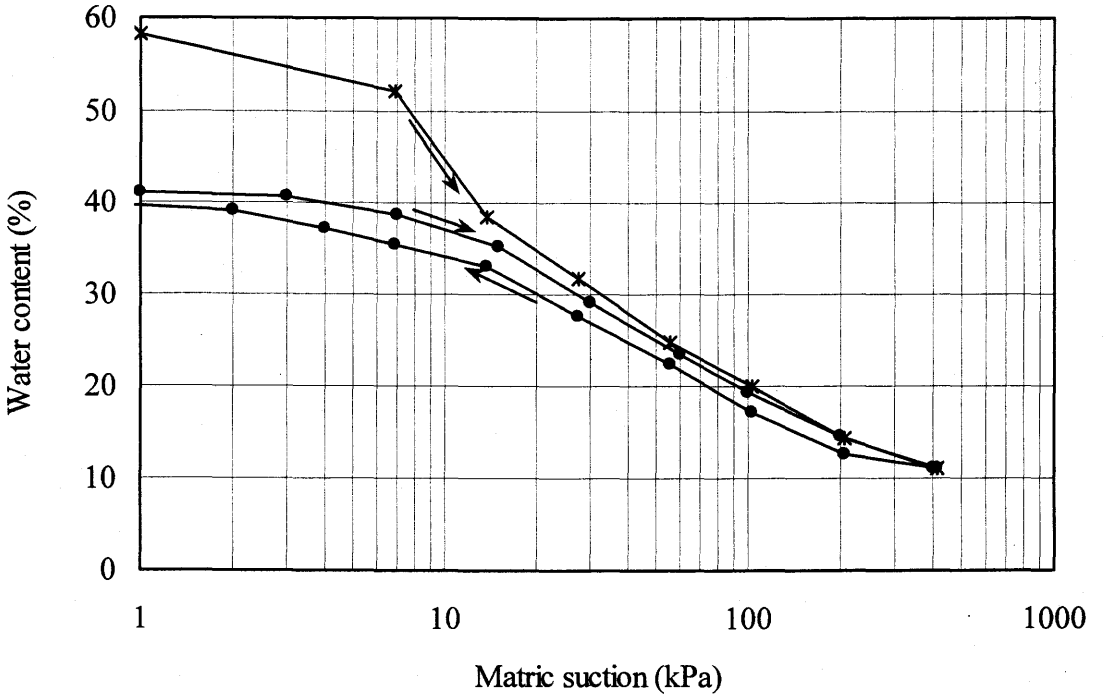

Figure 3.11 Measured initial drying curve and main hystersis loop of Ceramic-2

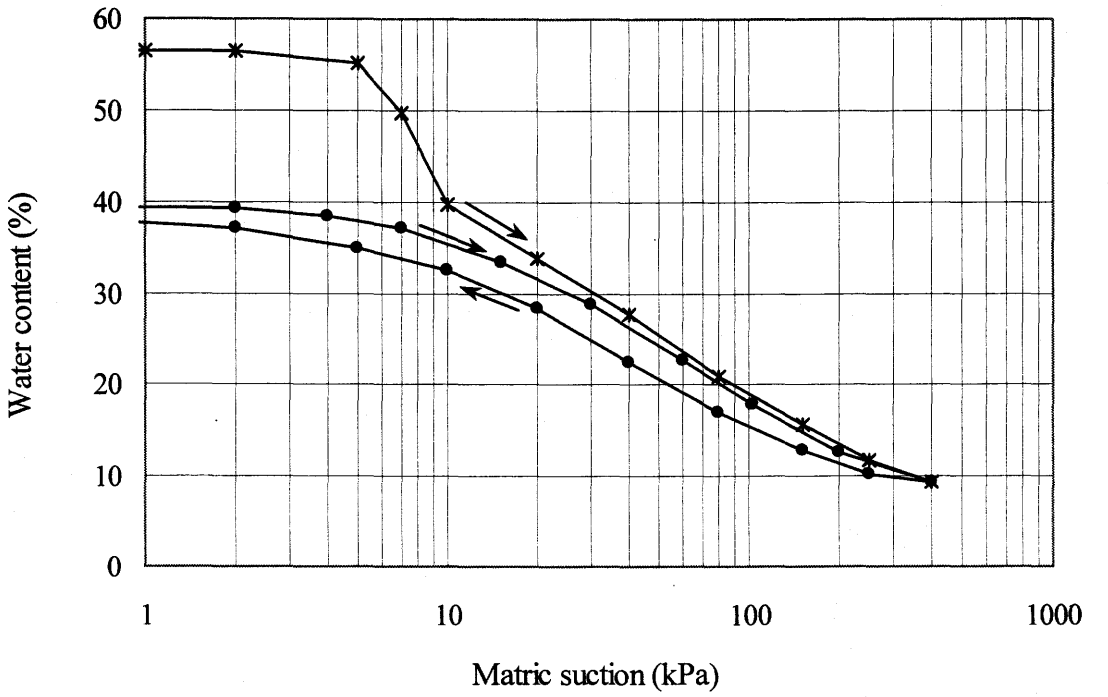

Figure 3.12 Measured initial drying curve and main hystersis loop of Ceramic-3

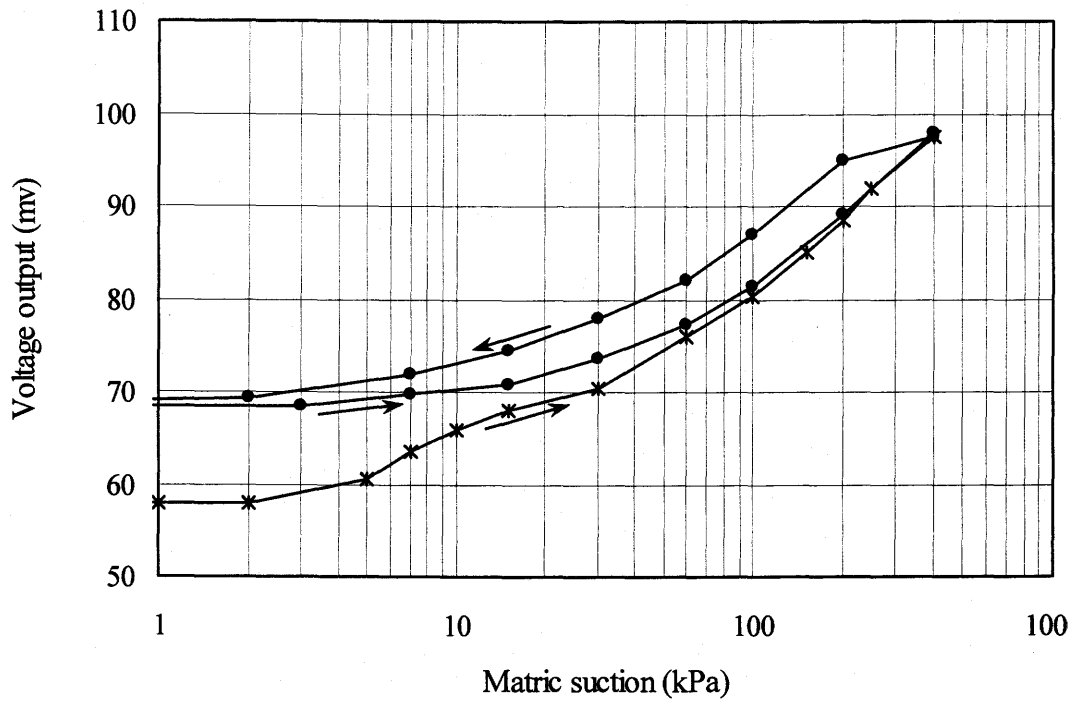

Figure 3.13 Measured initial drying curve and main hystersis loop of Sensor-1

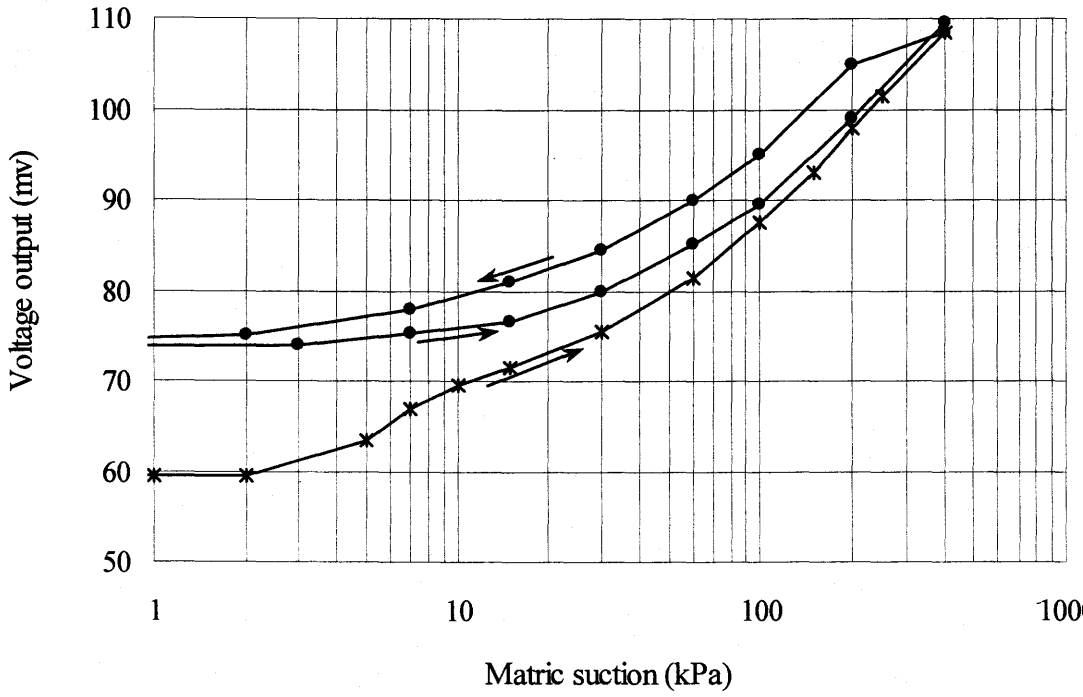

Figure 3.14 Measured initial drying curve and main hystersis loop of Sensor-2

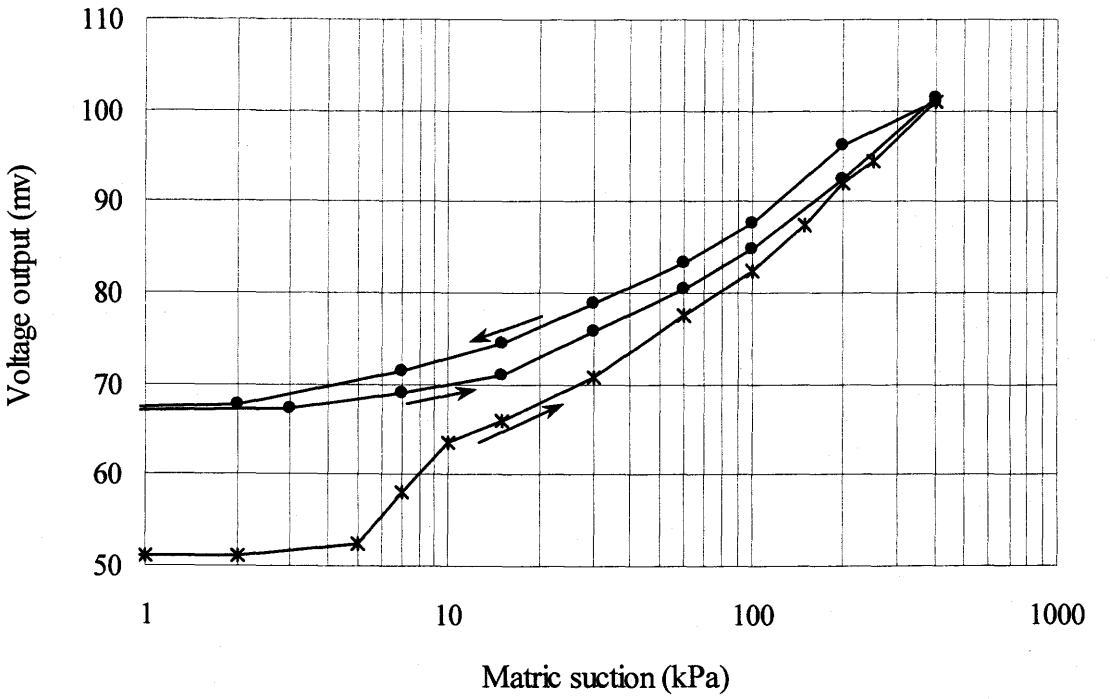

Figure 3.15 Measured initial drying curve and main hystersis loop of Sensor-3

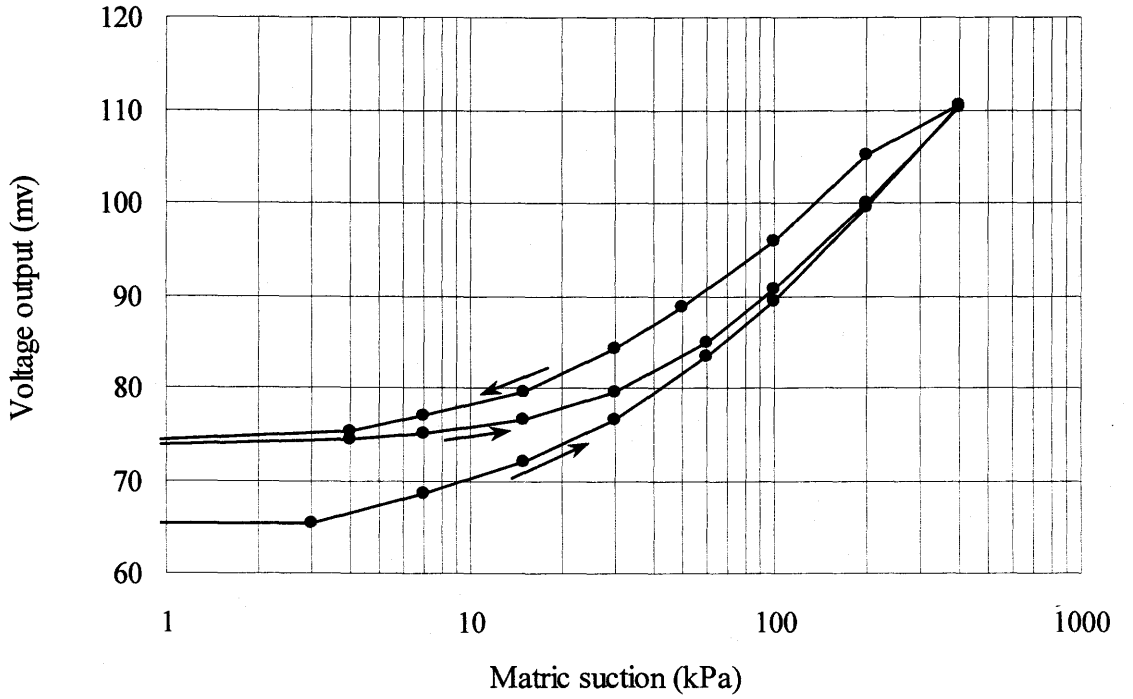

Figure 3.16 Measured initial drying curve and main hystersis loop of Sensor-4

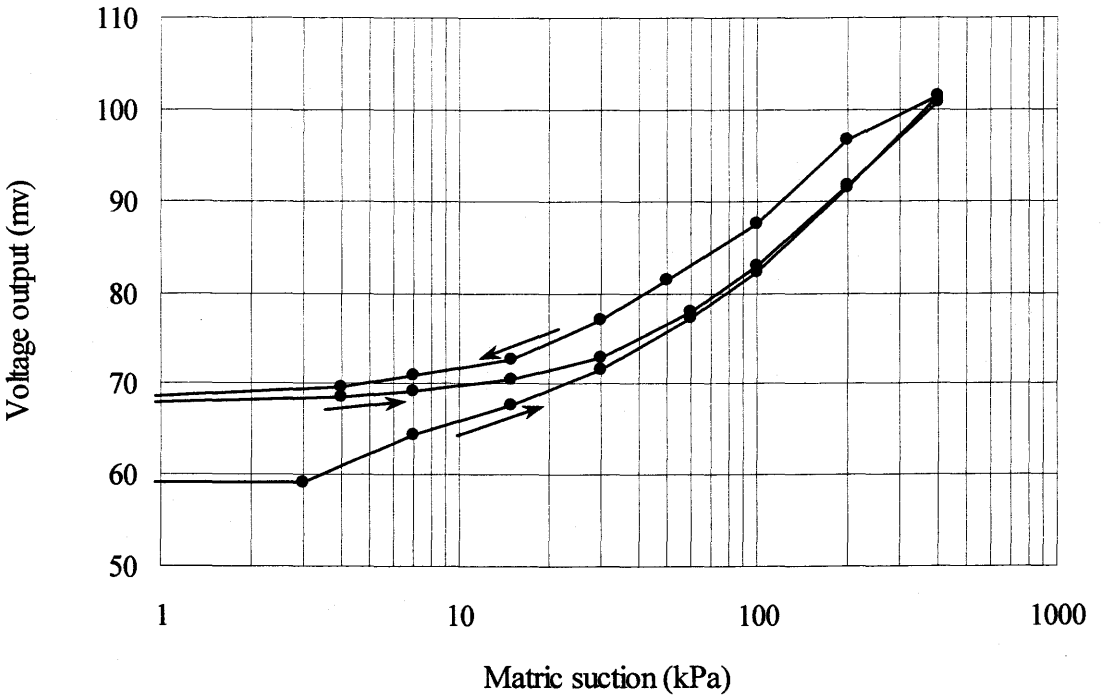

Figure 3.17 Measured initial drying curve and main hystersis loop of Sensor-5

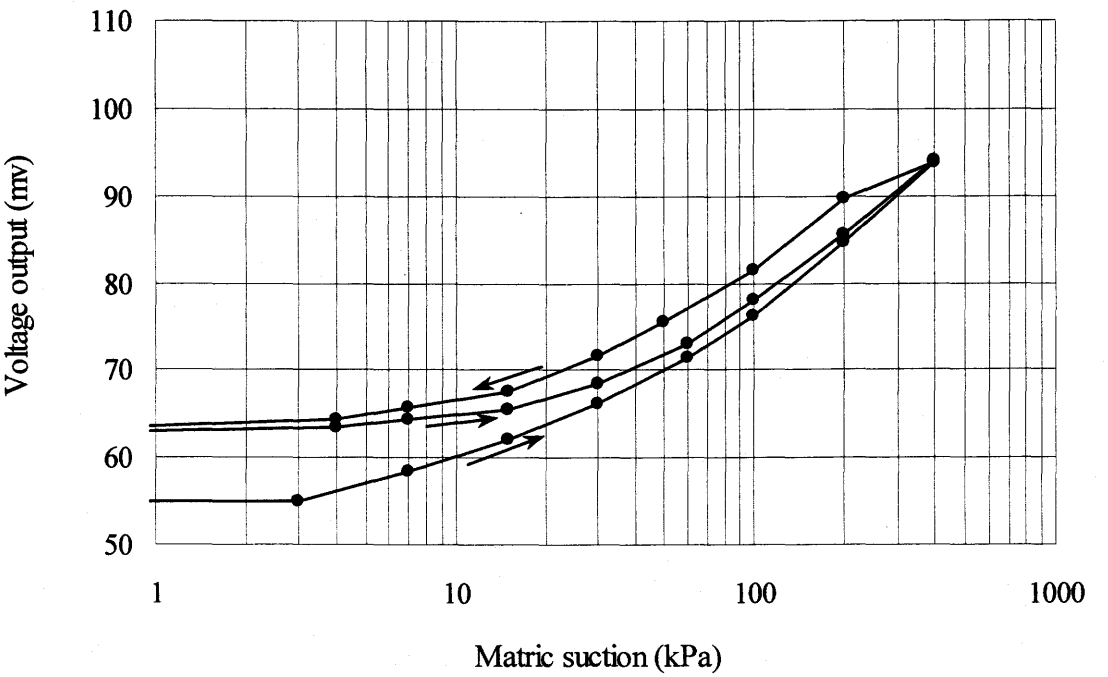

Figure 3.18 Measured initial drying curve and main hystersis loop of Sensor-6

3.3.1 Analysis of the Test Results of the Initial Drying Curve

Although the three ceramic tips were made from three different batches of production, they basically have the same initial drying curve shapes. The ceramic tips of Sensor 1, 2 and 3 were made in one batch of production, those of Sensor 4, 5 and 6 were made in another batch using the same formula and procedure as the ceramics of Sensor 1, 2 and 3. The six sensors also have a similar shaped initial drying curve. The air entry values of the initial drying curves are generally smaller than 5 kPa for both $\theta - \psi$ and V - ψ relationships.

One of the most distinct characteristics of the initial drying curve is that there is a relative large change in water content, θ, or voltage output, V, in the low matric suction range from the air entry value to approximately 15kPa, as shown in Table 3.2. In Table 3.2, the change in water content or voltage output when suction is increased from 0 to 15 kPa is denoted as Δ_{0-15}, and the change in water content or voltage output when suction is increased from 0 to 400 kPa is denoted as Δ_{0-400}.

Table 3.2 Changes in θ or V over the low suction range in initial drying processes

Specimen	Δ_{0-15}	Δ_{0-400}	$\frac{\Delta_{0-15}}{\Delta_{0-400}}$ (%)
Ceramic-1	20 %	46.5 %	43.0
Ceramic-2	17 %	48 %	35.4
Ceramic-3	19 %	47 %	40.4
Sensor-1	10 mv	39.5 mv	25.3
Sensor-2	12 mv	48 mv	25.0
Sensor-3	14 mv	48 mv	29.2
Sensor-4	7 mv	45 mv	15.6
Sensor-5	8 mv	43 mv	18.6
Sensor-6	7.5 mv	40 mv	18.8

The ratios of Δ_{0-15} to Δ_{0-400} for the three ceramic tips and the six sensors are also listed in Table 3.2. This ratio is 43%, 35.4% and 40.4% for Ceramic-1, 2 and 3,

respectively. In other words a relative large amount of water in an initially saturated ceramic tip is drained in a small range of matric suction from 0 to 15 kPa.

The change in voltage output of the sensors when suction is increased from 0 to 15 kPa is not as significant as the change in water content of the ceramics. As shown in Table 3.2, it appears that the values of $\Delta_{0-15}/\Delta_{0-400}$ are close to each other for sensors having a ceramic tip from the same batch of production, while different for sensors having a ceramic tip from different batches. The value of $\Delta_{0-15}/\Delta_{0-400}$ for Sensor 1, 2 and 3 is 25.2%, 25.0% and 29%, respectively, and 15.6%, 18.6% and 18.8% for Sensor 4, 5 and 6, respectively.

However, because the number of ceramics and sensors involved in the tests is too small, it is difficult to discern the causes of the difference in the ratio of $\Delta_{0-15}/\Delta_{0-400}$ for sensors having ceramic tips from different batchs. This ratio is more significant for the $\theta - \psi$ relationships of the ceramic tips than for the V - ψ relationships of the sensors (Table 3.2).

3.3.2 Analysis of the Test Results of the Main Hysteresis Loop

The initial drying process stopped at 400 kPa before the residual saturation could be determined. There were two reasons for not conducting the tests higher than 400 kPa. One reason was that the maximum air entry value of the ceramic disks available for the pressure cell was 500 kPa. The other reason was that the equalization time required for suction increments in suction ranges higher than 400 kPa was so long that the test would be extremely time consuming, and other factors would significantly affect the test results. Figs. 3.10 to 3.18 show that the residual saturation could still not be determined. The main wetting curve is actually a wetting scanning curve. However, as will be described later in this chapter, the main wetting curve almost coincides with the wetting boundary. In other words, the point of reversal at 400 kPa on the hysteresis loop is close to the point of residual saturation.

Main drying and wetting boundaries of the hysteresis loop are smooth curves. Unlike the initial drying curve, there is not a big change in water content or voltage output when suction is increased from 0 to 15 kPa.

When an initially saturated ceramic is drained to 400 kPa, the drying process follows the initial drying curve. If the ceramic is rewetted, the initial saturation is never reached because of the air entrapment in the pores of the ceramic. In the figures showing the initial drying curves and the main hysteresis loops of the three ceramics (i.e., Figs. 3.10 - 3.12), the zero suction points on the main hysteresis loop are well below the zero suction points on the initial drying curves. This indicates that a relatively large amount of air was entrapped in the rewetting process. In Table 3.3, θ_0 denotes the initial water content when the ceramic is saturated, and θ' denotes the water content when the ceramic is rewetted to a suction of 0.1 kPa. ΔV_0 is the sensor output change when the sensor ceramic tip is fully saturated from air-dried condition, and $\Delta V'$ is the sensor output change when the sensor ceramic tip is re-wetted in the pressure cell from air-dried condition to a suction of 0.1 kPa. Table 3.3 shows that only a degree of saturation of 70% to 75% is reached after the ceramic is rewetted to zero suction. The sensor output change after the sensor tip is re-wetted from air-dried condition to zero suction is only 70% - 85% of its output change when the sensor tip is fully saturated from air-dried condition.

Table 3.3 Water content or voltage output after initial drying and then re-wetting to zero suction

Specimen	Saturated θ_0 or ΔV_0	Rewetted θ'or $\Delta V'$	$\frac{\theta'}{\theta_0}$ or $\frac{\Delta V'}{\Delta V_0}$ (%)
Ceramic-1	41 %	56 %	73.2
Ceramic-2	41.5 %	59 %	70.3
Ceramic-3	40 %	56.5 %	70.8
Sensor-1	54 mv	43 mv	79.6
Sensor-2	68 mv	53 mv	77.9
Sensor-3	65 mv	50 mv	76.9
Sensor-4	65.3 mv	58.8 mv	90.0
Sensor-5	61.3 mv	53.3 mv	86.9
Sensor-6	56.1 mv	49.1 mv	87.5

The main hysteresis loop is always located below the initial drying curve for the θ–ψ relationships of the ceramics, and above the initial drying curve for the V-ψ relationships of the sensors. The difference in water content θ or voltage output V between the initial drying curve and the main drying curve varies with the matric suction. This difference is more significant at low matric suctions (i.e., suction lower that 15 kPa) than at high matric suction (i.e., suction higher than 15 kPa). For the three ceramic tips, the initial drying curve almost coincides with the main drying curve when suction exceeds 15 kPa. In the low suction range (0 - 15 kPa), there is a large gap between the initial drying curve and the main drying curve.

The reason for this large gap in the suction range of 0 - 15 kPa may be that there are a relatively large number of large pores in the porous ceramic tip. Consider an initially saturated ceramic, when the matric suction increases from 0 to 15 kPa, the water in the large pores is drained out, resulting in a distinct drop in the initial drying curve in the suction range from air entry value to 15 kPa. If the ceramic is rewetted along the main wetting curve, the water flows into the ceramic. When the matric suction is reduced below 15 kPa, the water starts to flow into the large pores in the ceramic, meanwhile, relatively large amount of air is entrapped in these large pores, resulting in the gap between the initial drying curve and the main hysteresis loop. The entrapped air can only escape by means of diffusing or water redistribution. This process takes place for a long time and is referred to as relaxation. The equalization curve of Ceramic-2 when suction is decreased from 7 to 0 kPa (Fig. 3.7) shows the process of relaxation.

The gap between the initial drying curve and the main hysteresis loop for the sensors is not as significant as that for the ceramics.

3.4 TEST RESULTS OF PRIMARY SCANNING CURVES

When a sensor is installed in the field, it experiences drying and wetting cycles. The drying and wetting processes may begin or end at any suction value following a primary or secondary scanning curve, or a main wetting or drying curve, depending upon the direction of water movement in the surrounding soils. Only tests on primary scanning curves were conducted. Figures 3.19 to 3.27 show the primary drying and wetting scanning curves of the $\theta - \psi$ relationships of the ceramic specimens and V - ψ relationships of the sensors.

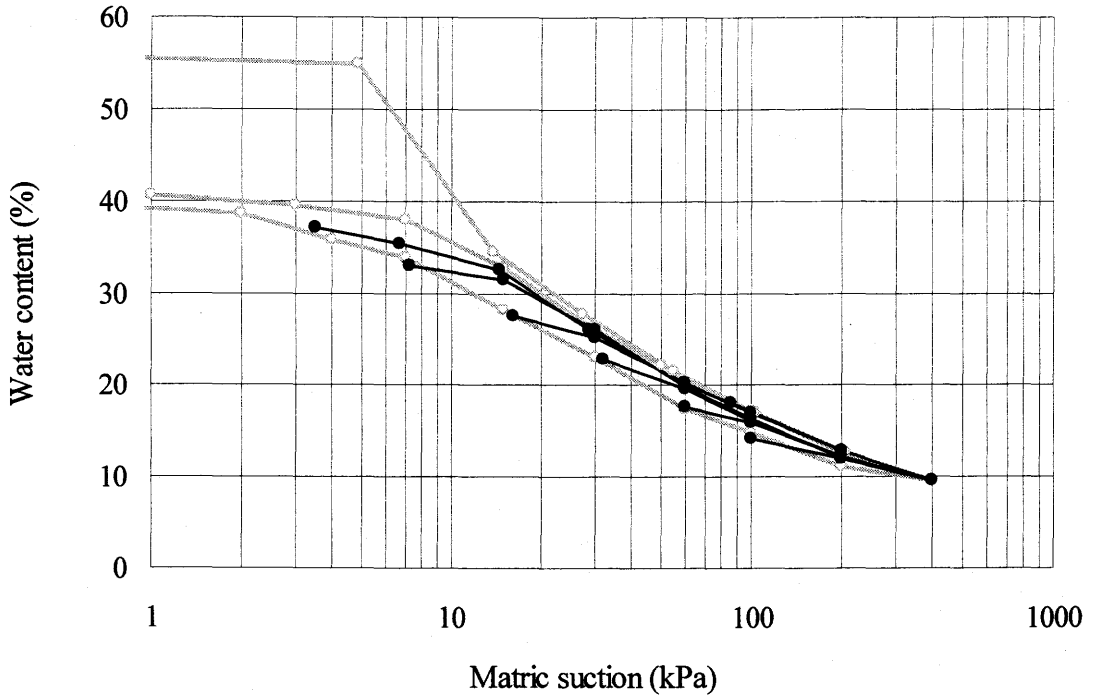

Figure 3.19a Measured primary drying scanning curves of Ceramic – 1

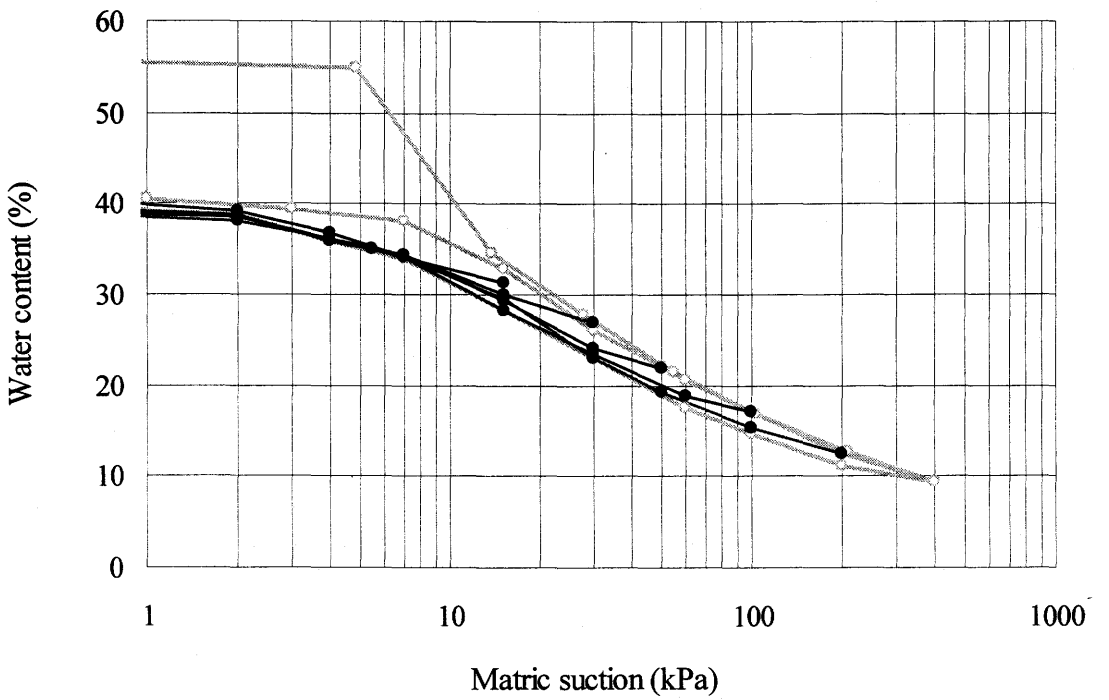

Figure 3.19b Measured Primary wetting scanning curves of Ceramic - 1

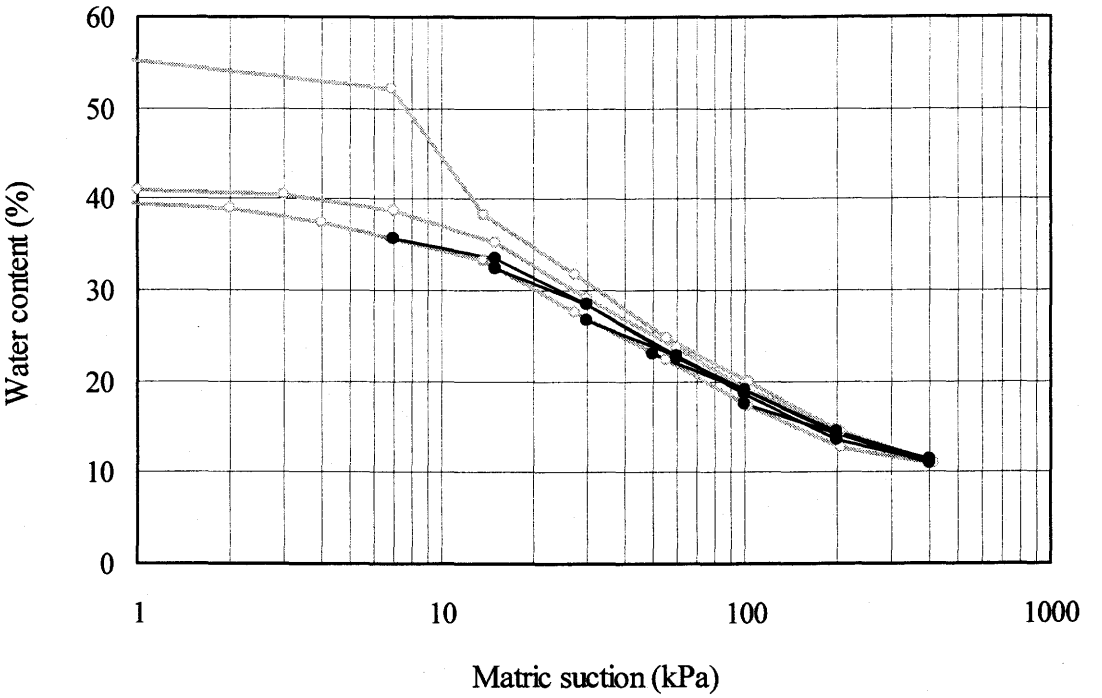

Figure 3.20a Measured primary drying scanning curves of Ceramic – 2

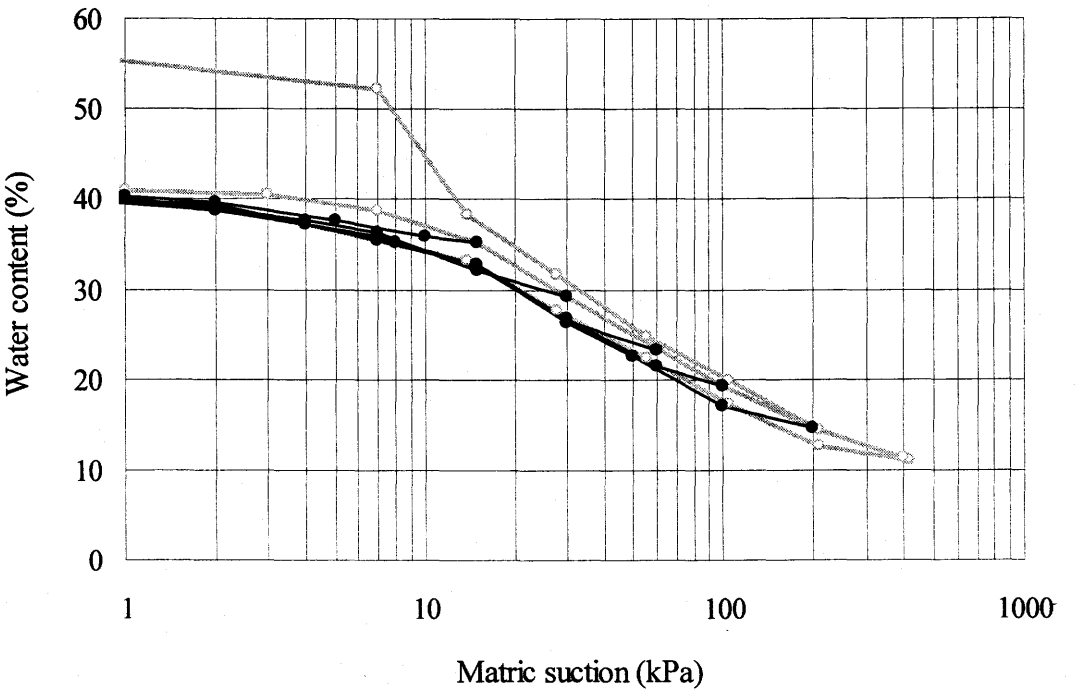

Figure 3.20b Measured Primary wetting scanning curves of Ceramic - 2

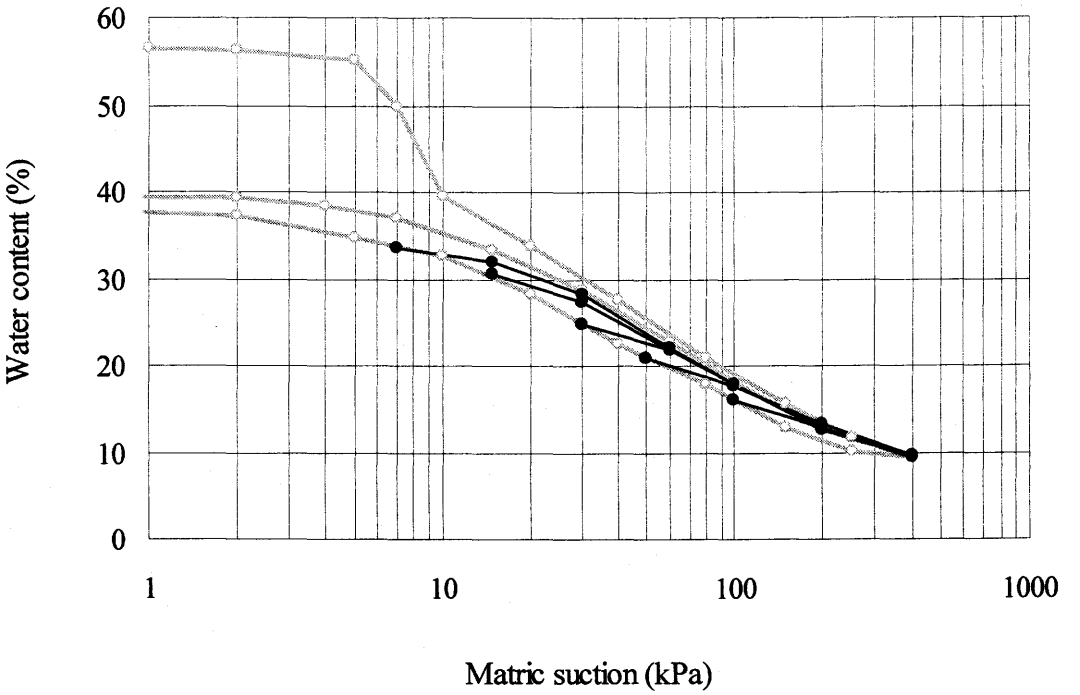

Figure 3.21a Measured primary drying scanning curves of Ceramic – 3

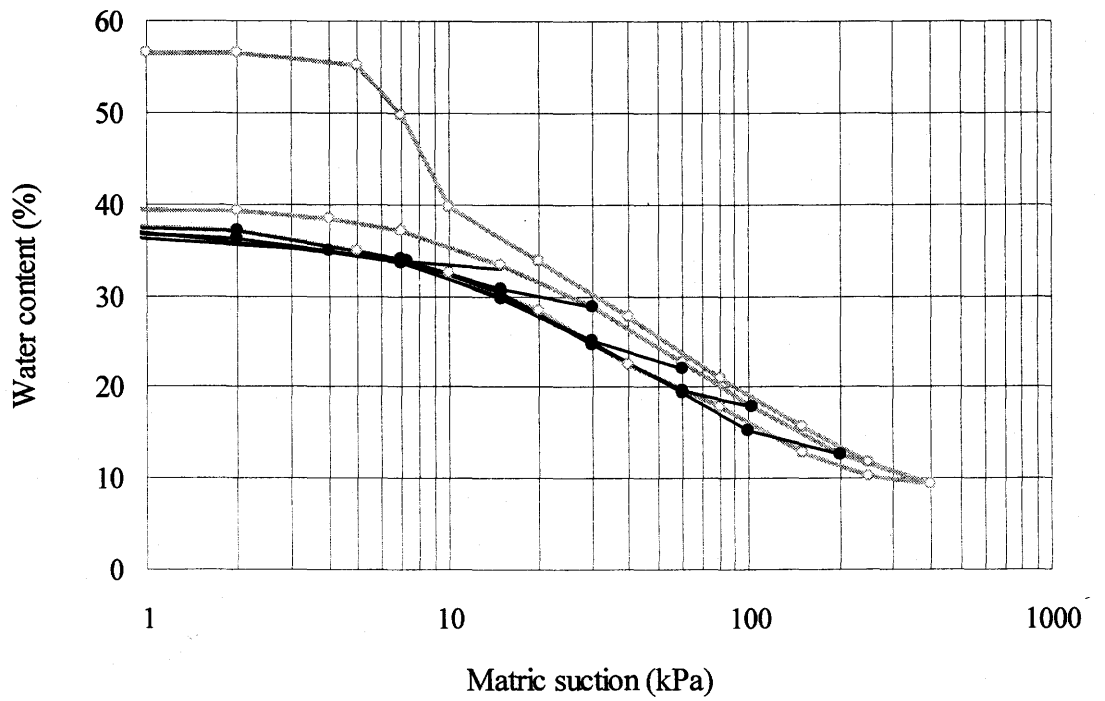

Figure 3.21b Measured Primary wetting scanning curves of Ceramic - 3

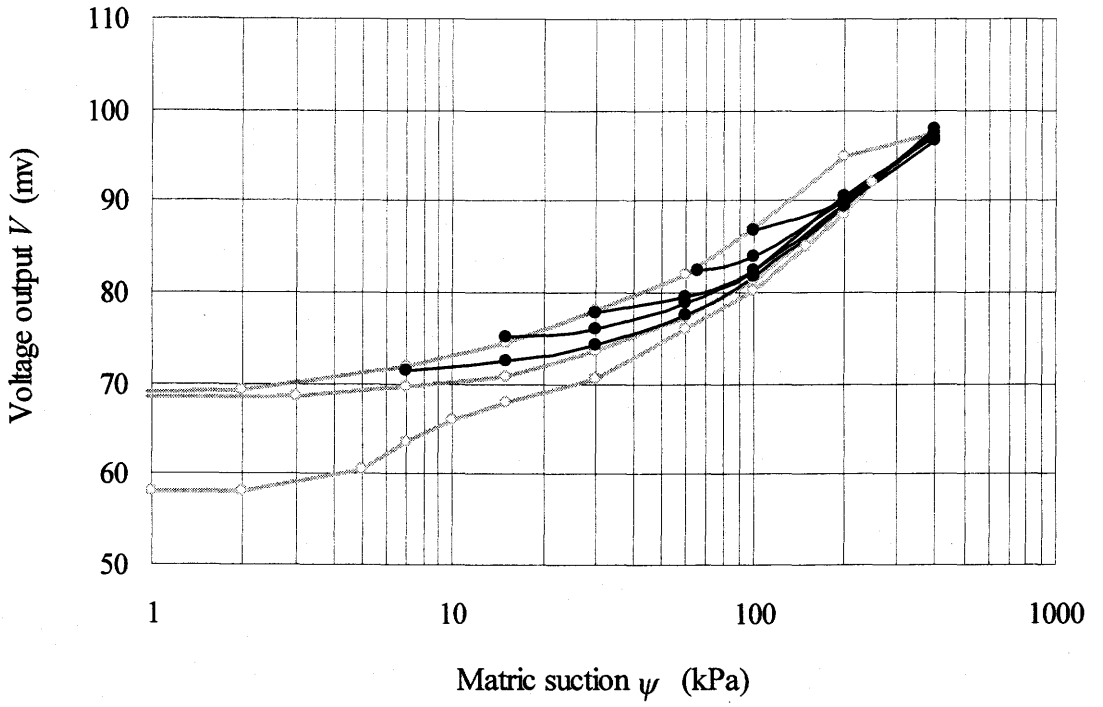

Figure 3.22a Measured primary drying scanning curves of Sensor – 1

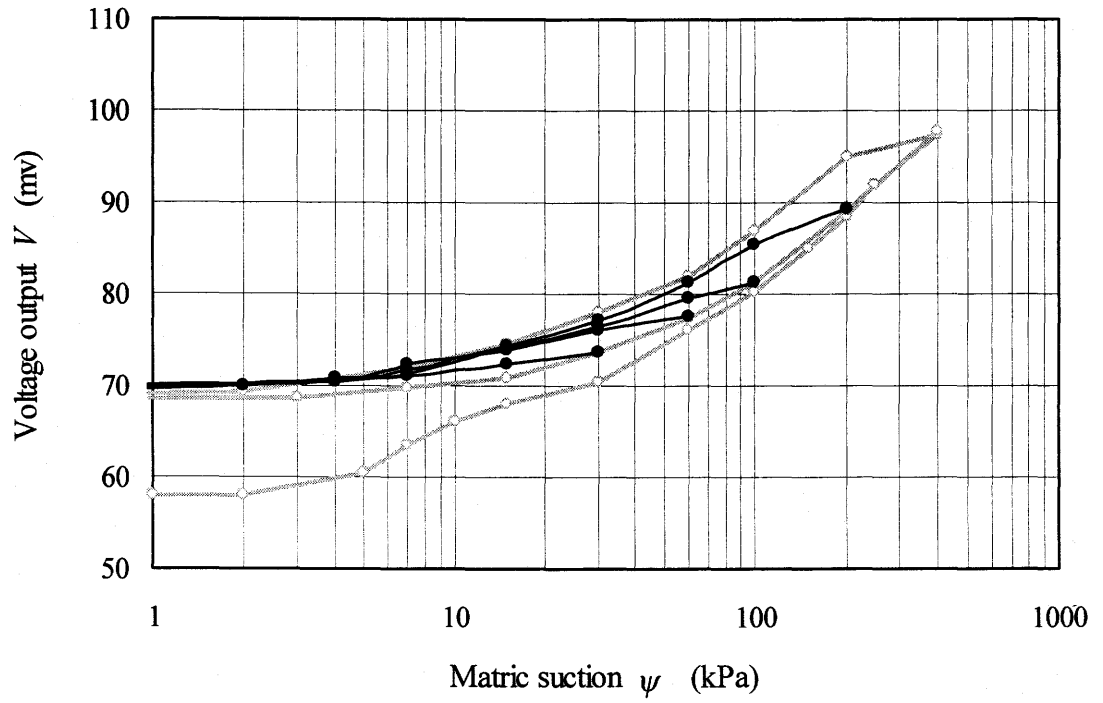

Figure 3.22b Measured primary wetting scanning curves of Sensor – 1

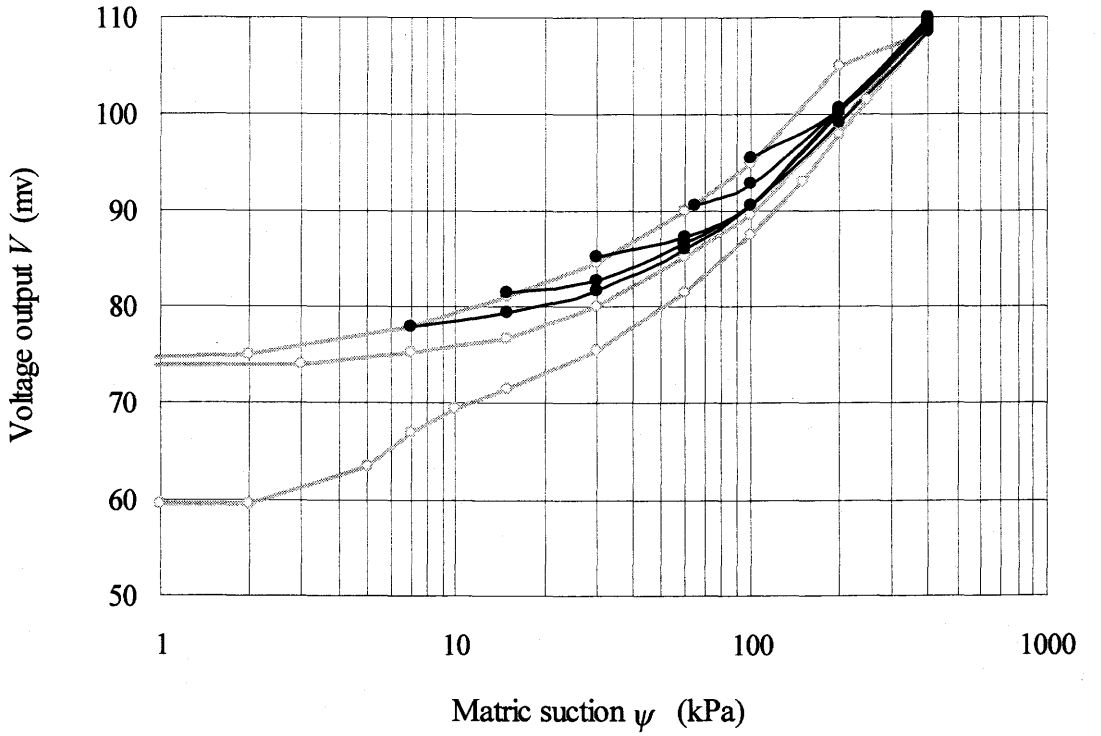

Figure 3.23a Measured primary drying scanning curves of Sensor – 2

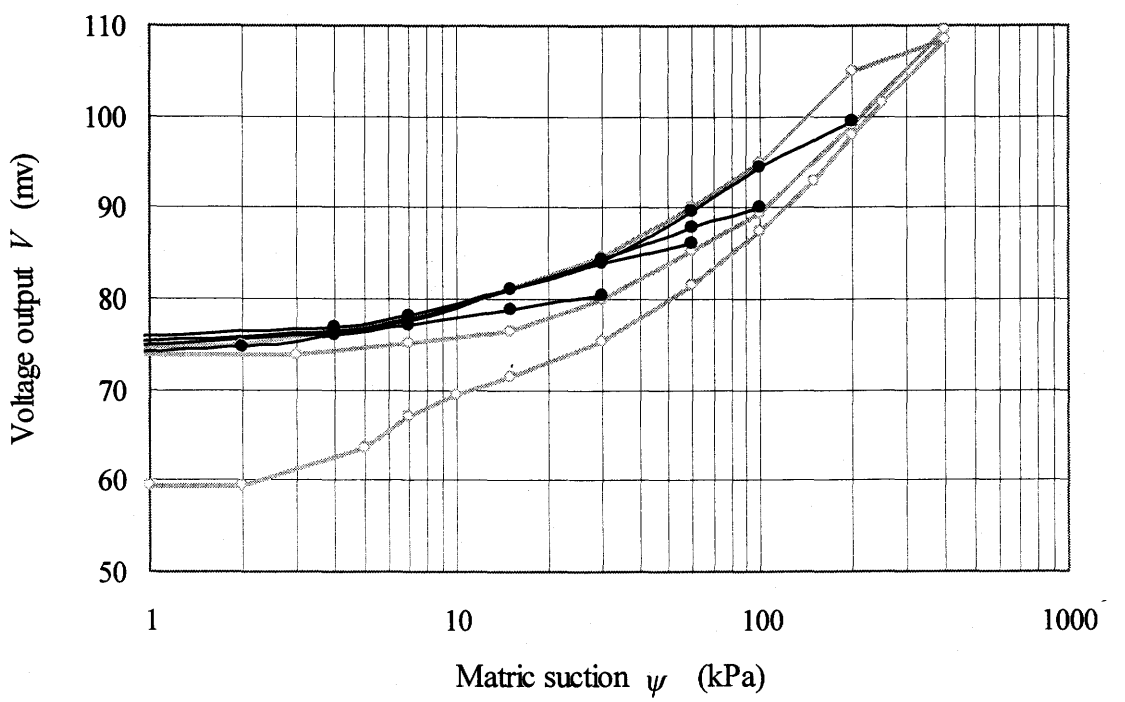

Figure 3.23b Measured primary wetting scanning curves of Sensor – 2

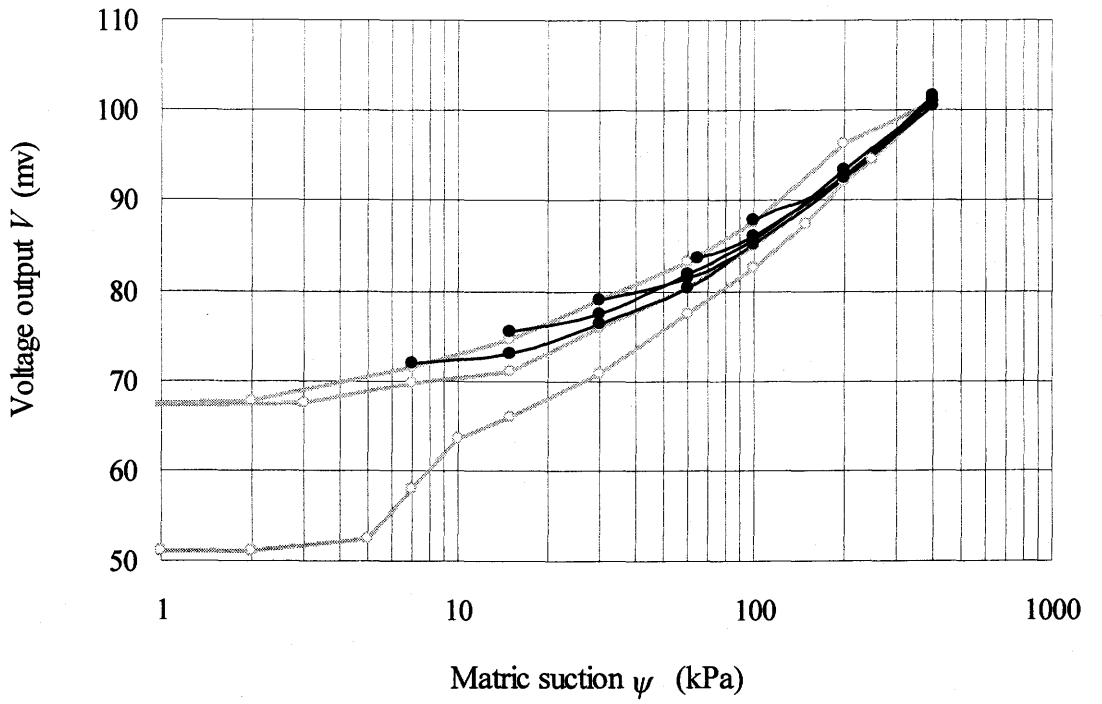

Figure 3.24a Measured primary drying scanning curves of Sensor – 3

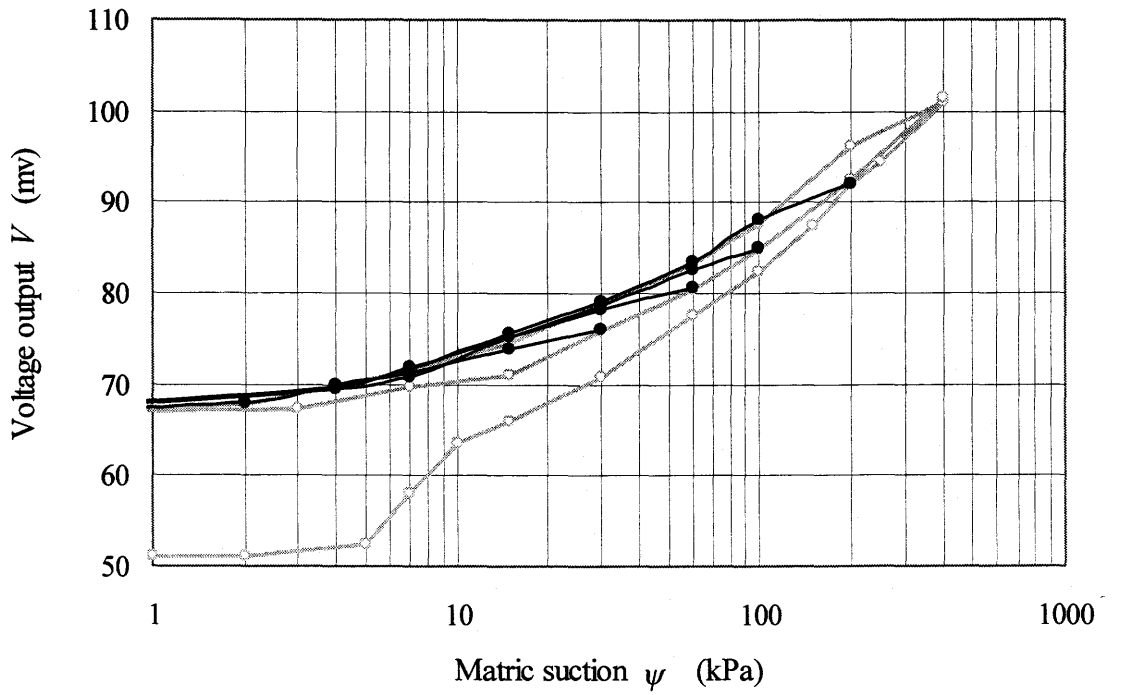

Figure 3.24b Measured primary wetting scanning curves of Sensor – 3

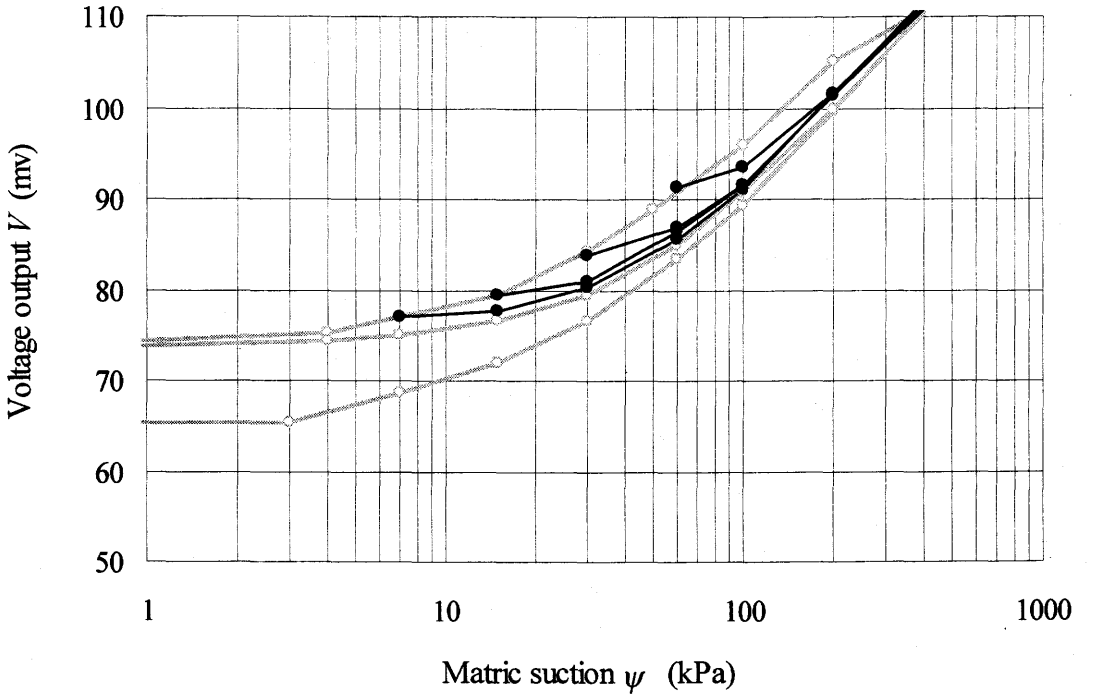

Figure 3.25 Measured primary drying scanning curves of Sensor – 4

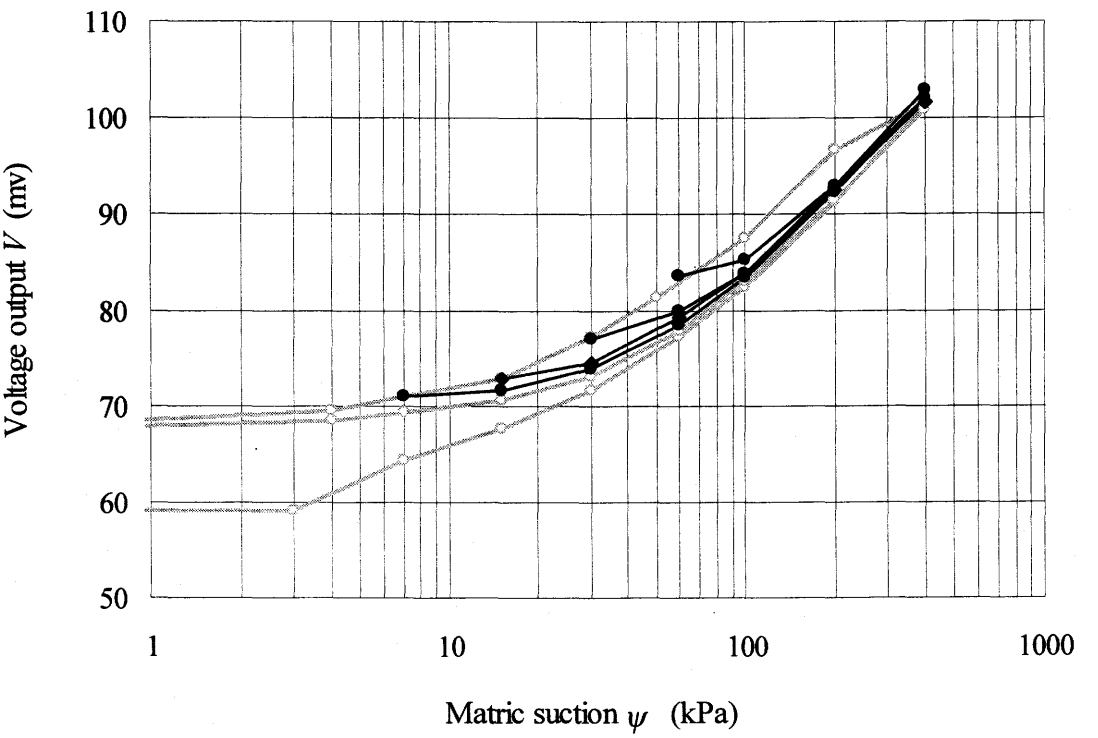

Figure 3.26 Measured primary drying scanning curves of Sensor – 5

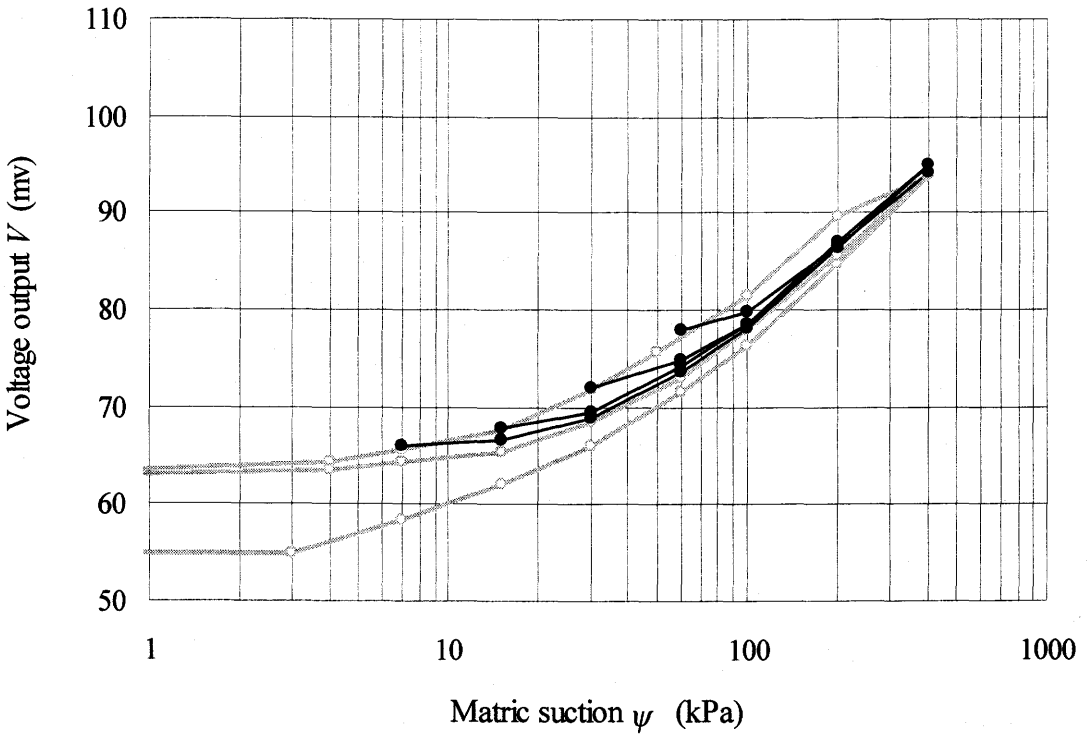

Figure 3.27 Measured primary drying scanning curves of Sensor – 6

The primary drying scanning curves were obtained by first decreasing the suction from 400 kPa directly to the suction of the starting point of the scanning curve and then increasing the suction in increments back to 400 kPa. Similarly, the wetting scanning curves were obtained by first increasing the suction by one step, from zero to the suction at the starting point of the wetting scanning curve and then decreasing the suction in increments back to zero.

Although the starting points of the primary scanning curves were reached by directly decreasing the suction from 400 kPa (for primary drying scanning curves) or increasing it from zero (for primary wetting scanning curves), all points fall almost on the hysteresis loop boundaries. The tests were carried out for almost one year, firstly on the initial drying curve, then on main drying and wetting curves, and finally on primary scanning curves. Therefore, the hysteresis loops of the sensor ceramics are reproducible and stable after several wetting and drying cycles and a relatively long

elapsed time. The wetting scanning curves of Sensors 4 to 6 were not measured because of the time limitation.

The water used in the tests was distilled water. A small quantity of bleach was added to the water flow line to prevent bacteria from growing. The water in the flow line and beneath the high air entry disc was flooded regularly using distilled water. More research work might be necessary to study the reproducibility of the hysteresis loop under field conditions, particularly on the influence of bacteria growth and ambient temperature changes.

The drying scanning curves are convex towards the drying boundary curve, and the wetting scanning curves are convex towards the main wetting curve. In other words, the primary scanning curves, starting from one hysteresis loop boundary, show a strong tendency to join the other boundary. The scanning curves come close to the other boundary only by one suction increment and then follow a path close to this boundary. This is an important characteristic of the capillary hysteresis of the ceramic tip of the sensor. Chapter 5, Mathematical Analysis, uses this characteristic of the ceramic to examine the applicability of the available hysteresis models on the ceramic.

The experimental points for the primary scanning curves mostly fall within the main hysteresis loop except some points in low suction range (i.e., suction less than 15 kPa) show a little scatter. This fluctuation can be minimized by carefully determining the point of equilibrium for each suction increment.

3.5 TEST RESULTS OF BOUNDARY WETTING CURVE

An air-dried ceramic or a sensor with an air-dried ceramic tip was installed in the pressure cell and a suction of 400 kPa was applied. The matric suction in an air-dried ceramic tip is usually considered to be around 10^6 kPa, much higher than 400 kPa. The sensor ceramic imbibed water until equilibrium with the applied suction of 400 kPa was reached. The suction was further decreased in increments to zero and the water content of the ceramic, or the output of the sensor, was measured at equilibrium for each suction increment.

The θ - ψ or V -ψ curve obtained using this procedure forms the lower boundary of all the θ - ψ or V-ψ relationships, and is hereby referred to as boundary wetting curve.

Tests on boundary wetting curve of Ceramic-1, 2 and 3, and Sensor-4, 5 and 6 were conducted and the results are shown in Fig. 3.28 to 3.33, together with initial drying curve and main hysteresis loops.

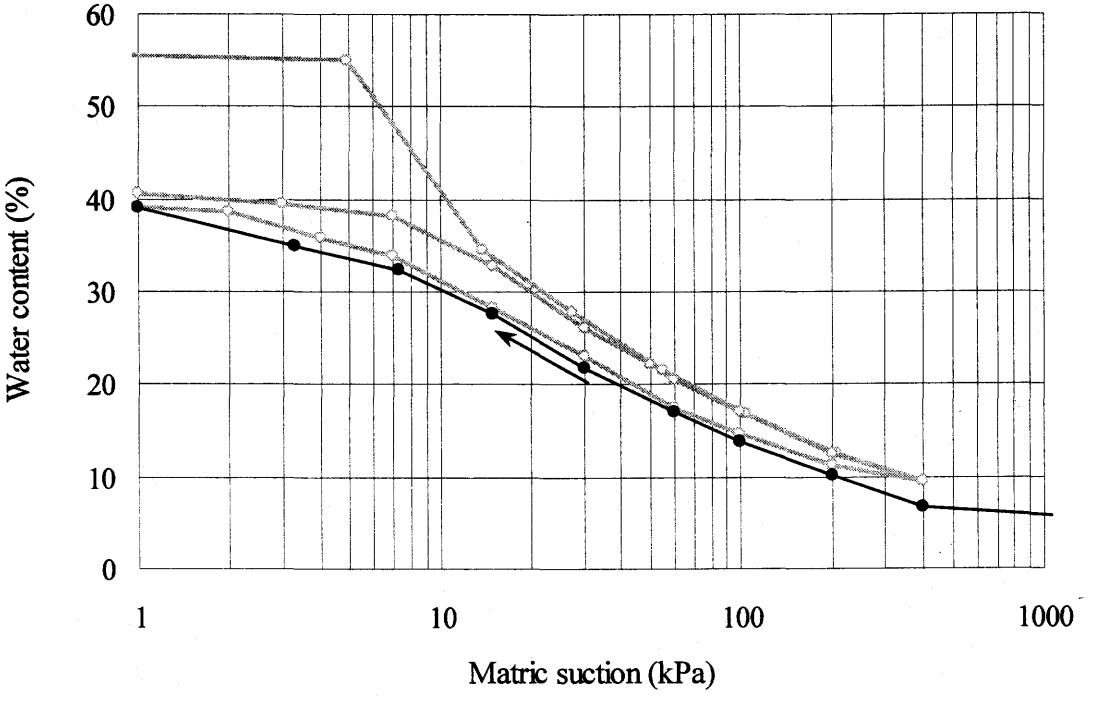

Figure 3.28 Boundary wetting curve of Ceramic-1

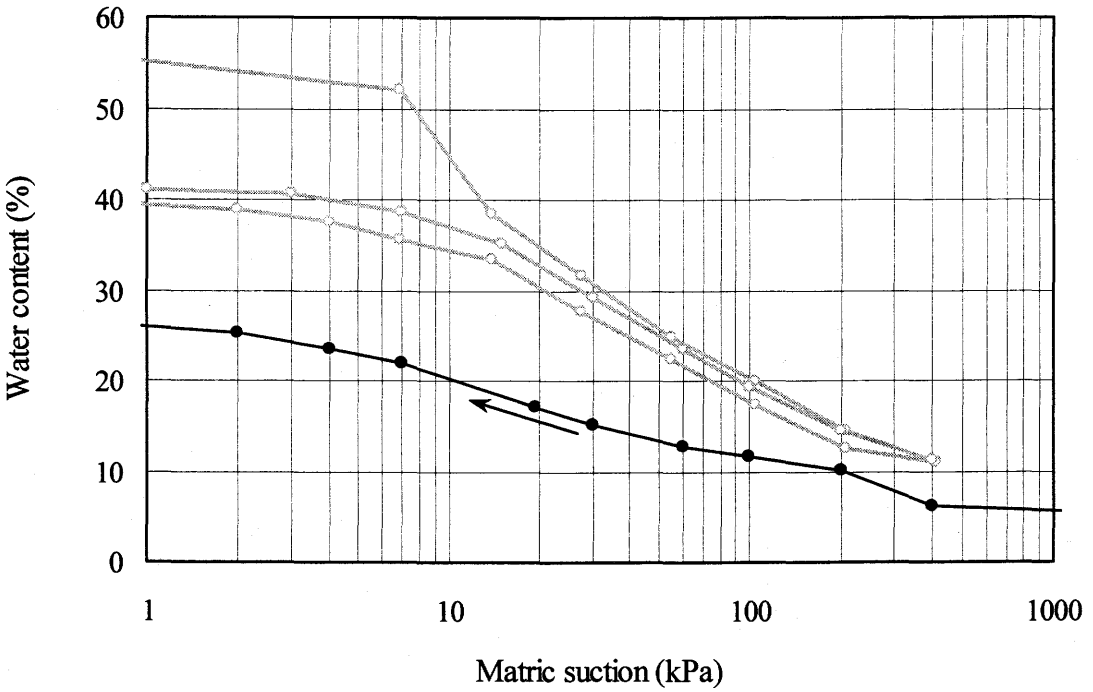

Figure 3.29 Boundary wetting curve of Ceramic-2

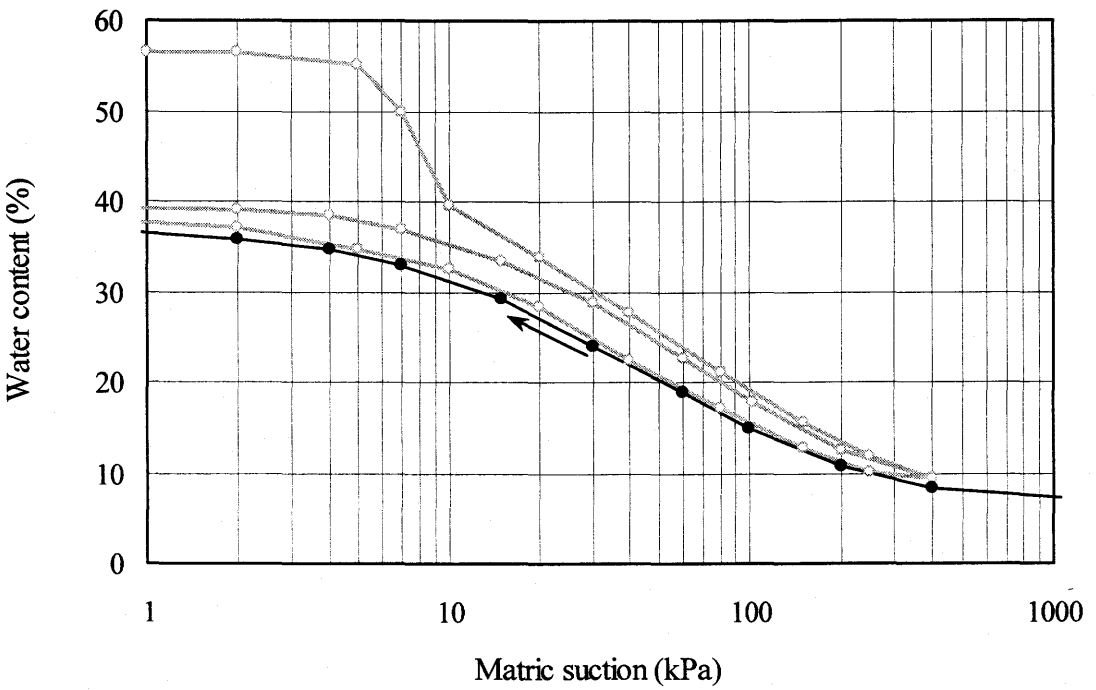

Figure 3.30 Boundary wetting curve of Ceramic-4

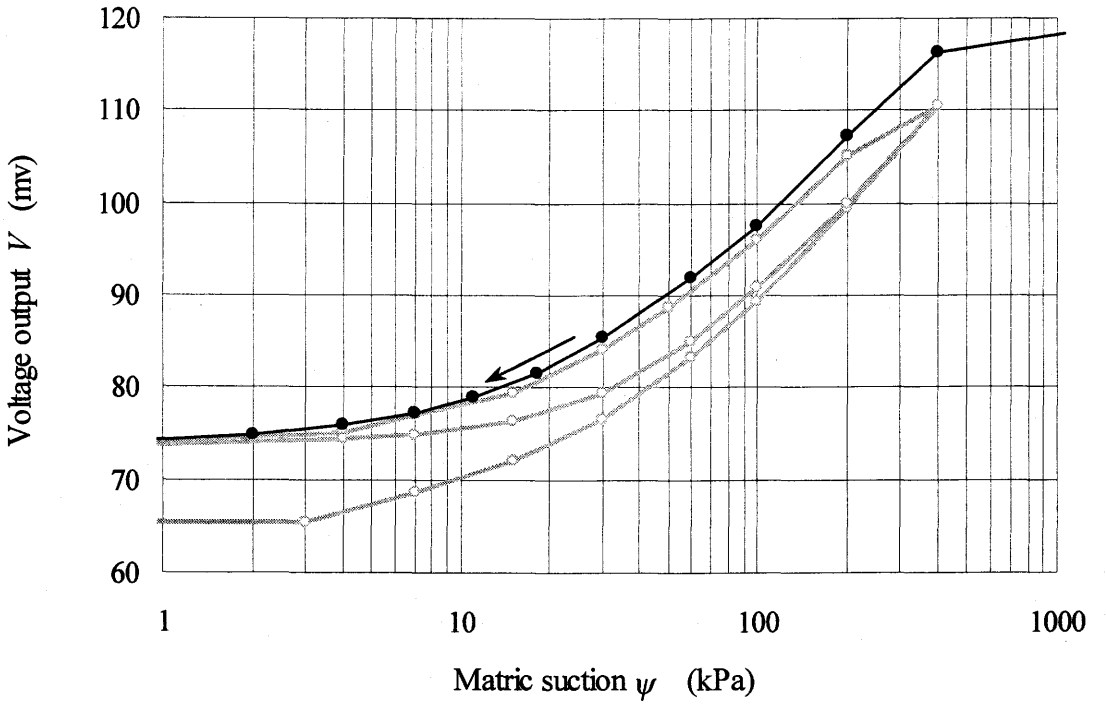

Figure 3.31 Boundary wetting curve of Sensor-4

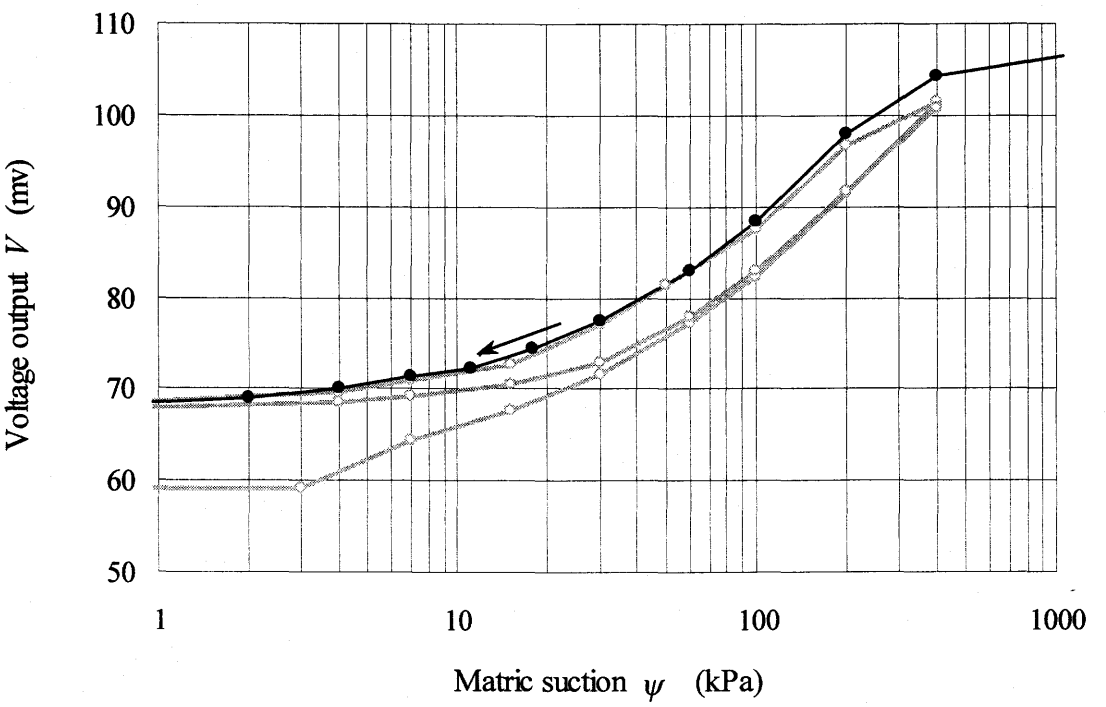

Figure 3.32 Boundary wetting curve of Sensor-5

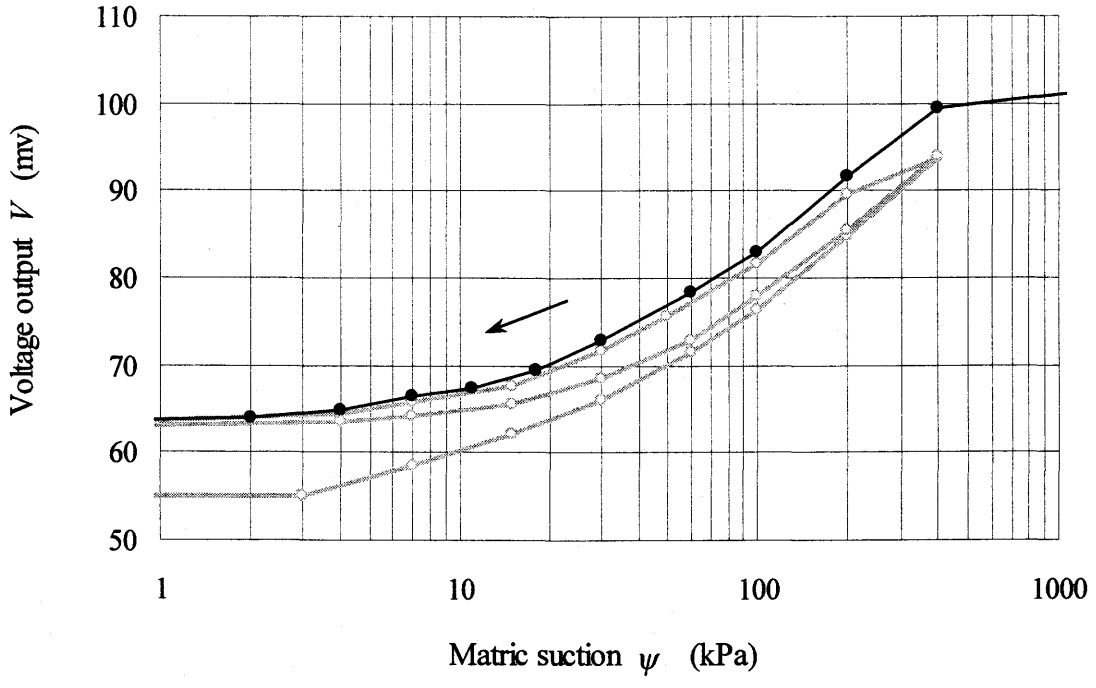

Figure 3.33 Boundary wetting curve of Sensor-6

The results show that the boundary wetting curve approximately coincides with the main wetting curve for the ceramic tips and sensors except for Ceramic-2. Therefore, the hysteresis loop can be reached either by drying the ceramic from saturated condition or by wetting the ceramic from air-dried condition. The sensor could be installed dry or wet in field.

The boundary wetting curve for Ceramic-2 is well below the main hysteresis loop (Fig. 3.29). A similar result was obtained for Ceramic-2 when investigating the behavior of air-dried ceramic tips submerged in water (the results are presented in a following section, Section 3.7). The reason for the abnormality of the results of Ceramic-2 when it is initially air-dried is not clear.

The main wetting curve, which is obtained by reversing the initial drying process at a matric suction of 400 kPa to zero, is actually a scanning curve by definition rather than the wetting boundary of the hysteresis loop. However, the main wetting curve almost coincides with the boundary wetting curve, except for the portion

of the curve adjacent to the point of reversal at 400 kPa. This indicates that this point is close to the point of residual saturation. That is also the reason why the equalization time is extremely long when matric suctions exceed 400 kPa.

3.6 TESTING RESULTS OF WETTING AND DRYING OUTSIDE THE MAIN HYSTERESIS LOOP

When a ceramic sensor in the field is soaked in water for a prolonged time, the water content of the ceramic tip of the sensor could be higher than the water content on the main hysteresis loop at zero suction. The subsequent drying and wetting will not fall within the main hysteresis loop. Tests were carried out to simulate the drying and wetting outside the main hysteresis loop. The results are presented in this section.

3.6.1 Case-1: The Sensor Ceramic is Fully Saturated

When a fully saturated ceramic is dried, it follows the initial drying curve. If the initial drying process is reversed before the suction reaches the maximum value, especially at low suction values, the wetting curve will be above the main hysteresis loop and below the initial drying curve. Tests were conducted on Ceramic-2 to further understand the behavior of the ceramic under such conditions. The results are shown in Fig. 3.34.

The ceramic was saturated using the vacuum method, followed by two drying and wetting cycles. The suction was increased in three increments to 7 kPa and then decreased back to zero, forming the first cycle (the thicker line in Fig. 3.34). The second cycle began at the end of the first cycle. The specimen was dried to a suction of 30 kPa, and then rewetted to zero suction, forming the second cycle (the thinner line in Fig. 3.34).

In the drying process of the first cycle, the θ-ψ relationship follows the initial drying curve. The wetting curve is almost horizontal. This may indicate that, if the water content of the ceramic is in the gap area, wetting of the ceramic takes place mainly by the escape of the entrapped air or so called relaxation.

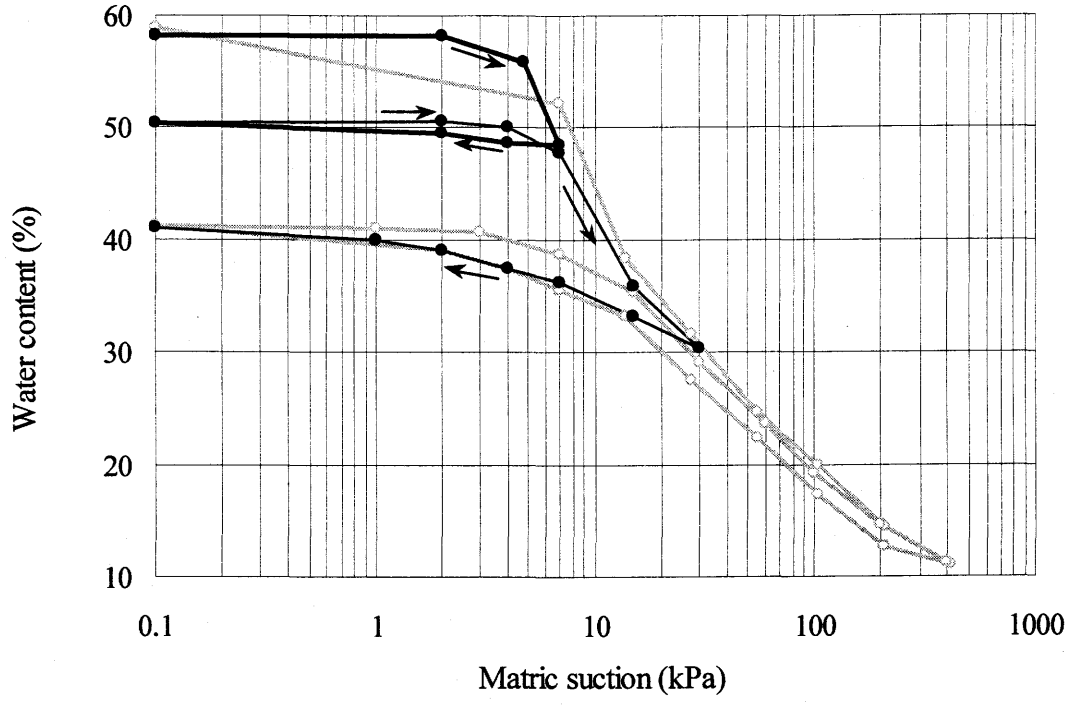

Figure 3.34 Wetting and drying outside the main hysteresis loop for Ceramic-2: Case-I

In the second cycle, the ceramic was re-dried to a point of 30 kPa, which is below the gap area. The rewetting curve almost coincides with the main wetting loop. This indicates that a dry-installed sensor will not reach water content in the area above the main hysteresis loop (i.e., the gap area). The wetting and drying will take place within the hysteresis loop, unless it is flooded for a long period. A saturated-installed sensor will also behave within the main hysteresis loop, after it reaches a certain value of suction (e.g., 15 kPa for Beta-97 sensors) in any drying process.

3.6.2 Case-II: The Sensor Ceramic is Partly Saturated

When a sensor in the field is soaked in water for a fairly long period, part of the entrapped air will escape. The water content of the sensor ceramic will be somewhere higher than that on the main hysteresis loop but lower than the saturated water content.

If the sensor is dried, the drying curve should be in between the initial drying curve and main hysteresis loop (i.e., within the gap area).

Laboratory tests were carried out to simulate the behavior of a flooded sensor using Ceramic-2. The results are shown in Fig. 3.35. After being rewetted to zero suction following a primary wetting scanning curve, the ceramic was taken out from the pressure cell and was submerged in water to try to get a water content above the main hysteresis loop. However the water content was only slightly above the main hysteresis loop, after 5 days of submergence. This fact shows again that the escape of the entrapped air is an extremely slow process. A positive pressure of 30 kPa was applied for about one hour, and then the ceramic specimen was left submerged for one more day, the final water content reached 47.5%, corresponding to a degree of saturation of 80.5%. The ceramic tip was dried and wetted following the path as shown in Fig. 3.35.

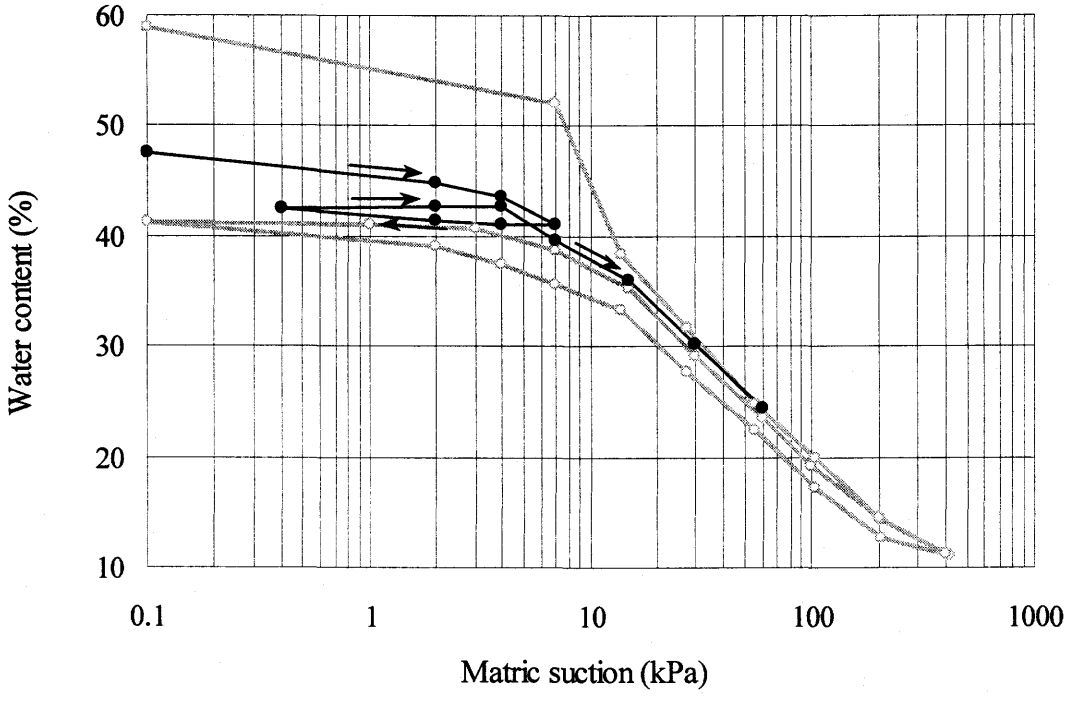

Figure 3.35 Wetting and drying outside the main hysteresis loop for Ceramic-2: Case-II

Figure 3.35 shows that, when a sensor is flooded for a prolonged period, it needs a certain value of matric suction, (e.g., 15 kPa for Ceramic-2), to bring the drying and wetting back to the main hysteresis loop. The test also shows that if a dry installed sensor is not submerged for a long period, the drying-wetting cycles always take place within the main hysteresis loop. The prolonged submergence may increase the water content of the sensor ceramic above the main hysteresis loop, and bring the wetting-drying cycles into the gap area above the main hysteresis loop. The behavior of a sensor submerged in water for a prolonged period is discussed in the next section.

3.7 TESTING RESULTS ON THE BEHAVIOR OF THE CERAMIC SUBMERGED IN WATER

The tests described above involved one-dimensional water flow into or from the ceramic of the sensor through the interface between the sensor ceramic and the high air entry disk. After the initial drying process, the drying and wetting will fall within the main hysteresis loop unless a low matric suction is maintained for an extremely long period to allow the relaxation to occur.

When a sensor is installed in the field, it is in contact with soil water through the end surface and the side surface. In some conditions, the ground water table may rise above the sensor, and the sensor is submerged. The purpose of the tests in this section was to study the behavior of a ceramic if it is or has been submerged in water.

An air-dried ceramic tip was simply soaked in distilled water, while the change in water content of the ceramic tip with time was measured. Three ceramic tips were tested, including Ceramic-1, Ceramic-2, and a ceramic tip that had not been used in the above tests, referred to as Ceramic-4. Figure 3.36 shows the increase in water content with time for the three ceramics.

The three curves have the same shape. An interesting phenomenon is that all the three curves have a turning point occurring at an elapsed time of around one to two hours. Before this point, the water content shows a rapid increase with time. Right after this point is passed, the rate of increase in water content slows down significantly, though the water content still shows a continuous increase. Equilibrium is still not reached at an elapsed time of 1800 hours (2.5 months). The degree of

saturation of Ceramic-1 is 73.6% after an eight-day submergence, and the degree of saturation of Ceramic-2 and Ceramic-4 are 66.3% and 75.1%, respectively, after a 2.5-month's submergence.

The degree of saturation at the turning points on the θ - t curves of Ceramics-1 and 2 is 63.5% and 46% for Ceramics-1 and 2, respectively. These are even lower than the degrees of saturation at the point of zero matric suction on the main hysteresis loop of the corresponding ceramic, which are 73.2% and 70.3%, respectively.

The reason for the existence of the turning point is considered to be that, before the turning point water stays only in the small pores and the large pores are still occupied by air. The airflow paths still exist in the ceramic. The pore air can easily flow out of the ceramic. At the turning point, the water content reaches such a value that the airflow paths start to be shut down. With further increase of water content, the remaining pore air is entrapped in the pores as air bubbles, and cannot flow out of the ceramic freely. However, since there is an energy difference between the entrapped air and the air in the atmosphere outside the ceramic, the entrapped air will try to escape from the ceramic by diffusing and pore-water redistribution. The water content shows a continuous increase at a low rate. The "escaping" is a process lasting an extremely long time.

An abnormal phenomenon is that the θ - t curve of Ceramic-2 is well below the curves of the other two ceramic tips. The degree of saturation at the turning point of Ceramic-2 is only 46.5%. Even at elapsed time of 10 days, the degree of saturation is only 55%. As described in the previous section (Section 3.5, Boundary Wetting Curve), the boundary wetting curve of Ceramic-2 is also well below the main hysteresis loop. The submergence curve, θ - t, together with the boundary wetting curve, shows an abnormal wetting behavior of air-dried Ceramic-2. The reason is not clear.

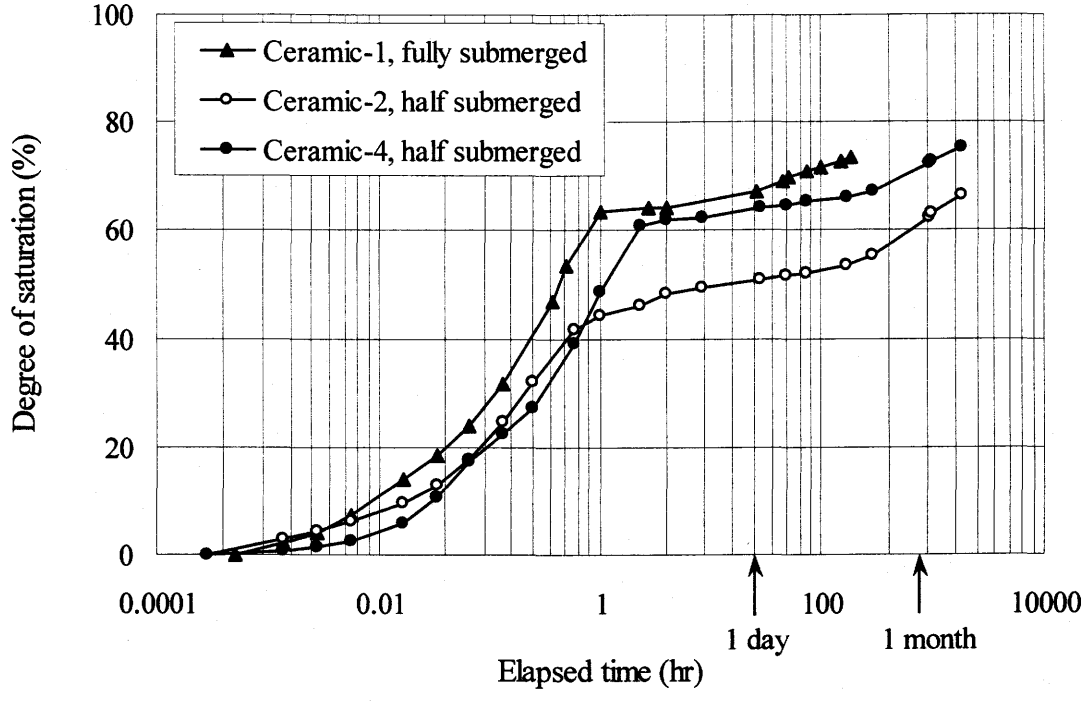

Figure 3.36 The increase in water content with time of ceramics submerged in water

CHAPTER 4

Discussions of the Test Results

The test results presented in the previous chapter show the capillary hysteresis properties of the ceramic tip of sensor Beta-97. This chapter presents a discussion of the test results, including

(1) a comparison with the results of other researchers,

(2) the effects of hysteresis on the measurement of matric suction, and

(3) comments on the conventional calibration and measuring procedures using thermal conductivity sensors.

4.1 A COMPARISON WITH THE TEST RESULTS OF OTHER RESEARCHERS

The experimental studies on the water capillary hysteresis found in the literature were mostly on coarse-grained materials, such as glass beads, sand, sandy loam, etc. Those materials have relatively big pore sizes and a high saturated coefficient of permeability. The water content of a coarse-grained material generally drops steeply after passing the air entry value and the residual saturation is reached at a relatively low suction value.

The ceramic tip of the sensor is designed to have as wide a pore size distribution as possible to accommodate a wide range of suction measurement, and to have as low an air entry value as allowed by the requirement of strength. The flat shape of the soil-water characteristic curve of the ceramic tip of the Beta-97 sensor indicates a wide pore size distribution of the ceramic tip. The saturated coefficient of permeability of the ceramic tip is 2×10^{-6} m/s. This permeability is in the range of permeability of silts and fine sands. The ceramics still have a water content of approximately 10% at a

suction of 400 kPa, as shown in the test results of the ceramics presented in the last chapter. This fact, together with the flat shape of the hysteresis curves of the ceramics, shows that the ceramic tip is equivalent to a well-graded fine-grained material in water capillary properties.

A fine-grained porous material is different from a coarse material in solid structure, shape of the pores, patterns of pore interconnections, and mechanism of water and air flow within the material. These differences result in the difference in the water capillary properties between a fine-grained material and a coarse-grained material.

4.1.1 Main Hysteresis Loop

Most studies on the water capillary hysteresis of soils were conducted by researchers from soil science. The materials used were generally coarse-grained. The residual saturation was reached at a low value of matric suction, usually smaller than 60 kPa. The experimental results of such materials found in the literature generally show a wide hysteresis loop. Figure 2.11 in chapter 2 shows the test results on Rubicon sandy loam (Topp, 1969) and gives a typical example of the wide hysteresis loop of a coarse-grained material.

Another example of the hysteresis loop of a coarse-grained material is shown in Fig. 4.1, which is the experimental curve of a porous body prepared from glass beads (Poulovassilis, 1962). There is a big difference in water content between the two boundaries at the same matric suction. For instance, the water content at 1.4 kPa of suction on the main drying curve is 5.3 times the water content on the main wetting curve at the same matric suction. In contrast, the ceramic tip of sensor Beta-97 has a narrow main hysteresis loop, as seen in Fig. 4.2, which shows the test results of Ceramic-1 with the axis of matric suction in arithmetic scale. The porous material of glass beads was totally dried at a suction of 2.6 kPa (Fig. 4.1), while the ceramic still had a water content of 10% at a suction of 400 kPa (Fig. 4.2). This indicates the existence of a large percentage of fine pores in the ceramic.

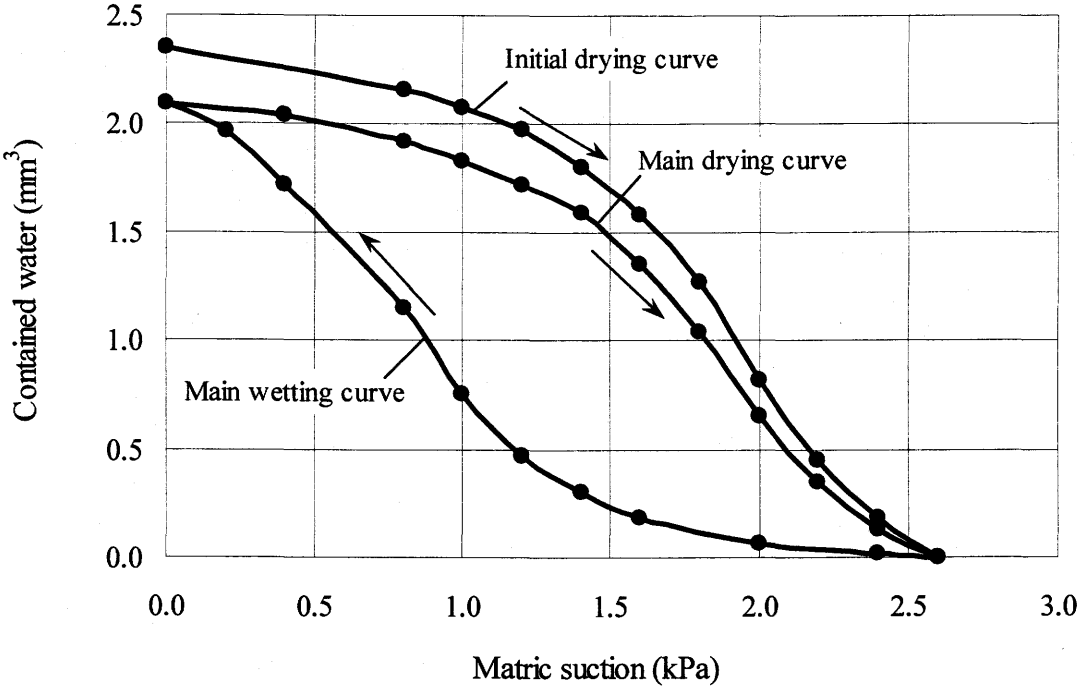

Figure 4.1 Measured hysteresis loop of a rigid glass beads body (from Poulovassilis, 1962)

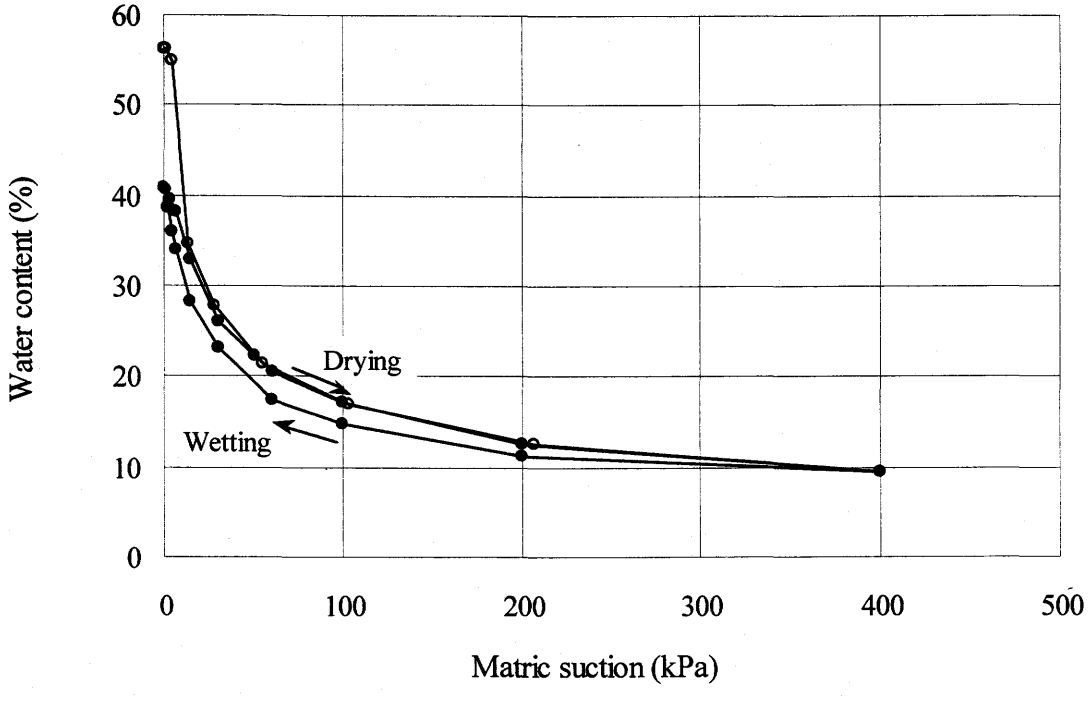

Figure 4.2 Initial drying curve and main hysteresis loop of Ceramic-1

4.1.2 Initial drying curve

A gap generally exists between the initial drying curve and the main drying curve due to air entrapment in the pores. Cary (1967) has measured simultaneously the soil moisture and the volume of entrapped air as a function of matric suction in wetting and drying processes. No general characteristic shape was achieved for the dependence of volume of entrapped air, V_a, on matric suction, ψ. Mualem (1974) used Cary's data to compute the relative space occupied by water, c, as a function of effective saturation, S_e, for the three soils investigated by Cary. The relative pore space occupied by water, c, is defined as

$$c = \frac{V_w}{V_w + V_a} \tag{4.1}$$

and the effective saturation is defined as

$$S_e = \frac{V_w - V_{w(\min)}}{V_{w(\max)} - V_{w(\min)}} = \frac{\theta - \theta_{\min}}{\theta_{sat} - \theta_{\min}} \tag{4.2}$$

where, V_w and V_a are the volumes of water and entrapped air respectively, in a particular point along the hysteresis loop, and θ_{sat} denotes the water content when the material is saturated.

When re-analyzing Cary's experimental data, Mualem (1974) found that: (1) there was no significant difference between the value of c in a wetting process and drying process and (2) there was no significant difference from soil to soil. The c values for the three soils varied between 0.85 to 0.95, and the average value of c was 0.9. Based on these observations, Mualem (1974) made the assumption that a value of 0.9 of the parameter c holds for all kinds of soils. Thus the following relationship between initial drying curve and the main drying curve exists.

$$\theta_d(\psi) = \frac{\theta_0 - \theta_{\min}}{\theta_{sat} - \theta_{\min}} \cdot (\theta_d^0(\psi) - \theta_{\min}) + \theta_{\min} = 0.9(\theta_d^0(\psi) - \theta_{\min}) + \theta_{\min} \tag{4.3}$$

where

$\theta_d(\psi)$ = the main drying curve

$\theta_d^0(\psi)$ = the initial drying curve

θ_{min} = the minimum value of water content or water content at residual saturation

θ_0 = the water content at $\psi = 0$ on the main drying curve, (i.e., the maximum water content on the main drying curve, $\theta_d(0)$).

Mualem used the experimental data measured by Poulovassilis (1970a, b) to compare with the proposed theory. Good agreement was found between the predicted initial drying curve and the experimental data for a sand soil and a glass bead sample.

In Fig. 4.3, experimental data of Ceramic-1 was used to check the validity of Eq. 4.3 on the sensor ceramic. As can been seen from the figure, the predicted initial drying curve using Mualem's theory is not in good agreement with the measured curve.

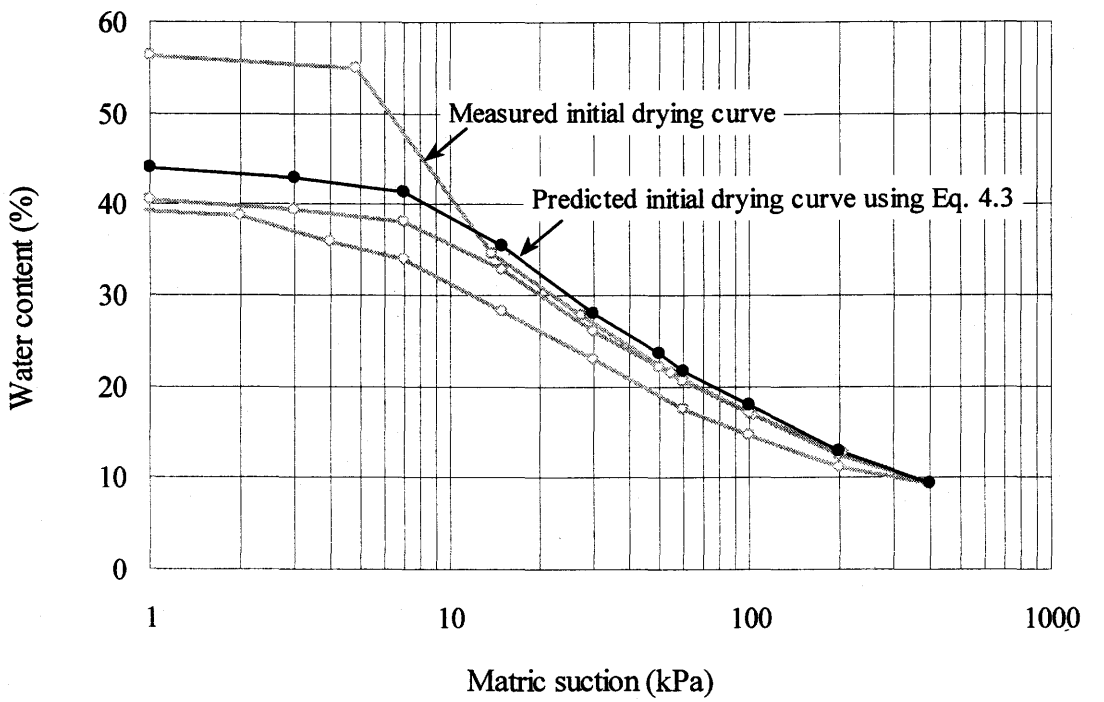

Figure 4.3 The initial drying curve of Ceramic-1 predicted using the equation Mualem proposed (1974)

4.2 THE EFFECTS OF CAPILLARY HYSTERESIS ON THE MATRIC SUCTION MEASUREMENTS

The thermal conductive sensor measures matric suction by measuring the temperature rise at the center of the sensor when a controlled amount of thermal energy is generated at the center. The output of the sensor is a voltage, and is a function of water content of the sensor ceramic tip. Due to the capillary hysteresis of the porous ceramic, a value of water content may correspond to various matric suction values. Therefore, the suction cannot be determined by the output of the sensor only. If the hysteresis is not considered, error will arise in determining the suction using the sensor output.

Assume that a sensor has been installed in the field and has not been soaked for a prolonged period. The wetting and drying cycles will fall within the main hysteresis loop (Fig. 4.4). For a certain value of voltage output of the sensor, the maximum possible value of the corresponding matric suction is on the main drying curve (i.e., ψ_d), and the minimum value on the main wetting curve (i.e., ψ_w). The matric suction corresponding to this voltage output could be anywhere between the minimum value and the maximum value depending upon the water flow history.

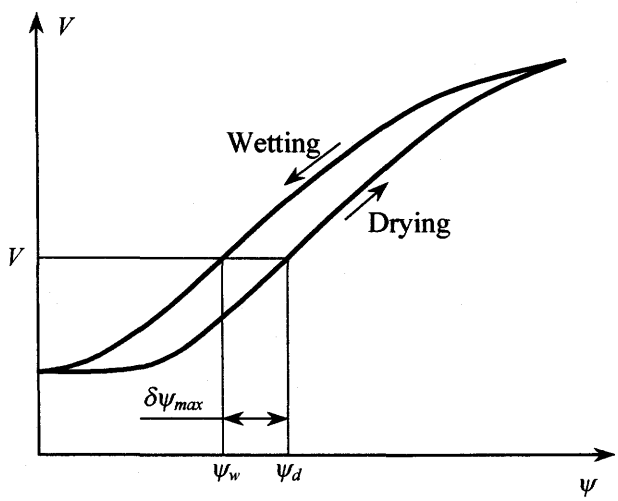

Figure 4.4 The possible error caused by the capillary hysteresis when using only main drying or main wetting curve as calibration curve

In the conventional calibration procedure, the sensor is first soaked in water for a few days and then dried by increasing the suction. The calibration curve is actually a drying curve. Assume that the calibration curve is the main drying curve. The measured suction corresponding to a voltage output of V will be the suction value on the main drying curve, ψ_d. The maximum absolute error occurs when the sensor is undergoing a main wetting process. In this case, the actual suction is ψ_w. The maximum error, $\delta\psi_{max}$, caused by the capillary hysteresis for the voltage output, V, is the horizontal distance between the main wetting curve and the main drying curve, i.e., $\delta\psi_{max} = \psi_d - \psi_w$, as shown in Fig. 4.4.

The maximum relative error caused by the capillary hysteresis is

$$\varepsilon_{\max} = \frac{\delta\psi_{\max}}{\psi_w} = \frac{\psi_d - \psi_w}{\psi_w} \tag{4.4}$$

Figures 4.5 to 4.8 show the relationships between the errors, $\delta\psi_{max}$ or ε_{max}, and the measured matric suction, ψ_d, of the three ceramic samples and the six sensors, when the main drying curve is used as the calibration curve.

The curves in Figs. 4.5 and 4.6 show that the maximum absolute error, $\delta\psi_{max}$, increases almost linearly with the measured matric suction. The maximum absolute error, $\delta\psi_{max}$, increases from zero when the measured suction is zero to around 100 kPa when measured suction is 300 kPa. When the measured suction is 300kPa, the actual matric suction is approximately in the range of 200kPa to 300 kPa, depending upon the wetting and drying history.

Figures 4.7 and 4.8 show the relationship between the maximum relative error, ε_{max}, and the measured matric suction, ψ_d, when the main drying curve is used as the calibration curve. It can be seen that the relative error shows a tendency of decreasing when the measured suction is low, and shows approximately constant when the measured suction is roughly in the range of 50 to 300 kPa. When the measured suction is low, the relative error is higher, around 50%. In the range of 50 to 300kPa, the average relative error varies from sensor to sensor, from 24% for Sensor-3 up to 40%

for Sensor-1. The above discussion indicates that the effects of capillary hysteresis on the matric suction measurement using thermal conductivity sensors are not negligible.

If the calibration is carried out by wetting of an air-dried sensor, the calibration curve will be the main wetting curve. In this case, the above analysis and results still apply.

In the conventional calibration procedure, the sensor is first soaked in water for a few days and then dried by increasing the suction. The initial degree of saturation is not known. The calibration curve could be above or below the main drying curve. Therefore, the error of measurement using a calibration curve obtained using the conventional calibration procedure could be even higher than indicated in the above analysis.

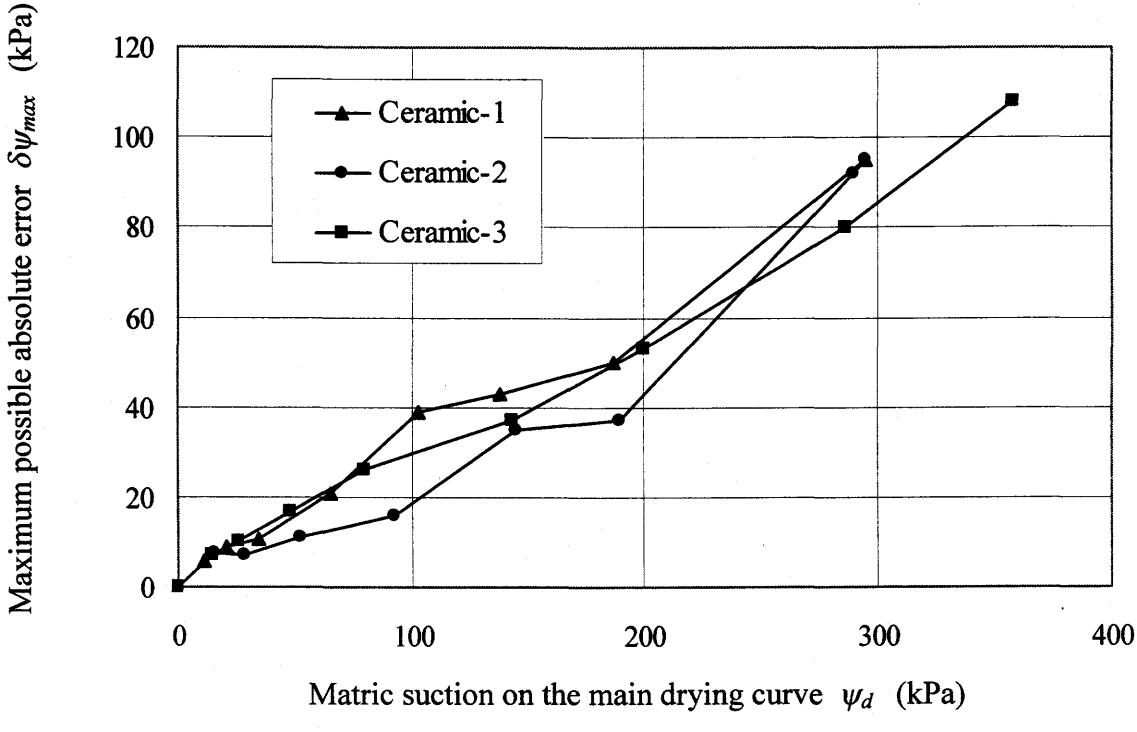

Figure 4.5 Possible absolute error caused by the capillary hysteresis for the three ceramic samples

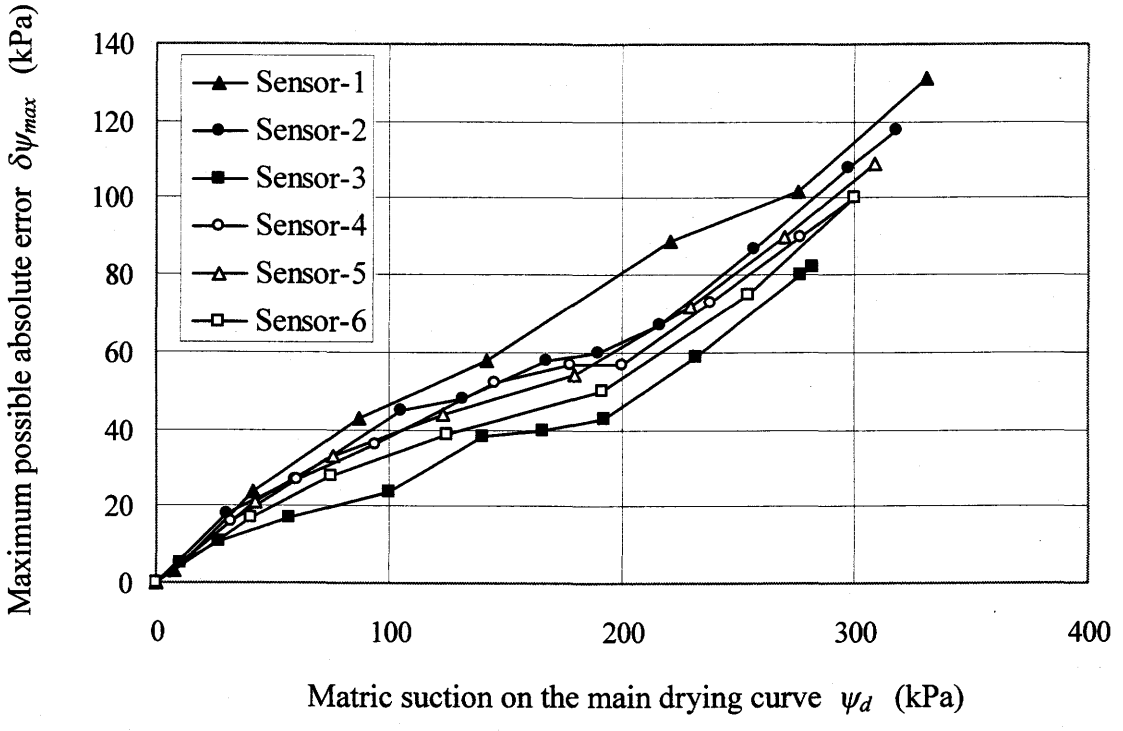

Figure 4.6 Possible absolute error caused by the capillary hysteresis for the six sensors

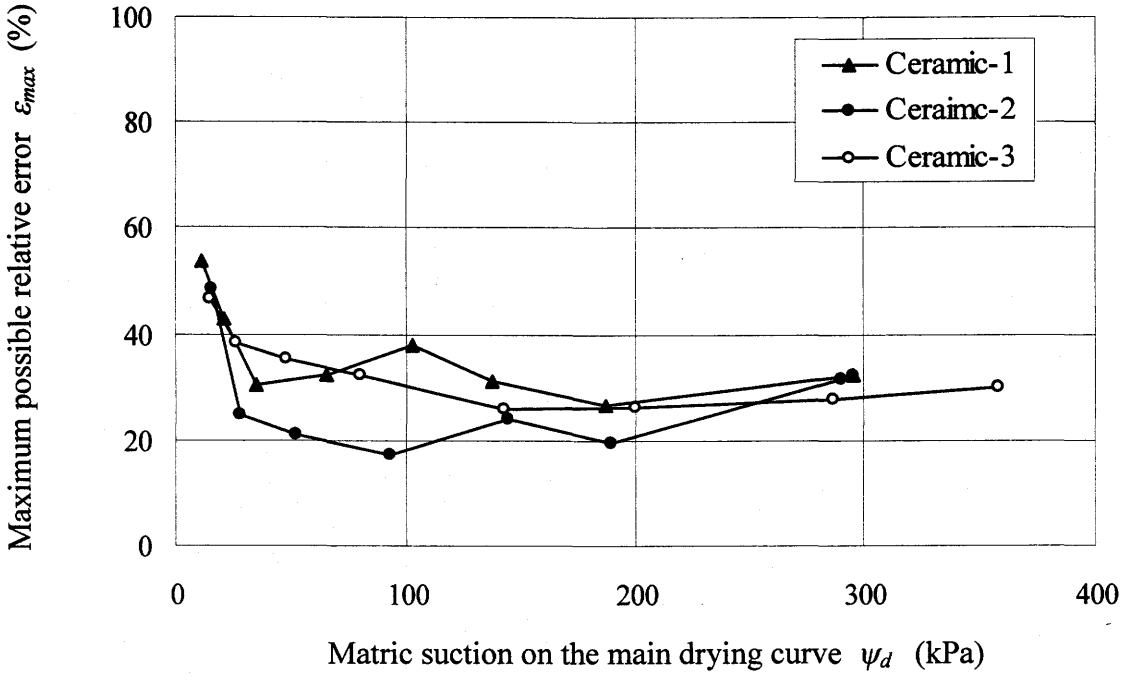

Figure 4.7 Possible relative error caused by the capillary hysteresis for the three ceramic samples

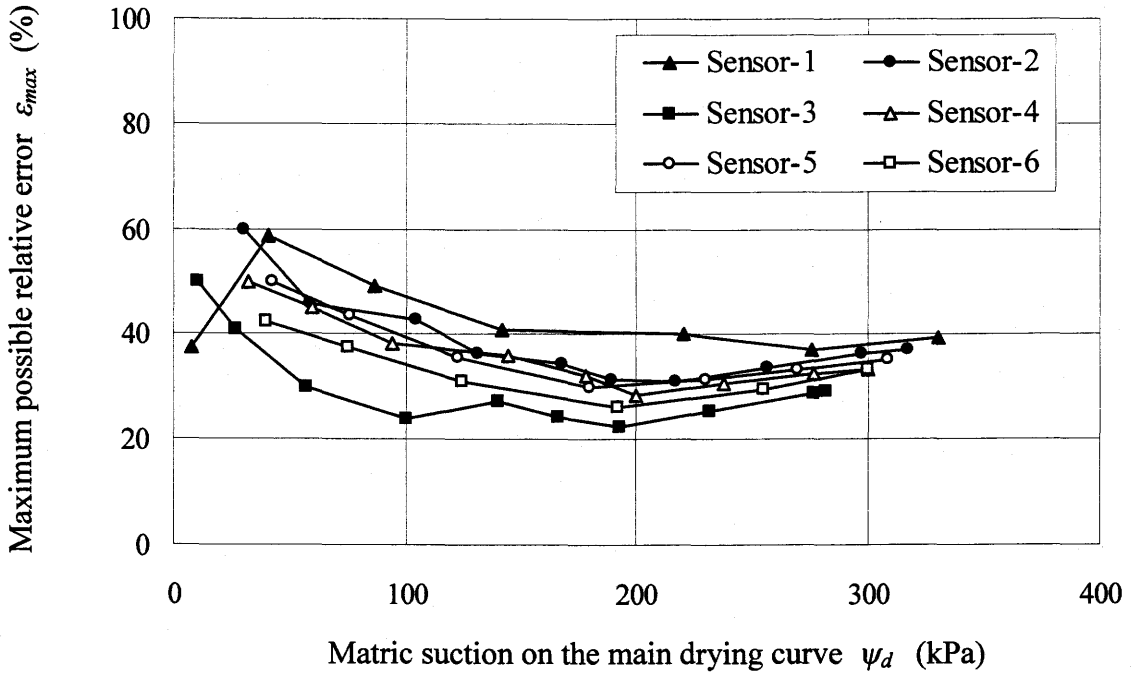

Figure 4.8 Possible relative error caused by the capillary hysteresis for the six sensors

When ψ axis is in logarithmic scale, the distance between the two branches of the main hysteresis loop is $\log\psi_d - \log\psi_w = \log(\psi_d/\psi_w)$. The values of (ψ_d/ψ_w) are plotted versus ψ_d in Figs. 4.9 and 4.10. It can be seen that the value of (ψ_d/ψ_w) does not show significant difference from ceramic to ceramic or from sensor to sensor. It is possible to measure only one branch of the main hysteresis loop and then to move this branch horizontally a distance of $\log(\psi_d/\psi_w)$ to make a reasonable estimation of the other branch. This method of estimating one branch using the other branch will be discussed in Chapter 5.

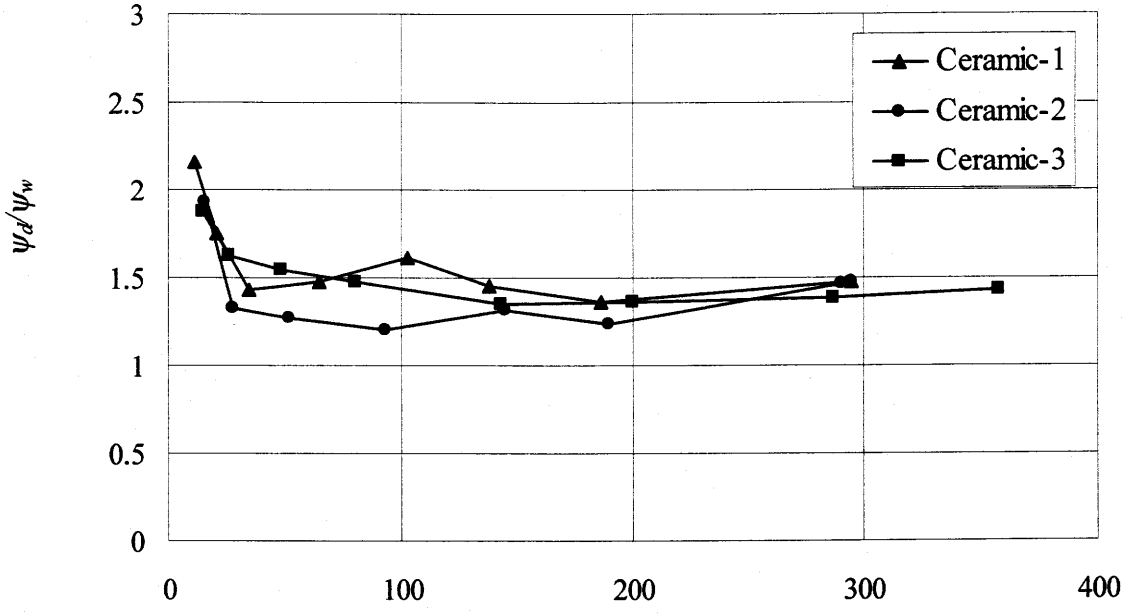

Figure 4.9 The ratios of ψ_d to ψ_w for the three ceramic sample

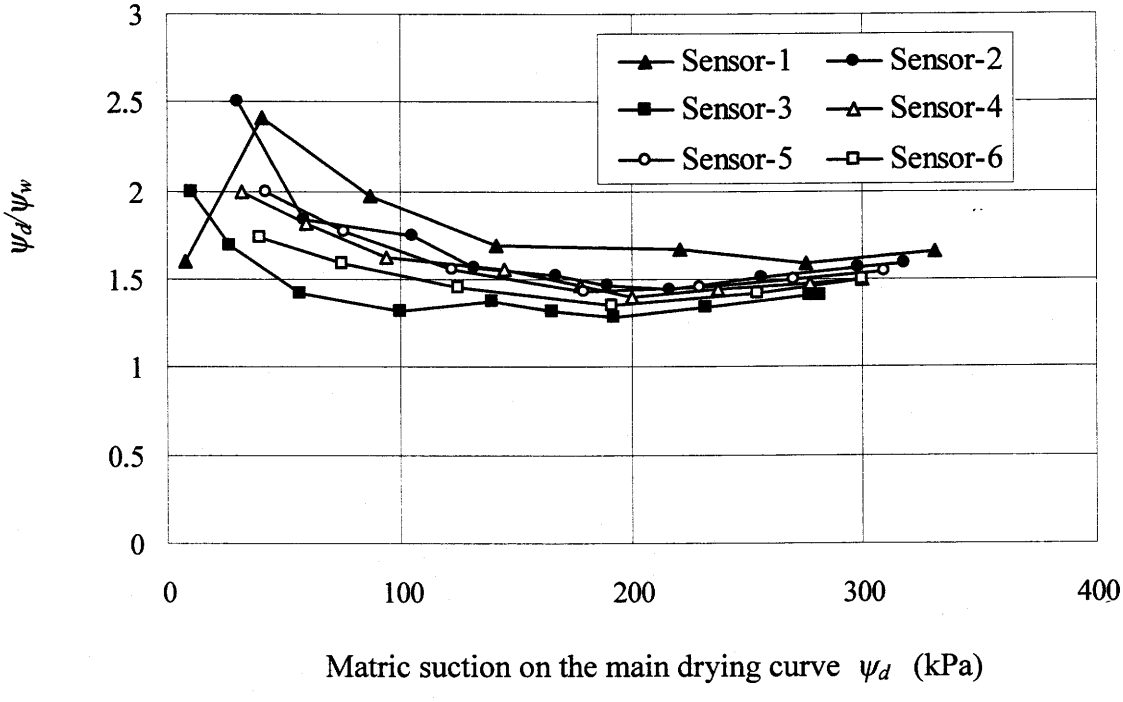

Figure 4.10 The ratios of ψ_d to ψ_w for the six sensors

4.3 THE PROBLEMS ASSOCIATED WITH THE CONVENTIONAL CALIBRATION AND MEASURING PROCEDURES

Research work has been done on the calibration of the thermal conductivity sensor (Fredlund and Wong, 1989). The calibration curve is obtained by measuring the output of the sensor at various applied matric suctions, and is generally non-linear. In the conventional calibration process, the ceramic tip of the sensor is first saturated by submergence in a water bath for a few days. The sensor is then mounted in a pressure cell. Matric suction is applied by increasing the air pressure in the pressure cell incrementally while maintaining a constant water pressure underneath the high air entry disk. Therefore, the calibration using the conventional method is a drying process. There are two problems associated with the conventional calibration method.

The first problem is that the conventional calibration procedure does not take the capillary hysteresis of the ceramic into consideration. The discussions in the previous section have shown that the neglecting of the capillary hysteresis in the calibration can cause an error of up to 50% of the actual soil suction.

The second problem is that the initial degree of saturation of the sensor ceramic is not known. The sensor ceramic is soaked in water for several days and assumed saturated before the calibration. However, it can be seen from the test results on the prolonged submergence of sensor ceramics in water presented in Chapter 3, a fairly long time is required for the ceramic to reach 100% degree of saturation. The degree of saturation of Ceramic-1 was only 73.6% after 8-days submergence in water, and the degree of saturation of Ceramic-2 and Ceramic-4 are only 66.3% and 75.1%, respectively, after a 2.5-months submergence. If the time of submergence is not specified, the degree of saturation of the sensor ceramic could be anywhere between that at the turning point on $\theta - t$ curve (see Fig. 3.36) and 100%. The degree of saturation at the turning point on $\theta - t$ curve is even lower than that at zero suction on the main hysteresis loop. Thus, the conventional calibration curve could be anywhere in the gap between the main drying curve and the initial drying curve, as illustrated by the shaded area in Fig. 4.11. If the submergence time is too short, the measured curves could even be below the main drying curve.

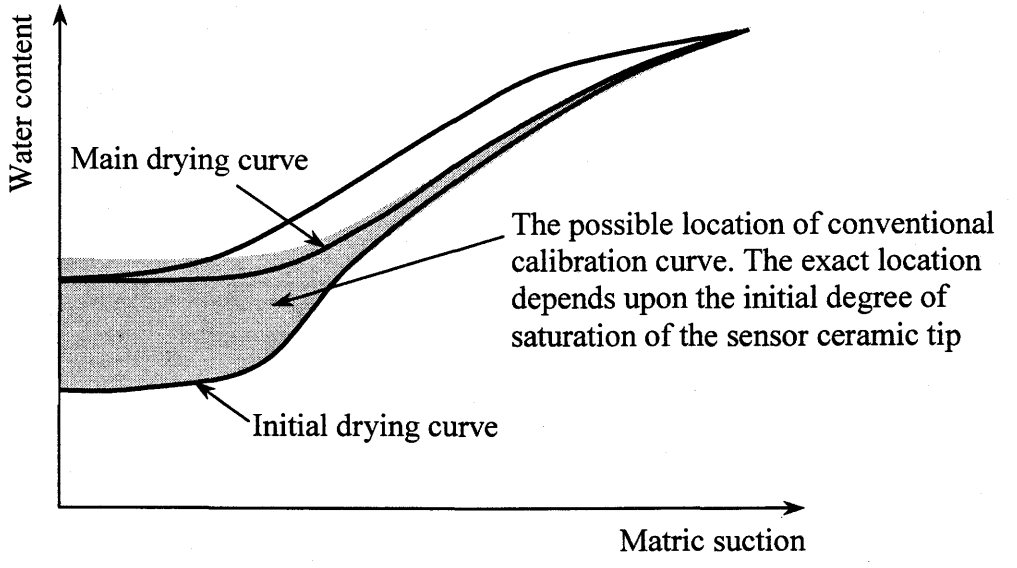

Figure 4.11 Schematic illustration of the position of the calibration curve using the conventional method of calibration

As described in Chapter 3, the drying and wetting cycles of the sensor generally take place within the main hysteresis loop, unless the sensor has been flooded for a long period. The error of measurement will be higher when the calibration is farther apart from the main hysteresis loop. If the sensor ceramic tip is only soaked for a few days, the conventional calibration curve is most probably somewhere slightly above the main hysteresis loop. The use of this calibration curve gives even higher error of measurement than using the main drying curve as a calibration curve. If the sensor ceramic is initially saturated, the conventional calibration curve will be the initial drying curve. If this is the case, the error of measurement will be the highest if the sensor ceramic is completely saturated before the sensor is installed in the soil.

To make the measurement of soil suction more accurate, the sensor should be calibrated following the entire possible wetting and drying processes the field soil may undergo. This calibration is obviously impractical. An alternative is to use a mathematical simulation to predict the hysteresis curves from a limited amount of measured data. In the last forty years, researchers have developed several models of capillary hysteresis. Some models can predict the hysteresis curves from only one branch of the main hysteresis loop. The next chapter will present the details of some models and test the models using the measured hysteresis curves of the ceramic.

The sensor can be installed dry or wet in the field. A moisture migration between the sensor ceramic and the surrounding soil occurs immediately after the sensor is installed. Test results showed that the equilibrium could be reached faster for a dry installed sensor than for a wet installed sensor. So it was recommended that the sensor be installed dry in the field (Fredlund, 1992).

It would be desirable if the sensor ceramic is partly saturated before the installation. The suction of the sensor ceramic should be slightly lower than the suction in the surrounding soil. In most case, it is difficult to control the initial suction of the sensor ceramic before the installation and the sensor has to be installed air-dried.

CHAPTER 5

Modeling of Capillary Hysteresis of the Sensor Ceramic

The output from the thermal conductivity sensor is measured in volts. The matric suction is obtained by converting the output using a calibration curve. The calibration of the sensor is an important step towards the use of thermal conductivity sensors. Because of the capillary hysteresis properties of the porous ceramic tip of the sensor, one voltage output of the sensor may correspond to different values of matric suction, depending upon the wetting and drying history of the sensor ceramic. Each of the drying and wetting processes requires a separate calibration curve to get an accurate value of the matric suction from a voltage output of the sensor.

However, as indicated in chapter 3, the calibration test is time consuming. It is practically impossible to obtain a whole family of drying and wetting curves for each sensor in the calibration. It is important to establish an appropriate mathematical approach that can predict the hysteresis properties of the sensor from a limited amount of calibration data. A brief review of the domain theory and the available models has been made in Chapter 2. This chapter makes a verification of some of the models using the experimental data of the ceramics and the sensors. A mathematical approximation is also presented in this chapter.

5.1 THE NÉEL-EVERETT INDEPENDENT DOMAIN MODEL

A review of the Néel-Everett independent domain theory has been presented in Chapter 2. This section describes the application of the Néel-Everett independent domain model to the capillary hysteresis of the porous material and an examination of the model using the test data of the thermal conductivity sensor.

Poulovassilis (1962) was among the first to apply the Néel-Everett independent domain model in the area of capillary hysteresis of water movement in soils. The procedure used in the Poulovassilis' method was adopted in this study.

The distribution function $f(\psi_w, \psi_d)$ is computed using the main hysteresis curves and one group of primary scanning curves. The other group of primary scanning curves and the secondary scanning curves are computed using the distribution function $f(\psi_w, \psi_d)$. The procedure used to compute $f(\psi_w, \psi_d)$ is illustrated by the hypothetical curves in Fig. 5.1. In Fig. 5.1, it is assumed that the main hysteresis loop and the wetting scanning curves have been measured.

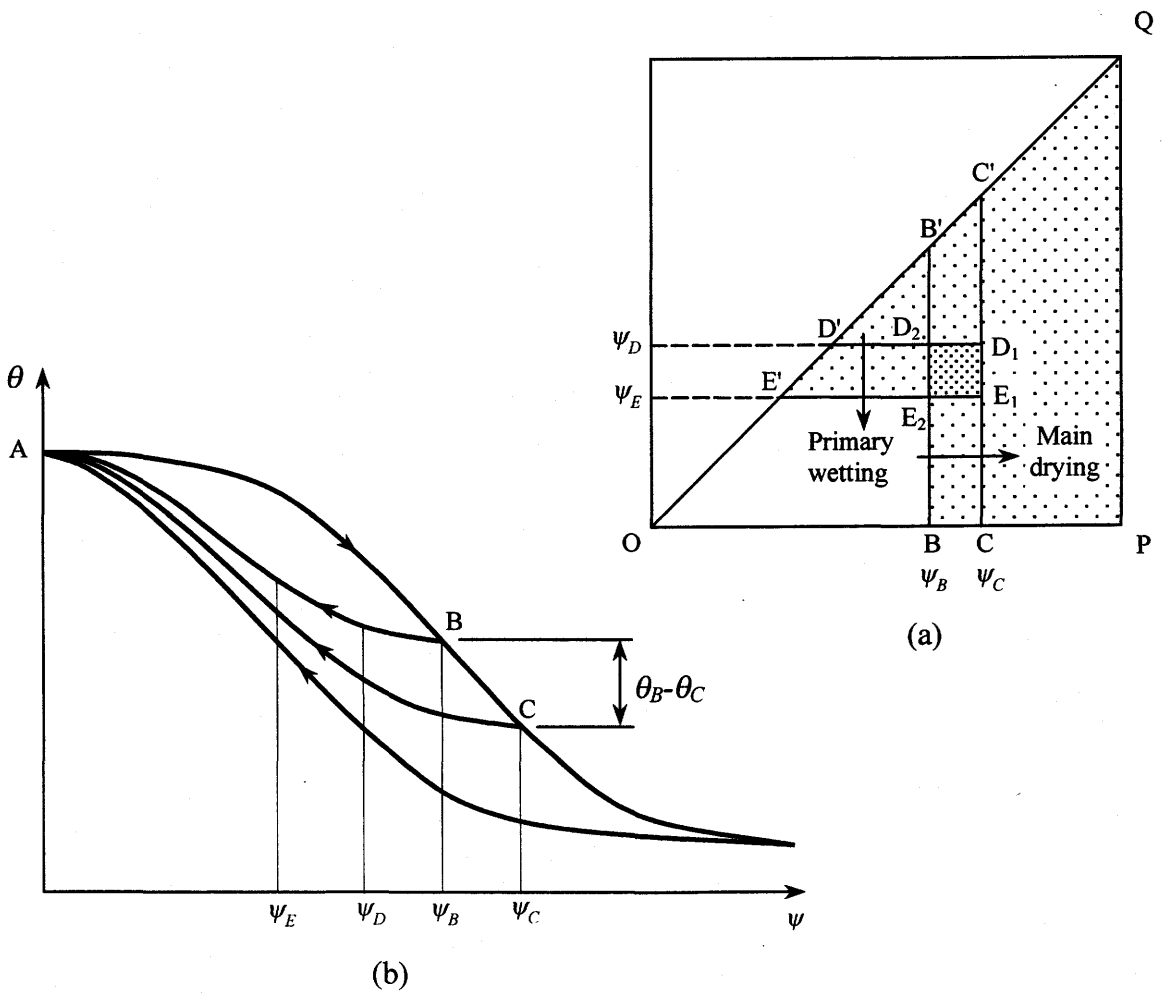

Figure 5.1 Hypothetical curves of main hysteresis loop and primary wetting scanning curves and the corresponding Néel's diagram.

The Néel's diagram is divided into small elements, S_{ij}, and the water volume of each small element is $f(\psi_w, \psi_d)S_{ij}$. When suction is increased from ψ_B to ψ_C along the main drying curve, the total volume of water being drained out is $(\theta_B-\theta_C)$, as shown in Fig. 5.1(b). In Néel's diagram this amount of water equals to the area of BCC'B' multiplied by the distribution function $f(\psi_w, \psi_d)$ (i.e., $f(\psi_w, \psi_d)S_{BCC'B'}$). This amount of water does not all re-enter the porous body when the suction decreases from ψ_C to ψ_B, instead, it re-enters the porous body only if the suction decreases from ψ_C all the way to zero following a primary wetting process, curve CA in Fig. 5.1b.

The two scanning curves, BA and CA in Fig. 5.1(b), are two hypothetical primary wetting scanning curves. For the primary wetting processes of BA and CA, the amount of water entering the porous body over a suction interval of ψ_D to ψ_E is $f(\psi_w, \psi_d)S_{E_1D_1D'E'}$ and $f(\psi_w, \psi_d)S_{E_2D_2D'E'}$, respectively. With the primary wetting scanning curve being measured, $f(\psi_w, \psi_d)S_{E_2D_2D'E'}$ and $f(\psi_w, \psi_d)S_{E_2D_2D'E'}$ are readily calculated and the water volume in the element $E_1D_1D_2E_2$ can be obtained as follows.

$$f(\psi_w, \psi_d)S_{E_1D_1D_2E_2} = f(\psi_w, \psi_d)S_{E_1D_1D'E'} - f(\psi_w, \psi_d)S_{E_2D_2D'E'} \qquad (5.1)$$

This volume of water, $\theta_B-\theta_C$, which is drained out over the suction increment from ψ_B to ψ_C in the main drying process is divided into small elements including the element of $E_1D_1D_2E_2$. The volume of water in the other elements is calculated using the same technique. In this way, the volume of water in all the elements in the triangle, OPQ, can be obtained. The primary drying curve and the secondary scanning curves are calculated by adding the volume of water in the filled elements in the Néel's diagram.

If the main hysteresis loop and the primary drying scanning curves are measured, the primary wetting scanning curves and secondary scanning curves are computed using a similar procedure.

The predicted primary drying and wetting scanning curves of Ceramic-1 to 3 and Sensor-1 to 3 using the Néel-Everett independent domain model are shown in Figs. 5.2 to 5.7. The gray lines in the figures are measured curves, and the black lines are the predicted scanning curves. By comparing the predicted scanning curves with

the measured scanning curves, it can be concluded that the Néel-Everett independent domain model works quite well for the capillary hysteresis of the ceramic and the output hysteresis of the sensor.

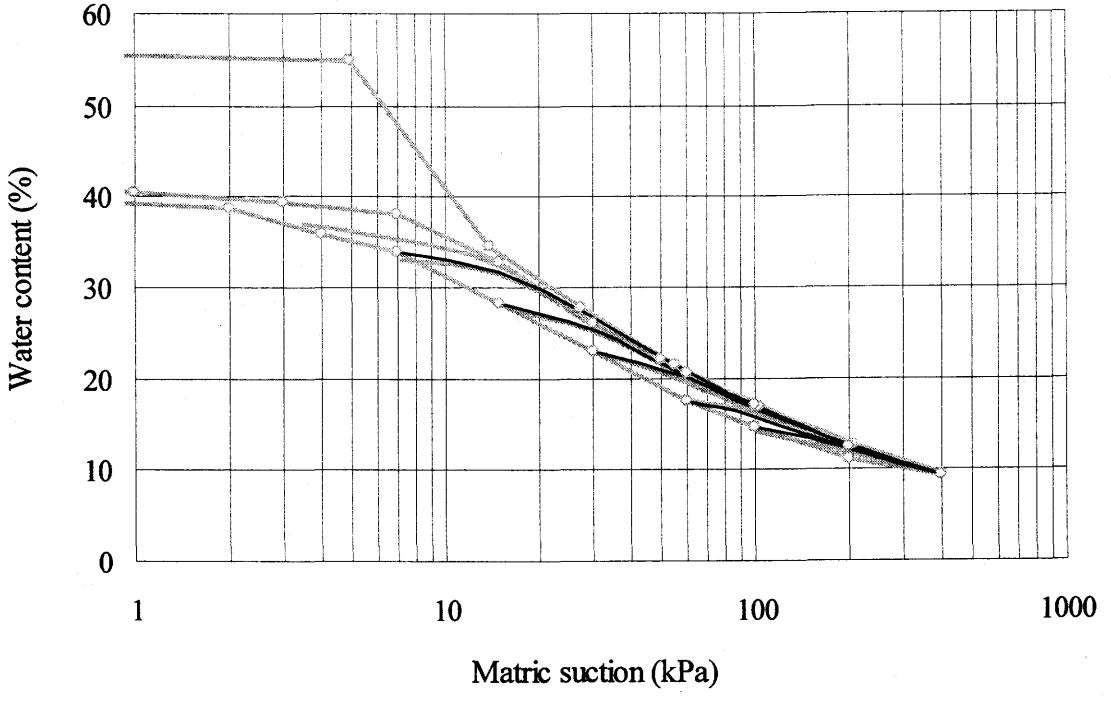

Figure 5.2a Predicted drying scanning curves of Ceramic-1 using the Néel-Everett model

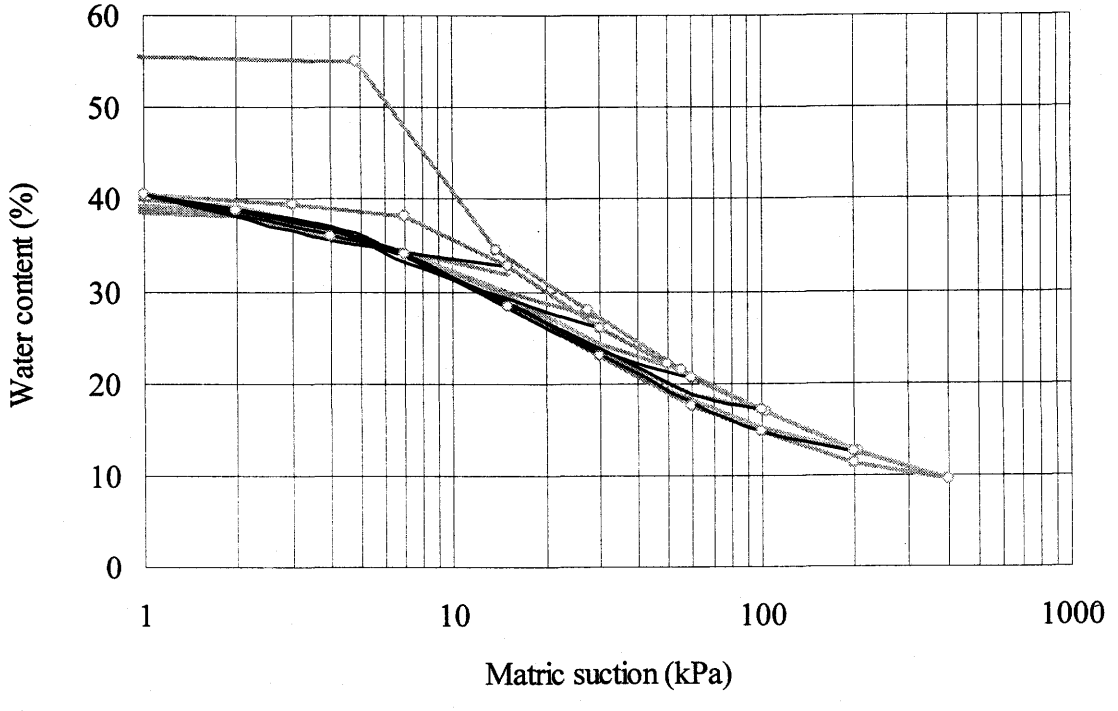

Figure 5.2b Predicted wetting scanning curves of Ceramic-1 using the Néel-Everett model

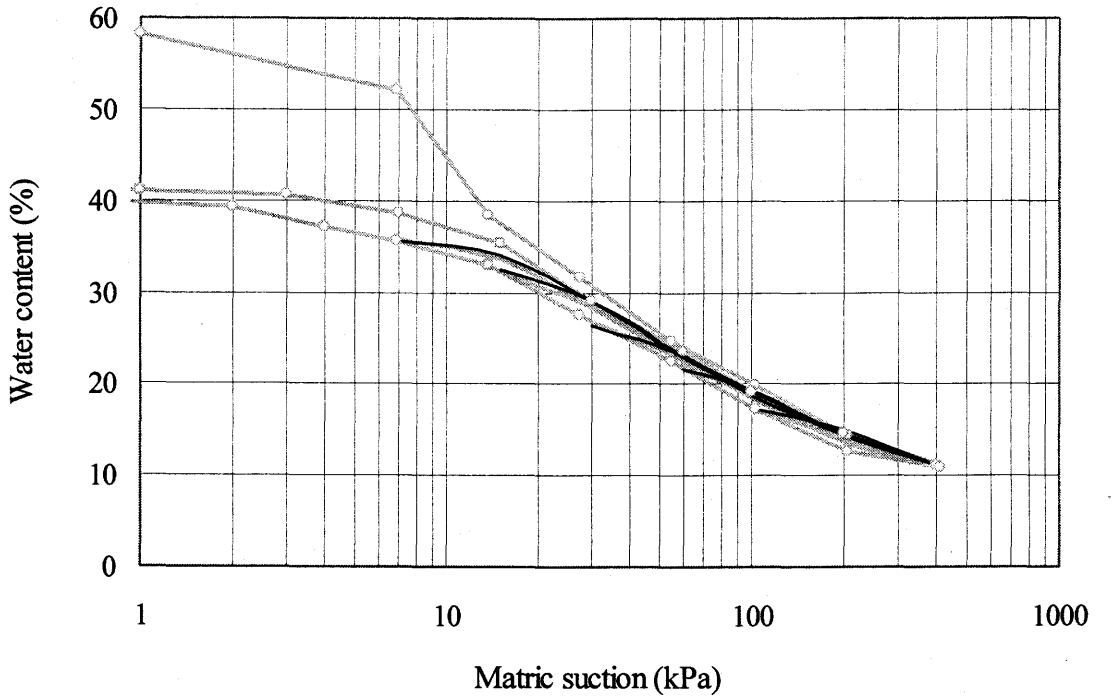

Figure 5.3a Predicted drying scanning curves of Ceramic-2 using the Néel-Everett model

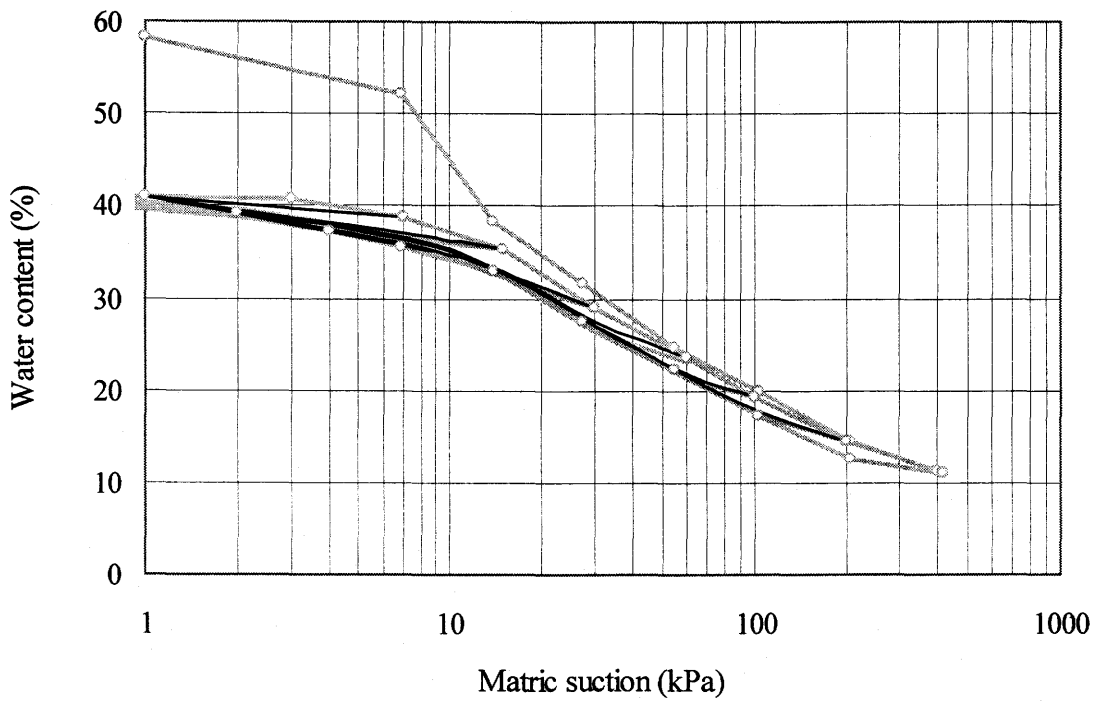

Figure 5.3b Predicted wetting scanning curves of Ceramic-2 using the Néel-Everett model

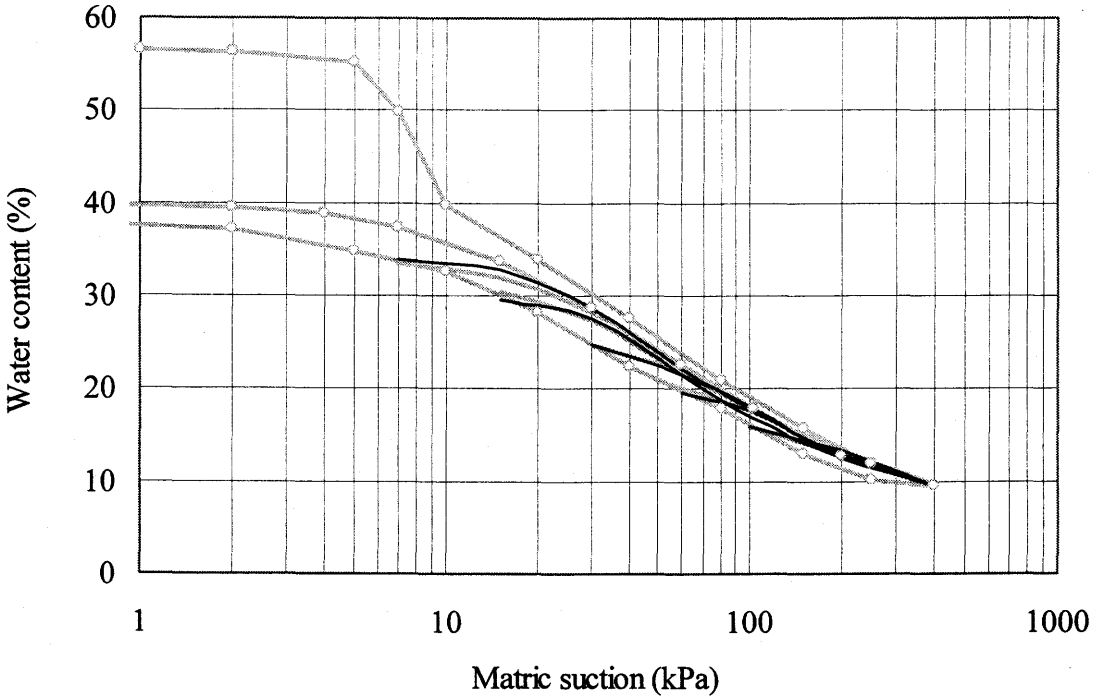

Figure 5.4a Predicted drying scanning curves of Ceramic-3 using the Néel-Everett model

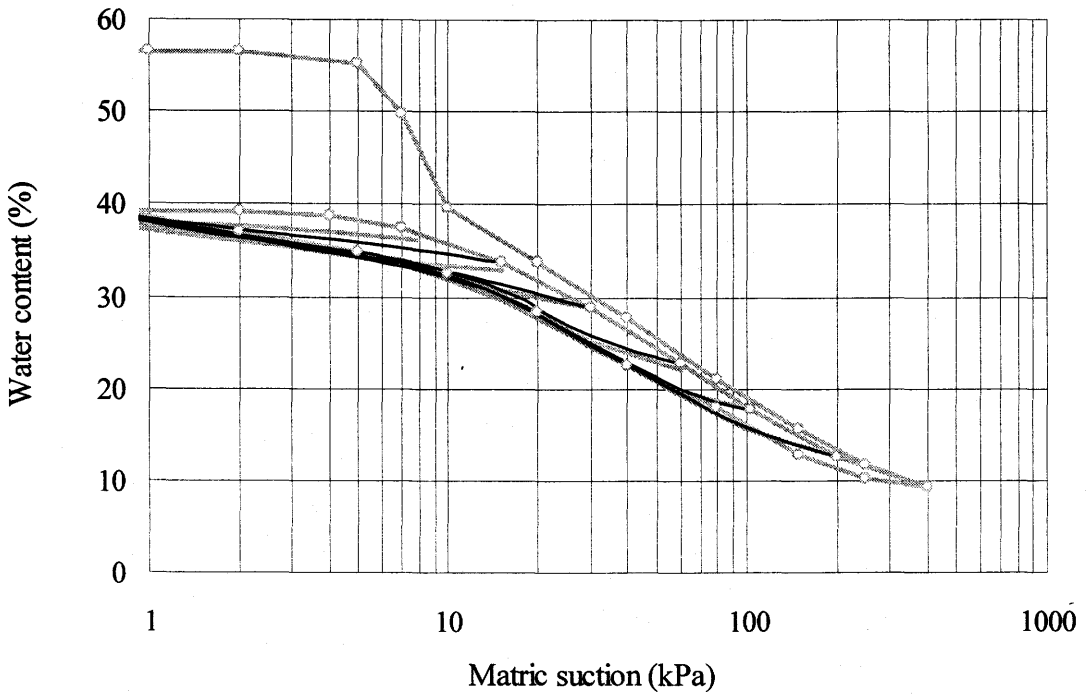

Figure 5.4b Predicted wetting scanning curves of Ceramic-3 using the Néel-Everett model

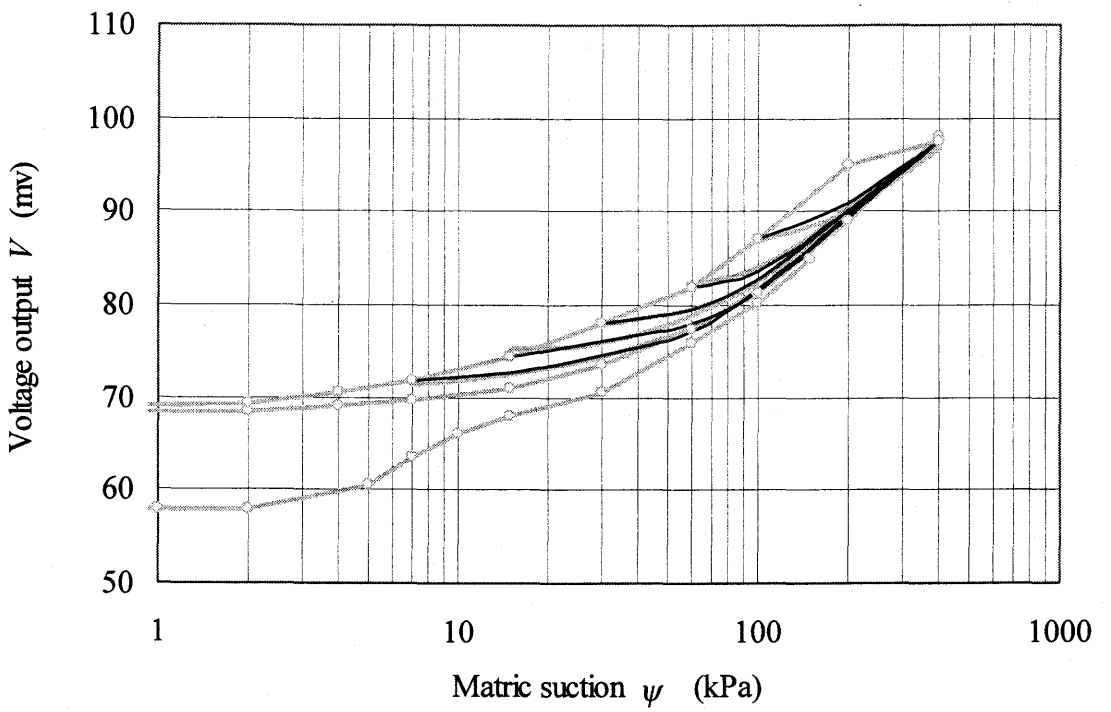

Figure 5.5a Predicted drying scanning curves of Sensor-1 using the Néel-Everett model

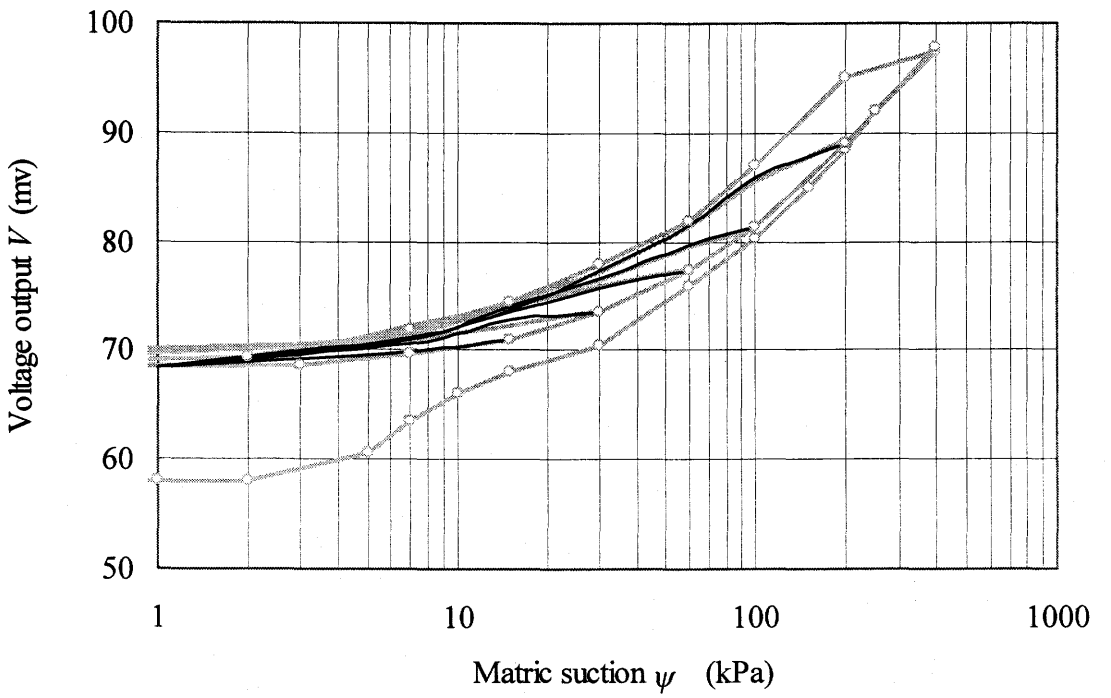

Figure 5.5b Predicted wetting scanning curves of Sensor-1 using the Néel-Everett model

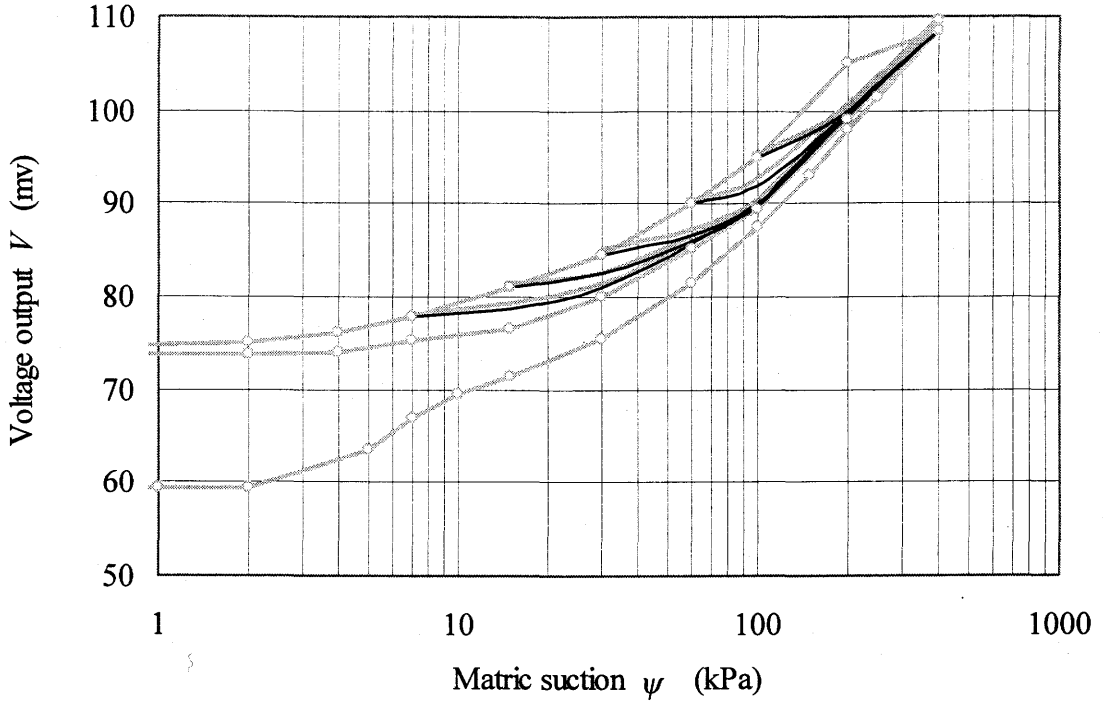

Figure 5.6a Predicted drying scanning curves of Sensor-2 using the Néel-Everett model

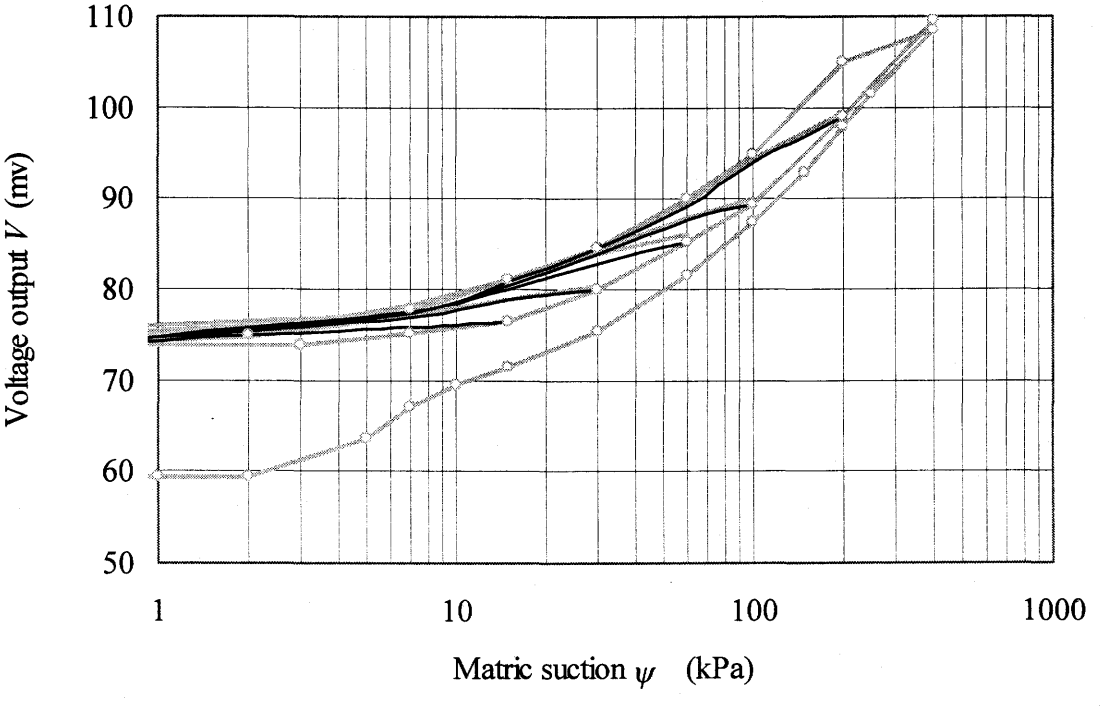

Figure 5.6b Predicted wetting scanning curves of Sensor-2 using the Néel-Everett model

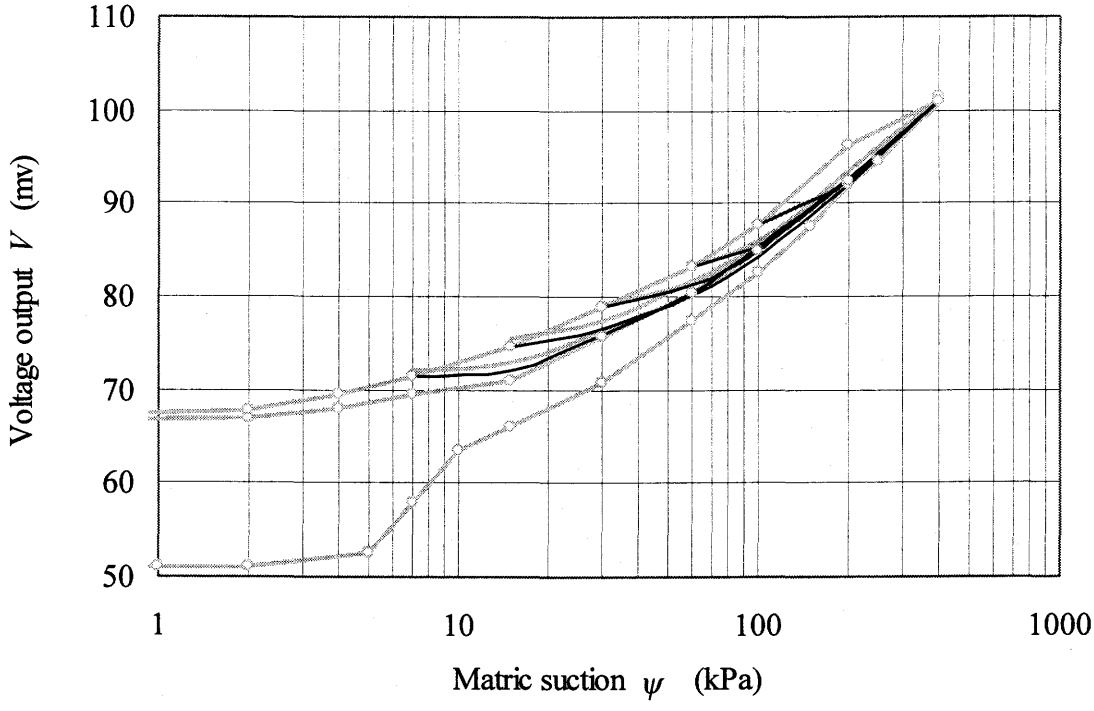

Figure 5.7a Predicted drying scanning curves of Sensor-3 using the Néel-Everett model

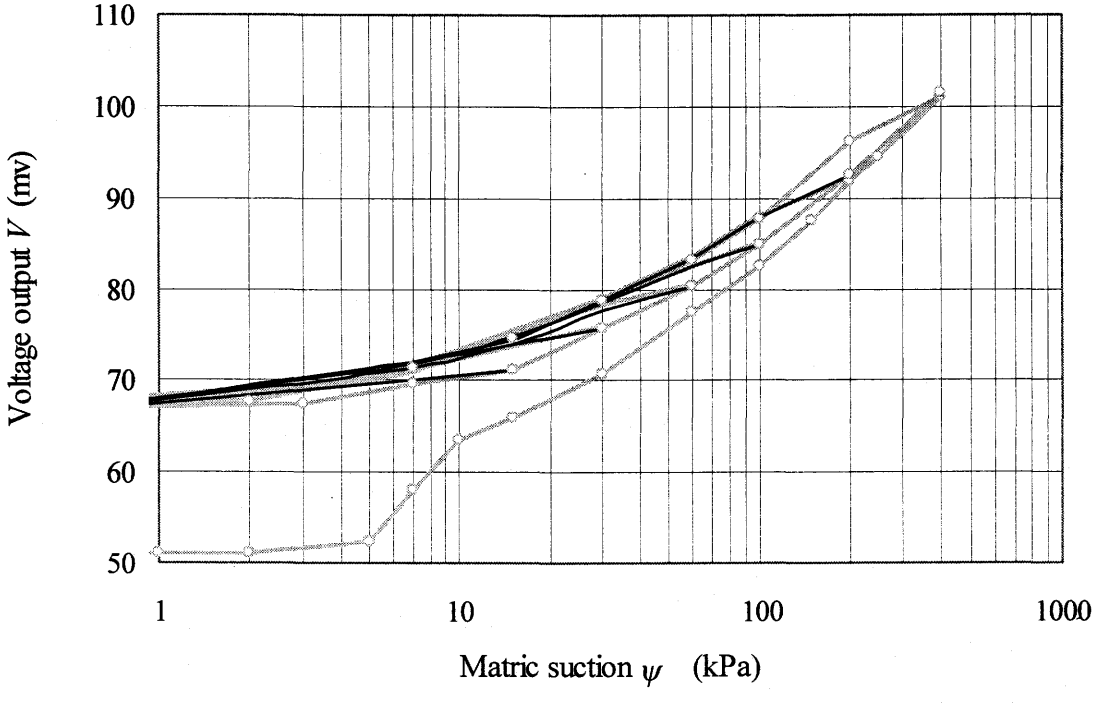

Figure 5.7b Predicted wetting scanning curves of Sensor-3 using the Néel-Everett model

5.2 THE MUALEM INDEPENDENT DOMAIN MODEL

Although good agreement between the predicted and the measured data was found for the capillary hysteresis of the sensor ceramic using the Néel-Everett domain model as shown in the previous section, the large amount of experimental data required has apparently prevented the application of the model. Philip (1964) made a significant simplification to the Néel-Everett domain model by introducing a similarity hypothesis to the domain model. Since the early seventies, Mualem and his co-workers have done a large amount of work to further simplify the domain model using the similarity hypothesis. A series of domain models have been developed based on the similarity hypothesis. These include independent domain models (model-I, Mualem, 1973; model-II, Mualem, 1974), dependent domain model (model-III, Mualem and Dagan, 1975; Mualem, 1984a), explicit domain model (model-III_{expl}, Mualem and Miller, 1979), and a new simplified independent domain model (models I-1 and II-1, Mualem, 1977; Mualem, 1984b). In the following sections, only the Mualem independent domain model-II and model II-1 are tested for the following three reasons:

(1) The dependent domain models (i.e., model-III and model-III_{expl}) lead to better agreement than independent domain models. However, the improvement is only significant for soils having a narrow pore size distribution and a relatively large air entry value, and a major portion of their hysteretic loop is in the range of suction values smaller than the air entry value (Mualem, 1975, 1977). For porous media having a small air entry value and a narrow hysteresis loop like the ceramic of the sensor, the dependent domain models do not show significant improvement over the independent domain models.

(2) The Néel-Everett domain model tested in the last section is also an independent domain model, and it provides a good prediction of the capillary hysteresis of the sensor ceramic.

(3) The dependent domain models require more experimental data than the independent domain models. For example, a primary drying scanning curve is

required in addition to the main hysteresis loop when using the Mualem dependent domain model, model-III.

There are two independent domain models in Mualem's models (i.e., model-I and model-II). The two models are based on the same fundamental hypothesis. Model-II was developed after model-I and is much simpler than model-I. Model-II also leads better prediction than model-I (Mualem, 1974). Therefore, model-II and the corresponding new simplified model, model II-1, are tested in this section.

5.2.1 The Mualem Independent Domain Model: Model-II

The Néel-Everett independent domain model has two parameters, ψ_w and ψ_d, that are used to specify the water characteristics of a pore. When suction is increased to a certain value, ψ_d, the pore is drained spontaneously, and when the suction is lowered to a certain value, ψ_w, the pore is filled spontaneously. The distribution function, $f(\psi_w, \psi_d)$, is developed based on the two parameters.

In the Mualem independent domain model, model-II, two parameters, r, the radius of the openings of the pores in a porous body, and ρ, the radius of the pores in the body, are defined to characterize a porous system. As implied by the definition, r corresponds to ψ_d and ρ to ψ_w. Based on r and ρ, a distribution function, $f(r, \rho)$, is defined as the relative volume of pores of radii ρ to $\rho + d\rho$ having openings of radii r to $r + dr$. For the sake of convenience, the two parameters are normalized as follows:

$$\bar{r} = \frac{r - R_{\min}}{R_{\max} - R_{\min}} \qquad \bar{\rho} = \frac{\rho - R_{\min}}{R_{\max} - R_{\min}} \tag{5.2}$$

where, R_{max} and R_{min} are the upper and lower limits of both r and ρ. R_{max} and R_{min} correspond to ψ_{min} and ψ_{max}, respectively.

The basic simplifying assumption laying under all of the Mualem models is that the distribution function may be represented as a product of two independent distribution functions. One distribution function corresponds to parameter ψ_w or ρ, and

the other corresponds to parameter ψ_d or r. For model-II, the distribution function, $f(r, \rho)$ is expressed as follows:

$$f(\bar{r}, \bar{\rho}) = h(\bar{r}) \cdot l(\bar{\rho}) \tag{5.3}$$

Equation (5.3) expresses a similarity principle since the distribution along each line of $\bar{r}$ equal to a constant is identical, except for a constant factor $h(\bar{r} = constant)$. The same statement holds for each line of $\bar{\rho}$ equal to a constant, except for a constant factor $l(\bar{\rho} = constant)$. The similarity hypothesis was proposed first by Philip in 1964. Mualem (1973) made a significant simplification on the mathematical formulation of the domain model that utilizes the similarity hypothesis.

In model-II, another assumption is made that the pores of any group characterized by $\bar{r}$ includes the whole range of pores of $0 \le \bar{\rho} \le 1$, and any group characterized by $\bar{\rho}$ includes the whole range of pores of $0 \le \bar{r} \le 1$. In the Néel's diagram, the distribution function is mapped on the whole rectangle OABC ($0 \le \bar{\rho} \le 1$, $0 \le \bar{r} \le 1$, Fig. 5.8) instead of on the triangle OAB as in the Néel-Everett model. Fig. 5.8 shows the contour maps of the pores filled for the wetting and drying boundary curves.

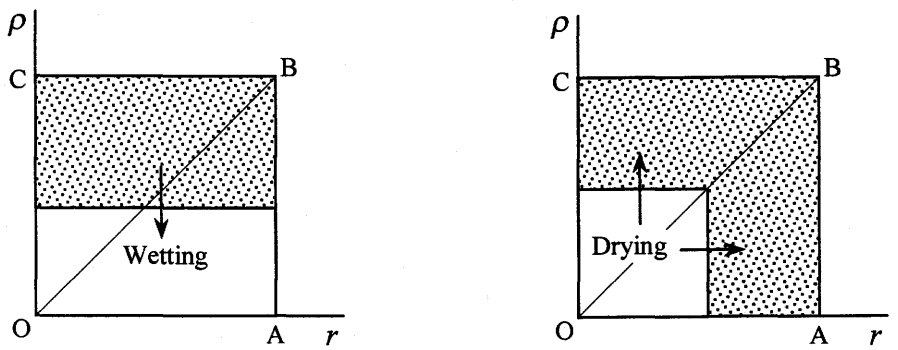

Figure 5.8 The filled pore diagrams in the $\bar{r}$, $\bar{\rho}$ plane (the dotted domains) for (a) the main wetting process and (b) the main drying process

Fig. 5.9 shows the contour maps for the primary wetting and primary drying scanning curves. The water content at any suction along either of the primary scanning

curves is obtained by integrating the distribution function on the filled area of the diagrams. Simple expressions for the scanning curves are obtained based on the above assumption:

$$\theta_d(\psi,\psi_1)=\theta_w(\psi)+\frac{[\theta_w(\psi_1)-\theta_w(\psi)]}{[\theta_0-\theta_w(\psi)]}\cdot[\theta_d(\psi)-\theta_w(\psi)] \tag{5.4a}$$

$$\theta_w(\psi,\psi_1)=\theta_w(\psi)+\frac{[\theta_0-\theta_w(\psi)]}{[\theta_0-\theta_w(\psi_1)]}\cdot[\theta_d(\psi_1)-\theta_w(\psi_1)] \tag{5.4b}$$

where, $\theta_d(\psi,\psi_1)$ and $\theta_w(\psi,\psi_1)$ denote the drying and wetting processes, respectively, and θ_0 denotes the water content at minimum suction.

Equations 5.4a and 5.4b show that only the main wetting curve, $\theta_w(\psi)$, and the main drying curve, $\theta_d(\psi)$, are required to compute the primary scanning curves. The secondary scanning curves can also be computed using a similar analytical procedure.

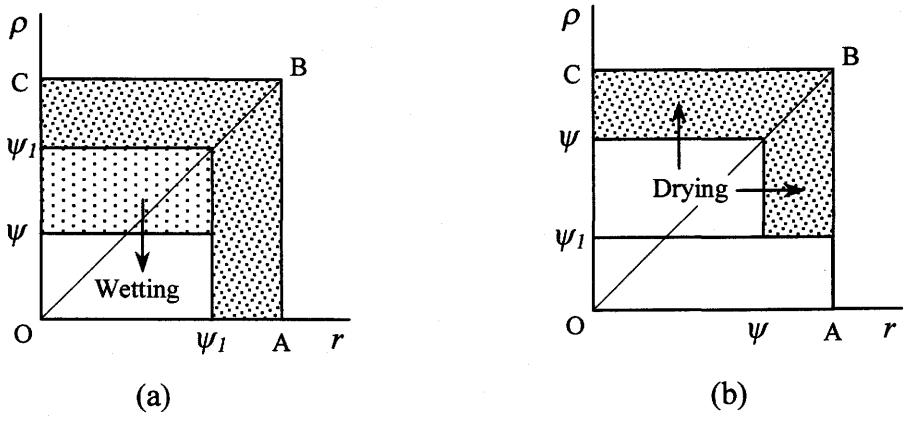

Figure 5.9 The filled pore diagrams in the $\bar{r}$, $\bar{\rho}$ plane (the dotted domains) for
(a) the primary wetting scanning curve and,
(b) the main drying scanning curve.

The Mualem independent model, (model-II), was tested using the experimental data of the ceramics and the sensors. The predicted primary scanning curves are shown in Figs. 5.10 to 5.13. The results of only two ceramics and two sensors are presented. The other ceramics and sensors have similar results. The gray lines are the

measured curves, and the black lines are the predicted scanning curves. The measured scanning curves of the ceramics are not shown on the figures for the sake of tidiness.

The experimental data (Chapter 3) show that the primary scanning curves have a tendency of joining the hysteresis boundary quickly after the starting points of the scanning curves. However, as seen from the shape of the predicted primary scanning curves, the predicted primary scanning curves do not joint the boundary until the minimum (for wetting scanning curves) or the maximum (for drying scanning curves) suction values are reached. This behavior of the predicted scanning curves is more significant when the suction of the starting point is low for the wetting scanning curve, and when the suction of the starting point is high for the drying scanning curves. Model-II fails to adequately reproduce the measured scanning curves of the hysteresis of the θ–ψ relationship of the ceramics and the V-ψ relationship of the sensors.

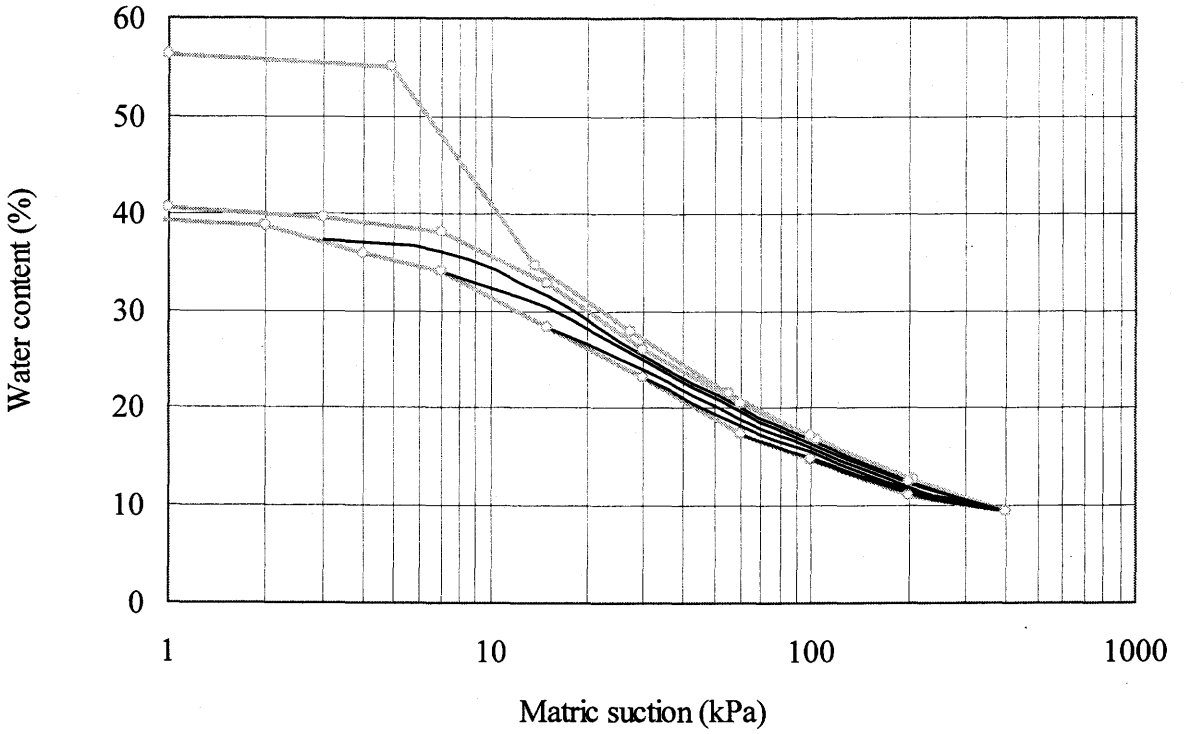

Figure 5.10a Predicted drying scanning curves of Ceramic-1 using the Mualem model-II

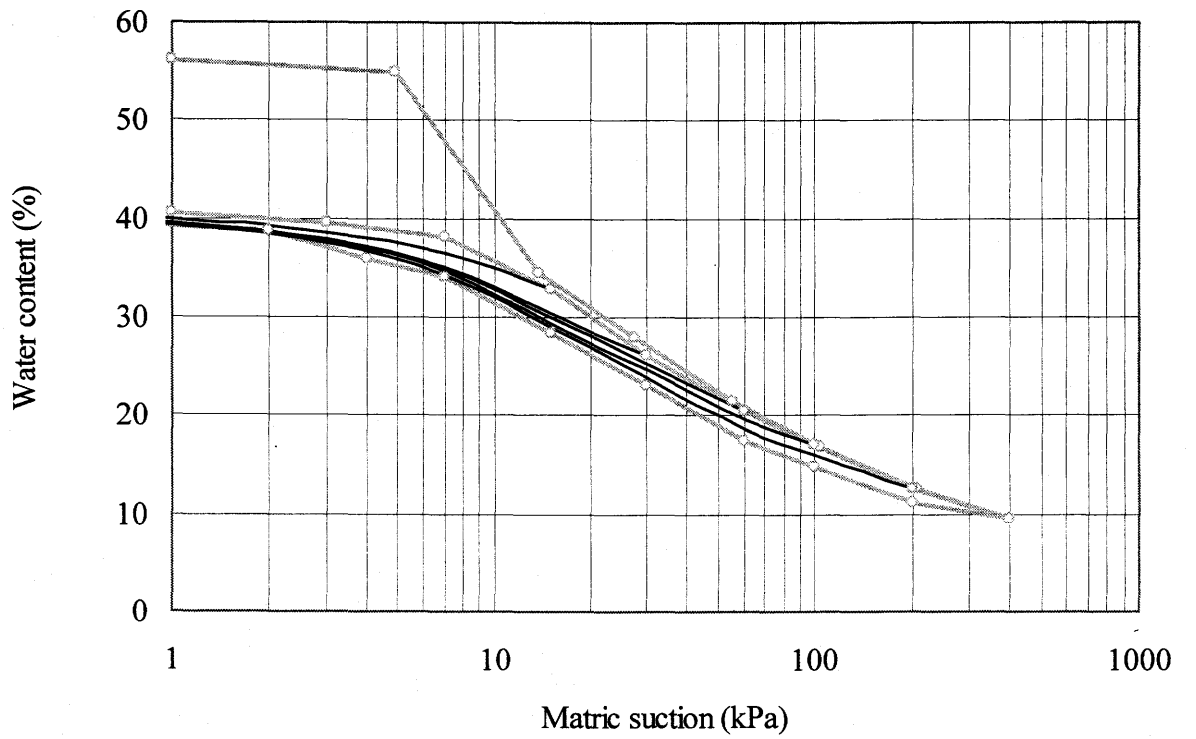

Figure 5.10b Predicted wetting scanning curves of Ceramic-1 using the Mualem model-II

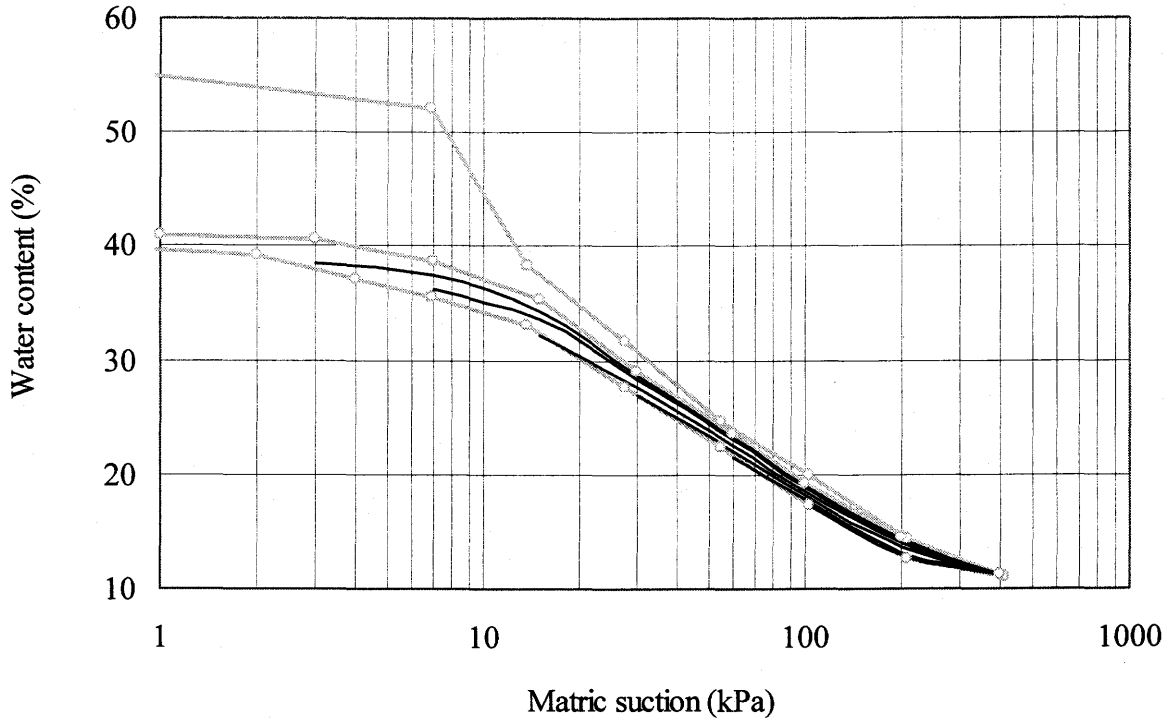

Figure 5.11a Predicted drying scanning curves of Ceramic-2 using the Mualem model-II

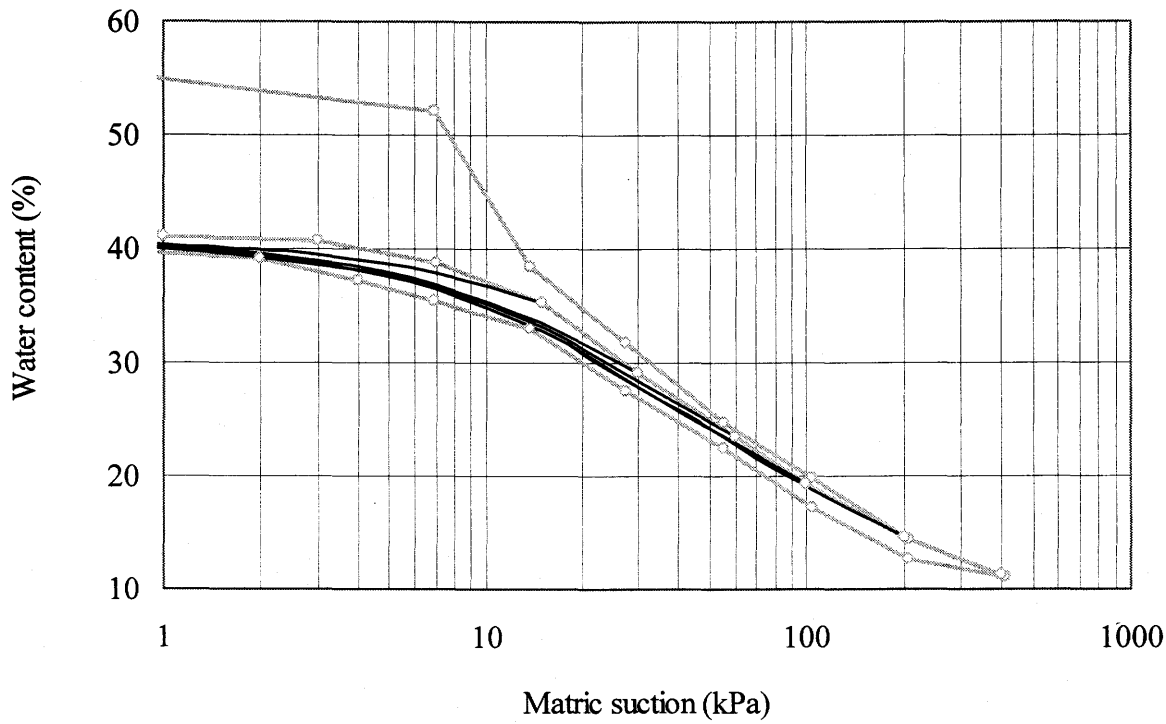

Figure 5.11b Predicted wetting scanning curves of Ceramic-2 using the Mualem model-II

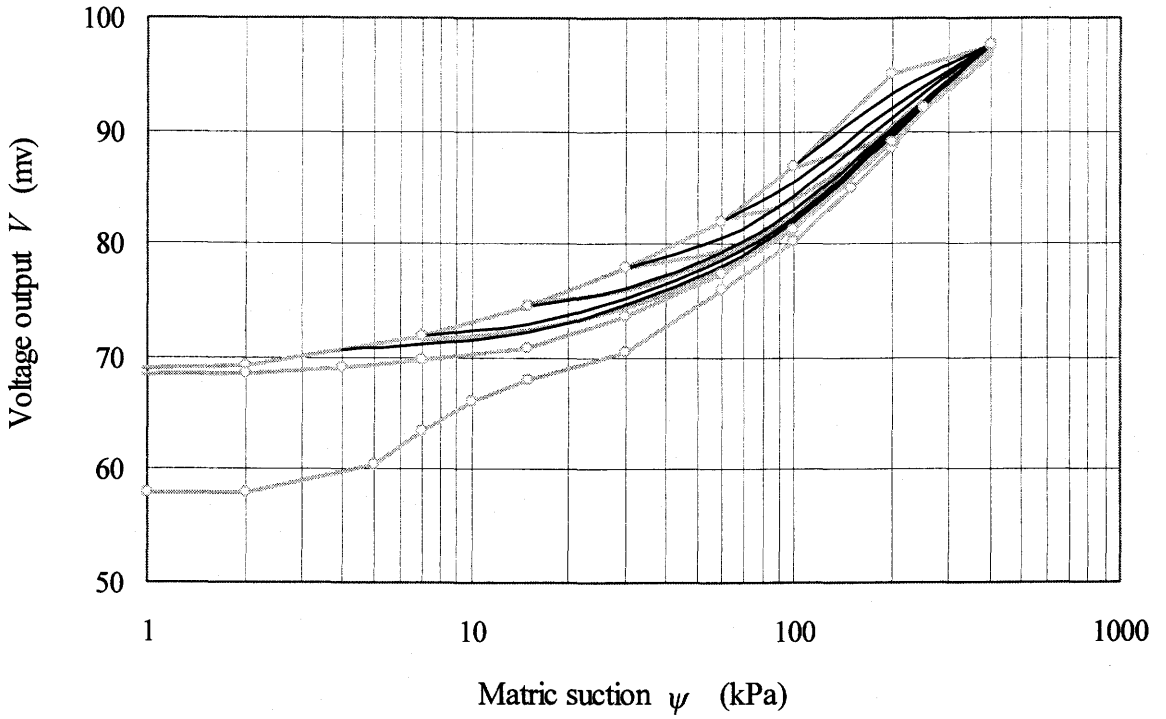

Figure 5.12a Predicted drying scanning curves of Sensor-1 using the Mualem model-II

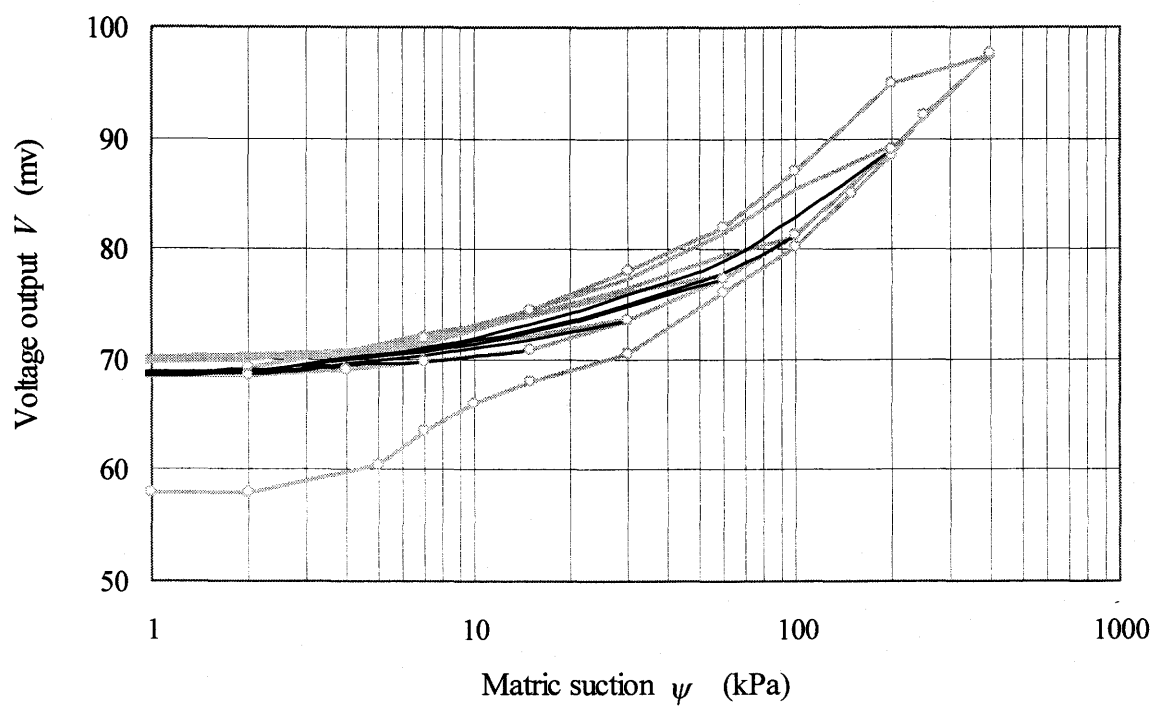

Figure 5.12b Predicted wetting scanning curves of Sensor-1 using the Mualem model-II

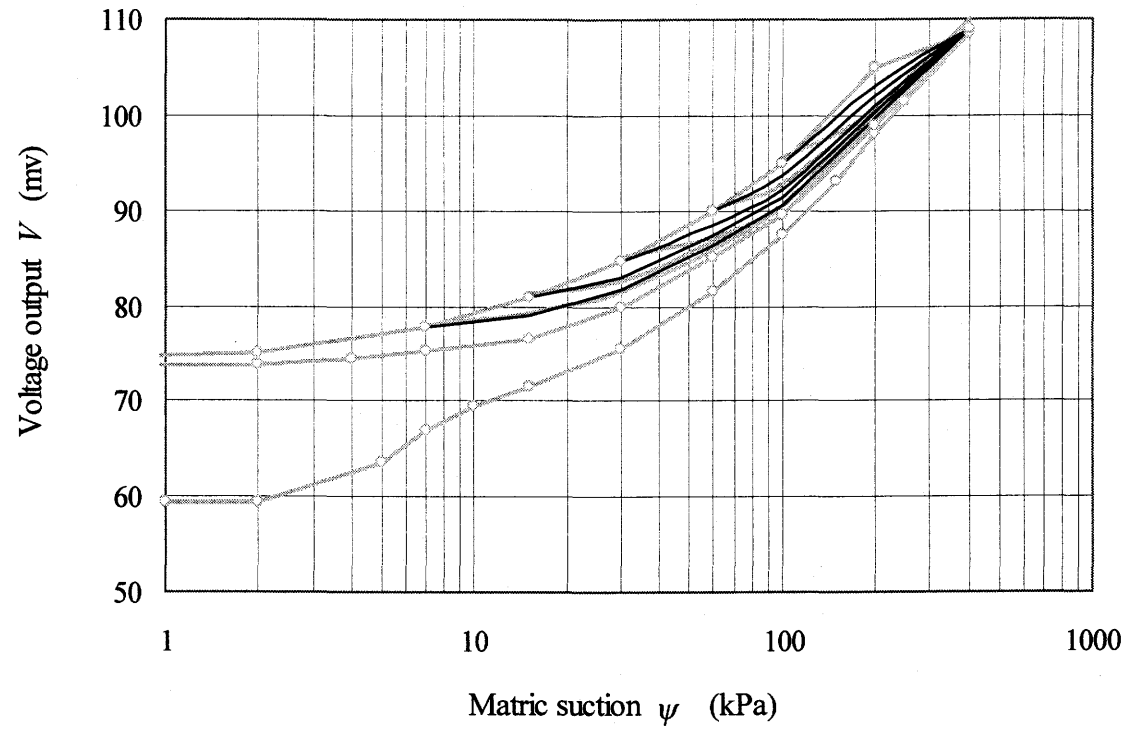

Figure 5.13a Predicted drying scanning curves of Sensor-2 using the Mualem model-II

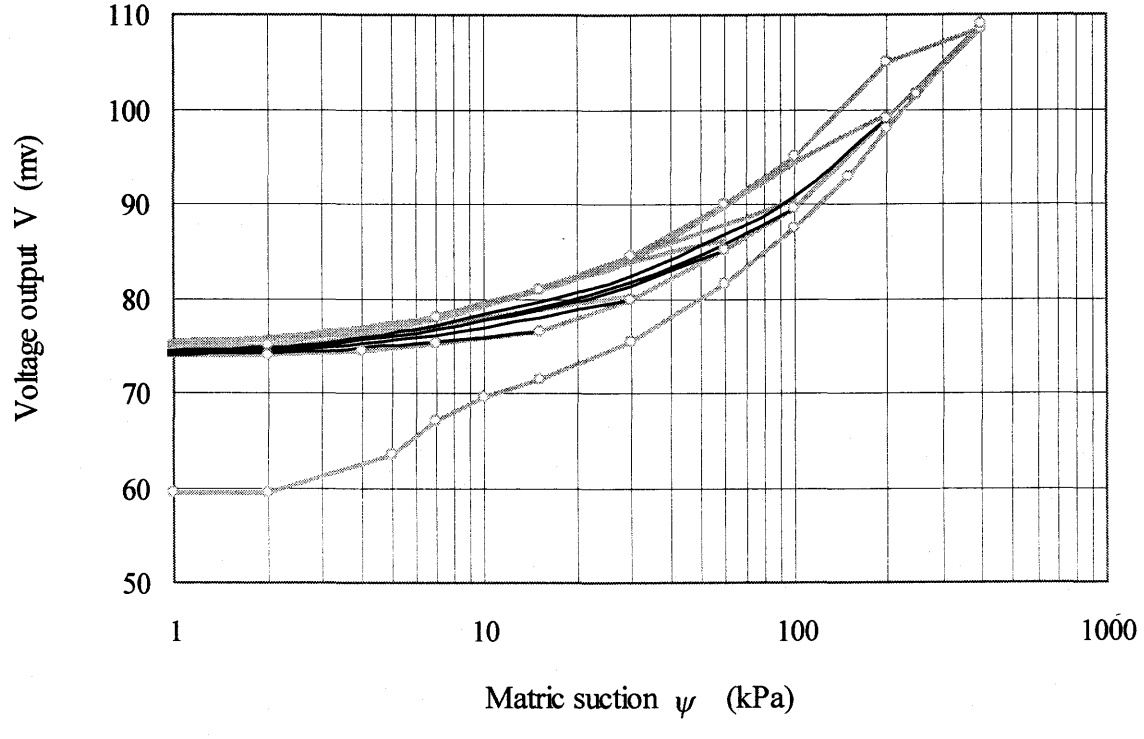

Figure 5.13b Predicted wetting scanning curves of Sensor-2 using the Mualem model-II

5.2.2 Mualem's New Simplified Model: Model II-1

Although a simpler formulation was achieved in the Mualem (1974) independent domain models, (i.e., model-II), the model still requires a fairly large amount of calibration data. The whole hysteresis boundary loop is required to predict the capillary hysteresis characteristics of a porous medium using model-II. Mualem (1977) made a further assumption to simplify the model. When this assumption is applied to the Mualem independent domain models, (i.e., model-I and model-II), it yields two new simplified independent domain models, (i.e., model I-1 and model II-1, respectively). The new simplified models require fewer measured data for calibration than previous models. Mualem (1977) concluded that model I-1 fails to reproduce the observed shape of hysteresis, while model II-1 seems to be efficient in the case in which the effect of water blockage against air entry is not apparent. The experimental capillary function curves of the ceramic of the Beta-97 sensor have an air entry value smaller than 5 kPa, which means a minor water blockage against air entry. Therefore, model II-1 is examined in this section.

The Mualem models have in common a basic similarity hypothesis, according to which the pore water distribution function $f(\bar{r},\bar{\rho})$ equals the product of two independent functions, i.e., $f(\bar{r},\bar{\rho}) = h(\bar{r})\cdot l(\bar{\rho})$. To further simplify the models, the following assumption was made:

$$h(\bar{r}) = l(\bar{r})$$

and

$$f(\bar{r},\bar{\rho}) = h(\bar{r})\cdot h(\bar{\rho}) \tag{5.5}$$

By applying the above assumption, a simple analytical relationship between the main wetting curve and the main drying curve is derived:

$$\theta_d(\psi) = \frac{1}{\theta_0}\left[2\theta_0 - \theta_w(\psi)\right]\cdot\theta_w(\psi) \tag{5.6}$$

It should be noted that Eq. 5.6 has only one parameter, the water content at minimum suction, θ_0. Therefore Eq. 5.6 implies a universal relationship between the main wetting process and main drying process, independent of the type of porous material (Mualem, 1984b). Using Eq. 5.6, the main wetting and drying curves can be predicted from each other. With one branch measured and the other predicted, the scanning curves can be predicted using the formula of model-II.

Model II-1 was examined using the measured data on the sensor ceramic. Only the results for Ceramic-1 and Sensor-1 are presented. The other ceramics and sensors have similar results of prediction. The predicted main wetting curve from the main drying and the predicted main drying curve from main wetting curve are shown in Figs. 5.14 and 5.15 for Ceramic-1 and Sensor-1, respectively.

Figures 5.14 and 5.15 show that the error of prediction is not acceptable. Nimmo (1992) stated that, on a fundamental level, there is no significant evidence that the phenomena that cause hysteresis are manifested in one branch of the hysteresis loop. Equation 5.6 does not works well on the water capillary hysteresis of the ceramic of the Beta-97 sensor. Moreover, the existence of a universal relationship between the main drying curve and the main wetting curve, independent of the properties of the porous medium, is questionable.

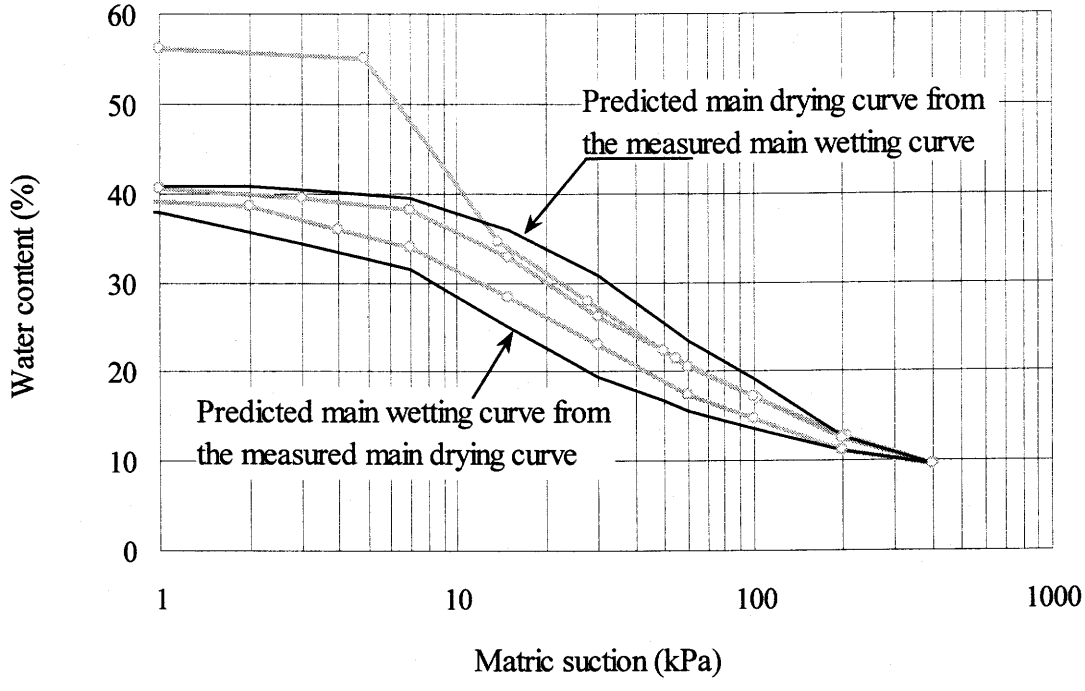

Figure 5.14 Predicted main wetting and drying curves of Ceramic-1 using the Mualem Model II-1

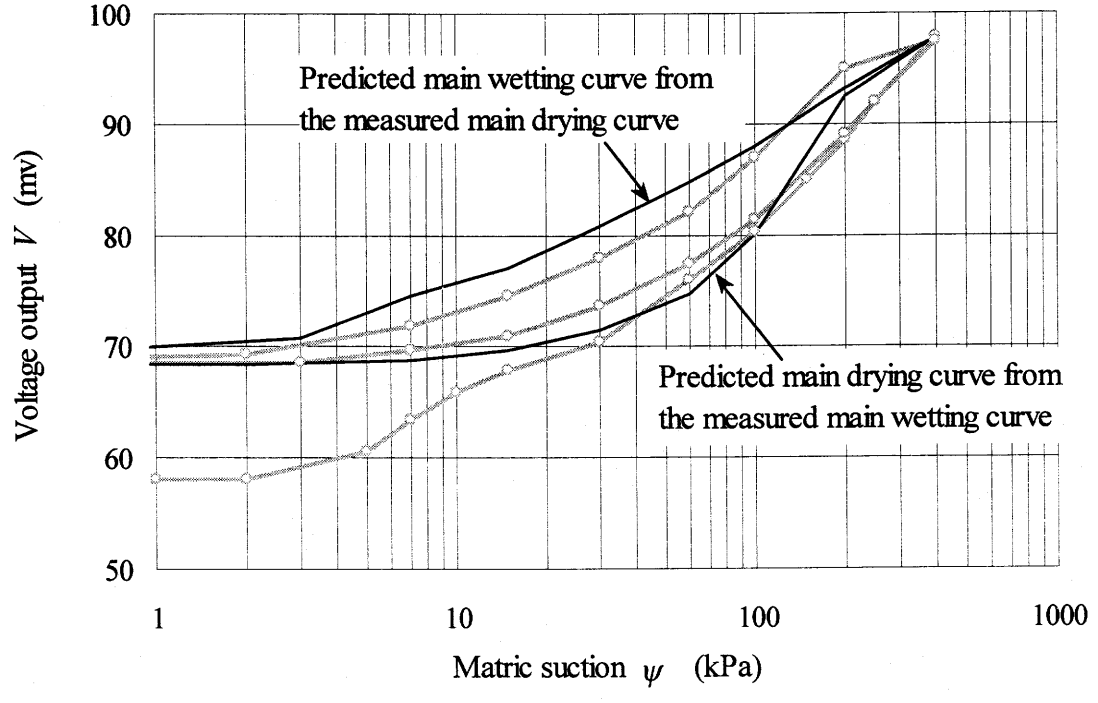

Figure 5.15 Predicted main wetting and drying curves of Sensor-1 using the Mualem Model II-1

5.3 THE PARLANGE MODEL

Parlange (1977) made a further simplification to the Mualem independent domain model to reduce the amount of experimental data required to calibrate the model. The model is simple in formulation and requires only one branch of the hysteresis loop to predict all other curves. The structure and the testing of the model are presented in this section.

5.3.1 The Theory of the Model

Mualem (1973) assumed in the Mualem model-I that, the pore water distribution function, $f(\psi_w, \psi_d)$, is the product of two functions depending on ψ_w and ψ_d, respectively,

$$f(\psi_w, \psi_d) = h(\psi_d)l(\psi_w) \tag{5.7}$$

Parlange (1977) made an assumption that $f(\psi_w, \psi_d)$ is independent of ψ_w. So the similarity hypothesis, Eq. 5.7, will be in the following form,

$$f(\psi_w, \psi_d) = h(\psi_d) \tag{5.8}$$

Parlange stated that, "it is obvious that the present assumption is at best a crude approximation which can hold only as ψ_w varies on a finite interval or equivalently, if the variation in size is much greater for the openings than for the pores."

When the Parlange (1977) assumption holds, (i.e., distribution function $f(\psi_w, \psi_d)$ is a function of ψ_d only), the main wetting process can be expressed as,

$$\theta_w(\psi) = \int_{\psi}^{\psi_M} d\psi_w \int_{\psi_w}^{\psi_M} f(\psi_w, \psi_d) d\psi_d \tag{5.9a}$$

and the derivative at the wetting boundary as,

$$\frac{d\theta_w}{d\psi} = -\int_{\psi}^{\psi_M} f(\psi_w, \psi_d) d\psi_d \tag{5.9b}$$

Figure 5.16 illustrates the contours of the filled pores for the primary drying and wetting scanning curves. The water content at a suction value of ψ on the primary scanning curves is computed by integrating the filled pores shown by the dotted regions. A drying scanning curve can be expressed as

$$\theta_d(\psi,\psi_1) = \theta_w(\psi) + \int_{\psi_1}^{\psi} d\psi_w \int_{\psi_w}^{\psi_M} f(\psi_w,\psi_d)d\psi_d \qquad (5.10)$$

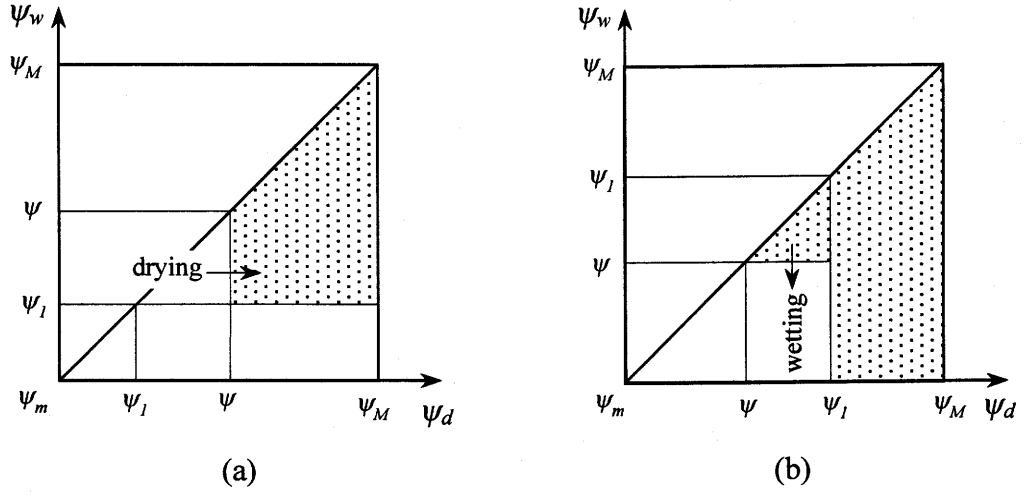

Figure 5.16 The filled pore diagram for (a) primary drying curve and (b) primary wetting scanning curve

Substituting Eq. 5.9b into Eq. 5.10, the following equation for the primary drying scanning curve is obtained.

$$\theta_d(\psi,\psi_1) = \theta_w(\psi) - (\psi - \psi_1)\left(\frac{d\theta_w}{d\psi}\right)_{\psi} \qquad (5.11a)$$

Similarly, a primary wetting scanning curve starting at a suction of ψ_1 on the drying boundary of the loop is given by,

$$\theta_w(\psi,\psi_1) = \theta_w(\psi) - (\psi - \psi_m)\left(\frac{d\theta_w}{d\psi}\right)_{\psi_1} \qquad (5.11b)$$

Where

ψ_M = the maximum value of suction

ψ_m = the minimum value of suction.

Palange (1977) assumed the minimum value of suction to be the re-saturation value on the main wetting curve.

Using Eqs. 5.11a and 5.11b, the primary scanning curves can be computed from the main wetting curve only. When assuming ψ_I is equal ψ_m, the main drying curve can also be obtained using Eq. 5.11a. Since only a derivative, ($d\theta_w/d\psi$), is involved in the Eqs. 5.11a and 5.11b, the curve fitting of the measured points on the main wetting curve is flexible without incurring difficulties in solving the equations.

Parlange (1977) found that for the singular case in which a significant part of the hysteresis is within the range below the air entry value, Eq. 5.11a fails to reproduce the main drying curve and the primary wetting scanning curves. Parlange suggested that the main drying curve, instead of the main wetting curve, should be used in predicting primary wetting scanning curves. Substituting ψ_I with ψ_m in Eq. 5.11a and integrating Eq. 5.11a, gives the following equation to compute the main wetting curve.

$$\theta_w(\psi) = \theta_0 + (\psi - \psi_m)\int_{\psi}^{\psi_m} \frac{\theta_d(\psi) - \theta_0}{(\psi - \psi_m)^2} d\psi \qquad (5.12)$$

where, θ_0 is the water content at ψ equal to ψ_m, (i.e., the maximum water content on the main hysteresis loop).

With $\theta_w(\psi)$ obtained from Eq. 5.12, the primary wetting scanning curves can then be predicted using Eq. 5.11b.

5.3.2 Testing of the Parlange Model

When examining the Parlange model, Mualem (1978) pointed out that Eq. 5.12, which is supposed to yield the main wetting curve from the main drying curve, is wrong because the predicted wetting curve displays an increase of water content above $\psi > \psi_m$ as illustrated in Fig. 5.17. Therefore, Eq. 5.12 can not be used in applying the Parlange model.

The hysteresis loop of the ceramic of the Beta-97 sensor does not show the singular case that Parlange has described. Since Eq. 5.12 was intended for the singular

case, Eq. 5.11b, instead of Eq. 5.12, was used to predict the primary wetting scanning curves of the ceramics and sensors.

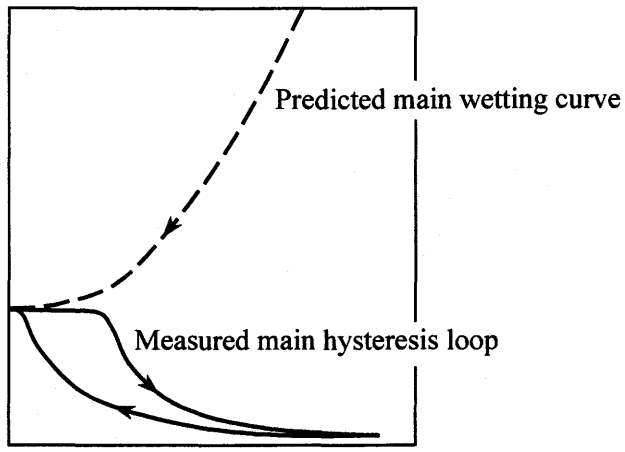

Figure 5.17 Measured main loop of the Rubicon sandy loam (solid lines) and predicted main wetting curve (dashed line) derived from the main drying curve using Eq. 5.12 (from Mualem, 1978).

Because the derivative of the main wetting curve is involved in the equations of the Parlange model, The following function was used to fit the measured data points.

$$\theta_w(\psi) = \frac{ab + c\psi^d}{b + \psi^d} \quad \text{(from M. Fredlund, personal communication)} \qquad (5.13)$$

where a, b, c and d are fitting parameters.

Equation 5.13 was used to fit the measured data points mainly because of its simplicity. This function was also used in the application of the Nimmo model presented in the next section. The properties of this function and the physical meaning of the parameters will be described later in this chapter.

Substituting Eq. 5.13 into Eqs. 5.11a and 5.11b gives,

$$\theta_d(\psi, \psi_1) = \theta_w(\psi) - (\psi - \psi_1)\frac{(c-a)bd\psi^{d-1}}{(b+\psi^d)^2} \qquad (5.14a)$$

for primary drying scanning curves, and

$$\theta_w(\psi,\psi_1)=\theta_w(\psi)-(\psi-\psi_m)\frac{(c-a)bd\psi_1^{d-1}}{(b+\psi_1^d)^2} \qquad (5.14b)$$

for primary wetting scanning curves.

The results of prediction of one ceramic, (i.e., Ceramic-1), and one sensor, (i.e., Sensor-1), are presented in Figs. 5.18 to 5.19. The predicted main drying curve and primary scanning curves is too far away from the measured curves.

If one or two points on the main drying curve are measured in addition to the main wetting curve, the predicted main drying curve can be adjusted to pass through the measured points using some arbitrary parameter. For the particular case of the sensor Beta-97, Eqs. 5.14a and 5.14b can be modified by adding an arbitrary parameter, α, as follows.

$$\theta_d(\psi,\psi_1)=\theta_w(\psi)-(\psi-\psi_1)\frac{(c-a)bd\psi^{d-1}}{(b+\alpha\cdot\psi^d)^2} \qquad (5.15a)$$

$$\theta_w(\psi,\psi_1)=\theta_w(\psi)-(\psi-\psi_m)\frac{(c-a)bd\psi_1^{d-1}}{(b+\alpha\cdot\psi_1^d)^2} \qquad (5.15b)$$

A value of 1.7 was used for the parameter α in Eqs. 5.15a and 5.15b. It can be seen that the predicted curves using Eqs. 5.15a and 5.15b are closer to the measured curves (Figs. 5.20 and 5.21). The predicted primary scanning curves show a tendency of approaching the main hysteresis loop right after the point of reversal, which is one of the principal properties of the measured scanning curves of the sensor ceramics. However, it must be noted that, although a better prediction is achieved by using the parameter, α, there is no theoretical basis for this parameter and it might not be suitable for other porous materials.

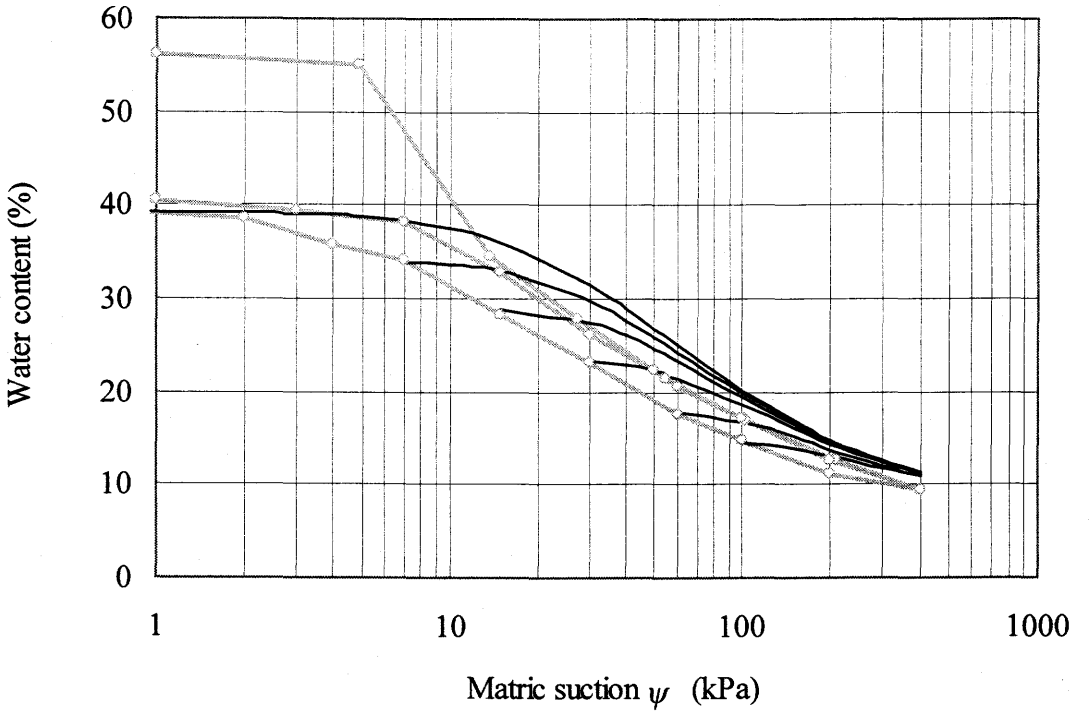

Figure 5.18a Predicted main drying and drying scanning curves of Ceramic-1 using the Parlange model

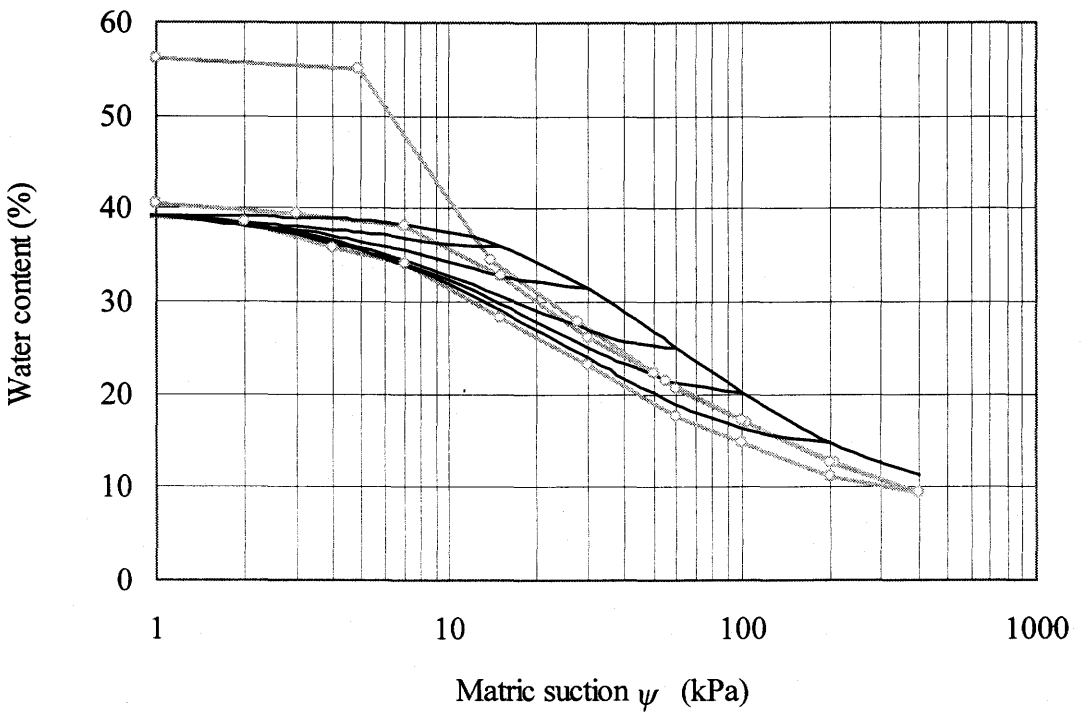

Figure 5.18b Predicted main drying and wetting scanning curves of Ceramic-1 using the Parlange model

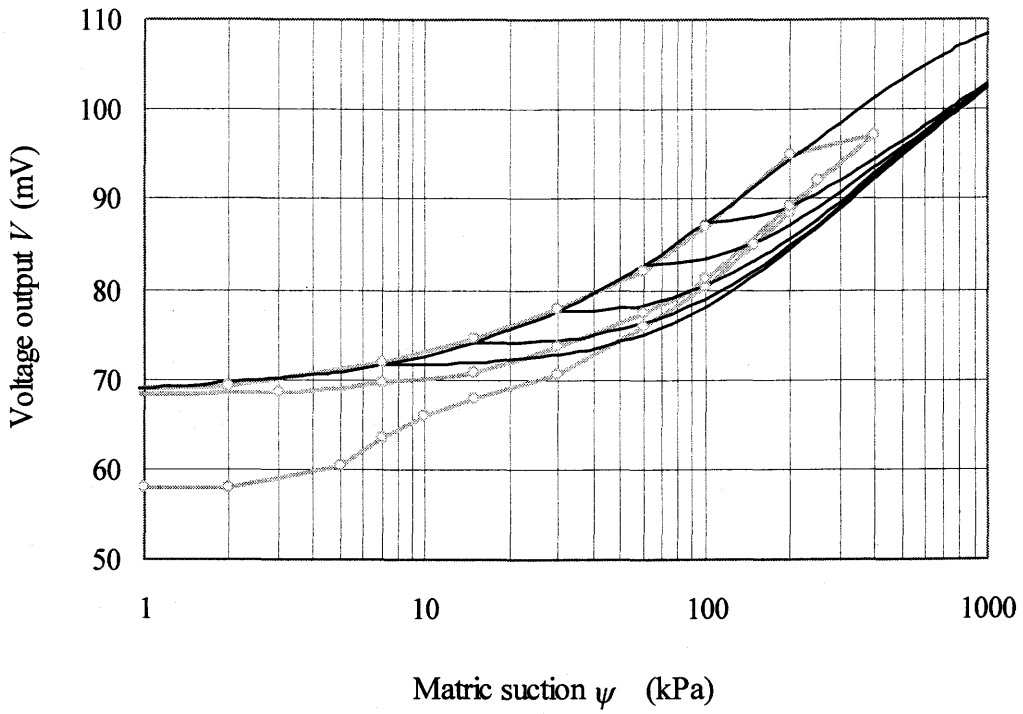

Figure 5.19a Predicted main drying and drying scanning curves of Sensor-1 using the Parlange model

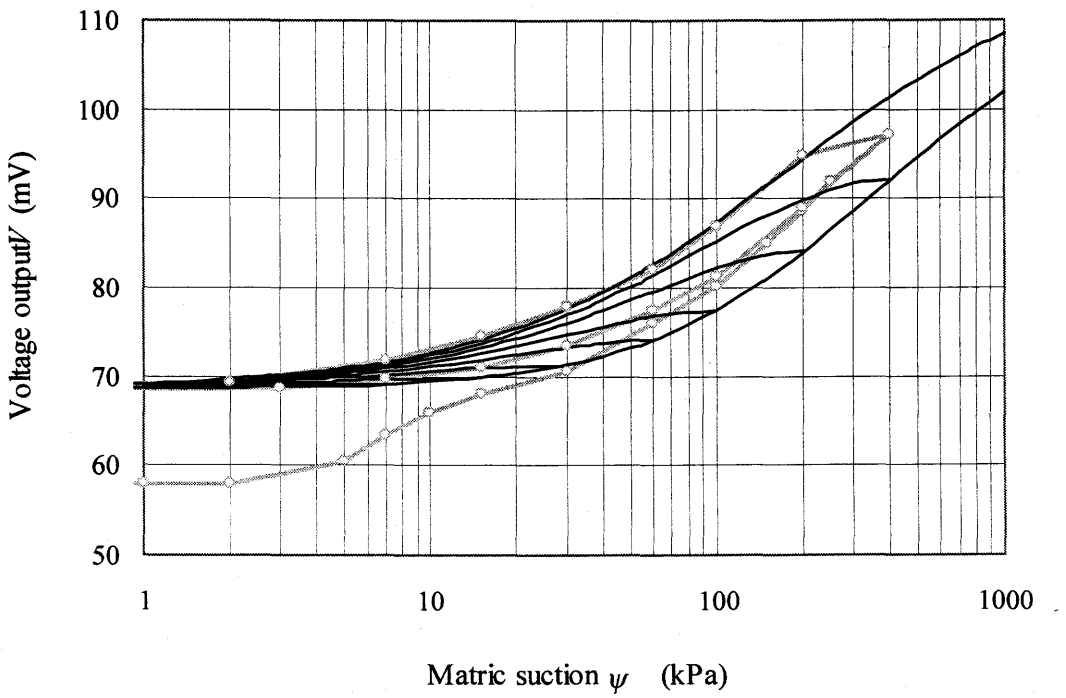

Figure 5.19b Predicted main drying and wetting scanning curves of Sensor-1 using the Parlange model

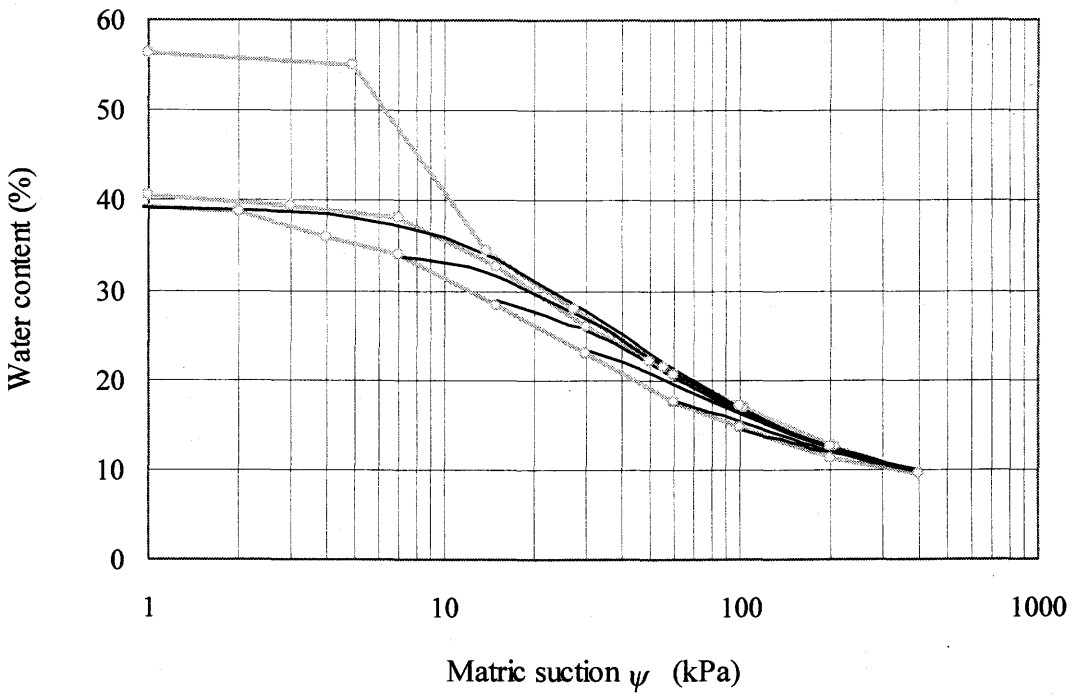

Figure 5.20a Predicted main drying and drying scanning curves of Ceramic-1 using the modified Parlange formula (Eqs. 5.15a and 5.15b)

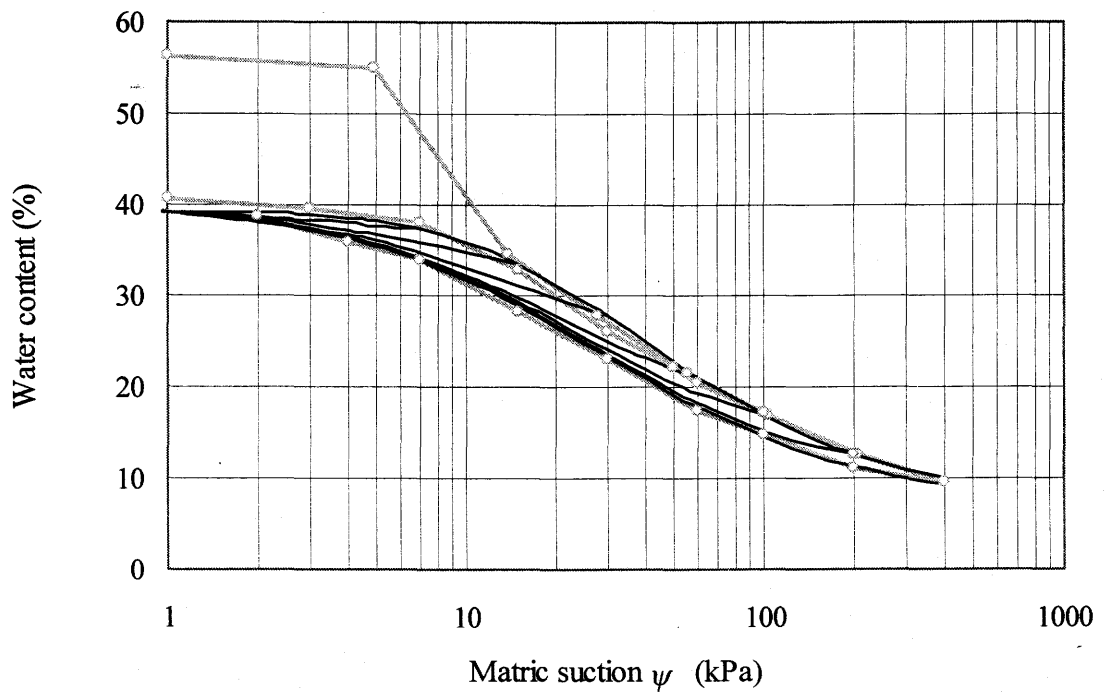

Figure 5.20b Predicted main drying and wetting scanning curves of Ceramic-1 using the modified Parlange formulas (Eqs. 5.15a and 5.15b)

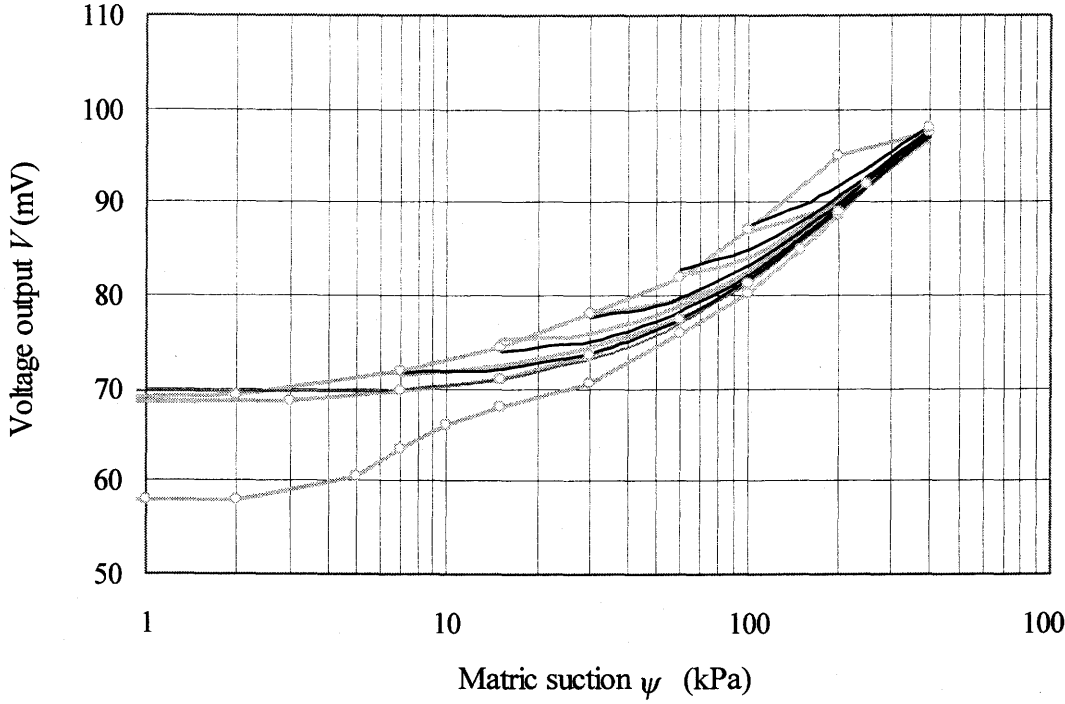

Figure 5.21a Predicted main drying and drying scanning curves of Sensor-1 using the modified Parlange formulas (Eqs. 5.15a and 5.15b)

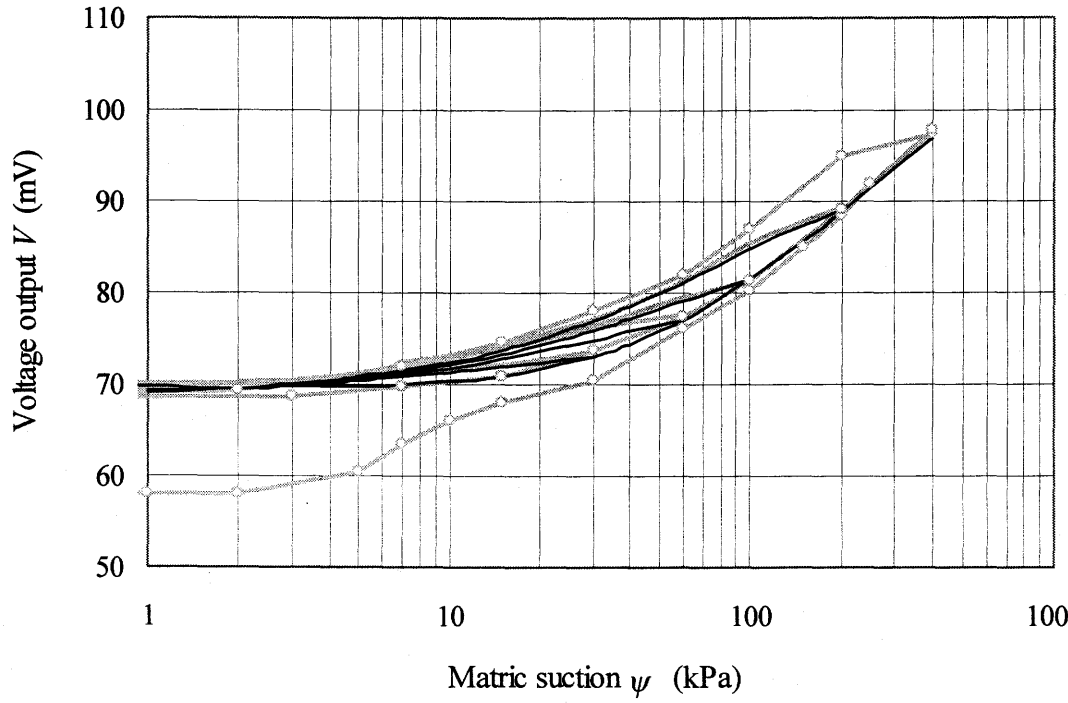

Figure 5.21b Predicted main drying and wetting scanning curves of Sensor-1 using the modified Parlange formulas (Eqs. 5.15a and 5.15b)

5.3.3 Another Version of the Parlange Model

Mualem (1978) made a thorough theoretical analysis of the Parlange model and pointed out that the Parlange model is theoretically defective with the basic assumption. Mualem (1978) suggested that the main drying curve, instead of main wetting curve, should be used in the model and the following prediction equations were derived.

$$\theta_d(\psi,\psi_1) = \theta_0 - [\theta_0 - \theta_d(\psi_1)]\frac{\psi - \psi_{\min}}{\psi_1 - \psi_{\min}} - (\psi - \psi_{\min})\int_{\psi}^{\psi_1} \frac{\theta_0 - \theta_d(\psi')}{(\psi' - \psi_{\min})^2} d\psi' \qquad (5.16a)$$

$$\theta_d(\psi,\psi_1) = \theta_0 \frac{\psi_{\max} - \psi_1}{\psi_{\max} - \psi_{\min}} - [\theta_0 - \theta_d(\psi)]\frac{\psi - \psi_1}{\psi - \psi_{\min}} + (\psi_1 - \psi_{\min})\int_{\psi_{\max}}^{\psi} \frac{\theta_0 - \theta_d(\psi')}{(\psi' - \psi_{\min})^2} d\psi' \qquad (5.16b)$$

where θ_0 is the maximum water content at ψ equal to ψ_{min}.

Parlange (1977) and Mualem (1978) have both pointed out that the value of ψ_{min} could have a significant influence on the prediction. With only the main drying curve measured, ψ_{min}, the re-saturation value, remains unknown. One way to apply Eqs. 5.16a and 5.16b is to use one measured point on the main wetting curve in addition to the measured main drying curve, as suggested by Parlange (1977).

For the case of capillary hysteresis of the ceramic of Beta-97 sensor, 1 kPa was used for ψ_{min}. Again, Eq. 5.13 was used to fit the measured data of main drying curve.

The predicted main wetting curves and primary scanning curves of Ceramic-1 and Sensor-1 (Figs. 5.22 and 5.23) show that ψ_{min} equal to 1 kPa is appropriate. Reasonably good agreement between the predicted and measured main wetting curve was achieved. The predicted scanning curves are all convex towards the corresponding hysteresis boundary. A comparison between the measured scanning curves (Chapter 3) and predicted scanning curves in Figs. 5.22 and 5.23, shows that the above two equations (Eqs. 5.16a and 5.16b) provide a close prediction of the water capillary hysteresis of the ceramic of the Beta-97 sensor.

This version of the Parlange model requires only a main drying curve and one or two points on main wetting curve, making the calibration easier and less time consuming. However, the prediction equations (i.e., Eqs. 5.16a and 5.16b) each involves an integration. The fit equation of measured points of the main drying curve must be appropriate so that the integration is solvable. In applying the model on Ceramic-1 and Sensor-1, the fit function of Eq. 5.13 was used, but the parameter d was set to 1 without incurring an unacceptable error.

Although this version of Parlange model can make a relatively good prediction of the hysteresis of the sensor ceramic, Mualem (1978) found that the Parlange model was theoretically wrong in its basic assumption and theoretical difficulties were encountered in using the Parlange model.

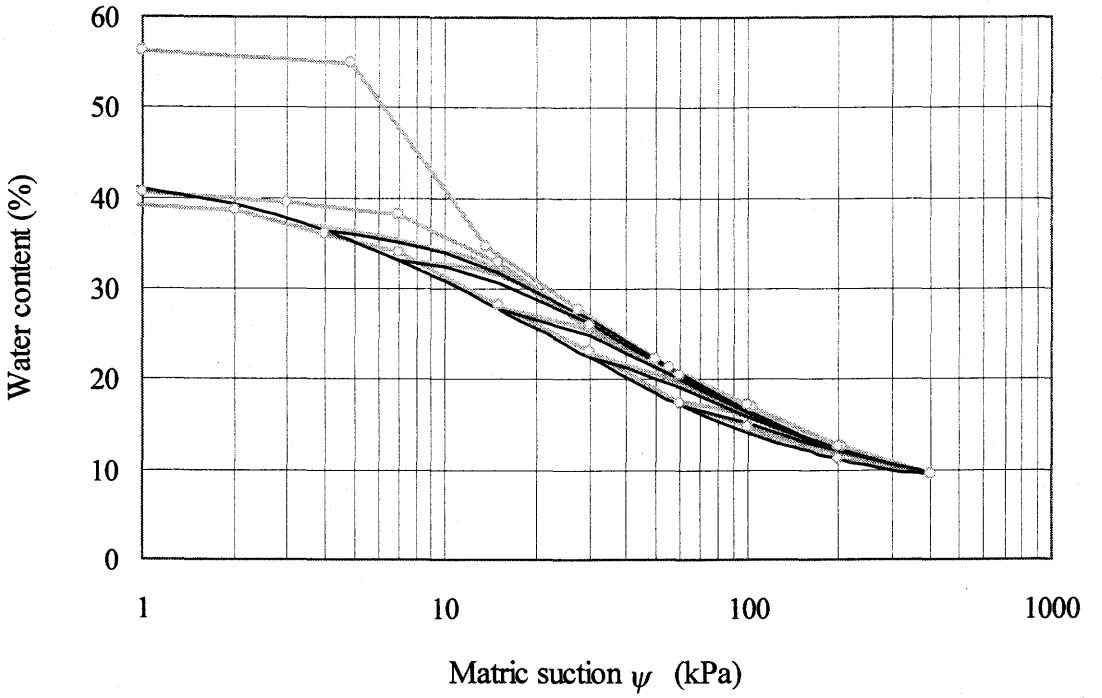

Figure 5.22a Predicted main wetting curve and drying scanning curves of Ceramic-1 using measured main drying curve (Eq. 5.16a)

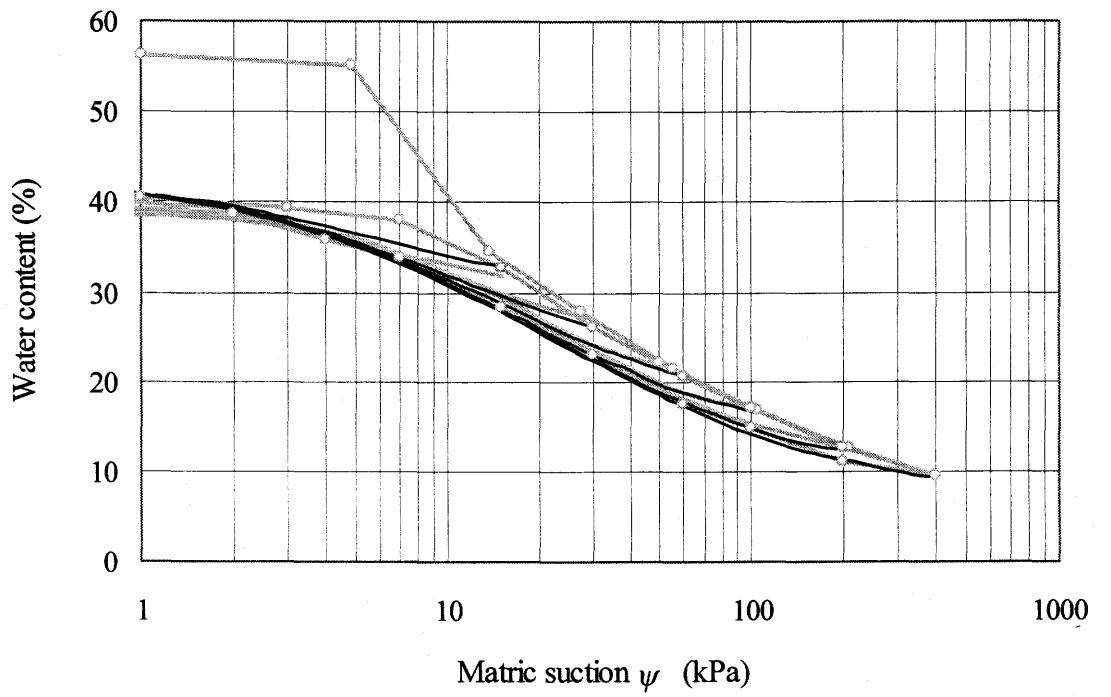

Figure 5.22b Predicted main wetting curve and wetting scanning curves of Ceramic-1 using measured main drying curve (Eq. 5.16b)

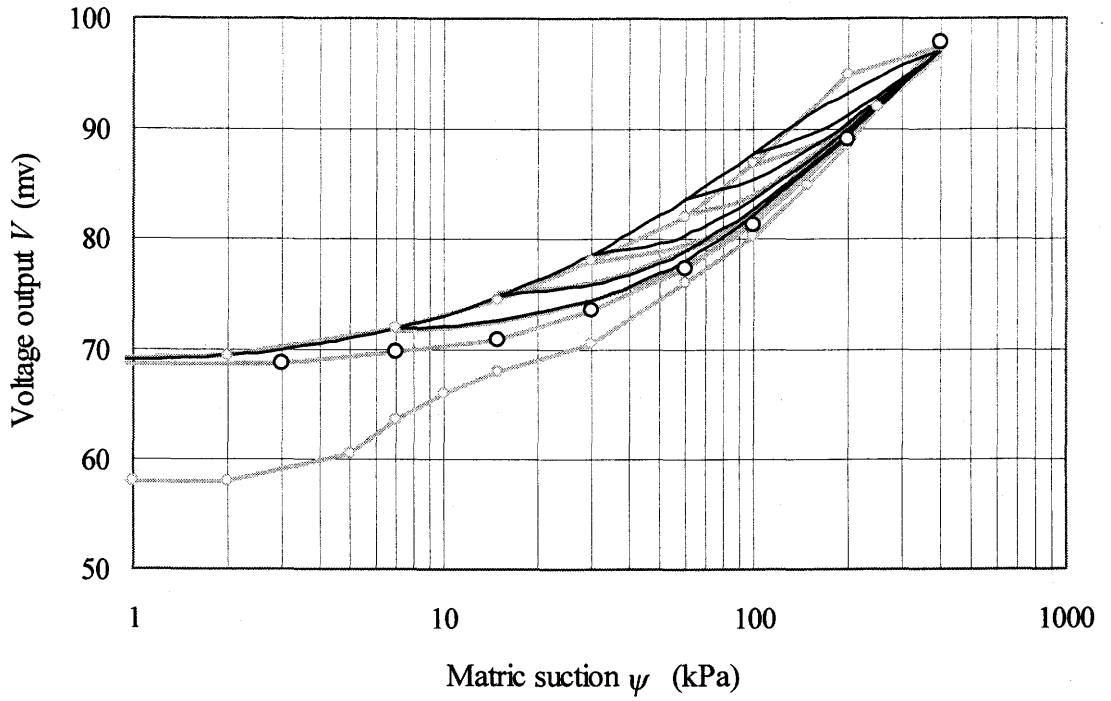

Figure 5.23a Predicted main wetting curve and drying scanning curves of Sensor-1 using measured main drying curve (Eq. 5.16a)

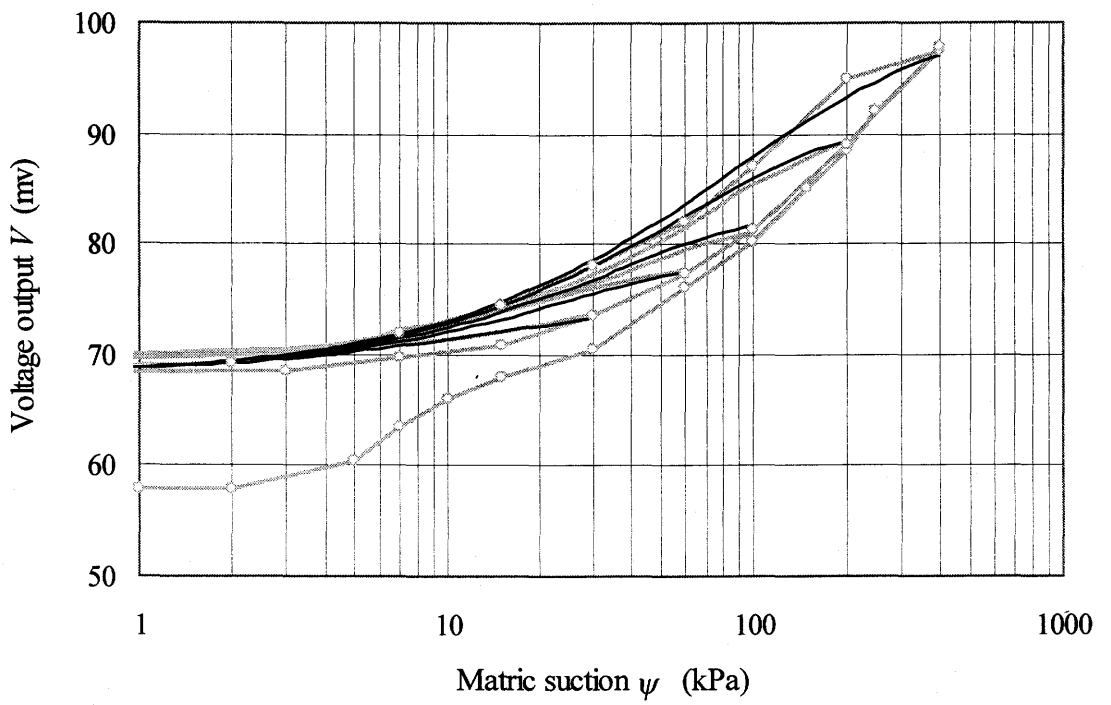

Figure 5.23b Predicted main wetting curve and wetting scanning curves of Sensor-1 using measured main drying curve (Eq. 5.16b)

5.4 THE NIMMO MODEL

The models described in the previous sections are all domain models. Nimmo (1992) proposed a semi-empirical model based on the analysis of the shape of the hysteresis loop. The Nimmo model requires only the main drying curve and two points on the main wetting curve. The structure of the Nimmo model and a test using the measured data are presented in this section.

5.4.1 The Theory of the Model

Two parameters, ν and β, are used in the Nimmo model. The two parameters are each associated with a physical property of porous media that affects hysteresis and with a visible feature of a graphed hysteretic relationship.

The first parameter, ν, is defined as the fraction of the pore space that is non-hysteretic. This parameter relates to the fact that not all pore space is subject to hysteresis. Some fraction of the pore space, including dead-end pores, film coating surfaces, and some of the space within hysteretic pores, do not drain or refill by Haines jumps. In Fig. 5.24, ν can be considered proportional to the ratio of the slopes of wetting and drying at the point of reversal. If ν has a value close to one, hysteresis is minimal, the wetting curve is close to the drying curve. If ν has a value close to zero, hysteresis is maximal.

The second parameter, β, represents the body-to-neck size ratio of the biggest pore ($r_{w-\max}/r_{d-\max}$). Since the radii are inversely proportional to the suction ψ, β is equal to the ratio of the air entry value (ψ_{ae}) to the re-saturation value (ψ_{re}), as illustrated in Fig. 5.24.

In general, the parameter ν should depend on the suction ψ and the water content θ, as there might be more or less non-hysteretic space in the small pores that are filled at a low water content than in the large pores that are filled at a high water content. Another possibility is that ν itself may depend on the history of drying and wetting events. One of the two hypotheses in the Nimmo model is assuming that ν is a constant, independent of suction and drying and wetting history. This hypothesis

implies a self-similarity of the pores with respect to the degree to which the pores are non-hysteretic.

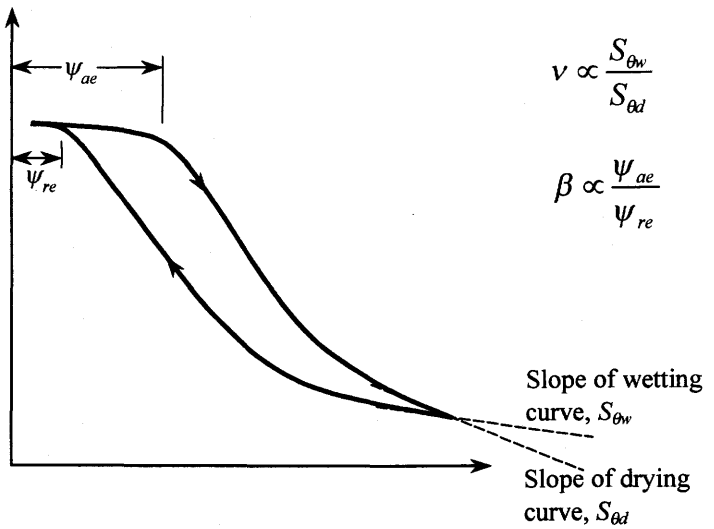

Figure 5.24 Schematic illustration of non-hysteretic space parameter ν and the pore-geometry parameter β (from Nimmo, 1992).

The second hypothesis is related to the pore size distribution. The pore-neck size distribution function $f_d(r)$ is related to the main drying curve $\theta_d(r)$ according to

$$\theta_d(r) = \int_0^r f_d(\tilde{r})d\tilde{r} \tag{5.17}$$

Applying the constant ν hypothesis, the distribution of non-hysteretic pores is $\nu f_d(r)$. The second hypothesis specifies the body size distribution of the pores that are hysteretic, making use of a function $f_{str}(\tilde{r},r)$ illustrated in Fig. 5.25. The portion of $f_d(r)$ between $\tilde{r}$ and $r_{d\text{-}max}$ is stretched linearly in the r direction to cover the region between $\tilde{r}$ and $r_{w\text{-}max}$. The function $f_{str}(\tilde{r},r)$ is algebraically related to $f_d(r)$ as follows.

$$f_{str}(\tilde{r},r) = f_d[\frac{1}{\alpha}(r-\tilde{r})+\tilde{r}] \tag{5.18}$$

where $\alpha = \dfrac{r_{w-\max}-\tilde{r}}{r_{d-\max}-\tilde{r}} = \dfrac{\beta r_{d-\max}-\tilde{r}}{r_{w-\max}-\tilde{r}}$

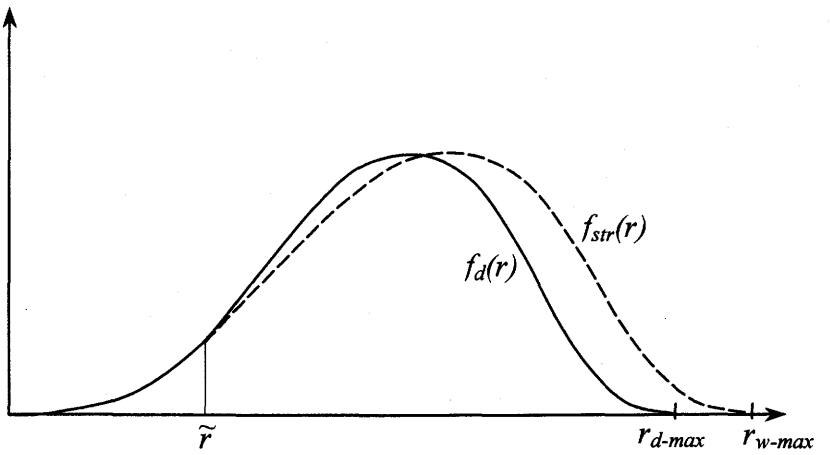

Figure 5.25 A pore neck-size distribution function $f_d(r)$ with the function $f_{str}(\tilde{r},r)$ relating to the size distribution of pore bodies with neck radius $\tilde{r}$ (the second hypothesis) (from Nimmo, 1992).

Figure 5.26 illustrates the application of the model in predicting the capillary hysteresis. This diagram has $f_d(r)$ based on effective neck sizes, body sizes varying upward from small to large, and areas under the curve directly proportional to pore space or water content. The main drying process is represented by the integration of Eq. 5.17 that defines the distribution function $f_d(r)$. After drying to ψ_{rev}, the water content is proportional to the gray area to the left of r_{rev}. After rewetting to r_s from the reversal at r_{rev}, the water content is equal to $\theta_w(r_s)$ on the main wetting curve and is proportional to the sum of three shaded areas: (1) all pore space with r_d less than r_{rev} (gray area) remains filled; (2) all of the non-hysteretic space between r_{rev} and r_s (dotted area) becomes filled; (3) the fraction of the hysteretic space between r_{rev} and r_s in which $r_w < r_s$ (hatched area) becomes filled. The curve bounding the upper portion of the hatched area does not have a simple relationship to the $f_d(r)$ curve and is shown hypothetically in the figure. This curve may be thought of as the locus of points for which r_w is equal to r_s. In determining the portion of Fig. 5.26 to be integrated, two rules are followed. A drying operation reduces the area to be integrated by sweeping a vertical line segment leftward through hysteretic and non-hysteretic space. A wetting operation increases the area by sweeping a vertical line segment rightward through

non-hysteretic space only, and adding the portion of hysteretic space on which r_w is less than r.

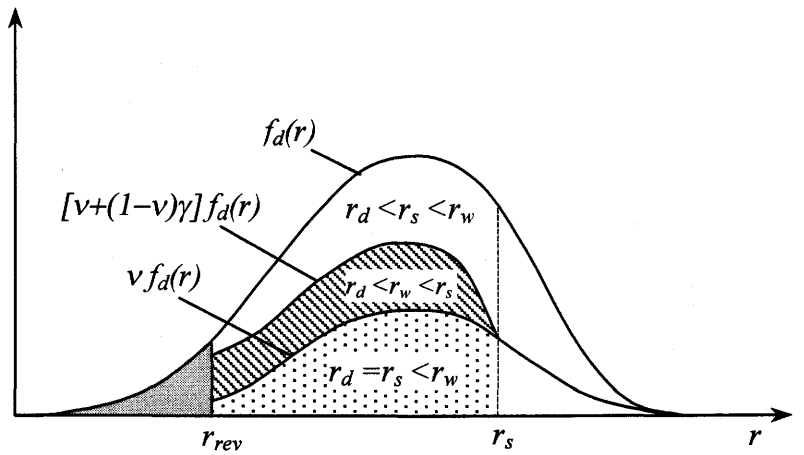

Figure 5.26 Diagram illustrating the application of the model to the situation existing after drying to r_{rev} and then rewetting to r_s. The water content for this condition is proportional to the sum of the three shaded areas: the gray area that never was emptied, the dotted area with non-hysteretic space that refills at the same r values at which it emptied, and the hatched area with hysteretic space that refills at $r \leq r_s$ (from Nimmo, 1992).

The derivation of formula of the model follows the integration of appropriate areas on the diagram of Fig. 5.26. For the convenience of computation, the following equations were all derived in term of the suction ψ instead of the radius r. The main wetting curve and the primary wetting scanning curves are computed by integrating the three areas in Fig. 5.26.

$$\theta_w(\psi) = \theta_{rev} + \int_{max(\psi,\psi_{ae})}^{\psi_{rev}} [v + (1-v)\gamma(\tilde{\psi},\psi)] f_d(\tilde{\psi}) d\tilde{\psi} \qquad (5.19a)$$

where, θ_{rev} is the gray area in the diagram, and

$$\gamma(\tilde{\psi},\psi) = \frac{\int_{\tilde{\psi}}^{\psi} f_{str}(\tilde{\psi},\psi_w) d\psi_w}{\int_{\tilde{\psi}}^{\psi_{w-max}} f_{str}(\tilde{\psi},\psi_w) d\psi_w} = \frac{\theta[(\psi-\tilde{\psi})/\alpha + \tilde{\psi}] - \theta(\tilde{\psi})}{\theta_{max} - \theta(\tilde{\psi})}$$

The primary drying scanning curves are given as,

$$\theta_d(\psi,\psi_s)=\theta_{rev}+\int_{max(\psi,\psi_{ae})}^{\psi_{rev}}[v+(1-v)\gamma(\tilde{\psi},\psi_s)]f_d(\tilde{\psi})d\tilde{\psi} \qquad (5.19b)$$

5.4.2 Testing of the Nimmo Model

There are two unknown parameters in the Nimmo semi-empirical model, v and β. Two points on the wetting curve are required in addition to the main drying curve to apply the Nimmo model. Again, Eq. 5.13 was used to fit the measured data of the main drying curve. The parameter d in Eq. 5.13 was set to be 1 when performing the integration in the formula of the model (Eqs. 5.19a and 5.19b). The predicted wetting curves and primary scanning curves of Ceramic-1, Ceramic-2, Sensor-1 and Sensor-2 are shown in Figs. 5.27 to 5.30. Other ceramics and sensors have similar prediction results.

As can be seen in Figs. 5.27 to 3.30, the predicted drying scanning curves that have a starting point (i.e., the point of reversal) at high suction are convex towards the wetting boundary, rather than towards the drying boundary. In other words, the predicted drying scanning curves do not show a tendency of joining the drying boundary in a relatively small suction change, contradicting the shape of the measured primary scanning curves. The predicted primary wetting scanning curves that have a starting point at low suction are convex towards the drying boundary, rather than towards the wetting boundary.

The reason that the Nimmo model fails to reproduce the drying scanning curves starting at a high suction and the wetting scanning curves starting at low suction, can be attributed to the first assumption of the model, (i.e., the constant v assumption). The parameter v is defined as the fraction of the pore space that is non-hysteretic and is assumed constant, independent of the suction and the drying and wetting history. This hypothesis implies that the angle between the main drying curve and the primary wetting scanning curves, as shown in Fig. 5.31, to be the same for all of the primary wetting scanning curves. If the suction at the starting point of the wetting scanning curve is high, the slope of the drying boundary at this point is low and the wetting

scanning curve is convex towards the wetting boundary. The predicted curves will be close to the measured curves. If the suction at the starting point of the wetting scanning curve is low, the slope of the drying boundary at this point is high and the wetting scanning curve is convex towards the drying boundary. The predicted primary wetting scanning curves will be apart from the measured scanning curves.

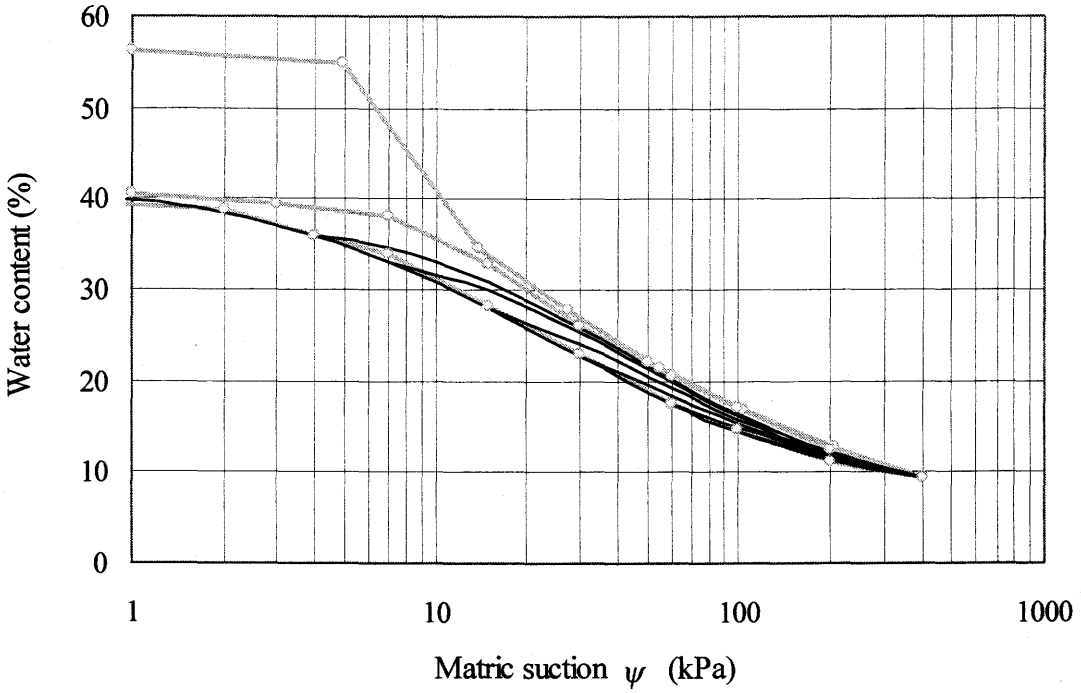

Figure 5.27a Predicted main wetting curve and drying scanning curves of Ceramic-1 using the Nimmo model

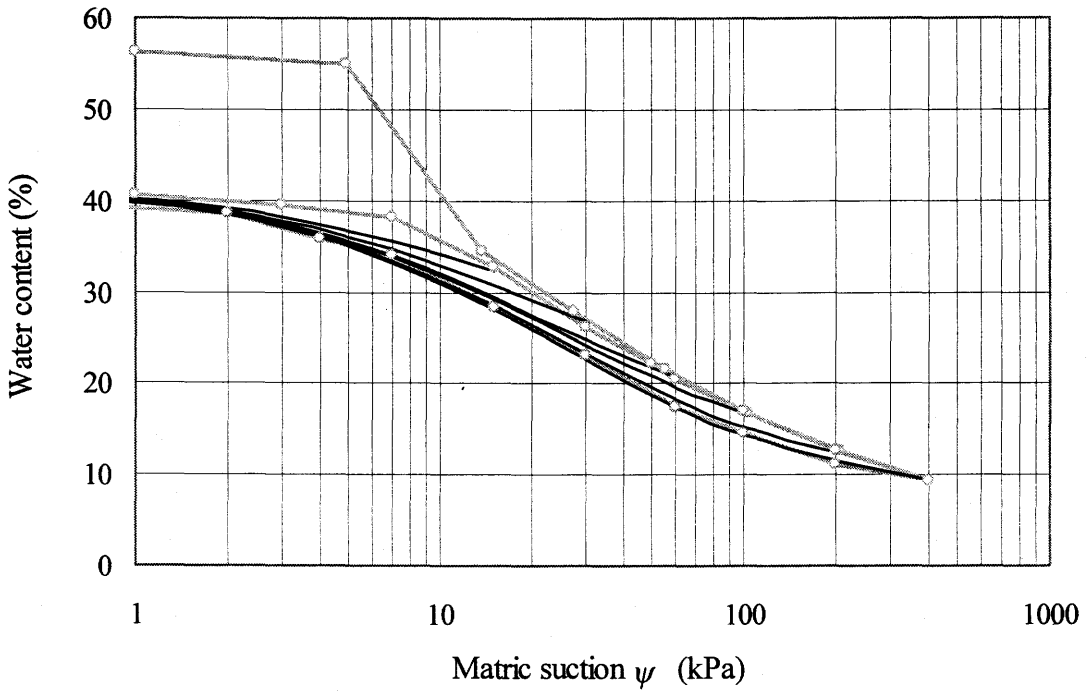

Figure 5.27b Predicted main wetting curve and wetting scanning curves of Ceramic-1 using the Nimmo model

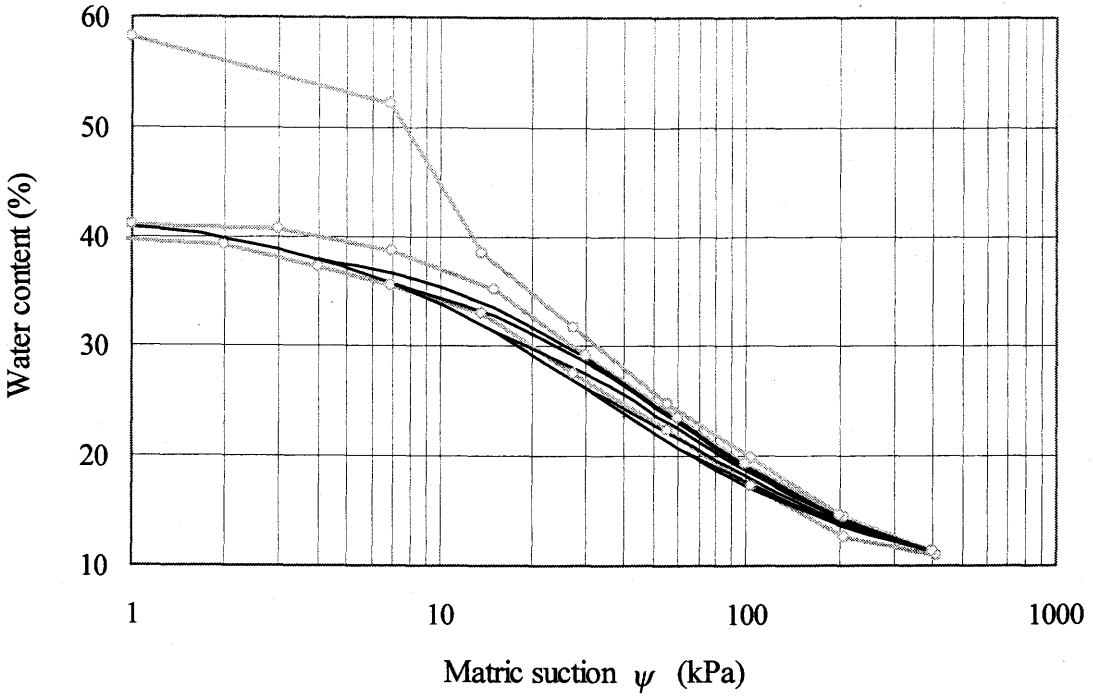

Figure 5.28a Predicted main wetting curve and drying scanning curves of Ceramic-2 using the Nimmo model

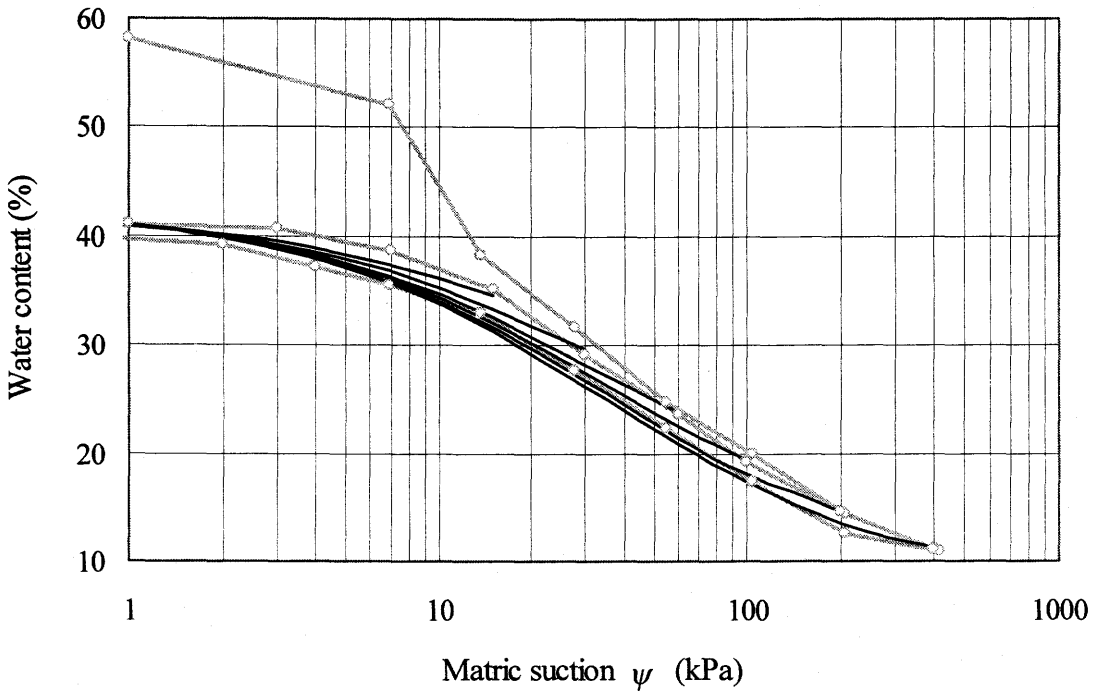

Figure 5.28b Predicted main wetting curve and wetting scanning curves of Ceramic-2 using the Nimmo model

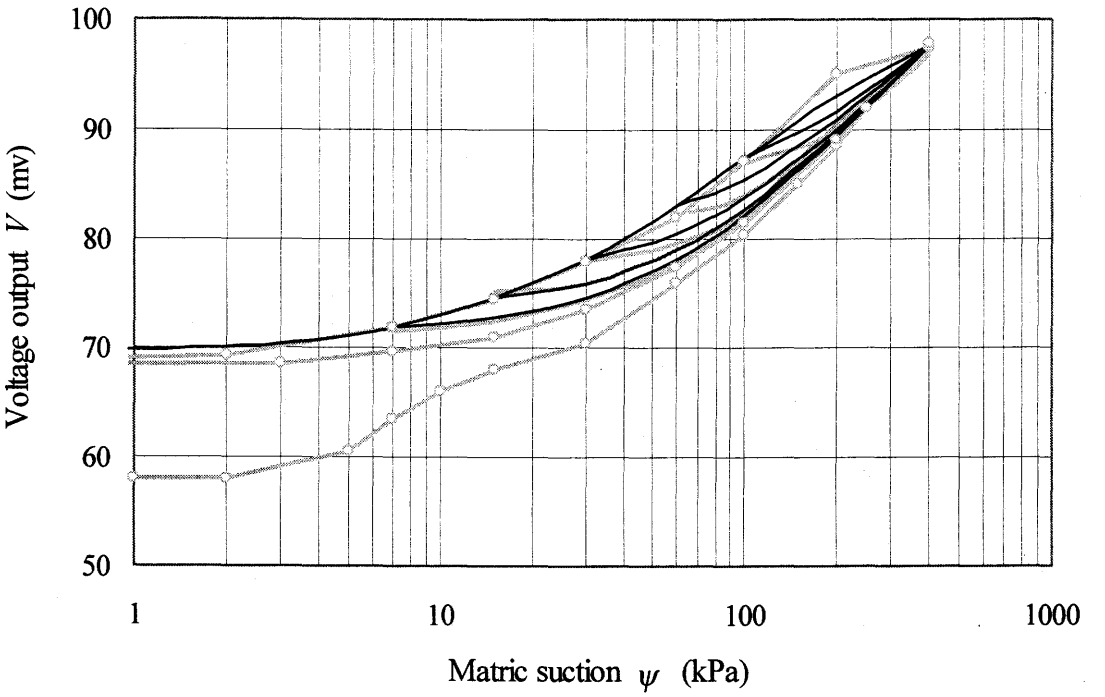

Figure 5.29a Predicted main wetting curve and drying scanning curves of Sensor-1 using the Nimmo model

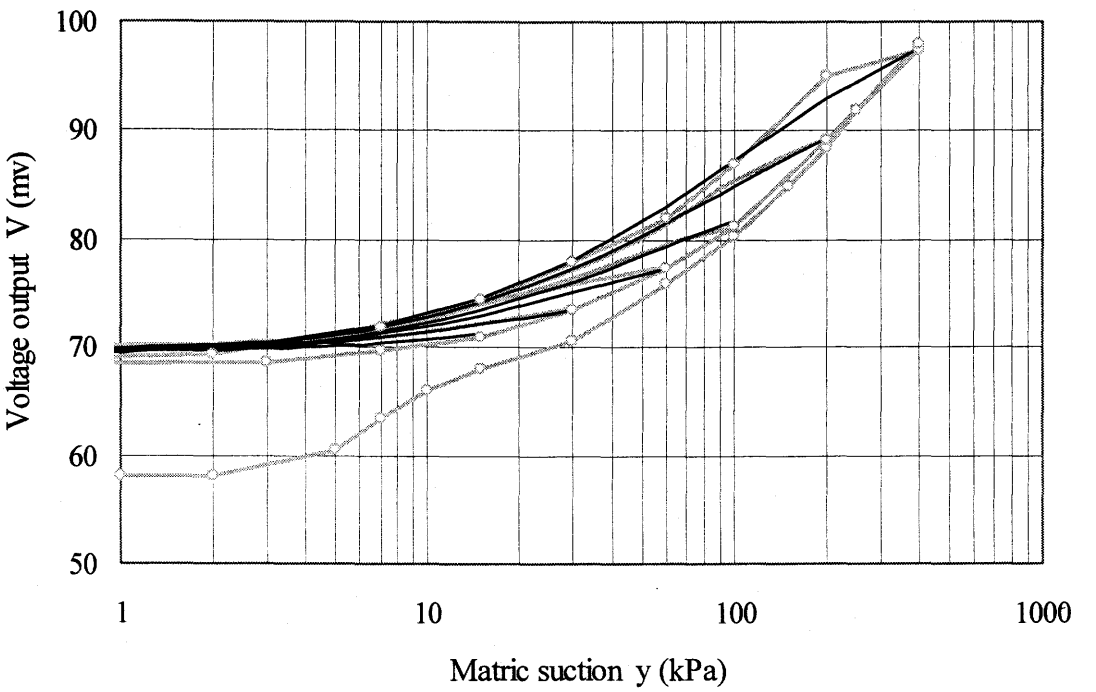

Figure 5.29b Predicted main wetting curve and wetting scanning curves of Sensor-1 using the Nimmo model

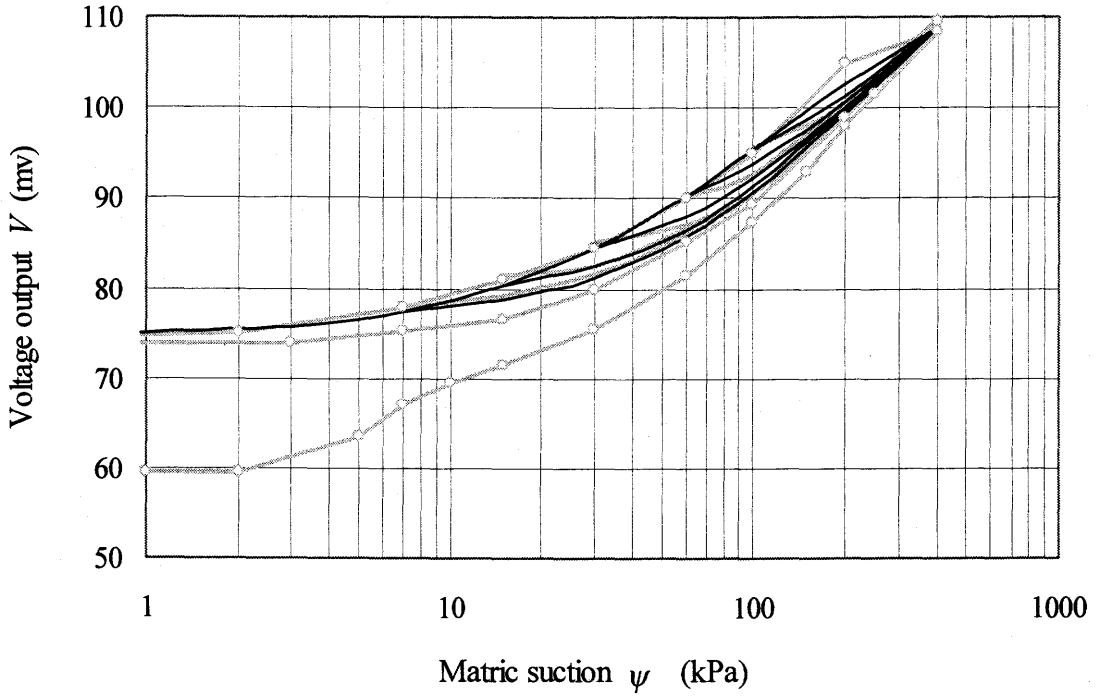

Figure 5.30a Predicted main wetting curve and drying scanning curves of Sensor-2 using the Nimmo model

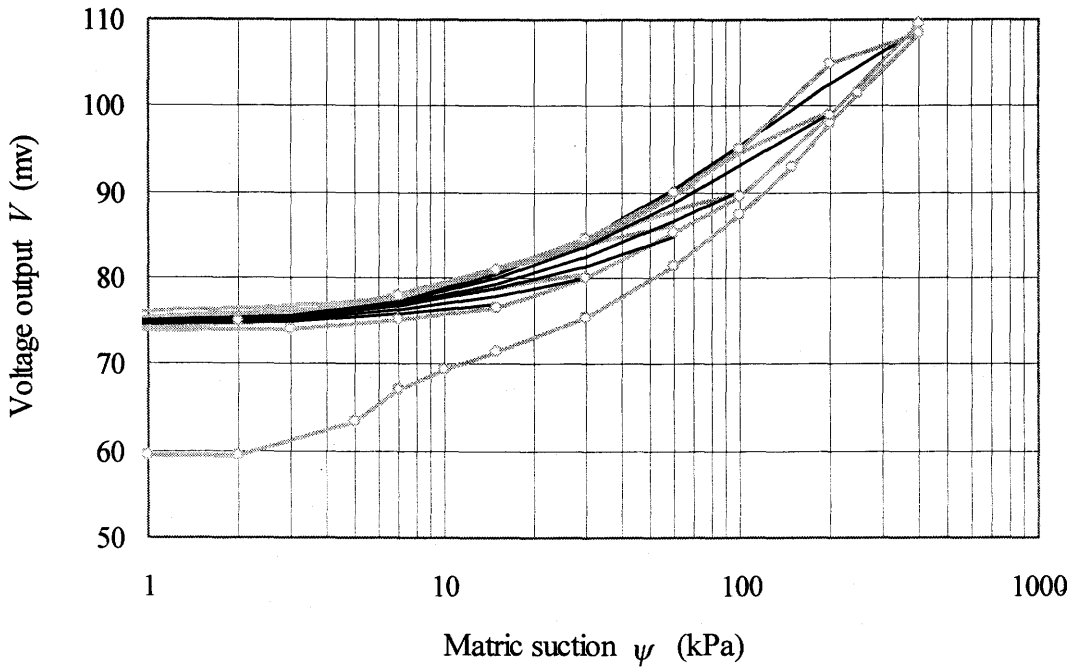

Figure 5.30b Predicted main wetting curve and wetting scanning curves of Sensor-2 using the Nimmo model

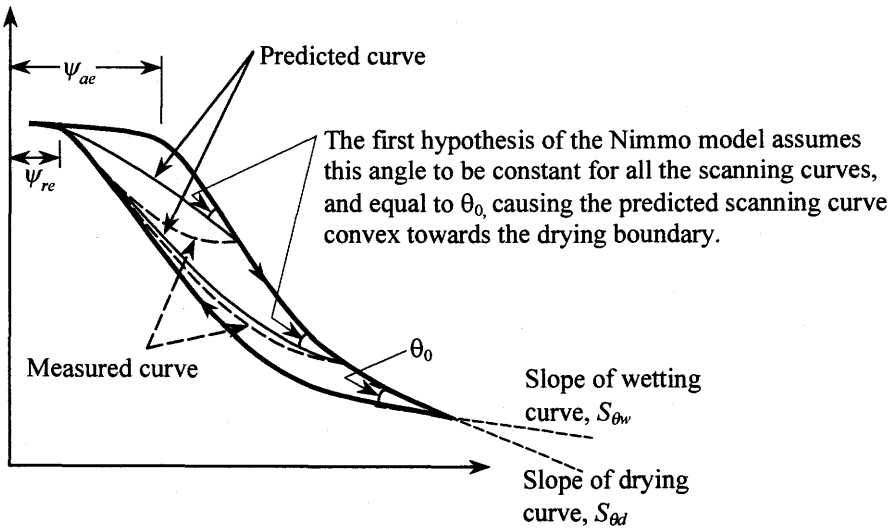

Figure 5.31 Schematic illustration of the first hypothesis of the Nimmo model that failed to predict the scanning curves.

5.5 PREDICTING THE CAPILLARY HYSTERESIS USING THE CURVE FITTING METHOD

It can be noted from the above description and testing of the hysteresis models that, most of the models available either require too much calibration data, or are too complicated for practical application, or the models fail in predicting the hysteresis processes. The experimental results show that the hysteresis curves of the sensor ceramics all have a similar shape. So it would seem logical to find a proper formulation that would fit the measured curves of sensors with known hysteresis curves and then to use the formulation to predict the hysteresis behavior of other sensors that have only limited calibration data. This section presents the results of curve fitting on the measured data.

5.5.1 The Fitting Equation

Equation 5.13 was again used as the fitting equation.

$$\theta(\psi) = \frac{ab + c\psi^{d}}{b + \psi^{d}} \quad \text{(M. Fredlund, personal communication)} \qquad (5.13)$$

The reason for using this equation is that the equation itself is simple and the parameters have clear and simple physical meanings.

Figure 5.32 shows the physical meanings of the parameters. The a parameter and c parameter are the values of water content at the point when ψ is 0 and at the point when ψ is infinitely large (i.e., 10^6 kPa), respectively. In other words, a is the water content at the upper point of the curve and c is the water content at the lower point of the curve. The b parameter determines the horizontal position of the curve, and the d parameter determines the slope of the linear portion of the curve.

It should be noted that the use of this equation is mainly for the sake of simplicity. As will be seen later in this section, this equation fits the measured data of both drying and wetting curves quite well in the suction range of 0 to 400 kPa. This equation may not fit well the portion beyond the point of residual saturation of the actual soil-water characteristic curve of the ceramic. The actual soil-water

characteristic curve bears a different shape than the curve of this equation beyond the point of residual saturation (Fredlund and Xing, 1994).

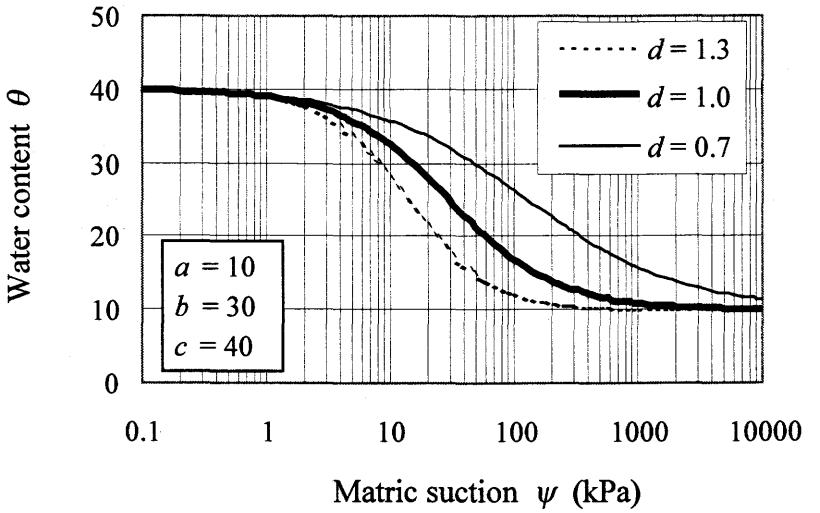

(a) Diagram illustrating the influence of change of d parameter on the shape of the curve

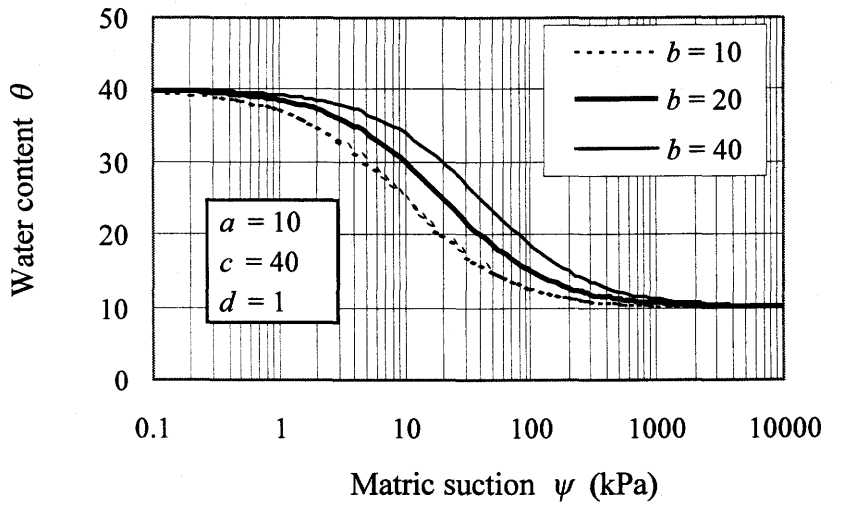

(b) Diagram illustrating the influence of change of b parameter on the shape of the curve

Figure 5.32 Diagrams illustrating the shape of the fitting curve using Eq. 5.13 and the physical meanings of the parameters of Eq. 5.13.

The portion of the curve before the point of residual saturation is usually considered when using the thermal conductivity sensor, since the sensitivity of measurement decreases significantly when the curve passes the point of residual

saturation. Therefore, it does not make a big difference even though the equation does not fit the actual soil-water characteristic curve in the high suction range. Should the portion of the curve in high suction range be considered, other forms of the fitting equation should be used.

It can also be seen from Fig. 5.32 that this fitting curve is symmetrical about a center point, (with coordinates, $\psi = \sqrt[d]{b}$, and $\theta = (a+c)/2$), in θ - $log(\psi)$ coordinate.

5.5.2 The Procedure to Fit the Measured Main Drying Curve and Predict the Main Wetting Curve and Primary Scanning Curves

It is generally easier to measure the main drying curve than to measure the main wetting curve. So the main drying curve is used to predict the other hysteresis curves. Eq. 5.13 is used to fit the measured main drying curve. Since the main wetting and main drying curves have the same water content at the point of ψ equal to 0 and ψ equal to $+\infty$, the two curves have the same values of parameters *a* and *c* when using Eq. 5.13. Given that the main drying curve is measured, only two of the four parameters, *b* and *d*, remain unknown for the main wetting curve. Theoretically, if two points are measured on the main wetting curve in addition to the main drying curve, the main wetting curve can be obtained.

The two points on the main wetting curve should be located such that one point is in the low suction range, (e.g., 10 kPa), the other point in the high suction range, (e.g., 100 kPa). The main wetting curve is adjusted to pass the two measured points by changing parameter *b* and *d*. For the ceramic of the Beta-97 sensor, the *d* parameter of the main wetting curve is close to the *d* parameter of the main drying curve and both are close to 1.

To fit the scanning curves, the following equations are used.

$$\theta_d(\psi,\psi_1) = \theta_d - (\frac{\psi_1}{\psi})^{\alpha}(\theta_d - \theta_w) \qquad (5.20a)$$

$$\theta_w(\psi,\psi_1) = \theta_w + (\frac{\psi}{\psi_1})^{\alpha}(\theta_d - \theta_w) \qquad (5.20b)$$

There is one more unknown parameter, α, in the above equations. The parameter α is an empirical parameter. It controls the degree of curvature of the scanning curves towards the corresponding hysteresis boundary.

The predicted main wetting curves and primary scanning curves of Ceramic-1, Ceramic-2, Sensor-1 and Sensor-2 are shown in Figs. 5.33 to 5.36. For the primary scanning curves of all the ceramics and sensors, α is assumed to be 1.8.

Figures 5.33 to 5.36 show that the above curve fitting method can make a relatively good prediction of the main wetting curve and the primary scanning curves. One value (i.e., a value of 1.8) of α parameter in the predicting equations of the primary scanning curves, (i.e., Eqs. 5.20a and 5.20b), was used for all three ceramics and six sensors.

Since the α value of 1.8 is suitable for all the three ceramic tips and the six sensors, it is reasonable to assume that it will not incur unacceptable error choosing 1.8 as the value of α parameter when predicting the primary scanning curves of other sensors with the same ceramic tips. The curve fitting method can be a useful method to predict the hysteresis curves of a porous material when there is a lack of proper predicting model.

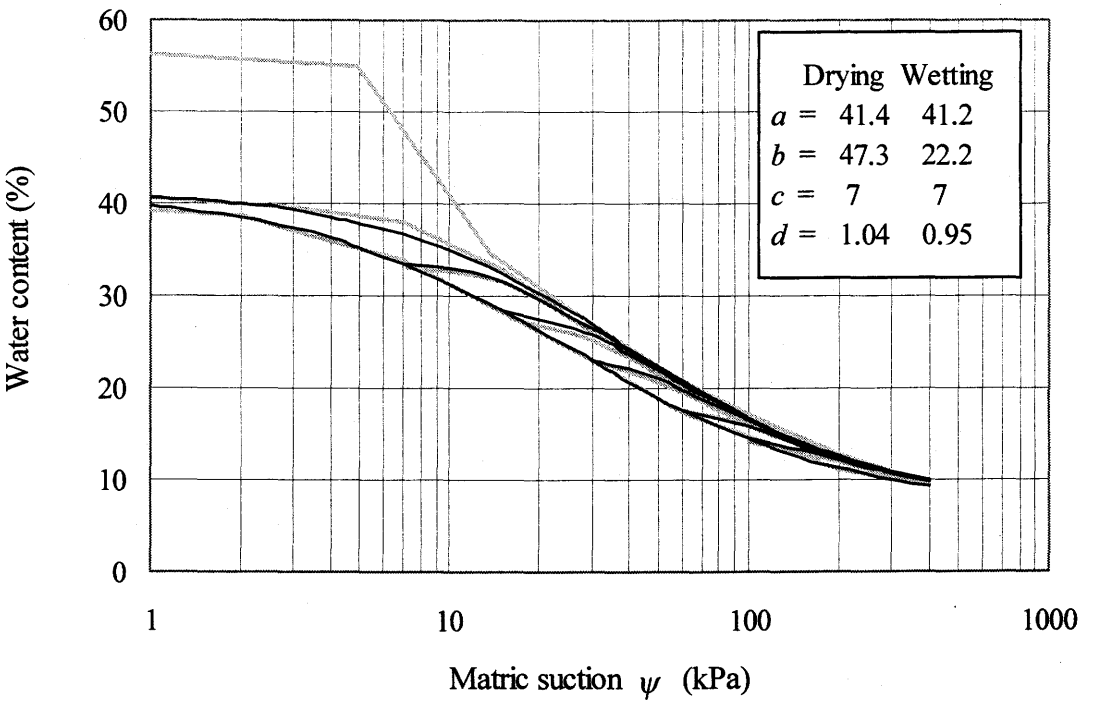

Figure 5.33a Main hysteresis loop and primary drying scanning curves of Ceramic-1 obtained using the curve fitting method

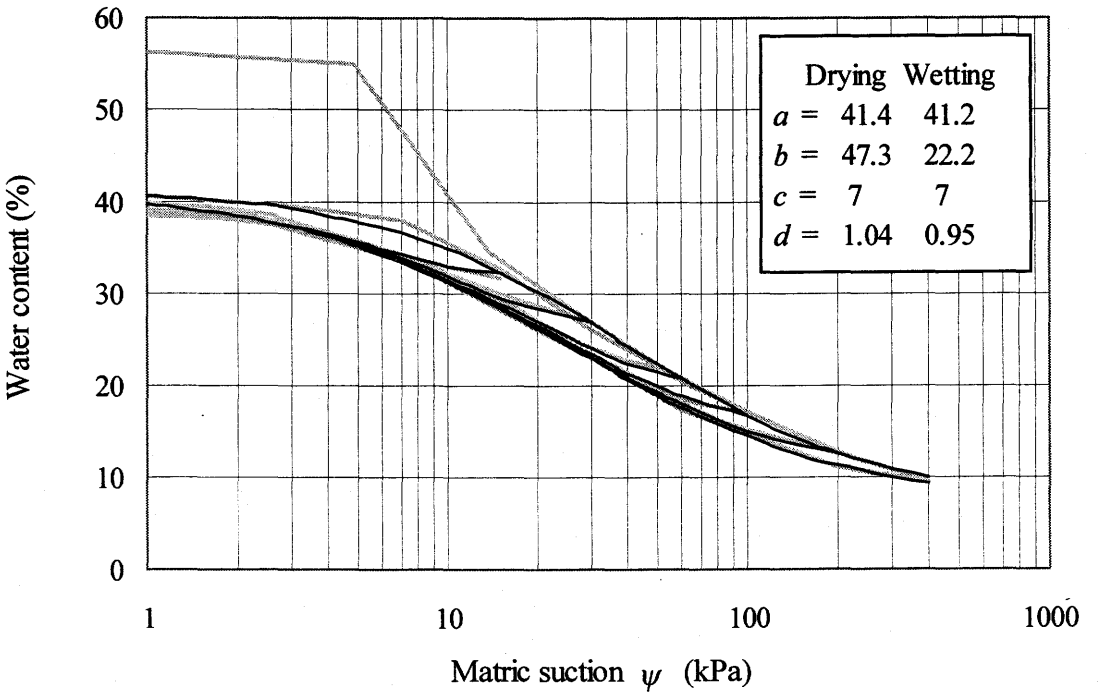

Figure 5.33b Main hysteresis loop and primary wetting scanning curves of Ceramic-1 obtained using the curve fitting method

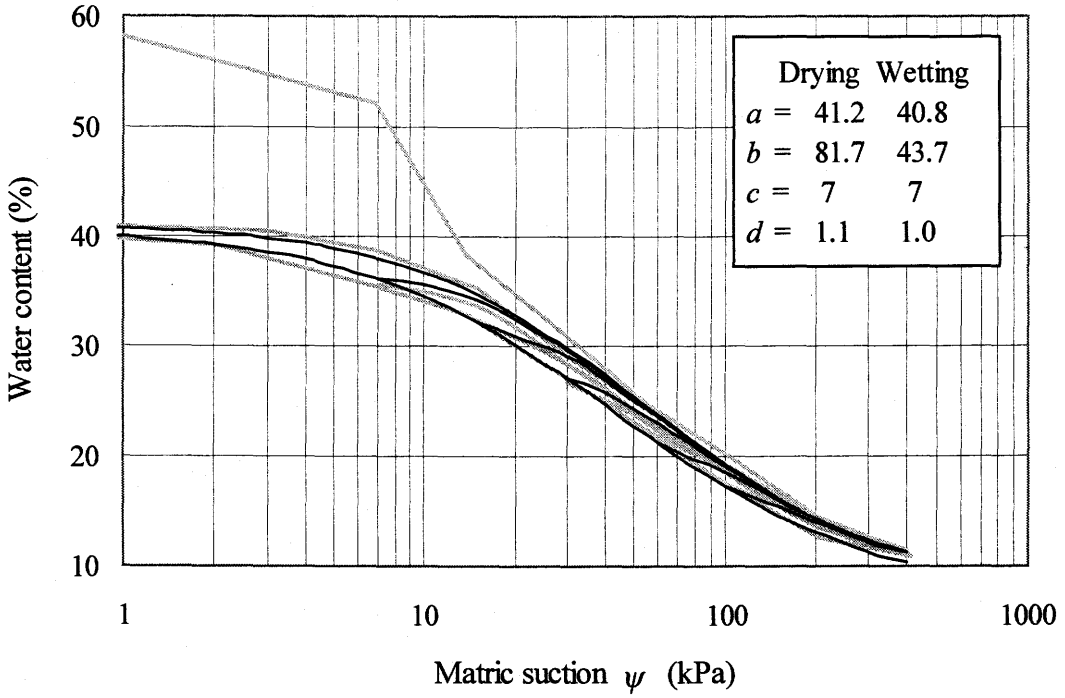

Figure 5.34a Main hysteresis loop and primary drying scanning curves of Ceramic-2 obtained using the curve fitting method

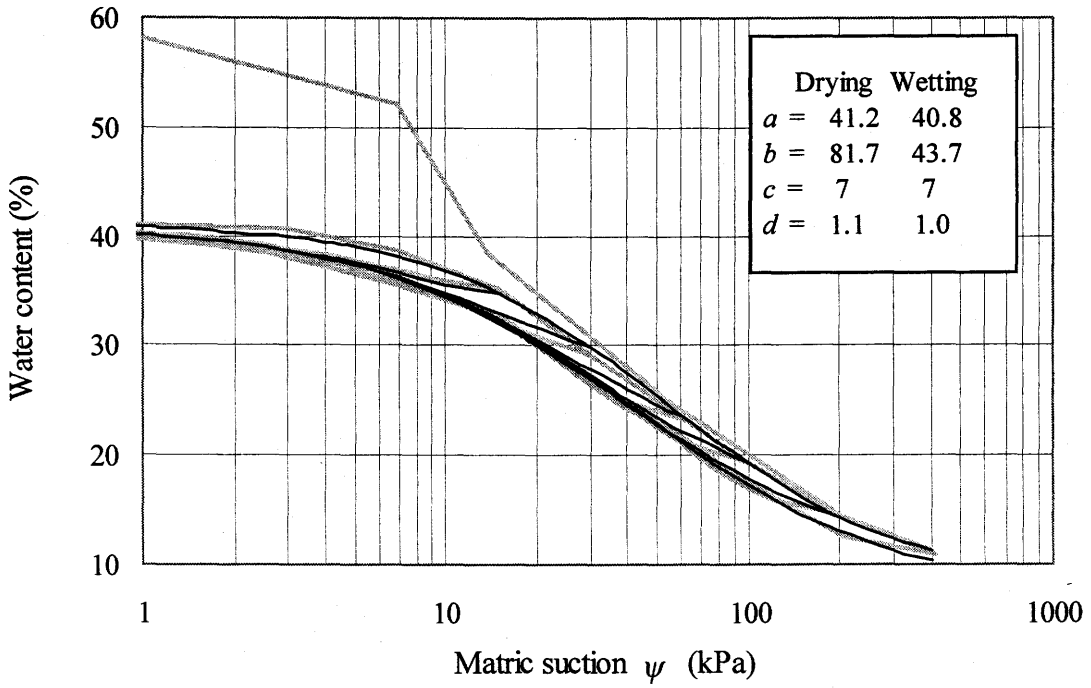

Figure 5.34b Main hysteresis loop and primary wetting scanning curves of Ceramic-2 obtained using the curve fitting method

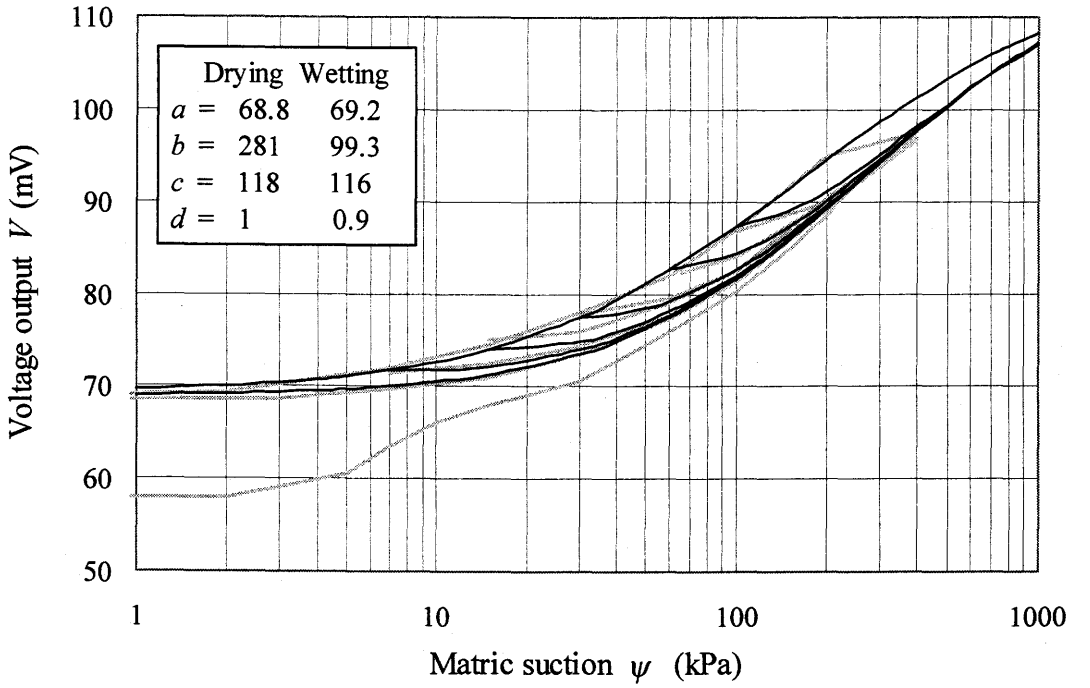

Figure 5.35a Main hysteresis loop and primary drying scanning curves of Sensor-1 obtained using the curve fitting method

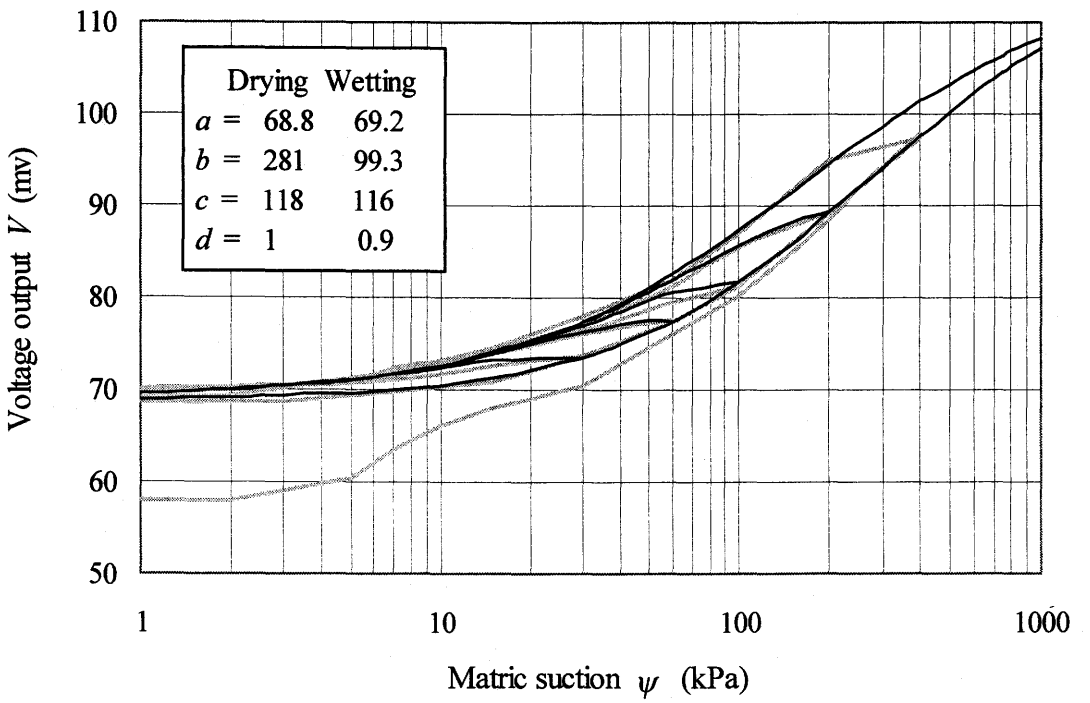

Figure 5.35b Main hysteresis loop and primary wetting scanning curves of Sensor-1 obtained using the curve fitting method

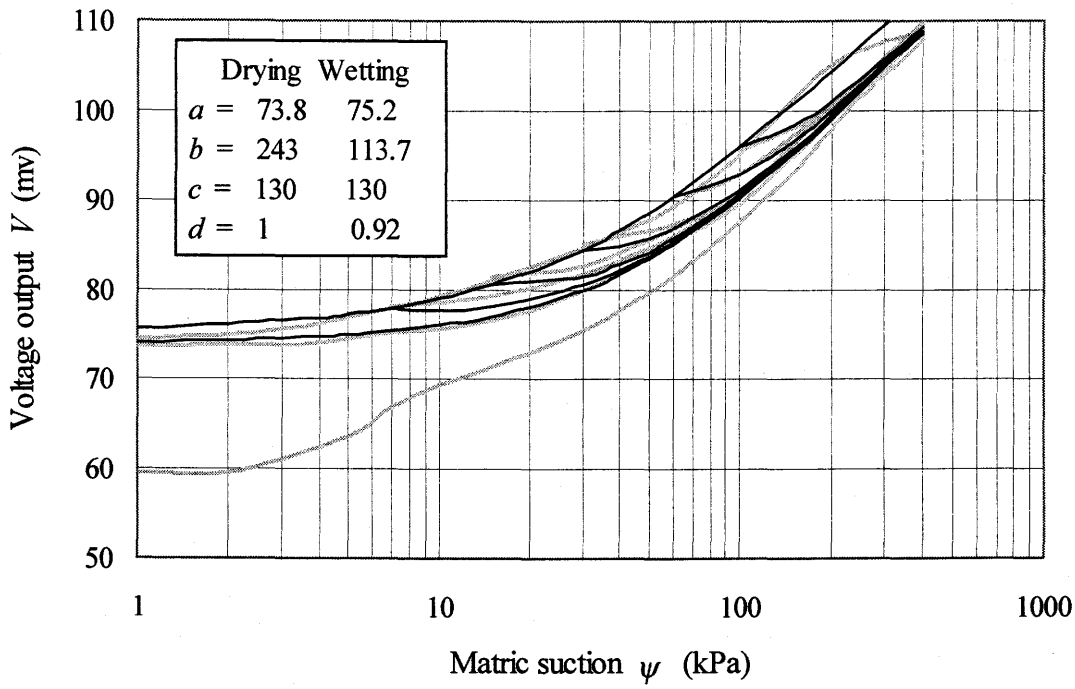

Figure 5.36a Main hysteresis loop and primary drying scanning curves of Sensor-2 obtained using the curve fitting method

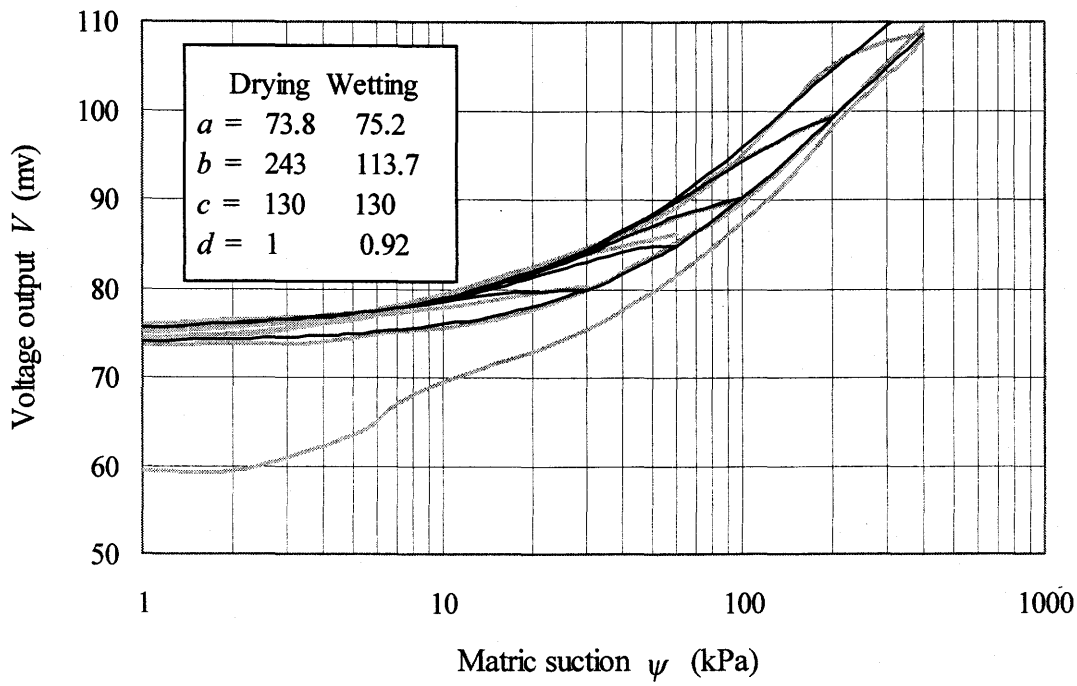

Figure 5.36b Main hysteresis loop and primary wetting scanning curves of Sensor-2 obtained using the curve fitting method

5.6 SUGGESTIONS FOR THE CALIBRATION OF THE SENSORS

Of all the models described in this chapter, only the Néel-Everett independent domain model can make a relatively good prediction of hysteresis curves of the Beta-97 sensors. The prediction using the Parlange model is also acceptable. Unfortunately, the Néel-Everett model requires too much measured data, while the Parlange model is theoretically defective (Mualem, 1978).

The predicted curves using the curve fitting method seem to fit the measured data reasonably well. The curve fitting method is simple and easy to apply. The test results (Chapter 3) show that the hysteresis properties of Beta-97 sensor are relatively consistent from sensor to sensor. When the hysteresis curves of typical sensors are known, the curve fitting procedure can be a relatively dependable means of predicting the hysteresis curves of other sensors. When there is a lack of a proper theoretical model for a porous material, the curve fitting procedure can be helpful.

The main drying curve and two points on the main wetting curve have to be measured in the calibration in order to use the curve fitting method. The following procedures are recommended in calibrating the Beta 97 sensors.

(1) saturate the sensor ceramic tip using the vacuum method, or by soaking the sensor tip in water and applying a positive pressure to the water,
(2) install the sensor in the pressure cell and apply a suction of 50 to 100 kPa,
(3) at equilibrium, reduce the suction to zero,
(4) at equilibrium, increase the suction in increments following the conventional calibration procedure to measure the main drying curve, and
(5) rewetting the sensor ceramic to obtain two points on the main wetting curve.

It should be noted that the above curve fitting equation (i.e., Eq. 5.13) and predicting equations (i.e., Eqs. 5.20a and 5.20b) might not apply to the hysteresis properties of other porous media. In such a case, new fitting equations may be necessary to apply the above procedure.

CHAPTER 6

Conclusions and Recommendations

The following conclusions and recommendations can be made from research conducted from this study.

6.1 CONCLUSIONS

1. A gap was observed between the initial drying curve and the main hysteresis loop in low suction range. The gap is believed to be caused by the large pores in the ceramic tip.
2. Unlike the hystersis loop of a coarse-grained porous material, the ceramic for the new sensor has a narrower capillary hysteresis loop.
3. The capillary hysteresis curves of the sensor ceramic appear to be quite reproducible and stable for a long period, under the conditions of the laboratory tests (i.e., distilled water and a relatively constant temperature). The thermal conductivity sensors appear to be a promising device for long-term monitoring of matric suction in the field.
4. The primary scanning curves starting from one boundary of the hysteresis loop show a tendency of quickly joining the other boundary of the hysteresis loop.
5. If the flooding of a dried sensor is not too long, (e.g., not longer than 10 days for the sensor of Beta-97), the drying and wetting cycles will always take place within the main hysteresis loop. If a sensor is flooded for a prolonged period, its wetting and drying will take place in the gap region between the initial drying curve and the main hysteresis loop, until a certain value of matric suction is reached, (e.g., 15 kPa for the Beta-97 sensor). In other words, as long as the ceramic tip of the sensor

does not experience a prolonged submergence, or the suction in the surrounding soil is higher than 15 kPa, the wetting and drying will remain within the main hysteresis loop.

6. The maximum relative error caused by the capillary hysteresis of the ceramic tip ranges from 24% to 40% if a single drying curve is used as the calibration curve. When the suction is low (i.e., lower than 50 kPa), the relative error can be up to 50%. The testing results show that the influence of the capillary hysteresis of the sensor ceramic tip is significant.
7. The conventional calibration curve is a drying curve, but it is neither the initial drying curve nor the main drying curve. Its position in the family of hysteresis curves is somewhat ambiguous. The conventional calibration curve does not reproduce the relationships between the voltage output and matric suction in the field.
8. The method of saturating a sensor ceramic tip by simply submerging the ceramic tip in water is not appropriate. The methods of applying a vacuum before submerging the ceramic tip or applying a positive pressure after submerging the tip are recommended.
9. Most of the models developed for simulating capillary hysteresis fail to reproduce the measured hysteresis data for the Beta-97 Sensor. Only the Néel-Everett independent domain model can make quite close predictions of the hysteresis curves for the ceramic. The Parlange model also works reasonably well. However, the Parlange model has been proved to be theoretically defective.
10. With the lack of a simple hypothetical model that can simulate the capillary hysteresis of the sensor ceramic, a curve fitting procedure seems to be the most effective method to estimate the hysteresis properties of the sensor ceramic.
11. The capillary hysteresis properties are consistent from sensor to sensor or from ceramic to ceramic for the Beta-97 thermal conductivity sensors.

6.2 RECOMMENDATIONS FOR FUTURE RESEARCH

1. The tests for this study were carried out in a room temperature with a maximum fluctuation of ±1.5°C. The studies conducted by Hopmans and Dane (1986) and Nimmo and Miller (1986) showed that the soil-water characteristic curves are temperature dependent. Also, temperature fluctuations may cause changes in the volume of the entrapped air in the ceramic sensor, and thus changes in the water content of the ceramic, even when the suction is maintained constant. Further studies on the influence of the ambient temperature and change in ambient temperature on the output of the sensor should be conducted.
2. The water used in the tests of this study was distilled water. A kind of green material was found growing on the surface of the ceramic tip during the tests. Therefore a small amount of bleach was added into the water to prevent bacteria growth. Further tests are recommended to study the influence of bacteria growth on the capillary hysteresis properties, especially on the reproducibility of the hysteresis curves.
3. It is impracticable to measure the whole family of hysteresis curves during calibration. A proper model to predict the hysteresis curves from a limited amount of measured data for a fine-grained porous material should be included in future research. The Parlange model deserves more study.
4. It may be helpful to conduct pore-size distribution tests to better understand the capillary hysteresis properties of the sensor ceramic. The pore-size distribution tests also provide useful information on further improvement of the sensor ceramic.

References

S. Al-Khafafa and R. J. Hanks (1974), "Evaluation of the Filter Paper Method for Estimating Soil Water Potential," *Soil Sci.*, vol. 117, pp. 194-199.

M. E. Bloodworth and J. B. Page (1957), "Use of Thermistor for the Measurement of Soil Moisture and Temperature," *Soil Sci. Soc. Amer. Proc.*, vol. 21, pp. 11-15.

J. W. Cary (1967), "Experimental Measurements of Soil-Moisture Hysteresis and Entrapped Air," *Soil Sci.*, vol. 104, pp. 174-180.

R. E. Collins (1961), *Flow of Fluids through Porous Materials*, Reinhold Publishing Co., NewYork, 270 p.

R. W. Cummings and R. F. Chandler (1940), "A Field Comparison of the Electrothermal and Gypsum Block Electrical Resistance Methods with the Tensiometer Method for Estimating Soil Moisture *in situ*," *Soil. Sci. Soc. Amer. Proc.*, vol. 5, pp. 80-85.

R. H. Dettre and R. E. Johnson (1964), "Contact Angle Hysteresis II - Contact Angle Measurement on Rough Surface," *Advances in Chemistry Series No. 43*, Amer. Chem. Soc., Washington, D. C.

F. A. L. Dullien (1979), *Porous media: Fluid transport and pore structure*, Academic Press Inc., New York, 396 p.

J. A. Enderby (1955), "The Domain Model of Hysteresis - Part 1: Independent Domains," *Trans. Faraday Soc.*, vol. 51, pp. 835-848.

J. A. Enderby (1956), "The Domain Model of Hysteresis - Part 2: Interacting Domains," *Trans. Faraday Soc.*, vol. 52, pp. 106-120.

D. H. Everett and W. I. Whitton (1952), "A General Approach to Hysteresis," *Trans. Faraday Soc.*, vol. 48, pp. 749-752.

D. H. Everett and F. W. Smith (1954), "A General Approach to Hysteresis - Part 2: Development of the Domain Theory," *Trans. Faraday Soc.*, vol. 50, pp. 187-197.

D. H. Everett (1954), "A General Approach to Hysteresis - Part 3: A Formal Treatment of the Independent Domain Model of Hysteresis," *Trans. Faraday Soc.*, vol. 50, pp. 1077-1096.

D. H. Everett (1955), "A General Approach to Hysteresis - Part 4: Am Alternative Formulation of the domain Model," *Trans. Faraday Soc.*, vol. 51, pp. 1551-1557.

D. H. Everett (1967), "Adsorption Hysteresis," in *Solid Gas Interface*, E. A. Flood Ed., Marcek Dekker, NewYork, pp. 1055-1113.

D. G. Fredlund (1992), "Background, Theory, and Research Related to the Use of Thermal Conductivity Sensors for Matric Suction Measurement," Published in *Advance in Measurement of Soil Physical Properties: Bringing Theory into Practice*, SSSA Special Publication No. 30, pp. 249-261.

D. G. Fredlund, J. K.-M. Gan and W.-X. Li (1994), "Thermal Conductivity Suction Sensor - Design Considerations," in *Proc. 13th Int. Conf. Soil Mech. Foundation Eng.*, New Delhi, India, pp. 291-296.

D. G. Frelund and N. R. Morgenstern (1977), "The Stress State Variables for Unsaturated Soils," *ASCE J. Geotech. Eng. Div. GT5*, vol. 103, pp. 447-466.

D. G. Fredlund and H. Rahardjo (1988), "State-of-Development in the Measurement of Soil Suction," in *Proc. Int. Conf. Eng. Problems of Reginal Soils*, Beijing, China, pp. 582-588.

D. G. Fredlund, P. J. Sattler, and J. Gan (1992), "*In situ* Suction Measurement Using Thermal Conductivity Sensors," in *Proc. 7th Int. Conf. Expansive Soils*, Dallas, Texas, USA.

D. G. Fredlund and D. K. H. Wong (1989), "Calibration of Thermal Conductivity Sensors for Measuring Soil Suction," *ASTM Geotech. Testing J.*, vol. 12, no. 3, pp. 188-194.

D. G. Fredlund and A. Xing (1994), "Equations for the Soil-Water Characteristic Curve," *Can. Geotech. J.*, vol. 31, pp. 521-532.

E. L. Greacen, G. R. Walker and P. G. Cook (1987), "Evaluation of the Filter Paper Method for Measuring Soil Suction," in *Proc. Int. Conf. on Measurement of Soil and Plant Water Status*, Utah State Univ., Logan, UT., vol. 1, pp. 137-143.

W. B. Haines (1930), "Studies in the Physical Properties of Soil - V: The Hysteresis Effect in Capillary Properties and the Modes of Water Distribution Associated therewith," *J. Agric. Sci.*, vol. 20, pp. 97-116.

J. W. Hopmans and J. H. Dane (1986), "Temperature Dependence of Soil Water Retention Curves," *Soil Sci. Soc. Am. J.*, vol. 50, pp. 562-567.

S. Iwata, T. Tabuchi and B. P. Warkentin (1988), *Soil-Water Interaction: Mechanisms and Applications*, Marcel Dekker, NewYork, pp. 40-44.

L. N. Johnson (1942), "Water Permeable Jacketed Thermal Radiators as Indicators of Field Capacity and Permanent Wilting Percentage in Soils," *Soil Sci.*, vol. 54, pp.123-126.

R. E. Johnson and R. H. Dettre (1964), "Contact Angle Hysteresis I - Study of an Idealized Rough Surface," *Advances in Chemistry Series No. 43*, Amer. Chem. Soc., Washington, D. C.

R. K. C. Lee (1983), "Measurement of Soil Suction by MCS Sensor," M.Sc. thesis, Univ. of Saskatchewan, Saskatoon, Sask., Canada, 162 pp.

R. K. C. Lee and D. G. Fredlund (1984), "Measurement of Soil Suction Using the MCS6000 Gauge," in *Proc. 5th Int. Conf. Expansive Soils*, Inst. of Eng., Adelaide, Australia, pp. 50-54.

J. Loi, J. Gan, and D. G. Fredlund (1989), "Monitoring Soil Suction in an Indoor Test Track Facility," presented to 71st Annual Meeting of the Transportation Bpard, Session #228 on Environmental Factors Except Frost, Washington, DC.

E. E. Miller and R. D. Miller (1956), "Physical Theory for Capillary Flow Phenomena," *J. Appl. Phys.*, vol. 27, pp. 324-332.

E. E. Miller and R. D. Miller (1955), "Theory of Capillary Flow," *Soil Sci. Soc. Amer. Proc.*, vol. 19, pp. 267-275.

N. R. Morrow (1974), "The Effects of Surface Roughness on Contact Angle with Special Reference to Petroleum Recovery," *J. Can, Pet. Tech.*, vol. 14, pp. 42-53.

N. R. Morrow (1976), "Capillary Pressure Correlations for Uniformly Wetted Porous Media," *J. Can, Pet. Tech.*, vol. 14, pp. 49-69.

N. R. Morrow and C. C. Hurris (1965) "Capillary Equilibrium in Porous Materials," *Soc. Petr. J.*, vol. 5, pp. 12-14.

Y. Mualem (1973), "Modified Approach to Capillary Hysteresis Based on a Similarity Hypothesis," *Water Resour. Res.*, vol. 9, no. 5, pp. 1324-1331.

Y. Mualem (1974), "A Conceptual Model of Hysteresis," *Water Resour. Res.*, vol. 10, no. 3, pp. 514-520.

Y. Mualem (1977), "Extension of the Similarity Hypothesis Used for Modeling the Soil Water Characteristics," *Water Resour. Res.*, vol. 13, no. 4, pp. 773-780.

Y. Mualem (1984a), "A Modified Dependent Domain Theory of Hysteresis," *Soil Sci.*, vol. 137, no. 5, pp. 283-291.

Y. Mualem (1984b), "Prediction of the Soil Boundary wetting Curve," *Soil Sci.*, vol. 137, no. 6, pp.379-390.

Y. Mualem and G. Dangan (1975), "A Dependent Domain Model of Capillary Hysteresis," *Water Resour. Res.*, vol. 11, no. 3, pp. 452-460.

Y. Mualem and E. E. Miller (1979), "A Hysteresis Model Based on an Explicit Domain-Dependence Function," *Soil Sci. Soc. Amer. J.*, vol. 43, pp. 1067-1073.

Y. Mualem and H. J. Morel-Seytoux (1978), "Analysis of a Capillary Hysteresis Model Based on a One-Variable Distribution Function," *Water Resour. Res.*, vol. 14, no. 4, pp. 605-610.

L. Néel (1942), "Théorie des lois d'aimantation de Lord Rayleigh, 1," *Cahiers Phys.*, vol. 12, pp. 1-20.

L. Néel (1943), "Théorie des lois d'aimantation de Lord Rayleigh, 2," *Cahiers Phys.*, vol. 13, pp. 18-30.

J. R. Nimmo (1992), "Semi-empirical Model of Soil Water Hysteresis," *Soil Sci. Soc. Am. J.*, vol. 56, pp. 1723-1730.

J. R. Nimmo and E. E. Miller (1986), "The Temperature Dependence of Isothermal Moisture vs. Potential Characteristics of Soils," *Soil Sci. Soc. Am. J.*, vol. 50, pp. 1105-1113.

Jean-Yves Parlange (1976), "Capillary Hysteresis and the Relationship Between Drying and Wetting Curves," *Water Resour. Res.*, vol. 12, no. 2, pp. 224-228.

G. Pavlakis and L. Barden (1971), "Hysteresis in the Moisture Characteristics of Clay Soil," *J. Soil Sci.*, vol. 23, no. 3, pp. 350-361.

C. J. Phene, G. J. Hoffman and S. L. Rawlins (1971a), "Measuring Soil Matric Potential in situ by Sensing Heat Dissipation within a Porous Body: I. Theory and Sensor Construction," *Soil Sci. Soc. Amer. Proc.*, vol. 35, pp. 27-33.

C. J. Phene, S. L. Rawlins and G. J. Hoffman (1971b), "Measuring Soil Matric Potential *in situ* by Sensing Heat Dissipation within a Porous Body: II. Experimental Results," *Soil Sci. Soc. Amer. Proc.*, vol. 35, pp. 225-229.

J. R. Philip (1964), "Similarity Hypothesis for Capillary Hysteresis in Porous Materials," *J. Geophys. Res.*, vol. 69, no. 8, pp. 1553-1562.

A. Poulovassilis (1962), "Hysteresis of Pore Water - An Application of the Concept of Independent Domains," *Soil Sci.*, vol. 92, pp. 405-412.

A. Poulovassilis (1970a), "Hysteresis of Pore Water in Gramular Porous Bodies," *Soil Sci.*, vol. 109, no. 1, pp. 5-12.

A. Poulovassilis (1970b), "The Effect of the Entrapped Air on the Hysteresis Curves of a Porous Body and on its Hydraulic Conductivity," *Soil Sci.*, vol. 109, no. 3, pp. 154-162.

A. Poulovassilis and W. M. El-Ghamry (1978), "The Dependent Domain Theory Applied to Scanning Curves of Any Order in Hysteretic Soil Water Relationships," *Soil Sci.*, vol. 126, no. 1, pp. 1-8.

A. Poulovassilis and E. C. Childs (1971), "The Hysteresis of Pore Water: The Non-Independence of Domains," *Soil Sci.*, vol. 112, no. 5, pp. 301-312.

H. Rahardjo, J. Loi and D. G. Fredlund (1989), "Typical Matric Suction Measurements in the Laboratory and in the Field Using Thermal Conductivity Sensor," In *Proc. Indian Geotech. Conf. Geotechniques of Problematic Soils and Rocks: Characterization, Design, and Ground Improvements*, Visakhapatnam, India, vol. 1, pp. 127-133.

C. F. Reece (1996), "Evaluation of a Line Heat Dissipation Sensor for Measuring Soil Matric Potential," *Soil Sci. Soc. Amer. J.*, vol. 60, pp. 1022-1028.

L. A. Richards and M. Fireman (1943), "Pressure-plate Apparatus for Measuring Moisture Sorption and Transmission by Soils," *Soil Sci.*, vol. 56, pp. 395-404.

L. A. Richards and L. R. Weaver (1944), "Moisture Retention by Some Irrigation Soils as Related to Soil Moisture Tension," *J. Agri. Res.*, vol. 69, No. 6.

D. A. Rose (1971). "Water Movement in Dry Soils - II: an Analysis of Hysteresis," *J. Soil Sci.*, vol. 22, no. 4, pp. 490-507.

M. B. Russel and L. A. Richards (1938), "The Determination of Soil Moisture Energy Relations by Centrifugation," *Soil Sci. Soc. Am. proc.*, vol. 3, pp. 65-69.

J. M. Royer and G. Vachaud (1975), "Field Determination of Hysteresis in Soil-Water Characteristics," *Soil Sci. Soc. Am. proc.*, vol. 39, no. 2, pp. 221-223.

P. J. Sattler and D. G. Fredlund (1989), "Use of Thermal Conductivity Sensors to Measure Matric Suction in the Laboratory," *Can. Geotech. J.*, vol. 26, pp. 491-498.

B. Shaw and L. D. Baver (1939), "An Electrothermal Method for Following Moilture Change of the Soil *in situ*," *Proc. Soil. Sci. Soc. Amer.*, vol. 4, pp. 73-78.

T. Talsma (1970), "Hysteresis in Two Sands and the Independent Domain Model," *Water Resour. Res.*, vol. 6, no. 3, pp. 964-970.

G. C. Topp (1969), "Soil Water Hysteresis Measured in a Sandy Loam Compared with the Hysteretic Domain Model," *Soil Sci. Soc. Amer. Proc.*, vol 33, pp. 645-651.

G. C. Topp (1971a), "Soil Water Hysteresis in Silt Loam and Clay Loam Soils," *Water Resour. Res.*, vol. 7, no. 4, pp. 914-920.

G. C. Topp (1971b), "Soil-Water Hysteresis: The Domain Theory Extended to Pore Interaction Conditions," *Soil Sci. Soc. Amer. Proc.*, vol 35, pp. 219-225.

G. C. Topp and E. E. Miller (1966), "Hysteretic Moisture Characteristics and Hydraulic Conductivity for Glass-Bead Media," *Soil Sci. Soc. Amer. Proc.*, vol. 30, pp. 156-162.

M. Tschapek, C. O. Scoppa and C. Wasowski (1978), "The Surface Tension of Soil Water," *J. Soil Sci.*, vol. 29, pp. 17-21.

E. Tzimas (1979), "The Measurement of Soil Water Hysteretic Relationships on a Soil Monilith," *J. Soil Sci.*, vol. 30, no. 4, pp. 529-534.

G. Vachaud and Jean-Louis Thony (1971), "Hysteresis During Infiltration and Redistribution in a Soil Column at Different Initial Water Content," *Water Resour. Res.*, vol. 7, no. 1, pp. 111-127.

P. van der Raadt (1988), "Field Measurement of Soil Suction Using Thermal Conductivity Matric Potential Sensors," M.Sc. thesis, Univ. of Saskatchewan, Saskatoon, Sask., Canada, 210 pp.

P. van der Raadt, D. G. Fredlund, A. W. Clifton, M. J. Klassen, and W. E. Jubien (1987), "Soil Suction Measurement at Several Sites in Western Canada," *Transportation Res. Rec. 1137, Soil Mech. Considerations in Arid and Semi-Arid Areas*, Transportation Res. Board, Washinton, DC, pp. 24-35.

K. K. Watson, R. J. Reginato and R. D. Jackson (1975), "Soil Water Hysteresis in a Field Soil," *Soil Sci. Soc. Am. proc.*, vol. 39, no. 2, pp. 242-246.

G. W. Wilson (1990), "Soil Evaporative Fluxes for Geotechnical Engineering Problems," Ph.D dissertation, University of Saskatchewan, Saskatoon, Canada, 464p.

D. K. H. Wong, D. G. Fredlund, E. Imre and G. Putz (1989), "Evaluation of AGWA-II Thermal Conductivity Sensors for Soil Suction Measurement," Transportation Research Board, National Research Council, Washington, D. C., pp. 131-143.

A. Xing and D. G. Fredlund (1994), "Numerical Modeling of a Thermal Conductivity Matric Suction Sensor," *ASTM Geotechnical Testing J.*, vol. 17, pp. 415-424.

APPENDIX A

Experimental Data

Table A-1 The initial drying curve, main hysteresis loop and primary scanning curves of Ceramic-1

Initial drying curve and main hysteresis loop		Primary drying scanning curves		Primary wetting scanning curves	
Suction (kPa)	Water content (%)	Suction (kPa)	Water content (%)	Suction (kPa)	Water content (%)
0.1	56.243	100	14.168	200	12.569
4.89	55.02	200	11.900	100	15.246
13.79	34.543	400	9.521	50	19.298
27.58	27.899			30	23.053
55.16	21.503	60	17.662	15	29.522
103.42	16.892	100	15.915	7	34.243
206.85	12.603	200	12.235	4	36.176
400	9.484	400	9.595	2	38.035
200	11.157			0.1	39.931
100	14.726	32	22.793		
60	17.477	60	19.595	100	17.109
30	23.053	100	16.101	60	18.745
15	28.295	200	12.160	30	23.429
7	33.983	400	9.521	15	28.337
4	35.879			7	34.211
2	38.667	16	27.700	4	36.813
0.1	40.897	30	25.284	2	39.230
1	40.594	60	20.228	0.1	42.241
3	39.512	100	16.956		
7	38.121	200	12.755	50	21.942
15	32.781	400	9.484	30	24.173
30	26.091			15	29.378
50	22.209	7.2	33.016	7	34.397
60	20.51	15	31.529	4	35.847
100	17.109	30	26.064	2	38.672
200	12.569	60	19.819	0.1	40.531
400	9.484	100	16.213		
		200	11.900	30	26.994
		400	9.521	15	29.968
				7	34.280
		3.5	37.1055	4	36.102
		6.7	35.4697	2	38.555
		14.4	32.5328	0.1	40.414
		29	26.0642		
		60	19.8929	15	31.418
		86	18.0713	5.5	35.024
		200	12.9038	4	36.027
		400	9.595	2	38.481
				0.1	39.633

Table A-2 The initial drying curve, main hysteresis loop and primary scanning curves of Ceramic-2

Initial drying curve and main hysteresis loop		Primary drying scanning curves		Primary wetting scanning curves	
Suction (kPa)	Water content (%)	Suction (kPa)	Water content (%)	Suction (kPa)	Water content (%)
0.1	59.001	15	35.269	0.1	41.207
6.9	52.141	10	35.918	1	41.062
13.79	38.378	5	37.670	3	40.616
27.58	31.700	2	39.575	7	38.700
55.16	24.734	1	40.304	15	35.269
103.43	19.912	0.1	41.801	30	29.122
206.85	14.414			60	23.579
413.7	11.032	30	29.121	100	19.257
206.85	12.623	15	32.187	200	14.572
103.43	17.272	7	36.262	400	11.190
55.16	22.391	4	37.570		
27.58	27.600	2	39.008	7	35.688
13.79	33.300	1	40.017	15	33.606
6.9	35.500	0.1	41.100	30	28.439
4	37.155			60	22.454
2	39.203	60	23.234	100	18.959
0.1	41.197	30	26.468	200	14.535
		15	32.565	400	11.413
0.1	41.197	7	35.836		
1	41.028	4	37.212	15	32.342
3	40.616	2	38.804	30	28.401
7	38.700	0.1	42.119	60	22.677
15	35.269			100	18.587
30	29.122	100	19.257	200	13.680
60	23.579	60	21.450	400	11.078
100	19.257	30	26.877		
200	14.572	15	32.665	30	26.766
400	11.190	8	35.167	60	22.788
		4	37.212	100	19.033
		2	39.145	200	14.238
		0.1	41.933	400	10.967
		200	14.572	50	22.974
		100	16.952	100	18.959
		50	22.677	200	14.320
		30	26.431	400	11.152
		15	32.751		
		7	35.502	100	17.532
		4	37.175	200	14.141
		2	39.368	400	10.929
		0.1	41.004		

Table A-3 The initial drying curve, main hysteresis loop and primary scanning curves of Ceramic-3

Initial drying curve and main hysteresis loop		Primary drying scanning curves		Primary wetting scanning curves	
Suction (kPa)	Water content (%)	Suction (kPa)	Water content (%)	Suction (kPa)	Water content (%)
0.1	56.575	100	16.022	200	12.634
1	56.575	200	12.855	100	15.175
2	56.427	400	9.466	60	19.374
5	55.212			30	24.788
7	49.834	50	20.847	15	29.650
10	39.632	100	17.753	7	33.775
20	33.812	200	13.333	4	34.807
40	27.661	400	9.613	2	36.280
80	20.994			0.1	38.637
150	15.691	30	24.862		
250	11.786	60	21.768	103	17.827
400	9.392	100	17.827	60	19.742
250	10.166	200	12.855	30	24.567
150	12.855	400	9.540	15	30.276
80	17.901			7.3	33.812
40	22.468	15	30.497	0.1	40.368
20	28.324	30	27.366		
10	32.560	60	21.878	60	22.026
5	34.807	100	17.827	30	25.193
2	37.127	200	12.634	15	29.945
0.1	38.895	400	9.466	7	33.554
				2	36.280
0.1	39.595	7	33.481	0.1	38.232
2	39.227	15	31.971		
4	38.490	30	28.361	30	28.766
7	37.017	60	22.136	15	30.829
15	33.333	100	17.974	7	33.959
30	28.766	200	12.634	2	37.017
60	22.652	400	9.429	0.1	38.158
103	17.827				
200	12.634			15	32.855
400	9.392			7	33.775
				4	34.807
				0.1	38.343
				7	36.280
				4	37.017
				2	37.753
				0.1	38.490

Table A-4 The initial drying curve, main hysteresis loop and primary scanning curves of Sensor-1

Initial drying curve and main hysteresis loop		Primary drying scanning curves		Primary wetting scanning curves	
Suction (kPa)	Sensor output (mv)	Suction (kPa)	Sensor output (mv)	Suction (kPa)	Sensor output (mv)
0.1	58.0	100	86.8	200	89.4
1	58.0	200	90.0	100	85.5
2	58.0	400	97.6	60	81.4
5	60.5			30	77.3
7	63.5	65	82.4	15	74.4
10	66.0	100	84.0	7	71.7
15	68.0	200	90.0	4	70.7
30	70.5	400	97.5	0.1	68.2
60	76.0				
100	80.3	30	77.9	100	81.2
150	85.0	60	79.5	60	79.6
200	88.5	100	82.5	30	76.5
250	92.0	200	89.6	15	74.1
400	97.5	400	96.7	7	71.4
200	95.0			4	70.4
100	87.0	15	75.2	0.1	69.0
60	82.0	30	76.0		
30	78.0	60	79.0	60	77.6
15	74.5	100	82.5	30	76.0
7	71.9	200	90.5	15	74.0
2	69.3	400	97.0	7	72.3
0.1	68.4			4	70.6
3	68.6	7	71.5	0.1	69.4
7	69.7	15	72.5		
15	70.9	30	74.4	30	73.8
30	73.6	60	77.7	15	72.2
60	77.4	100	81.8	7	71.0
100	81.3	200	89.5	4	70.8
200	89.1	400	98.0	2	70.0
400	97.9			0.1	69.0

Table A-5 The initial drying curve, main hysteresis loop and primary scanning curves of Sensor-2

Initial drying curve and main hysteresis loop		Primary drying scanning curves		Primary wetting scanning curves	
Suction (kPa)	Sensor output (mv)	Suction (kPa)	Sensor output (mv)	Suction (kPa)	Sensor output (mv)
0.1	59.5	100	95.5	200	99.5
1	59.5	200	100.4	100	94.5
2	59.5	400	109.4	60	89.7
5	63.5			30	84.2
7	67.0	65	90.6	15	81.0
10	69.5	100	92.8	7	77.7
15	71.5	200	100.7	4	76.3
30	75.5	400	109.5	0.1	73.1
60	81.5				
100	87.5	30	85.1	100	90.0
150	93.0	60	87.3	60	87.9
200	98.0	100	90.5	30	84.5
250	101.5	200	99.3	15	81.2
400	108.5	400	108.6	7	77.9
200	105.0			4	76.5
100	95.0	15	81.4	0.1	73.7
60	90.0	30	82.6		
30	84.6	60	86.7	60	86.1
15	81.0	100	90.5	30	84.0
7	77.9	200	100.5	15	81.1
2	75.0	400	109	7	78.2
0.1	73.8			4	77.0
3	73.9	7	78	0.1	74.6
7	75.2	15	79.3		
15	76.6	30	81.6	30	80.4
30	80.0	60	86	15	78.8
60	85.2	100	90.5	7	77.2
100	89.5	200	100.2	4	76.0
200	99.0	400	110.0	2	74.8
400	109.5			0.1	73.0

Table A-6 The initial drying curve, main hysteresis loop and primary scanning curves of Sensor-3

Initial drying curve and main hysteresis loop		Primary drying scanning curves		Primary wetting scanning curves	
Suction (kPa)	Sensor output (mv)	Suction (kPa)	Sensor output (mv)	Suction (kPa)	Sensor output (mv)
0.1	51.0	100	87.8	200	92.1
1	51.0	200	92.4	100	88.1
2	51.0	400	101.2	60	83.6
5	52.5			30	79.1
7	58.0	65	83.6	15	75.6
10	63.5	100	86	7	71.6
15	66.0	200	92.7	4	69.7
30	70.8	400	101.1	0.1	65.7
60	77.5				
100	82.5	30	78.9	100	85.1
150	87.5	60	81.5	60	82.6
200	92.0	100	85.3	30	78.7
250	94.5	200	92.5	15	75.2
400	101.1	400	100.5	7	70.9
200	96.2			4	69.5
100	87.7	15	75.5	0.1	65.6
60	83.2	30	77.4		
30	78.9	60	81.8	60	80.6
15	74.6	100	85.6	30	78.3
7	71.4	200	93.5	15	75.2
2	67.7	400	101.0	7	71.8
0.1	66.6			4	69.8
3	67.4	7	72.1	0.1	65.9
7	69.6	15	73.0		
15	71.1	30	76.4	30	76.0
30	75.8	60	80.3	15	73.8
60	80.4	100	85.1	7	71.2
100	84.9	200	92.4	4	70.0
200	92.5	400	101.5	2	68.0
400	101.4			0.1	66.5

Table A-7 The initial drying curve, main hysteresis loop and primary scanning curves of Sensor-4, 5 and 6

Initial drying curve and main hysteresis loop				Primary drying scanning curves			
Suction (kPa)	Sensor output (mv)			Suction (kPa)	Sensor output (mv)		
	Sensor-4	Sensor-5	Sensor-6		Sensor-4	Sensor-5	Sensor-6
0.1	65.4	59.2	55.0	7	77.0	71.0	66.0
3	65.4	59.2	55.0	15	77.8	71.5	66.6
7	68.6	64.4	58.4	30	80.4	73.8	69.0
15	72.0	67.6	62.2	60	85.6	78.5	73.6
30	76.6	71.5	66.1	100	91.0	83.5	78.2
60	83.4	77.3	71.5	200	101.6	92.4	86.3
100	89.4	82.3	76.3	400	111.6	102.2	94.9
200	99.6	91.4	84.7				
400	110.6	101.5	93.8	15	79.4	72.8	67.9
200	105.2	96.8	89.6	30	81.0	74.5	69.5
100	96.0	87.5	81.5	60	86.5	79.2	74.2
50	88.8	81.4	75.6	100	91.6	83.9	78.5
30	84.2	77.1	71.7	200	101.5	92.6	87.0
15	79.5	72.8	67.6	400	111.2	101.7	95.0
7	77.0	71.0	65.7				
4	75.2	69.6	64.4	30	83.9	77.0	72.0
0.1	72.8	67.1	62.4	60	87.0	80.0	74.8
4	74.4	68.5	63.5	100	91.6	83.9	78.5
7	75.0	69.3	64.3	200	101.4	93.0	86.3
15	76.5	70.5	65.5	400	111.8	103.0	94.9
30	79.5	73.0	68.5				
60	85.0	77.9	73.0	60	91.4	83.6	78.0
100	90.8	83.0	78.0	100	93.5	85.2	79.7
200	100.0	91.6	85.6	200	101.6	93.0	86.5
400	110.4	100.9	94.0	400	110.8	102.2	94.1

Table A-8 The boundary wetting curves of Ceramic1, 2 and 4

Ceramic-1		Ceramic-2		Ceramic-4	
Suction (kPa)	Water content (%)	Suction (kPa)	Water content (%)	Suction (kPa)	Water content (%)
1000000	0	1000000	0	1000000	0
400	6.695	400	6.171	400	8.324
200	10.041	200	10.074	200	10.866
100	13.796	100	11.599	100	14.954
60	17.142	60	12.714	60	19.006
30	21.715	30	15.242	30	23.978
15	27.588	19.5	17.175	15	29.282
7.3	32.273	7	21.896	7	33.039
3.3	35.061	4	23.420	4	34.807
1	39.039	2	25.167	2	35.912
0.1	42.756	0.1	28.253	0.1	38.974

Table A-9 The boundary wetting curves of Sensor-4, 5 and 6

Ceramic-1		Ceramic-2		Ceramic-4	
Suction (kPa)	Sensor output (mv)	Suction (kPa)	Sensor output (mv)	Suction (kPa)	Sensor output (mv)
500000	131.3	500000	120.3	500000	111.1
400	116.4	400	104.4	400	99.4
200	107.3	200	98.0	200	91.7
100	97.5	100	88.5	100	82.9
60	92.0	60	83.0	60	78.4
30	85.5	30	77.6	30	72.8
18	81.6	18	74.5	18	69.5
11	78.9	11	72.3	11	67.5
7	77.3	7	71.3	7	66.5
4	76.0	4	70.0	4	65.0
2	75.0	2	69.0	2	64.0
0.1	72.5	0.1	67.0	0.1	63.0

Table A-10 Drying and wetting outside the main hysteresis loop for Ceramic-2

Case-I			Case-II		
	Suction (kPa)	Water content (%)		Suction (kPa)	Water content (%)
	2	58.216		2	44.758
drying	4.7	55.911	drying	4	43.643
	7	48.476		7	41.041
	7	48.476		7	41.041
Wetting	4	48.587	wetting	4	41.041
	2	49.591		2	41.413
	0.1	50.483		0.4	42.416
	0.1	50.483		0.4	42.416
	2	50.520		2	42.751
	4	50.000		4	42.602
drying	7	47.732	drying	7	39.554
	15	35.836		15	35.948
	30	30.372		30	30.260
	15	33.287		60	24.387
	15	33.287			
	7	36.262			
wetting	4	37.570			
	2	39.000			
	1	40.000			
	0.1	41.100			

Table A-11 The increase in water content when the ceramic is submerged in water

Ceramic-1		Ceramic-2		Ceramic-4	
Elapsed time (hr)	Degree of saturation (%)	Elapsed time (hr)	Degree of saturation (%)	Elapsed time (hr)	Degree of saturation (%)
0.0005	0	0.0003	0	0.0003	0
0.0014	2.149	0.0014	2.827	0.0014	0.881
0.003	4.232	0.003	4.523	0.003	1.636
0.006	7.227	0.006	6.093	0.006	2.705
0.02	14.128	0.02	9.422	0.02	5.724
0.03	18.295	0.03	13.066	0.03	10.694
0.07	24.025	0.07	17.777	0.07	17.487
0.13	31.577	0.13	24.687	0.13	22.457
0.38	46.813	0.25	31.974	0.25	27.175
0.5	53.584	0.6	41.584	0.6	39.252
1.0	63.480	1.0	44.160	1.0	48.877
2.8	64.066	2.3	46.296	2.3	60.829
4.0	64.131	4.0	48.243	4.0	62.087
26.0	67.061	8.5	49.499	8.5	62.464
44.0	69.014	28.0	50.881	28.0	64.225
50.0	69.730	49.5	51.635	49.5	64.729
75.0	70.707	73.0	52.138	73.0	65.169
97.5	71.423	168.5	53.582	168.5	65.924
148.0	72.856	296.5	55.278	296.5	67.245
188.0	73.572	924.0	62.440	924.0	72.151
		991.0	63.193	991.0	72.780
		1813.5	66.334	1813.5	75.171